AD-A216 222

TURBULENCE SCALE EFFECTS ON HEAT TRANSFER IN A LINEAR TURBINE CASCADE

THESIS

Lello Galassi
Captain, USAF

AFIT/GAE/ENY/89D-11

DEPARTMENT OF THE AIR FORCE

AIR UNIVERSITY

AIR FORCE INSTITUTE OF TECHNOLOGY

Wright-Patterson Air Force Base, Ohio

89 12 29 031

TURBULENCE SCALE EFFECTS ON HEAT TRANSFER
IN A LINEAR TURBINE CASCADE

THESIS

Lello Galassi
Captain, USAF

DTIC
S ELECTE
DEC 29 1989
B D

AFIT/GAE/ENY/89D-11

TURBULENCE SCALE EFFECTS ON HEAT TRANSFER
IN A LINEAR TURBINE CASCADE

THESIS

Presented to the Faculty of the School of Engineering

of the Air Force Institute of Technology

Air University

In Partial Fulfillment of the

Requirements for the Degree of

Master of Science in Aeronautical Engineering

Lello Galassi, B.S.A.A.

Captain, USAF

Dec, 1989

Acknowledgments

This thesis would not have been possible without the the sincere dedication of many individuals. I would like to express my appreciation to all whom have contributed to to this effort. First, my wife, Gretchen diserves recognition for her patience and understanding during the numerous hours I diserted her in order to do research. Secondly, the support of my thesis advisor, LtCol Paul King, provided the depth of knowledge and guidance throughout the entire thesis. His expertise formed the "backbone" of this thesis. Similarly, I would like to thank my thesis committee members, Dr. William Elrod, and Capt Daniel Fant; and my sponsor, Dr. Richard Rivir, for their contribution during the formulation, testing and review of this thesis. Lastly, I am deeply indepted to Mr. Jay Anderson and Mr. Dan Rioux, of the AFIT Aeronautical Laboratory for their technical assistance with this project; Mr. John Brohas and the AFIT Model Shop personnel, for their support; and Mr. Tony Brigelli, who so willingly repaired the instrumentation I so frequently broke. Thank you everyone.

Lello Galassi

ii

Table of Contents

List of Figures

xi

List of Tables

List of Symbols

Symbol	Definition (units)

lower-case symbols:

a_1, a_2	- First velocity calibration coefficient for hot-wires 1 and 2
b	- Outside diameter of jet-grid tube (mm)
b_1, b_2	- Second velocity calibration coefficient for hot-wires 1 and 2
c	- Axial chord of the turbine blade (mm)
c_1, c_2	- Third velocity calibration coefficient for hot-wires 1 and 2
D	- Injection orifice diameter (mm)
h	- Convection heat transfer coefficient ($\frac{W}{m^2 K}$)
k_1	- Angle calibration coefficient for hot-wire 1
k_2	- Angle calibration coefficient for hot-wire 2
k_{air}	- Thermal conductivity of air ($\frac{W}{m K}$)
k_{foam}	- Thermal conductivity of urethane foam ($\frac{W}{m K}$)
m	- Coefficient, wedge flow parameter (m)
n	- Turbulence frequency (s^{-1})
n_1	- Normal to hot-wire 1
n_2	- Normal to hot-wire 2
q'	- Heat transfer rate (W)
$q'_{conduction}$	- Heat transfer rate due to conduction (W)
$q'_{convection}$	- Heat transfer rate due to surface convection (W)
$q'_{electrical}$	- Heat transfer rate due to electrical heating (W)
$q'_{radiation}$	- Heat transfer rate due to radiation (W)
q_∞	- Free-stream dynamic pressure (kPa)
s	- Distance measured from the turbine blade leading edge along the blade surface (mm)
t	- time (s)
u'	- Fluctuating component of X-direction velocity ($\frac{m}{s}$)
$\bar{u}$	- Mean velocity along the X-direction ($\frac{m}{s}$)

$\overline{u'}$	- Mean fluctuating velocity component along the tunnel X-direction ($\frac{m}{s}$)
$\overline{v'}$	- Mean fluctuating velocity component along the tunnel Y-direction ($\frac{m}{s}$)
x	- Distance along the tunnel X-direction (mm)
y	- Distance along the tunnel X-direction (mm)
z	- Distance along the tunnel X-direction (mm)

upper case symbols:

A	- Section surface area of the heated turbine blade (m^2)
A_{tot}	- Total surface area of the heated turbine blade (m^2)
B	- Bisector designator
C	- Coefficient used in the momentum solution for wedge flow
C_p	- Coefficient of pressure on the turbine blade surface
E_1	- Computed voltage output of hot-wire 1 (volt)
E_2	- Computed voltage output of hot-wire 2 (volt)
E_1'	- Measured hot-wire 1 output from the velocity calibration (volt)
E_2'	- Measured hot-wire 2 output from the velocity calibration (volt)
E_1''	- Measured hot-wire 1 output from the angle calibration (volt)
E_2''	- Measured hot-wire 2 output from the angle calibration (volt)
$ERR_{1_{SSE}}$	- Mean squared error between computed and measured hot-wire 1 output from the velocity calibration (volt)
$ERR_{2_{SSE}}$	- Mean squared error between computed and measured hot-wire 2 output from the velocity calibration (volt)
$ERR_{1_{SSE}}^A$	- Mean squared error between computed and measured hot-wire 1 output from the angle calibration (volt)
$ERR_{2_{SSE}}^A$	- Mean squared error between computed and measured hot-wire 2 output from the angle calibration (volt)
$H(u')$	- Contribution to $\overline{u'^2}$ from the Fourier transform of u' ($\frac{m^2}{s^2}$)
I	- Electrical current (ampere)
L	- Linear distance between an exterior thermocouple and an interior thermocouple on the turbine blade (mm)

N	- Turbulence frequency cutoff (s^{-1})
N_{tot}	- Highest turbulence frequency measured (s^{-1})
Nu	- Nusselt number on the turbine blade surface
P	- Static surface pressure on the turbine blade (kPa)
P_0	- Free-stream total pressure (kPa)
P_∞	- Free-stream static pressure (kPa)
Pr	- Free-stream Prandtl number
R	- Axisymmetric radius
R'	- Electrical resistance (ohm)
Re_c	- Reynolds number based on the turbine blade axial chord
Re_s	- Reynolds number based on distance along the blade surface from the leading edge of the turbine blade
Re_{Δ_i}	- Reynolds number based on boundary layer enthalpy thickness
St	- Stanton number on the turbine blade surface
T_∞	- Free-stream temperature (K)
T_{int}	- Turbine blade internal temperature (K)
T_{mean}	- Mean fluid temperature (K)
T_s	- Turbine blade surface temperature (K)
Tu	- Free-stream turbulence in percent
Tu_x	- X-component of free-stream turbulence in percent
Tu_y	- Y-component of free-stream turbulence in percent
$U_{1,eff}$	- Effective flow velocity measured by hot-wire 1 ($\frac{m}{s}$)
$U_{2,eff}$	- Effective flow velocity measured by hot-wire 2 ($\frac{m}{s}$)
U_∞	- Free-stream velocity ($\frac{m}{s}$)
V	- Vector sum of $\bar{u} + \bar{v}$
W_1	- Hot-wire 1
W_2	- Hot-wire 2
$\underline{W_1}$	- Hot-wire 1 quadratic fit velocity matrix
$\underline{W_2}$	- Hot-wire 2 quadratic fit velocity matrix

lower-case Greek symbols:

ϵ — Surface heat radiation emissivity

μ — Dynamic viscosity coefficient ($\frac{kg}{m \cdot s}$)

ν — Local kinematic viscosity ($\frac{m^2}{s}$)

ν_∞ — Free-stream kinematic viscosity ($\frac{m^2}{s}$)

ρ — Local air density ($\frac{kg}{m^3}$)

ρ_∞ — Free-stream air density ($\frac{kg}{m^3}$)

ψ — Hot-wire probe yaw angle

θ_w — Wedge half angle

θ_1 — Free-stream velocity incidence angle with hot-wire 1 (degrees)

θ_2 — Free-stream velocity incidence angle with hot-wire 2 (degrees)

upper case Greek symbols:

$\Im$ — X-type hot-wire bisector angle

Δ — Offset angle of hot-wire bisector from the tunnel reference direction

Δn — Turbulence frequency bandwidth (s^{-1})

Δt — Time interval (s)

Δ_{th} — Thermal boundary layer thickness (m)

Δ_2 — Enthalpy thickness of a boundary layer (m)

Δ_4 — Conduction thickness (m)

Subscripts

Unless otherwise noted, subscripts are designated as follows:

i — designates the i th blade surface section

x — pertains to no jet-grid in the flow

0 — Station 0 in the tunnel, $\frac{x}{b} = 15.75$

02 — Station 02 in the tunnel, $\frac{x}{b} = 25.67$

1 — pertains to wire 1

2 — pertains to wire 2

∞ — pertains to the free-stream

Abstract

Heat transfer for a turbine cascade is examined for turbulence scale effects. The turbulence integral scale and microscale lengths of the free-stream flow are controlled by air-jet injection through a grid placed in the free-stream flow. Air is injected into the flow in three primary directions: co-flow, cross-flow, and counter-flow, at several injection pressures. Results are obtained for heat transfer on the blade without the jet-grid in the free-stream flow. Surface pressures on the turbine blade are examined for three injection directions. Surface heat transfer on the blade and turbulence intensity and turbulence scale results are obtained for two grid locations, three air injection orientations, and three injection orifice diameters over a range of injection pressures. Turbulence integral scale and microscale lengths are measured in two free-stream flow coordinates. The turbulence intensity decay is determined. Heat transfer on the turbine blade is compared with the turbulence integral scale and microscale lengths.

Results show the integral scale length is primarily dependent on the diameter of the jet-grid tube, but may be controlled to a lesser degree by changing the orientation of the jet-grid injection to a co-flow or counter-flow direction; or by changing the secondary air-jet injection pressure. The turbulence microscale is primarily dependent on the location of the jet-grid within the flow, but, to a lesser degree, controlled by the orientation of the jet-grid injection, jet orifice diameter, and injection pressure.

In general, jet-grid injection produces a lower turbulence intensity of the free-stream than a non-blowing grid, larger turbulence microscale, and lower surface heat transfer co-efficient. The turbulence integral scale is nearly constant with turbulence intensity and its length is on the order of the outside diameter if the jet-grid tube. The Stanton number and the Nusselt number increase with increasing turbulence intensity and decreasing turbulence microscale length. Turbulent boundary layer heat transfer predictions compare favorably on the pressure surface of the turbine blade, except at the leading edge of the turbine blade for moderate free-stream turbulence levels (4-6 percent). Laminar boundary

layer heat transfer predictions compare favorably on the turbine blade suction surface for low free-stream turbulence levels (0-1.3 percent).

TURBULENCE SCALE EFFECTS ON HEAT TRANSFER
IN A LINEAR TURBINE CASCADE

I. INTRODUCTION

1.1 General

The accurate knowledge of heat transfer distribution on gas turbine blades is of practical interest in the design of turbomachinery. Accurate prediction of convective heat transfer within the turbine blade cascade is of particular importance to the design of gas turbine airfoil design, which, in turn, affects the overall engine cooling design, cycle efficiency, and hardware durability. Documentation of heat transfer data for turbine blades is relatively scarce as compared to similar documentation available for flat plate geometries. Documentation of turbulence scales in relation to turbine blade heat transfer is nonexistent.

Heat transfer within a gas turbine blade cascade has been studied for turbulence intensity and Reynolds number effects (Consigny, 1982), (Priddy, 1985). Other studies have concentrated on turbulent boundary layer development over the turbine blade surface and related heat transfer to the blade (Blair, 1989a), (Priddy, 1985). Blair (Blair, 1989b) reports a 20-30 percent increase in effective heat transfer rates for high turbulence level (8-10 percent) free-stream flow over low turbulence free-stream flow. More recently, heat transfer on a flat plate for various turbulence levels generated by "jet-grid" injection of a secondary flow into the primary flow has been studied (Young, 1989). Results indicate an increase of up to 45 percent in Stanton numbers may be achieved with high turbulence free-stream flow as compared to low turbulence free-stream flow. Additionally, the same study found the Stanton number, for the flat plate, to be inversely proportional to the turbulence microscale.

This thesis continues in the manner of the latter study for a turbine cascade. Specifically, turbulence integral scales, microscales, turbulence intensity and their relation to surface heat transfer is investigated for a turbine blade cascade.

1.2 Objectives

The objectives of this thesis are as follows:

(1) Determine the turbulence level induced by jet-grid injection at two downstream locations. Determine the effects of injection pressure, injection orifice diameter, and injection direction of a secondary flow on free-stream turbulence.

(2) Measure turbulence energy, integral scales and microscales for each flow condition imposed on the free-stream flow by jet-grid injection. Determine the relationship between turbulence intensity and turbulence integral scale and microscale lengths for the jet-grid configurations given in objective 1.

(3) Measure the surface pressures on the turbine blade for the various jet-grid injection configurations.

(4) Determine the heat transfer on the turbine blade in terms of the Stanton and Nusselt numbers for each jet-grid injection configuration given in objective 1. Determine the relationship between surface heat transfer and turbulence scales.

1.3 Method

A brief overview of the experimental methods used is now presented.

Turbine blade surface pressures, and heat transfer were measured for various turbulence levels. Free-stream turbulence levels were controlled by varying the location of the jet-grid, the jet-grid injection pressure, injection orifice diameter, and the direction of injection with respect to the mainsteam flow. A total of 66 different free-stream flow conditions were tested, along with 3 baseline free-stream flow configurations. Each test configuration is identified by a three place letter, number or combination thereof. The free-stream flow conditions tested are listed in Table 1.1 and Table 1.2. Table 1.1 is a list of flow configurations tested with the turbulence jet-grid placed at the first station (designated as *station 0*) ahead of the turbine blade row. Its upstream location is denoted by the nondimensional distance $\frac{x}{b}$, where x is a linear distance and b is the outside diameter of the turbulence jet-grid tube. Table 1.2 lists the flow configurations tested with the turbulence jet-grid placed at the second station (designated as *station 02*) upstream from the

turbine blade row. Configurations tested without any jet-grid placed in the free-stream are denoted with the grid location (ξ) denoted appropriately as N/A. Streamwise secondary air injection is denoted as co-flow, injection perpendicular to the free-stream is denoted as cr-flow, and injection against the free-stream is denoted as ct-flow in Tables 1.1 and 1.2.

The derrivation of turbulence scales and the theory of laminar and turbulent boundary layer heat transfer are discussed in Chapter 2. The experimental apparatus used to perform the experiment and instrumentation are discussed in Chapter 3. Chapter 4 presents detailed experimental procedures used to measure the turbine blade surface pressures, the free-stream turbulence and turbulence integral and microscale lengths, and measure the heat transfer on the turbine blade surface. The results of this study are discussed in Chapter 5. The results of the blade surface pressure measurements are presented as nondimensional pressure coefficients (C_p). Both turbulence integral scale length and microscale length are calculated for the primary tunnel reference directions. Surface heat transfer on the blade is presented in the form of nondimensional Nusselt numbers (Nu) and Stanton numbers (St).

Table 1.1. Test configurations for the turbine cascade wind tunnel–station 0

test	station ξ	injection direction	orifice diameter D mm	injection pressure kPa
XXX	no grid	N/A	N/A	N/A
000	15.75	N/A	N/A	N/A
A11	15.75	co-flow	0.66	83.5
A12	15.75	co-flow	0.66	156.3
A13	15.75	co-flow	0.66	245.8
A14	15.75	co-flow	0.66	300.0
A15	15.75	co-flow	0.66	106.2
A21	15.75	co-flow	1.32	78.2
A22	15.75	co-flow	1.32	157.5
A23	15.75	co-flow	1.32	243.1
A24	15.75	co-flow	1.32	296.3
A31	15.75	co-flow	1.98	78.0
A32	15.75	co-flow	1.98	160.5
A33	15.75	co-flow	1.98	233.9
A34	15.75	co-flow	1.98	291.8
B11	15.75	cr-flow	0.66	83.4
B12	15.75	cr-flow	0.66	158.2
B13	15.75	cr-flow	0.66	247.1
B14	15.75	cr-flow	0.66	303.3
B21	15.75	cr-flow	1.32	80.0
B22	15.75	cr-flow	1.32	153.4
B23	15.75	cr-flow	1.32	238.9
B24	15.75	cr-flow	1.32	293.3
B31	15.75	cr-flow	1.98	79.2
B32	15.75	cr-flow	1.98	150.2
B33	15.75	cr-flow	1.98	228.7
C11	15.75	ct-flow	0.66	83.9
C12	15.75	ct-flow	0.66	163.5
C13	15.75	ct-flow	0.66	238.6
C14	15.75	ct-flow	0.66	295.1
C21	15.75	ct-flow	1.32	81.1
C22	15.75	ct-flow	1.32	155.0
C23	15.75	ct-flow	1.32	238.8
C24	15.75	ct-flow	1.32	292.4
C31	15.75	ct-flow	1.98	80.7
C32	15.75	ct-flow	1.98	143.2
C33	15.75	ct-flow	1.98	241.1
C34	15.75	ct-flow	1.98	293.2

Table 1.2. Test configurations for the turbine cascade wind tunnel-station 02

test	station $\frac{x}{L}$	injection direction	orifice diameter D mm	injection pressure kPa
002	25.67	N/A	N/A	N/A
D11	25.67	co-flow	0.66	86.6
D12	25.67	co-flow	0.66	154.2
D13	25.67	co-flow	0.66	248.4
D21	25.67	co-flow	1.32	76.5
D22	25.67	co-flow	1.32	161.4
D23	25.67	co-flow	1.32	235.9
D31	25.67	co-flow	1.98	80.4
D32	25.67	co-flow	1.98	160.6
D33	25.67	co-flow	1.98	240.1
E11	25.67	cr-flow	0.66	82.8
E12	25.67	cr-flow	0.66	163.8
E13	25.67	cr-flow	0.66	238.4
E21	25.67	cr-flow	1.32	81.7
E22	25.67	cr-flow	1.32	169.0
E23	25.67	cr-flow	1.32	239.9
E31	25.67	cr-flow	1.98	80.2
E32	25.67	cr-flow	1.98	160.4
E33	25.67	cr-flow	1.98	238.1
F11	25.67	ct-flow	0.66	81.5
F12	25.67	ct-flow	0.66	156.1
E13	25.67	ct-flow	0.66	244.4
F21	25.67	ct-flow	1.32	83.1
F22	25.67	ct-flow	1.32	152.5
F23	25.67	ct-flow	1.32	237.6
F31	25.67	ct-flow	1.98	80.3
F32	25.67	ct-flow	1.98	160.8
F33	25.67	ct-flow	1.98	236.4

II. THEORY

2.1 Turbulence Integral Scale and Microscale Lengths

The turbulence integral scale (Λ) and microscale (λ) are of interest from the standpoint of turbulence. The integral scale defines the size of the large turbulent eddies in a turbulent flow. The microscale is a measure of the smallest measurable homogeneous group of fluid, where all particles within the group share the same velocity. Figure 2.1 shows the concept of turbulence integral scales and microscales. Note that the turbulence integral scales are comprised of microscales.

For analysis purposes, consider the velocity of a fluid in a single direction.

The velocity in the X-direction (u) may be considered as consisting of a steady state component ($\overline{u}$) and a fluctuating component (u') of velocity.

$$u = \overline{u} + u' \tag{2.1}$$

In the same manner that vibrations in a solid occur at different frequencies and strength, turbulence in a fluid, such as air, occurs at different frequencies and with different strengths of turbulence. These frequencies are measurable and related to the turbulence scale lengths by the spectral distribution of the turbulence. If $E_{u'}(n)$ defines the spectral distribution of $\overline{u'^2}$ in the frequency bandwidth between n and $n + dn$, then

$$\overline{u'^2} = \int_0^\infty E_{u'}(n)dn \tag{2.2}$$

In Equation 2.2, the quantity dn is the unit frequency interval. $E_{u'}(n)$, the *turbulence power per frequency bandwidth* (Δn), is obtained from the Fourier transform of u'^2 from the time domain to the frequency domain in the following manner. .

For a discrete function, Parseval's theorem is written (Brigham, 1986) as

$$\sum_{k=0}^{N-1} u'^2 = \frac{1}{N} \sum_{n=0}^{N-1} \left[H(u') \right]^2 \tag{2.3}$$
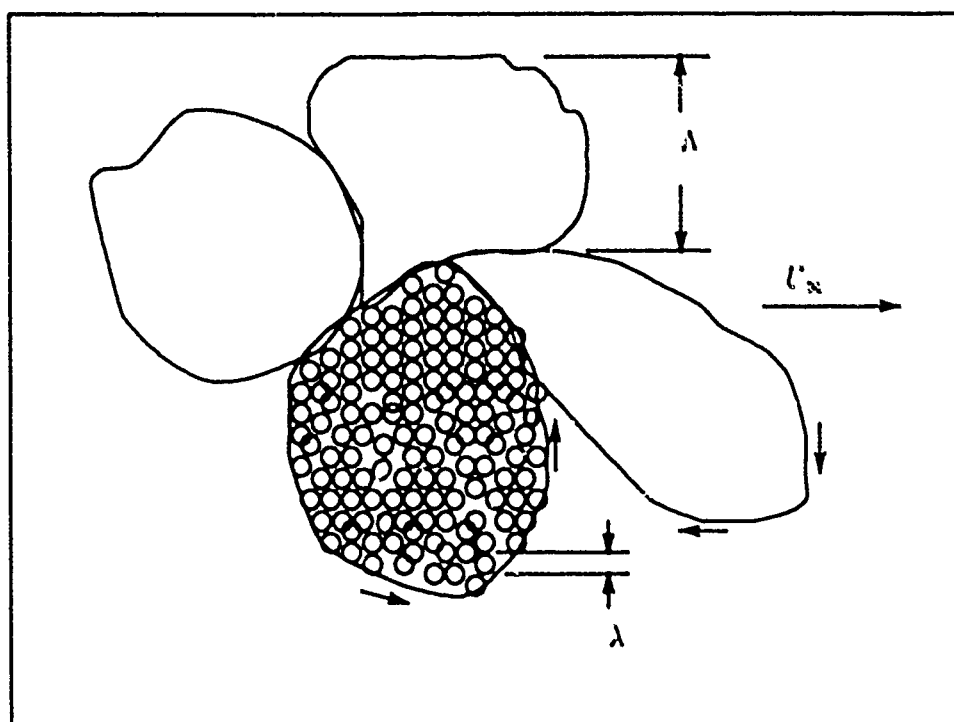
Figure 2.1. Schematic of turbulence integral scales and microscales

where

$H(u')$ = spectral function of u' from the Fourier transform of u'

or rewriting Equation 2.3,

$$u'_{rms}{}^2 = \sum_{n=0}^{N} \left[\frac{H(u')}{N}\right]^2 \tag{2.4}$$

Comparing Equation 2.4 with Equation 2.2, $E_{u'}(n)$ must be related to $H(n')$ as

$$E_{u'}(n) = \left[\frac{H(u')}{N}\right]^2 \frac{1}{\Delta n} \tag{2.5}$$

From the theory of Fourier Transforms, the longitudinal correlation function ($f(x)$) of the spectral distribution of turbulence is related to the spectral power density (Hinze, 1959). The function $f(x)$ is related to $E_{u'}(n)$ as

$$f(x) \equiv \frac{1}{u'^2} \int_0^{\infty} E_{u'}(n) \cos\left(\frac{2\pi n x}{\overline{u}}\right) dn \tag{2.6}$$

By inverse transform relation, Equation 2.6 becomes

$$E_{u'}(n) = \frac{4\overline{u'^2}}{\overline{u}} \int_0^{\infty} f(x) \cos\left(\frac{2\pi n x}{\overline{u}}\right) dx \tag{2.7}$$

The primary derivation of the longitudinal correlation function is for a time series. In Equations 2.6 and 2.7, time (t) has been replaced using Taylor's hypothesis. Namely,

$$t = \frac{x}{\overline{u}}$$

As $n \to 0$, then Equation 2.7 becomes

$$\lim_{n \to 0} \left(\frac{\overline{u}}{4\overline{u'^2} E_{u'}(n)}\right) = \int_0^{\infty} f(x) dx \equiv \Lambda_u \tag{2.8}$$

where

$$\Lambda_u \qquad = X\text{-component turbulence integral scale}$$

The microscale (λ_u) is

$$\lambda_u{}^2 = \left[\frac{-2}{\left(\frac{\partial^2 f}{\partial x^2} \right)_{x=0}} \right] \qquad (2.9)$$

Differentiating Equation 2.6 twice yields

$$\lambda_u = \left(\frac{1}{\frac{2\pi^2}{\overline{u}^2 u'^2} \int_0^\infty n^2 E_u(n)\, dn} \right)^{\frac{1}{2}} \qquad (2.10)$$

In experimental measurements of turbulence, the integrals in Equations 2.9 and 2.10 are replaced by summations over a finite frequency domain, $E_u'(n)$ is computed using Equation 2.5, and n is a finite frequency bandwidth defined as

$$n = \frac{1}{(N_{tot}\Delta t)} \qquad (2.11)$$

where

N_{tot} = total sample size

Δt = sample time interval

The foregoing analysis is based on a similar analysis presented by Cebeci and Smith (Cebeci, 1974). In a similar manner, the turbulence scales are determined for any other coordinate direction of interest.

2.2 Turbulence Intensity Decay

The decay of turbulence in a free-stream flow is a measure of the dissipation of the turbulence microscale lengths. The dissipation is in the form of turbulence microscale growth, where the microscales dissipate their energy by combining with other microscales. Studies by Young and Han (Young, 1989) and Blair (Blair, 1983a) indicate the microscale dissipation is related to the size of the turbulence generating grid. Blair offers the following

correlation for dissipation of the turbulence level (Tu),

$$Tu = 0.78 \left(\frac{x}{b}\right)^{-\frac{5}{7}}$$ (2.12)

Equation 2.12 is applicable only where the free-stream turbulence is uniform. Blair determined uniform free-stream turbulence is not reached until approximately ten grid tube diameters downstream of the turbulence generating grid; therefore Equation 2.12 is only applicable for $\frac{x}{b} \geq 10$.

The studies of Young and Han, found excellent agreement with Equation 2.12 with the jet-grid place in the flow, but with no injection. With secondary flow injection through the jet grid, the turbulence levels were generally higher than those predicted by Equation 2.12. The dissipation of the integral scale was not correlated. In a turbine cascade wind tunnel, the turbulence decay has not been correlated.

2.3 Laminar Heat Transfer on a Surface with a Pressure Gradient

Laminar heat transfer for flow over a constant-temperature body of arbitrary shape is developed.

The rate of growth of any thermal boundary layer thickness Δ_{th} is a function of local parameters only (Eckert, 1942).

$$\frac{d\Delta_{th}}{ds} = f\left(\Delta_{th}, U_\infty, \frac{dU_\infty}{ds}, \nu, Pr\right)$$

where

U_∞	= free-stream velocity on the boundary layer edge
s	= the distance along the surface of the body
ν	= local kinematic viscosity
Pr	= Prandtl number of the fluid

Using the thermal conduction thickness ($\Delta_4 = \frac{k}{h}$), where k is the fluid thermal conductivity, and h is the convection heat transfer coefficient, then the variation of Δ_4 is

given in nondimensional form as

$$\frac{U_\infty}{\nu}\frac{d\Delta_4^2}{dx} = f\left(\frac{\Delta_4^2}{\nu}, \frac{dU_\infty}{ds}, Pr\right)$$ (2.13)

Assuming the function f is the same as for the family of wedge flows, then Equation 2.13 is readily evaluated using similarity solutions.

From Kays and Crawford (Kays, 1987), for flow over a flat plate and $Pr = 0.7$,

$$NuRe_s^{-\frac{1}{2}} = C_1$$

from which

$$h \propto U_\infty^{\frac{1}{2}} s^{-\frac{1}{2}}$$

where C_1 is a coefficient which depends on m, the wedge parameter, and Pr. Employing the wedge condition,

$$U_\infty = Cs^m$$

$$\Delta_4 = \frac{k}{h}$$

the following expressions are developed,

$$\frac{U_\infty}{\nu}\frac{d\Delta_4^2}{ds} = \frac{1-m}{(C_1)^2}$$ (2.14)

$$\frac{\Delta_4^2}{\nu}\frac{dU_\infty}{ds} = \frac{m}{(C_1)^2}$$ (2.15)

In the expressions above, m is the wedge flow parameter is defined as

$$m \equiv \frac{\frac{\theta_w}{\pi}}{2 - \frac{\theta_w}{\pi}}$$ (2.16)

where $\theta_w = $ to the wedge half-angle.

For $Pr = 0.7$, Equations 2.14 and 2.15 are plotted for the exact wedge solutions.

Smith and Spaulding (Smith, 1958) propose a linear fit to the wedge flow solution

2-6
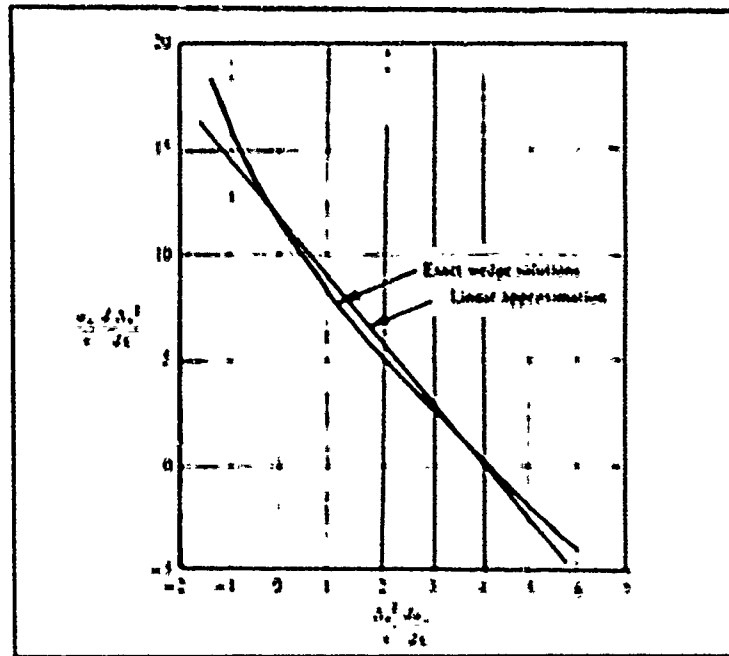
Figure 2.2. Wedge flow solution for a laminar boundary layer, (Kays, 1987)

shown in Figure 2.2 of the form

$$\frac{U_\infty}{\nu}\frac{d\Delta_4^2}{ds} = 11.68 - 2.87\frac{\Delta_4^2}{\nu}\frac{dU_\infty}{ds} \tag{2.17}$$

Equation 2.17 is integrated and reduced to

$$\Delta_4^2 = \frac{11.68\nu \int_0^s U_\infty^{1.87} ds}{U_\infty^{2.87}} \tag{2.18}$$

Noting $\Delta_4 \equiv \frac{k}{h}$, Equation 2.18 is put into the form of a Stanton number (St).
$Pr = 0.7$ is assumed.

$$St = 0.418\frac{\mu^{\frac{1}{2}}(\rho U_\infty)^{0.435}}{\left[\int_0^s (\rho U_\infty)^{1.87} ds\right]^{0.5}} \tag{2.19}$$

where

μ = local viscosity

ρ = local fluid density

Equation 2.19 provides a useful method for calculating the laminar heat transfer for a

2-7

two-dimensional body. Application of the laminar heat transfer theory to the turbine blade is necessarily restricted to those areas along the blade that exhibit laminar or laminar-like flow conditions.

2.4 Heat Transfer on an Axisymetric Body with Arbitrary Varying Freestream Velocity and Surface Temperature

Prediction of surface heat transfer for a turbine blade has been suggested (Ambrok, 1957) to include the arbitrarily varying pressure gradient on an axisymmetric body with a turbulent boundary layer. The model does not account for complex flow phenomena, such as a secondary vortex core, or laminar separation bubbles that may be present within a turbine cascade.

For a constant surface-temperature, constant free-stream velocity, the Stanton number may be expressed in the form

$$St = C Re_s^{-n} \tag{2.20}$$

where

C = a coefficient

Re_s^{-n} = Reynolds number based on surface
distance s raised to the $-n$ power

The energy integral for a flat plate is given as

$$St = \frac{d\Delta_2}{ds} \tag{2.21}$$

where

Δ_2 = enthalpy thickness

Substituting Equation 2.20 into Equation 2.21, and integrating yields

$$\Delta_2 = \frac{C U_\infty^{-n} s^{1-n}}{\nu^n (1 - n)} \tag{2.22}$$

where

$$U_\infty \qquad = \text{the local freestream velocity}$$

$$\nu \qquad = \text{local kinematic viscosity of the fluid}$$

Equation 2.22 is substituted into Equation 2.20 to give the Stanton number as a function of the Reynolds number with respect to Δ_2 rather than s.

$$St = C(\frac{1-n}{C})^{\frac{-n}{n-1}}(Re_{\Delta_2})^{\frac{-n}{n-1}} \qquad (2.23)$$

Equation 2.23 does not presume any previous history of the turbulent boundary layer on the surface.

For turbulent boundary layers on a flat plate, from (Kays, 1987)

$$C = 0.0287 Pr^{-0.4}$$

and

$$n = 0.2$$

$$Pr = \text{Prandtl number of the fluid flow}$$

Evaluation of Equation 2.23 using the given values of C and n give

$$St = 0.0125 Pr^{-0.5} Re_{\Delta_2}^{-0.25} \qquad (2.24)$$

In order to evaluate the local surface heat flux in terms of the local surface temperature difference, the integral energy equation is used.

$$q' = \frac{C_p}{R}\frac{d}{ds}[\Delta_2 R \rho_\infty U_\infty (T_s - T_\infty)] \qquad (2.25)$$

where

$$q' \qquad = \text{heat flux per unit surface area}$$

$$C_p \qquad = \text{specific heat at constant pressure}$$

$$\rho_\infty \qquad = \text{local free-stream density}$$

$$T_\infty \qquad = \text{local free-stream temperature}$$

$$T_s \qquad = \text{local surface temperature}$$

$$R \qquad = \text{axisymmetric radius}$$

Noting

$$St \equiv \frac{q'}{(T_s - T_\infty)\rho_\infty C_p U_\infty} \tag{2.26}$$

then Equation 2.25 may be algebraically manipulated into the form

$$\frac{1 - n}{C}^{\frac{1}{n-1}} R^{\frac{1}{1-n}} \mu^{\frac{n}{1-n}} \rho_\infty U_\infty (T_s - T_\infty)^{\frac{1}{1-n}} ds = d[\rho_\infty U_\infty \Delta_2 R(T_s - T_\infty)]^{\frac{1}{1-n}} \tag{2.27}$$

where

μ = local fluid viscosity

Equation 2.27 may be integrated directly if we assume at the stagnation point $U_\infty = 0$ where $s = 0$. Using Equation 2.26 with Equation 2.27 gives

$$St = 0.0287 Pr^{-0.4} \frac{R^{0.25}(T_s - T_\infty)^{0.25}\mu^{0.2}}{[\int_0^s R^{1.25}(T_s - T_\infty)^{1.25}\rho_\infty U_\infty ds]^{0.2}} \tag{2.28}$$

where C and n are the same numerical values previously proposed.

For the turbine blade, R is a constant, and ρ_∞ is relatively constant for low Mach numbers. Equation 2.28 is further simplified for the above conditions as

$$St = 0.0287 Pr^{-0.4} \frac{(T_s - T_\infty)^{0.25}\mu^{0.2}}{[\int_0^s (T_s - T_\infty)^{1.25}U_\infty ds]^{0.2}} \tag{2.29}$$

Equation 2.29 may be evaluated for turbulent flow over an axisymmetric body with a pressure gradient. Others (Kays, 1987) have found Equation 2.29 to be in good agreement for a variety of applications, including turbine blades. However, it fails badly for strongly accelerated flows where $K > 1 \times 10^{-6}$. K is defined as the acceleration parameter

$$K = \frac{\nu}{U_\infty^2} \frac{dU_\infty}{ds} \tag{2.30}$$

For very strongly accelerated flows, $K > 3.5 \times 10^{-6}$, the entire turbulent boundary layer begins to relaminarize as the viscous sublayer thickens, engulfing the entire boundary layer (Kays, 1970); hence, this theory no longer applies for this condition.

III. EXPERIMENTAL APPARATUS

EXPERIMENTAL APPARATUS

3.1 Turbine Cascade Wind Tunnel

Testing was conducted in a large scale, low-aspect ratio, linear turbine cascade wind tunnel shown in Figure 3.1. The facility is owned by the Air Force Institute of Technology (AFIT) Aeronautical Engineering Department, Wright-Patterson AFB, Ohio. Specific tunnel dimensions and tunnel flow characteristics are listed in Table 3.1. The wind tunnel is a draw-down tunnel, powered by a Buffalo Forge, Model No. BL - 365, centrifugal fan. The fan was powered at a constant velocity by a 14.9 kW, 240 volt electric motor. The tunnel wind velocity was manually controlled with a series of variable angle inlet vanes which were set at an angle opposite to the direction of revolution of the fan; hence, tended to reduce flow swirl normally associated with centrifugal fans.

3.2 Turbine Blade Cascade and Turbine Blade Profile

A photograph of the turbine blade cascade test section is shown in Figure 3.2. The turbine blade cascade consists of four geometrically identical turbine blade sections. A reference plane was arbitrarily established at the leading edge of the turbine blades and a reference axis system established with the origin in the reference plane. Figure 3.3 is a schematic of the turbine blade test section, the reference axes, and the reference plane. The Z-axis is into the paper, with Z = 0 corresponding to the point located on the inside of the upper endwall of the tunnel. The X-axis was defined in the direction parallel to the incoming flow incidence angle. The Y-axis lies in the reference plane, at a 134.7 degree angle measured in a clockwise direction from the normal to the reference plane. The wind tunnel flow direction was adjusted with inlet side boards so the flow incidence angle to the turbine blade row was 44.7 degrees, as measured in a clockwise direction from the normal of the reference plane. This incidence angle was chosen to match earlier tests using an identical turbine blade profile (Moore, 1984c), (Langston, 1977).

3-1

Figure 3.1. The AFIT low-aspect ratio, linear turbine cascade wind tunnel

Table 3.1. Turbine cascade wind tunnel dimensions and flow parameters

Wind Tunnel Dimensions and Flow Parameters	
nozzle dimension	0.536 m x 0.536 m
nozzle contraction ratio	11.5:1
nozzle length	1.025 m
inlet height	0.114 m
inlet width	0.218 m
inlet length	0.450 m
test section height	0.114 m
tunnel exit length	0.650 m
tunnel inlet to exit angle	75.0°
inlet flow velocity range	42-51 $\frac{m}{s}$ **
exit flow velocity range	76-93 $\frac{m}{s}$
diffuser length	1.922 m
freestream turbulence level	1.26 % **

** Measured at $\frac{x}{b} = 15.75$, $\frac{y}{b} = 8.00$, and $\frac{z}{b} = 0.00$

Two locations upstream of the reference plane were chosen for placement of the jet-grid device. The first position (station 0) was at a nondimensional distance of $\frac{x}{b} = 15.75$ ahead of the reference plane, where x is the linear distance and b is the jet-grid tube diameter. The second position (station 02) of the jet-grid was at $\frac{x}{b} = 25.67$ upstream of the reference plane. Figure 3.3 shows the position of each station relative to the reference plane.

The turbine blade true chord was 114.3 mm, with a unity chord to span aspect ratio. Based on the blade axial chord length (c) the range in the exit Reynolds number (Re_c) was 3.0-7.0 x 10^5. The turbine blade nomenclature is given in Figure 3.4. The flow turn angle through the blade row was 105 degrees.

3.3 Turbulence Generating Jet-Grid Device

Free-stream turbulence was generated with a jet-grid device. The jet-grid device allows the user to vary the intensity of freestream turbulence by varying the injection pressure (secondary mass flow), and by varying the direction of the injection jets. Additionally, the turbulence intensity may be varyied through placement of the jet-grid at
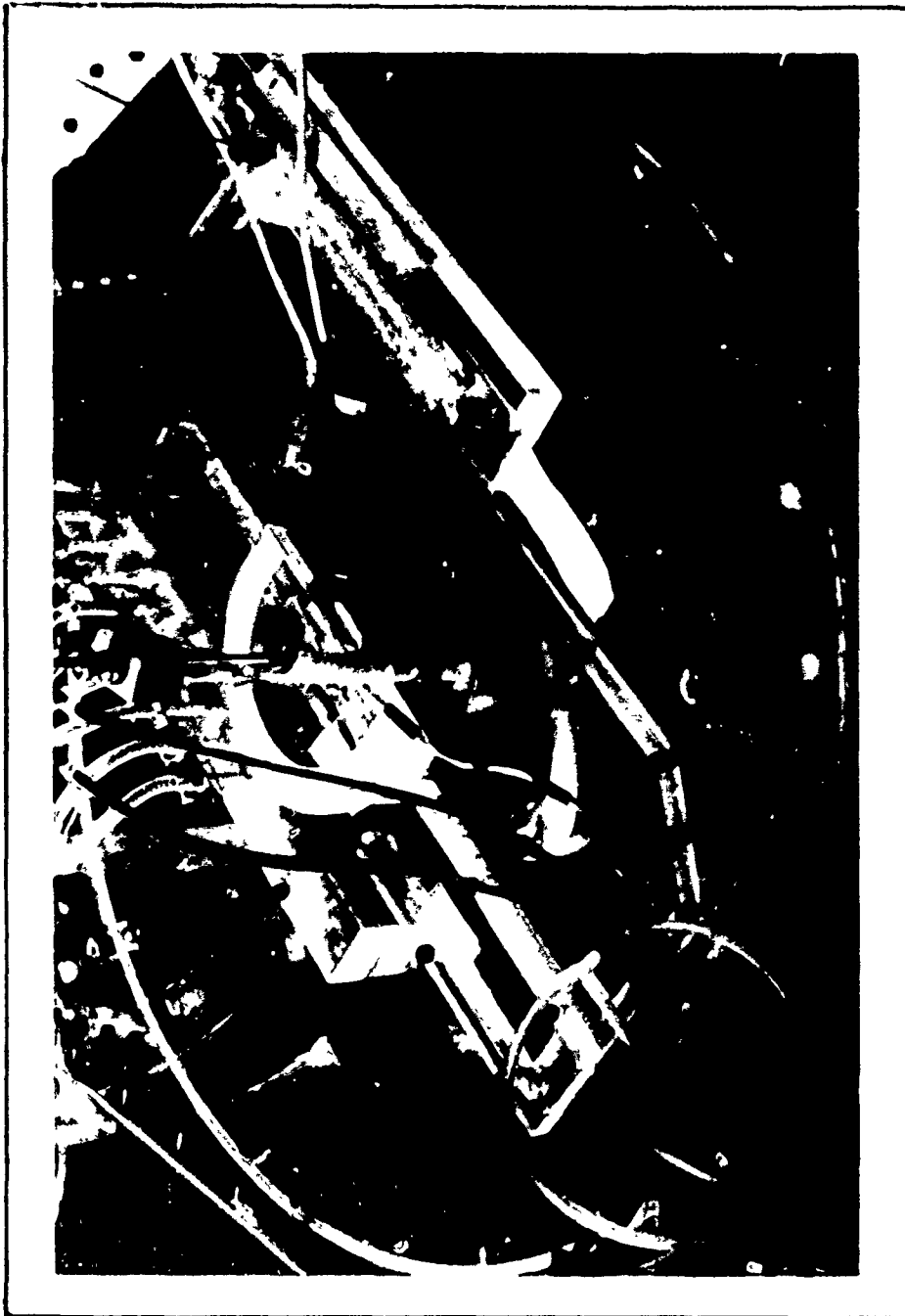
Figure 3.2. Turbine blade cascade test section
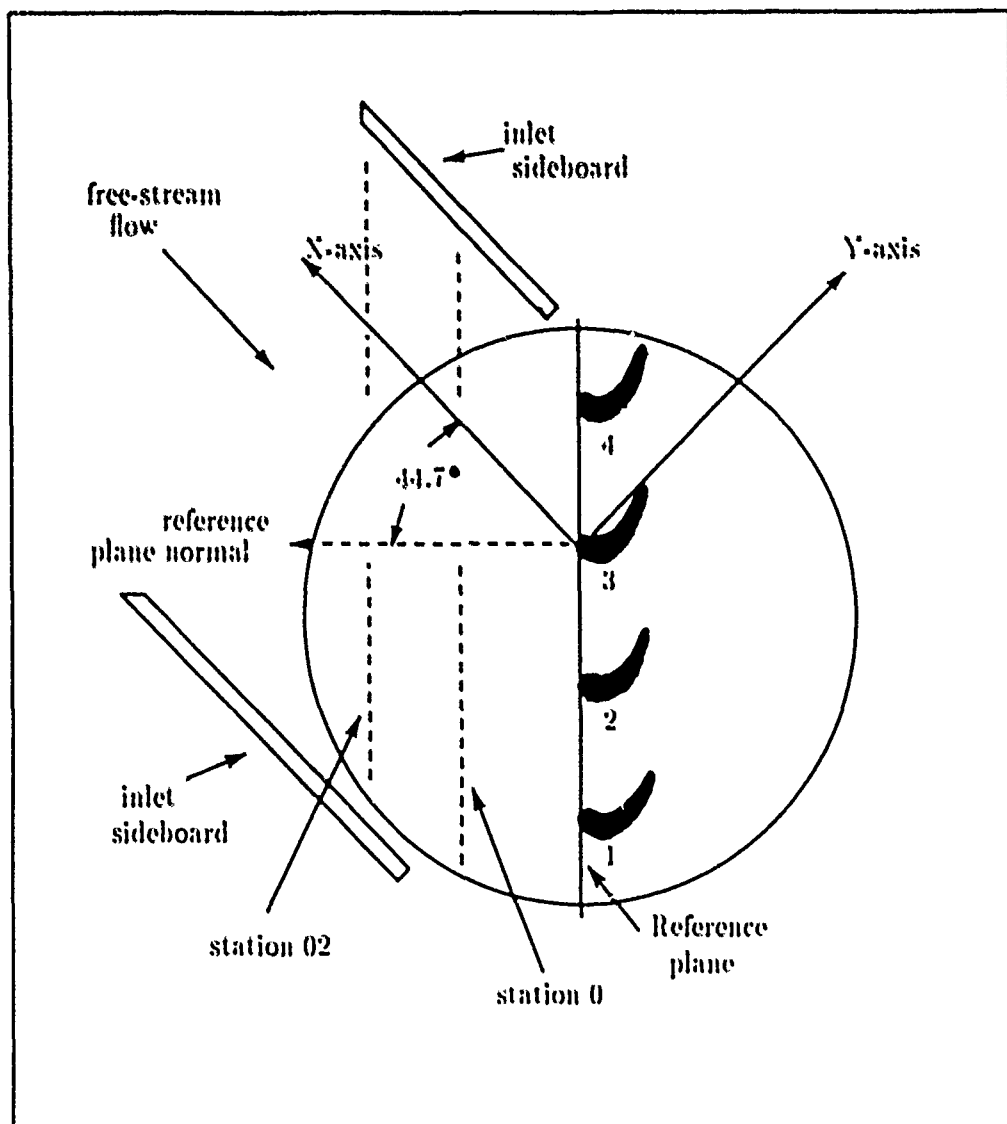
Figure 3.3. Schematic of the turbine blade cascade test section and reference directions
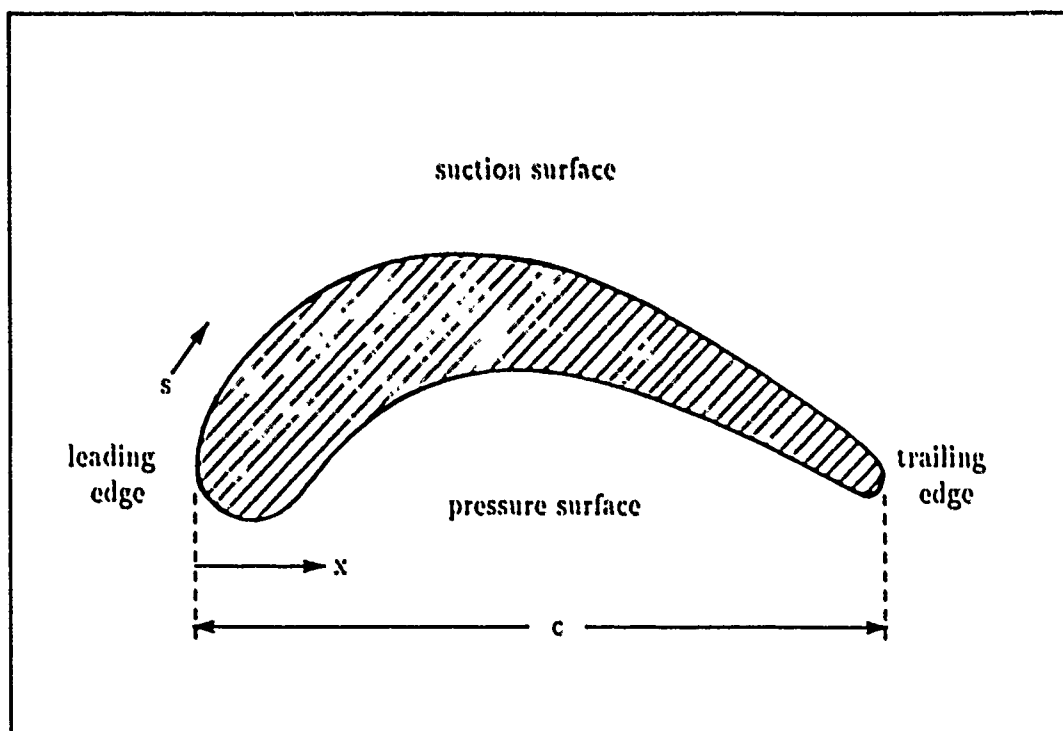
Figure 3.4. Turbine blade section

Table 3.2. Jet-grid injection device specifications

Jet-Grid Specifications	
number of tubes	10
tube spacing (center to center)	25.40 mm
tube outer diameter (b)	6.350 mm
number of injection orifices/tube	7
total number of orifices	70
smallest orifice diameter	0.66 mm
medium orifice diameter	1.32 mm
largest orifice diameter	1.98 mm

different stations relative to the test section. Previous studies on flat plate surface heat transfer have employed such a device with remarkable success (Young, 1989). The jet-grid device employed by Young and Han (Young, 1989) was limited to secondary flow injection in a downstream or upstream flow direction.

This study used a jet-grid device consisting of ten vertical aluminum tubes with a series of evenly spaced orifices drilled along the longitudal axis of each tube. The tubes were placed directly into the free-stream flow through the wind tunnel endwall. The wind tunnel endwall was drilled to accept the tubes. Each tube was secured in place using a simple holding bar attached to the outer surface of the endwall. Each tube was blocked on one end, with the other end attached to flexible tubing. Figure 3.5 shows a photograph of the jet-grid device and Table 3.2 lists specifications of the jet-grid device.

Three primary injection directions were used during this study; streamwise with the free-stream flow, perpendiducar to the free-stream, and opposing the free-stream, and were designated throughout this study as co-flow, cross-flow, and counter-flow, respectively. A schematic of the jet-grid injection directions is given in Figure 3.6.

All feeder lines to the jet-grid were attached to a pressure manifold which allowed even distribution of the secondary flow to each tube prior to injection. The injection pressure was measured with an Endevco, Model 1675-2A, 685,000 kPa differential pressure transducer, centrally located along the length of the manifold. A single (2.54 cm inner diameter) high pressure air line was attached to each end of the manifold. The incoming
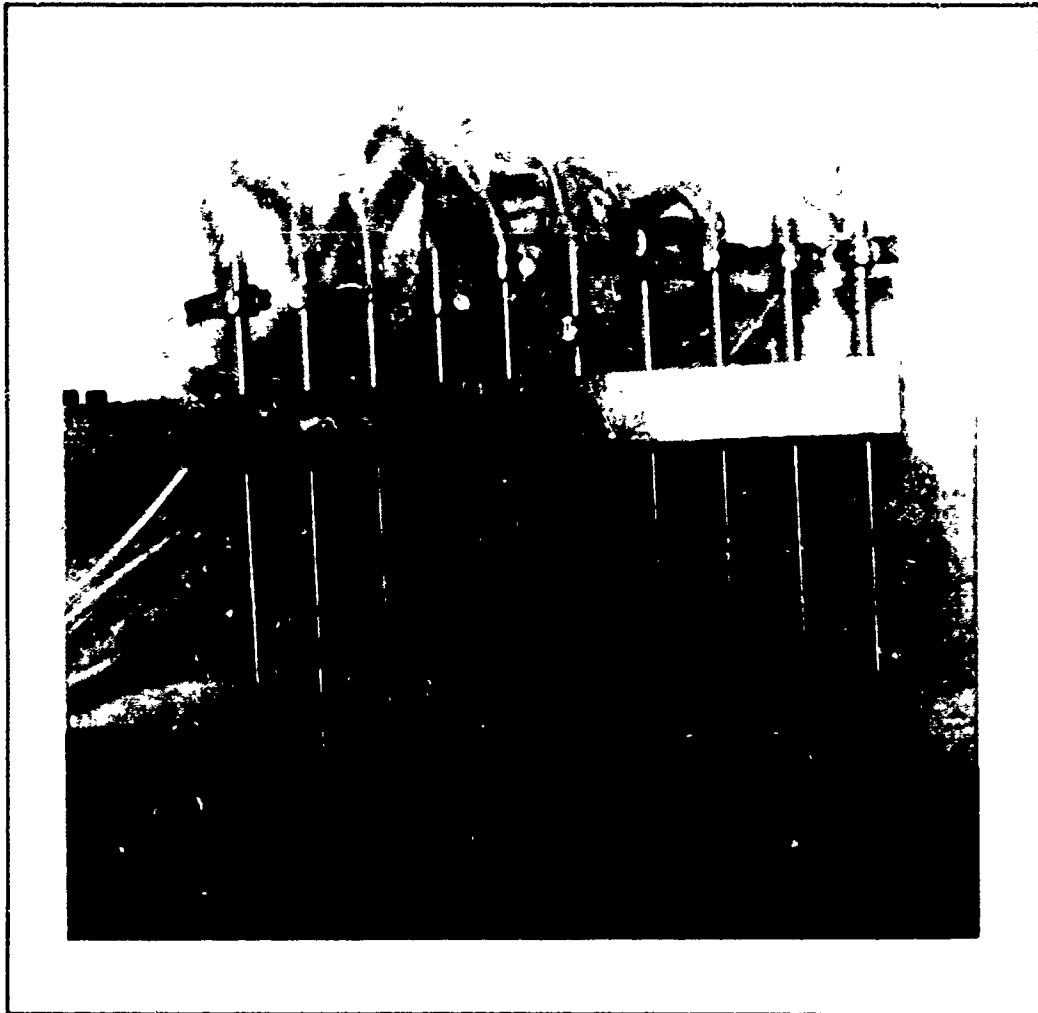
Figure 3.5. Jet-Grid injection device
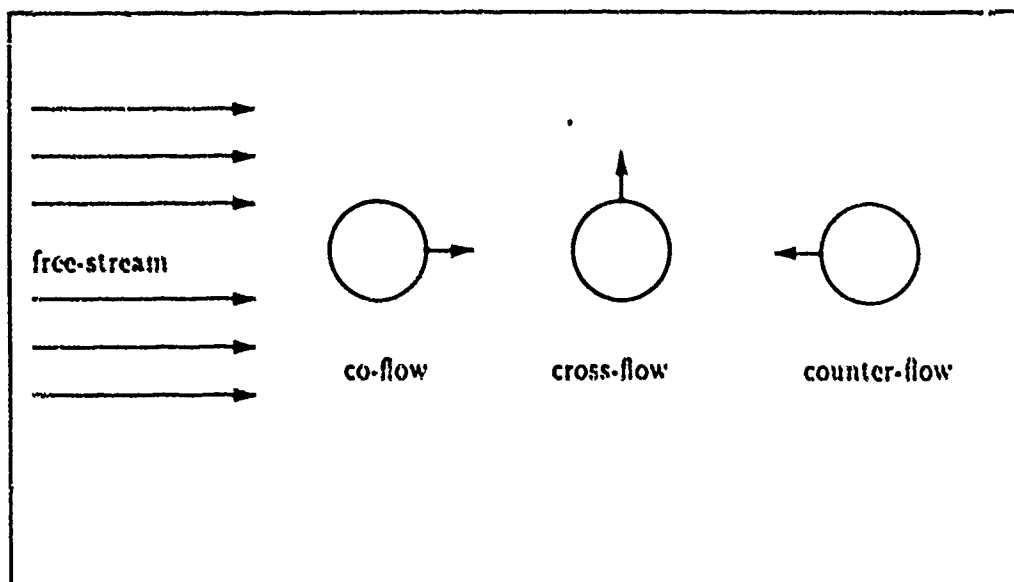
Figure 3.6. Schematic of orifice injection directions

air was triple-filtered and dried using a simple mechanical air-moisture separator. Filtering of the air was necessary for protection of the hot-wire probe and to prevent contamination of the hot-wires and the surface temperature test surface. Two separated sources of high-pressure air were needed to provide adequate mass flow through the larger diameter orifices and maintain a steady injection manifold pressure. The primary air source was low-volume, high-pressure shop air; the secondary air source was high-volume, pressurized air from an Ingersoll-Rand, Model 554E9, three stage air compressor, with a 1,200 liter primary storage tank and a 4,000 liter secondary dump tank.

3.4 Hot-Wire Anemometers

Instantaneous local velocity was measured using a Thermo Systems Model No. 100 (IFA-100) *Intelligent Flow Analyzer*, constant-temperature anemometer controller and a Thermo Systems, Model No. 1240-T1.5, serial no. 7713, X-type tungsten hot-wire probe, also called an *X-wire* probe. This X-wire was a cross-flow type probe which allowed entry into the wind tunnel from the endwall with minimum interference with the free-stream

flow. The probe has two 0.0038 mm diameter tungsten wires, offset from each other by approximately 90 degrees. The tungsten hot-wire probe was chosen over more durable hot-film probes because of its excellent frequency response to turbulence in the flow. The exact intersection angle of the hot-wires was measured with a microscope. Each hot-wire output signal was amplified and filtered using the Thermo Systems, Model No. 15S, signal conditioner prior to input into the high-speed data acquisition system.

3.5   Surface Pressure Test Surface

The surface pressure test surface was an aluminum turbine blade instrumented with 23 static pressure ports. The leading edge static pressure port was located at 37.8 percent of the span. The trailing edge static pressure port was at the 60 percent span position. Remaining pressure ports were on the imaginary line extending from the leading edge pressure port to the trailing edge pressure port on both, the pressure and suction surfaces. This staggered distribution of static pressure ports was selected to alleviate some of the effects of leading orifices disturbing the flow on the turbine blade surface prior to the static pressures being measured by subsequent pressure taps. The pressure port taps were connected to steel tubing which extends through the plexiglass endwall of the wind tunnel test section. Each pressure tap was connected to the Scanivalve 48 port selector with flexible plastic tubing. A 6.895 kPa differential pressure transducer measured the static pressures at each pressure port on the blade. Figure 3.7 is a photograph of the surface pressure instrumented turbine blade. The staggered distribution of the pressure taps is visible along the pressure surface in this figure. The location of each pressure tap in terms of a nondimensional chord length ($\frac{x}{c}$) and a nondimensional surface distance ($\frac{s}{c}$) is given in Table 3.3. The distance along the surface of the blade from the leading edge of the turbine blade is s; c is the turbine blade true chord length.

3.6   Heat Transfer Test Surface and Thermocouples

The heat transfer test model was constructed of an expanded urethane foam core with a stainless steel foil surface wrapped around the exterior of the foam core. The test turbine blade surface was heated by passing an electric current through the stainless steel

Table 3.3. Location of static pressure taps on the turbine blade

pressure tap no.	$\frac{\xi}{c}$	$\frac{s}{c}$	pressure surface (ps) suction surface (ss)
1	0.01739	0.0000	ps
2	0.06522	0.08772	ps
3	0.1244	0.1991	ps
4	0.1913	0.3245	ps
5	0.3156	0.4474	ps
6	0.4365	0.6184	ps
7	0.6000	0.8026	ps
8	0.7687	0.8974	ps
9	0.8522	0.9763	ps
10	0.9235	1.0290	ps
11	1.0000	1.1815	ps
12	0.9026	1.1167	ss
13	0.7643	1.0988	ss
14	0.6670	0.9035	ss
15	0.5817	0.8026	ss
16	0.4870	0.6974	ss
17	0.3852	0.6404	ss
18	0.3322	0.5252	ss
19	0.2191	0.3991	ss
20	0.1078	0.2737	ss
21	0.03565	0.1298	ss
22	0.0000	0.07460	ss
23	0.008696	0.0395	ss

True chord c	= 114.3 mm
Pressure tap no. 1	= leading edge port
Pressure tap no.s 2-10	= pressure surface ports
Pressure tap no. 11	= trailing edge port
Pressure tap no.s 12 -23	= suction surface ports
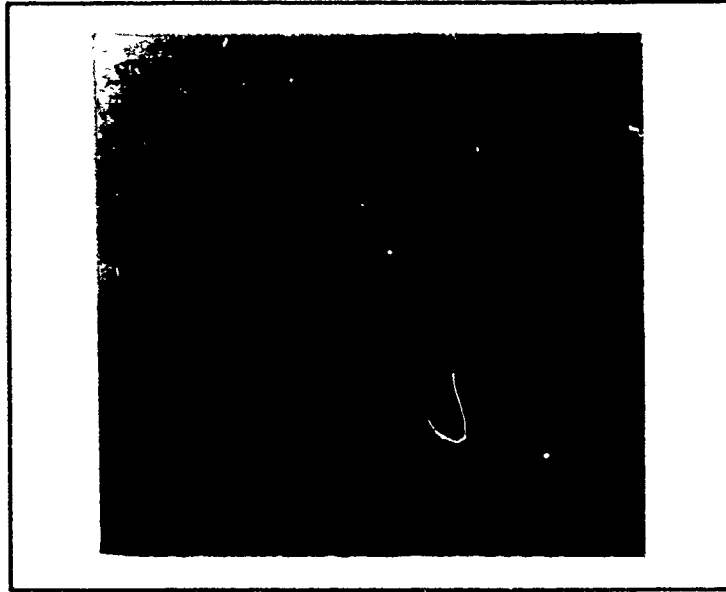
Figure 3.7. Turbine blade instrumented for surface pressure measurements

foil. A 50 amp, 2.5 volt DC current was needed to drive the temperature of the turbine blade test surface high enough to provide a measurable temperature difference between free-stream flow temperature and the blade surface temperature. The urethane core was cast from a mold of the pressure instrumented turbine blade in order to assure identical blade geometry with the pressure test surface. A small amount of the outer surface of the urethane foam core was removed to accept the stainless steel foil and maintain the proper blade dimensions. The dimensions of the stainless steel foil were 2.54 x 10^{-3} mm thick, 263.2 mm in length, and 110.0 mm in width. The width of the stainless steel foil was 3 mm less than the span of the foam core in order to prevent an electrical short between the electrically heated test surface and the tunnel endwalls. Copper bus bars were attached to each end of the stainless steel foil, then the foil-bus bar assembly was glued to urethane foam core turbine blade using unexpanded urethane. The foil surface was continuous from one bus bar on the pressure surface trailing edge to the other bus bar on the suction surface trailing edge. The stainless steel foil was not connected at the trailing edge. A 5 mm section of urethane foam separated the bus bars and prevented electrical contact of the bus bars. Figure 3.8 shows the turbine blade constructed for surface heat transfer

Figure 3.8. Heat transfer test turbine blade

tests. The copper bus bars extended beyond the span of the turbine blade in order to pass through the plexiglass wind tunnel endwall. The test turbine blade was secured within the test section with two bolts passing through each endwall into the side of the turbine blade. Metal inserts were placed within the urethane foam core to support the attachment bolts.

Temperature was measured using 23 iron-constantan (Type J), 36-guage thermocouples attached to the underside of the foil surface. Along the interior of the foam blade, five Type J thermocouples were placed along the camber line and directly in line with the surface thermocouples. The interior thermocouples were used to account for heat conduction into the turbine blade. Each thermocouple was calibrated for temperature sensitivity and accuracy using an ice bath. The accuracy of the thermocouples was ± 1 degree Celsius. Each thermocouple was attached to the stainless steel foil using a low-current arc welder. A small amount of silver-tin, Sn 63, solder was applied at each thermocouple contact with the steel foil for added support of the thermocouple. The thermocouples were located on the heat transfer test turbine blade at the same position as the pressure port taps were located on the surface pressure instrumented turbine blade. Thus, Table 3.3 gives the location of the thermocouples for the heat transfer test turbine blade as well as the location of

3-13

the pressure port taps on the surface pressure instrumented turbine blade. Thermocouples in the interior of the turbine blade were numbered as 24-28, from leading edge to trailing edge, respectively. During the final construction phase of the turbine blade, three thermocouples, numbers 1, 2 and 24 were broken and remained inactive throughout the tests. All other thermocouples remained active. All thermocouple leads exit the turbine blade around the quarter chord point and pass through the tunnel endwall. Each thermocouple lead was connected to the high-speed data acquisition system.

3.7 Instrumentation

A block diagram of the instrumentation control is shown in Figure 3.9.

A Hewlett-Packard High-Speed Data Acquisition System, Model No. HP3852A, controlled the majority of instrumentation used during the experiment. The HP3852A is a mainframe with a 16-bit processor and 2 megabyte internal memory buffer. The backplane is configured for separate component inputs. The following components were used during this study:

(1) HP44701A, Integrating Voltmeter.

(2) HP44702B, High-Speed Voltmeter.

(3) HP44713, High-Speed FET Multiplexer.

(4) HP44728, Relay Actuator.

The Integrating Voltmeter sampled pressure and temperature signals input to the High-Speed FET Multipexer. A second High-Speed Fet Multipexer was used in conjunction with the High-Speed Voltmeter connected with a dedicated ribbon cable for high-speed sampling rates (100,000 signals per second per channel). The high-speed sampling rates were necessary in order to digitize the hot-wire probe output signals accurately. The Relay Actuator controlled the *Scanivalve* drive motor and the power supply used to heat the stainless steel foil surface of the turbine blade.

A Zenith 248 personal computer with a National GPIB, IEEE-488, internal interface

3-14

board was used to control the mainframe and transfer data to floppy disk for permanent storage. All data acquisition software was written using Microsoft *QuickBASIC*.

Measurement instrumentation used my be classified as pressure measurment devices, turbulence measurement devives, and temperature measurement devices, and are discussed as follows.

The wind tunnel free-stream total and static pressures were measured with a K. & E. Company, 0.63 cm U-tube manometer, using distilled water as a pressure indicator medium. A Scanivalve II, 48 port driver motor with a 6.895 kPa differential pressure transducer was used to measure surface pressures on the turbine blade. The jet-grid injection manifold pressure was measured with an Endevco, Model 1675-2A, 6895 kPa pressure transducer. Each pressure transducer output signal was calibrated for pressure using a known applied pressure. Calibration equations were entered into the high-speed data aquisition system where pressure transducer output signals (volts) were converted to pressure units (kPa) and transferred to permanent storage on a floppy disk.

Turbulence measurements were made with the Thermo Systems *Intelligent Flow Analyzer*, IFA-100. Hot-wire probe output signals were amplified and filtered using the Thermo Systems, Model No. 158, Signal Conditioner. Each hot-wire probe was calibrated for flow speed and angle. Temperature calibration of the hot-wires was not performed. Instead, the hot-wires were recalibrated for angle and velocity calibration when the ambient temperature varied more than 5 degrees Celcius from the temperature of the current calibration. Appendix C lists the hot-wire calibration procedure. All hot-wire signals were read by the High-Speed Voltmeter and stored into the data acquisition system memory buffer, and later transferred to floppy disk for permanent storage.

Temperature was measured using iron-constantan (Type J) thermocouples. The high-speed data acquisition system converts thermocouple voltages to temperatures using an internal ice-point. A single Type J thermocouple and an Omega Digicator was used to visually indicate the free-stream temperature.

A Hewlett-Packard, Model No. HP6727, 100 ampere, 20 volt DC Power Supply, supplied a continuous DC current through the stainless steel foil surface of the heat transfer

test turbine blade. The current was measured with the power supply ampere guage. A $3\frac{1}{2}$ place, Hewlett-Packard Digital Multimeter was used to measure the heated blade resistance and the power supply voltage.
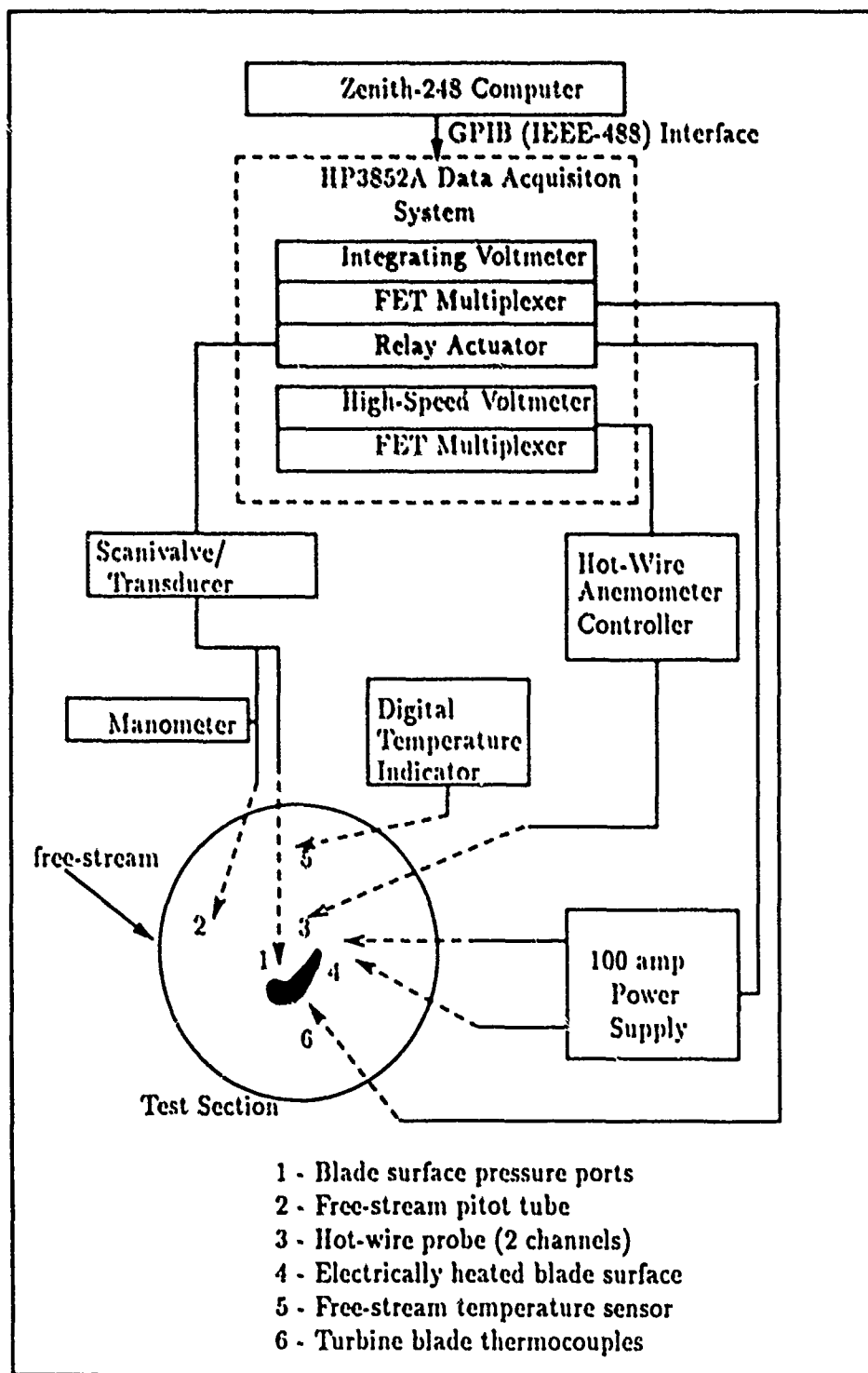
Figure 3.9. Block diagram of instrumentation and control structure

IV. EXPERIMENTAL PROCEDURES AND DATA REDUCTION

4.1 Turbine Cascade Test Section Parameters

The flow within the wind tunnel was adjusted to match equivalent test conditions studied in earlier tests performed on the same turbine blade profile (Moore, 1984c). The primary areas of concern are the cascade inlet, cascade exit, and the wind tunnel flow speed, e.g., the exit Reynolds number.

4.1.1 Free-Stream Flow Inlet Incidence Angle and Velocity Profile

The free-stream flow incidence angle was measured along the span of the wind tunnel using the following procedure.

A dual passage pressure probe was inserted into the inlet of the wind tunnel. The passages of the pressure probe were connected one to each side of a U-tube water manometer. Water or any fluid of similar density gives excellent sensitivity to pressure differences exerted on either side of the probe. The pitot probe was rotated along the tunnel Z-axis until the differential height of the manometer was nulled. The corresponding flow incidence angle was read from an attached protractor to within $\pm$ 1 degree. The flow incidence angle was set to the desired value using adjustable inlet side boards. During the present study, the flow incidence angle was adjusted to 44.7 degrees measured from the reference plane to the incoming free-stream velocity vector. See Figure 3.3 for the layout of the test section geometry. Results of three traverses at three Z-axis positions are presented in Figure 4.1. All traverses were at the same position upstream of the reference plane ($\frac{x}{b} = 17.5$, $b =$ jet-grid tube diameter (6.35 mm)). The results of Figure 4.1 represent the optimum flow conditions after the inlet side boards were adjusted. From Figure 4.1, it can be seen the flow incidence angle was not completely uniform; however, the largest deviation from desired incidence angle did not occur directly ahead of the turbine blade cascade section where surface pressures and surface heat transfer were measured.

The speed of the incoming flow was measured for uniformity along the span of the cascade. A 1.6 mm diameter pitot probe was inserted into the flow, and the flow speed was measured using a U-tube manometer. The speed of the flow was computed using the
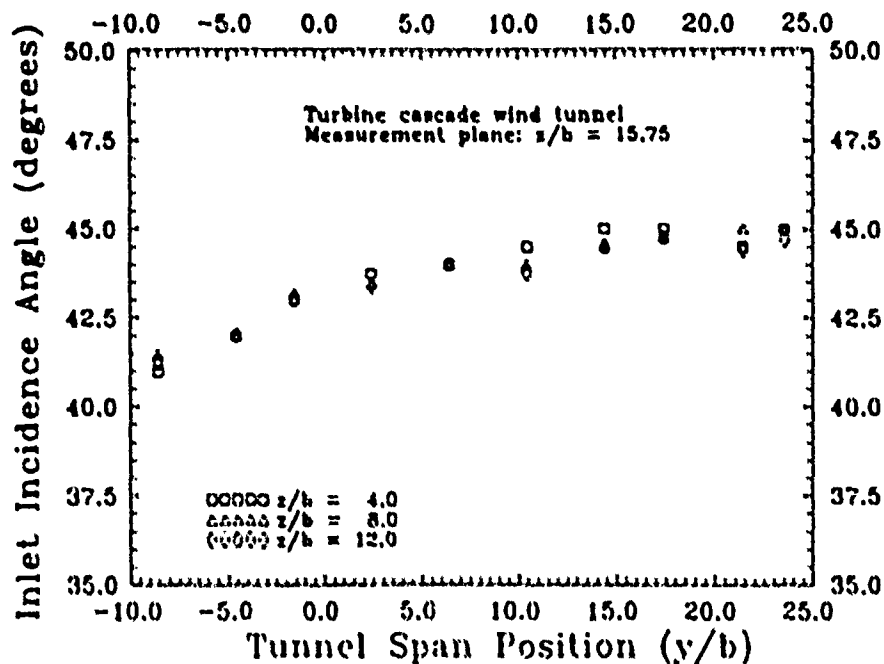
Figure 4.1. Turbine cascade flow incidence angle. Measurement station: $\frac{x}{b} = 15.75$

Bernoulli incompressible flow equation.

$$P_o = P_\infty + \frac{1}{2}\rho_\infty U_\infty{}^2 \qquad (4.1)$$

where

P_o = free-stream total pressure

P_∞ = free-stream static pressure

ρ_∞ = free-stream air density

U_∞ = free-stream flow velocity (speed)

The quantity $\frac{1}{2}\rho_\infty U_\infty{}^2$ is the dynamic pressure and is denoted as q_∞. Manipulation of Equation 4.1 gives

$$U_\infty = \left[\frac{2}{\rho_\infty}(P_o - P_\infty)\right]^{\frac{1}{2}} \qquad (4.2)$$

Figure 4.2 presents the results of a typical traverse along the span of the wind tunnel inlet. The free-stream flow speed exhibited the same trend as the flow incidence angle results presented above.
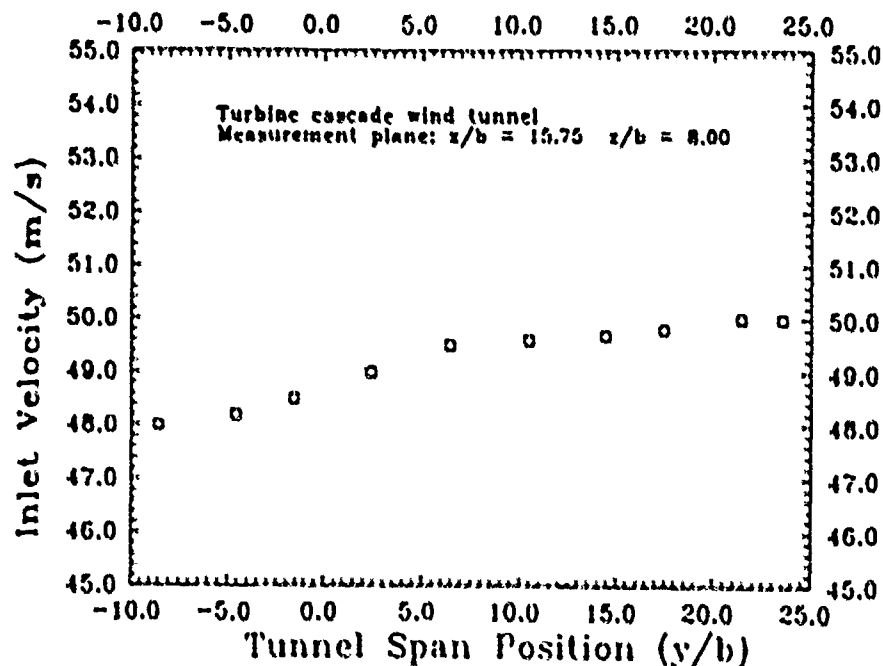
Figure 4.2. Free-stream flow velocity along the inlet span

Table 4.1. Wind tunnel inlet boundary layer measurements

tunnel surface	$\frac{z}{b}$	$\frac{x}{b}$	$\frac{z}{b}$	boundary layer thickness (mm)
side board	17.5	20.1	8.0	5.6
side board	17.5	22.4	8.0	4.0
end wall	17.5	0.0	0.0	3.5
end wall	17.5	0.0	18.0	4.1

The boundary layer along the inlet side boards and wind tunnel end walls was measured with the pitot probe. Boundary layer measurements for the turbine cascade wind tunnel inlet are presented in Table 4.1.

4.1.2 Free-Stream Flow Exit Angle and Velocity Profile The flow exiting the turbine cascade was measured for periodicity of the flow. The flow exit speed was approximately 85 m/s (average). At this speed, the flow angle probe used in the inlet incidence angle measurements was overly sensitive to any fluctuation in the angle of incoming flow; hence, flow exit angle was not measured. Rather exit speed was measured with a pitot probe for
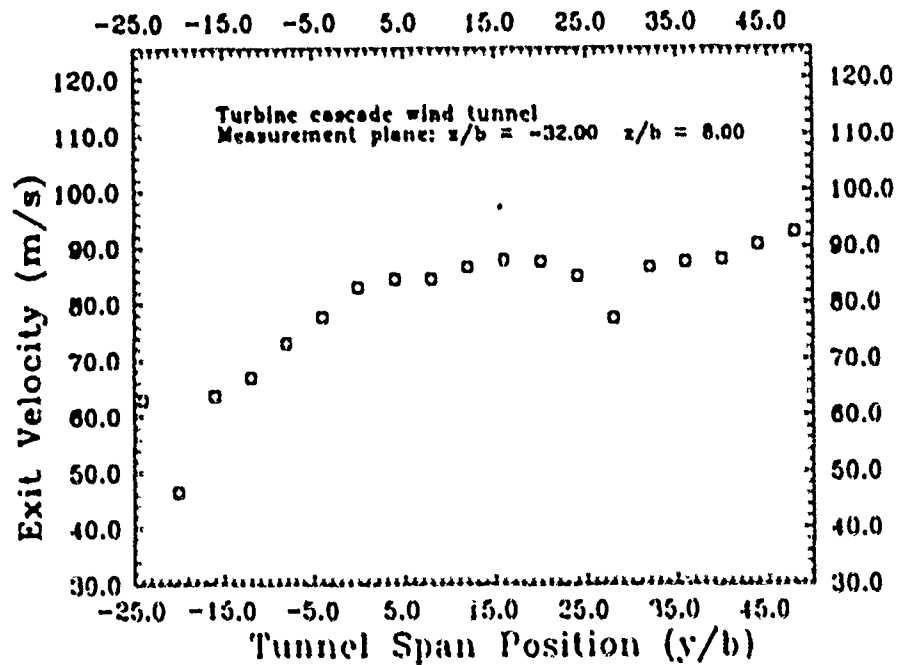
Figure 4.3. Exit velocity profile of turbine cascade wind tunnel

periodicity. The exit speed was found to be periodic, with slowed flow regions immediately behind the trailing edge of the turbine blade. From Figure 4.3, the flow speed varied from 63.0 m/s along one side of the exit section to 91.3 m/s along the opposite side of the exit. Results are given for a single traverse at a selected station ($\frac{x}{b} = -32.0$, $\frac{z}{b} = 8.0$). The wake of turbine blades 2 and 3 are readily apparent as regions of slowed flow. Although the flow exit velocity is non-uniform along the span of the tunnel exit, in the region of turbine blade 3, where blade surface pressures and surface heat transfer was measured, the exit velocity was nearly uniform (except in the wake).

Neither the flow exit angle nor the flow exit speed were adjusted in this study. Although specific flow exit speed profiles were not presented by Moore and Ransmayr, they conclude the exit flow exhibits a "strongly nonuniform spanwise distribution of losses" (Moore, 1984c). The word "spanwise" as it was used by Moore applies to the span of the turbine blade, not to the span of the cascade test section. It is likely flow exit conditions exhibited during this study were similar to exit flow conditions of other linear turbine cascade studies.

4.1.3 Inlet and Exit Reynolds Number Variation The free-stream velocity increased dramatically as the flow passed through the turbine cascade. Some portions of the exiting flow were over 100 percent faster than the incoming flow. The exit Reynolds number (Re_e) was chosen as the free-stream velocity figure of merit for this study. The exit Reynolds number is defined as

$$Re_e = \frac{U_\infty c}{\nu_\infty} \qquad (4.3)$$

where

U_∞ = exit free-stream velocity

c = axial chord length of the turbine blade

ν_∞ = exit free-stream kinematic viscosity

As discussed in the previous section, the location of the measurement of the exit flow velocity was critical since the exiting flow velocity profile was highly nonuniform. The flow exit velocity was measured in the geometric center of the tunnel exit. The station location was $\frac{x}{b} = -32.0$, $\frac{y}{b} = 24.0$, and $\frac{z}{b} = 8.0$.

The exit Reynolds number for this wind tunnel varied from 3.9–5.2×10^5. All turbulence and heat transfer measurements in this study were made at $Re_e \approx 5 \times 10^5$.

4.2 Turbine Blade Surface Pressure

The pressure coefficient (C_p) on the turbine blade is computed as

$$C_p = \frac{P - P_\infty}{q_\infty} \qquad (4.4)$$

where

P = static pressure on the turbine blade

P_∞ = free-stream static pressure

q_∞ = free-stream dynamic pressure ($\frac{\rho U_\infty^2}{2}$)

The turbine blade static pressures were measured with a differential pressure transducer. Static pressures along the surface of the instrumented blade, the free-stream total

pressure (P_o), and free-stream static pressure were scanned using the 48 port Scanivalve port selector. Pressures were read into the Hewlett-Packard data acquisition system as voltage signals. Each static pressure signal was sampled 400 times, averaged to a single value, then the average output signal was converted to a pressure using an internally stored calibration equation which was previously determined for this specific pressure transducer. The coefficient of pressure was computed using Equation 4.4. Subroutine *PRESS.BAS* of *MAINDRV.BAS* listed in Appendix E automated the aforementioned pressure measurement process.

4.3 Jet-Grid Injection

The jet-grid was introduced into the free-stream flow at two upstream stations. The stations were denoted as station 0 ($\frac{x}{b} = 15.75$); and as station 02 ($\frac{x}{b} = 25.67$). The upper end wall of the tunnel was drilled to accept the jet-grid tubes. Flow was injected as either co-flow, cross-flow, or counter-flow, at a pressure range from 70 kPa – 310 kPa, depending on the test being performed. Tables 1.1 and 1.2 lists configurations tested.

Secondary flow was slowly introduced to the jet-grid pressure distribution manifold until the desired pressure was obtained. Filtered shop air (6.55×10^5 kPa) provided the primary feed flow to the pressure distribution manifold. A pressure regulator maintained constant flow pressure. Distribution manifold pressures were measured with an embedded 6.985×10^6 kPa pressure transducer and pressures were recorded by the Hewlett-Packard data acquisition system.

The larger diameter orifice tubes required a second source of feed flow. An Ingersoll-Rand three stage compressor with 5,200 liter storage capacity provided a second source of high-volume flow. During the highest demand for secondary flow, a steady injection pressure could be maintained for approximately 2 minutes, using both feed sources of secondary air flow.

The injected air flow temperature differed from the free-stream temperature by as much as ≈ 4 degrees Celsius. For computations involving the free-stream temperature,

the flow temperature was measured downstream of the jet-grid. Heat transfer calculations were based on the "mixed" flow temperature.

4.4 Time Discrete Velocity and Turbulence Intensity

The time discrete velocity of the air flow was measured using an X-wire probe. The X-wire selected was a Thermo Systems Model No. 1240-TI.5. This hot-wire anemometer used a pair of 0.00508 mm diameter tungsten wires which offered excellent response to fluctuations in the flow and allow measurement of turbulence microscale lengths on the same order of magnitude as the wire diameter. A brief discussion of the velocity equations and the turbulence equations used in this study follows. Appendix C gives further details on the calibration of the hot-wire probe for velocity/turbulence measurement.

The geometry of the hot-wires in *normal* configuration is shown in figure 4.4. This is the same geometry assumed for calibration of the X-wire probe. From Figure 4.4

$$\theta_1 = \frac{\pi}{2} - b_1 + \beta \tag{4.5}$$

$$\theta_2 = \frac{\pi}{2} - b_1 - \beta \tag{4.6}$$

If we let $\alpha = \frac{\pi}{2} - b_1$, then θ_1 and θ_2 may defined as

$$\theta_1 = \alpha + \beta \tag{4.7}$$

$$\theta_2 = \alpha - \beta \tag{4.8}$$

The effective velocity each hot-wire measures is defined for each wire as

$$U_{1_{eff}}{}^2 = U_\infty{}^2(\cos^2\theta_1 + k_1\sin^2\theta_1) \tag{4.9}$$

$$U_{2_{eff}}{}^2 = U_\infty{}^2(\cos^2\theta_2 + k_2\sin^2\theta_2) \tag{4.10}$$

Note Equation 4.9 and Equation 4.10 represent two equations for two unknowns, namely
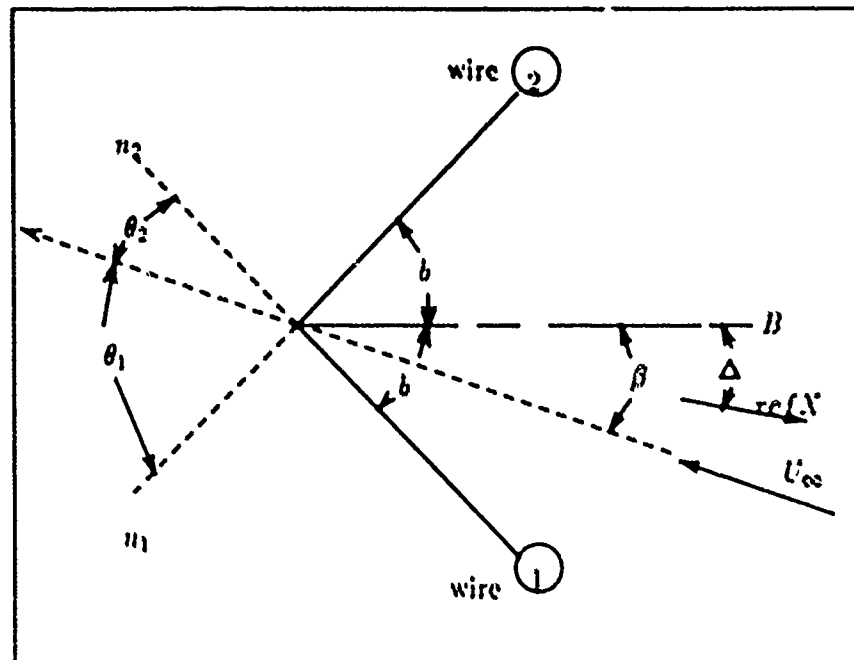
U_∞	= local flow velocity vector
W_1, W_2	= Wire 1 and Wire 2, respectively
B	= X-wire bisector
b_1	= angle subtended by B and either X-wire
β	= angle subtented by U_∞ and B
n_1	= normal to W_1
n_2	= normal to W_2
θ_1	= angle subtended by U_∞ and n_1
θ_2	= angle subtended by U_∞ and n_2
Δ	= angle subtended by B and the reference X-axis

Figure 4.4. Geometry of X-type hot-wire probe - End flow, *normal* configuration

U_∞ and β. Solving Equations 4.9 and 4.10 for U_∞^2 yields

$$\frac{U_{1,eff}^2}{\cos^2\theta_1 + k_1 \sin^2\theta_1} = \frac{U_{2,eff}^2}{\cos^2\theta_2 + k_2\sin^2\theta_2} \tag{4.11}$$

From Equations 4.5 and 4.6, θ_1 and θ_2 are recognized as complementary angles. Hence, $\cos^2\theta_2 = \sin^2\theta_1$ and $\sin^2\theta_2 = \cos^2\theta_1$. Substitution of these values into Equation 4.11 yields with some manipulation

$$U_{1,eff}^2(\cos^2\theta_2 + k_2\sin^2\theta_2) = U_{2,eff}^2(\sin^2\theta_2 + k_1\cos^2\theta_2) \tag{4.12}$$

Dividing Equation 4.12 by $\cos^2\theta_2$ and solving for θ_2

$$U_{1,eff}^2(1 + k_2\tan^2\theta_2) = U_{2,eff}^2(\tan^2\theta_2 + k_1)$$

$$\tan^2\theta_2(U_{1,eff}^2 k_2 - U_{2,eff}^2) = U_{2,eff}^2 k_1 - U_{1,eff}^2$$

$$\tan^2\theta_2 = \frac{U_{2,eff}^2 k_1 - U_{1,eff}^2}{U_{1,eff}^2 k_2 - U_{2,eff}^2}$$

$$\theta_2 = \tan^{-1}\left[\left(\frac{U_{2,eff}^2 k_1 - U_{1,eff}^2}{U_{1,eff}^2 k_2 - U_{2,eff}^2}\right)^{\frac{1}{2}}\right] \tag{4.13}$$

Combining Equation 4.8 with Equation 4.13 gives

$$\beta = \alpha - \tan^{-1}\left(\frac{U_{2,eff}^2 k_1 - U_{1,eff}^2}{U_{1,eff}^2 k_2 - U_{2,eff}^2}\right) \tag{4.14}$$

The correct root of Equation 4.14 must be determined from the geometry of the flow. From Figure 4.4, a clockwise rotation from the bisector (B) defines a positive incidence angle (β). This specific flow geometry is labeled case 1. Case 2 defines a counterclockwise rotation from the bisector with a negative incidence angle ($-\beta$).

In case 1, $\qquad U_{1,eff} > U_{2,eff}$

In case 2, $\qquad U_{2,eff} > U_{1,eff}$

The term within the parenthesis of Equation 4.14 represents the physics of the incidence angle of the flow as it approaches each wire. The incidence angle of the time discrete

velocity vector indicates the term within the parenthesis of Equation 4.14 must be positive if $U_{1_{eff}} > U_{2_{eff}}$ and negative if $U_{2_{eff}} > U_{1_{eff}}$. Equation 4.14 is rewritten to include the physics of the flow and account for the two roots of Equation 4.14.

$$\beta = \alpha - \tan^{-1}\left[sgn\left(\frac{U_{2_{eff}}{}^2 k_1 - U_{1_{eff}}{}^2}{U_{1_{eff}}{}^2 k_2 - U_{2_{eff}}{}^2}\right)\right] \qquad (4.15)$$

where

$sgn = +1$ if $U_{1_{eff}} > U_{2_{eff}}$

$sgn = -1$ if $U_{1_{eff}} < U_{2_{eff}}$

Equation 4.15 is solved at each time step. The X-wire calibration equations provide $U_{1_{eff}}$ and $U_{2_{eff}}$ during each sampling interval, and α is known for each X-wire; therefore, β is computed for each time step. Equations 4.5 and 4.6 are solved for θ_1 and θ_2 at each time step, respectively. Equation 4.7 or Equation 4.8 is now solved for U_{∞} at each time step. In essence, the time discrete local velocity is determined, where both angle and magnitude of the local flow is known at each time step.

If N velocity measurements are made by the X-wire probe over a finite time interval, then the time discrete velocity is decomposed into local velocity components, u and v, for each time step i.

$$u_i = U_{\infty_i} \cos(\beta_i - \Delta)$$
$$v_i = U_{\infty_i} \sin(\beta_i - \Delta) \qquad (4.16)$$

where

Δ = the angle subtended by the X-wire bisector and and the wind tunnel reference X-axis. Positive Δ is in the same sense as positive β

The mean velocity components are given as

$$\bar{u} = \frac{\sum_i^N u_i}{N} \qquad (4.17)$$

$$\overline{v} = \frac{\sum_i^N v_i}{N} \tag{4.18}$$

The fluctuating velocity components, u' and v', are defined for each time step, i, as

$$u'_i = u_i - \overline{u} \tag{4.19}$$

$$v'_i = v_i - \overline{v} \tag{4.20}$$

The root-mean-square of the fluctuating velocity components, are given as

$$\overline{u'} = \left(\frac{\sum_i^N u'^2}{N}\right)^{\frac{1}{2}} \tag{4.21}$$

$$\overline{v'} = \left(\frac{\sum_i^N v'^2}{N}\right)^{\frac{1}{2}} \tag{4.22}$$

The x- and y-components of turbulence, Tu_x and Tu_y, respectively, are defined as

$$Tu_x(\%) = \frac{\overline{u'}}{\overline{V}} \cdot 100\% \tag{4.23}$$

$$Tu_y(\%) = \frac{\overline{v'}}{\overline{V}} \cdot 100\% \tag{4.24}$$

where

$\overline{V}$ = the vector sum of $\overline{u} + \overline{v}$

The consolidated turbulence (Tu) is computed as

$$Tu = \left(\frac{Tu_x^2 + Tu_y^2}{2}\right)^{\frac{1}{2}} \tag{4.25}$$

4.5 Turbulence Integral Scale and Microscale Measurements

The turbulence integral scale and microscale lengths were determined from the time-discrete local velocity measurements. The method of analysis follows the turbulence scale discussion presented by Cebecci and Smith (Cebeci, 1974). All turbulence scales were resolved to the tunnel reference coordinate axis.

The X-component turbulence integral scale (Λ_u) and the Y-component turbulence integral scale (Λ_v) are computed as

$$\Lambda_u \equiv \lim_{n \to 0} \left(\frac{\overline{U}}{4\overline{u'^2}} E_{u'}(n) \right) \tag{4.26}$$

$$\Lambda_v \equiv \lim_{n \to 0} \left(\frac{\overline{v}}{4\overline{v'^2}} E_{v'}(n) \right) \tag{4.27}$$

where

n = turbulence frequency

$E_{u'}(n)$ = X-component turbulence power per frequency bandwidth

$E_{v'}(n)$ = Y-component turbulence power per frequency bandwidth

The limit is taken as the turbulence frequency (n) approaches zero.

The X-component of turbulence microscale (λ_u) and the Y-component of turbulence microscale (λ_v) are determined as

$$\lambda_u \equiv \left[\left(\frac{\overline{u^2}\,\overline{u'^2}}{2\pi^2} \right) \frac{1}{\int_0^{n_{max}} n^2 E_{u'}(n)\,dn} \right]^{\frac{1}{2}} \tag{4.28}$$

$$\lambda_v \equiv \left[\left(\frac{\overline{v^2}\,\overline{v'^2}}{2\pi^2} \right) \frac{1}{\int_0^{n_{max}} n^2 E_{v'}(n)\,dn} \right]^{\frac{1}{2}} \tag{4.29}$$

where

n_{max} = highest measured frequency of the turbulence

The turbulence power per frequency bandwidth was determined from the Fast Fourier Transform (FFT) of the fluctuating velocity components (u' and v'). The highest frequency of the turbulence used for the microscale calculations in this study was arbitrarily set at 19,000 Hz. This cut-off frequency eliminated a spike in the FFT data at 20,000 Hz, which was attributed to instrumentation noise. In addition, during the experiment it became apparent the physical limit of turbulence frequency in this tunnel was around 15,000 Hz. The magnitude of the frequency components is nearly zero for frequencies beyond 13-15,000 Hz.

A program, *TUBAT.BAS* was written to compute the turbulence integral scale lengths and microscale lengths. Program *TUBAT.BAS* is included in Appendix E.

4.6 Surface Heat Tranfer Measurement

4.6.1 Turbine Blade Surface Temperature Measurement The heat transfer test turbine blade was heated using the external power supply. A 50 amp current, at a potential of approximately 2.5 volts was conducted through the stainless steel foil surface. The turbine blade was allowed to come to steady state conditions. The steady state temperature condition on the blade was reached in approximately five minutes. During this time, the temperature of the blade was constantly monitored by the HP3852A Data Acquisition System in order to prevent overheating of the turbine blade surface. Overheating will cause the underlying urethane foam to out-gas and separate the foil surface from the urethane core.

Once steady state conditions were reached, the HP3852A Data Acquisition System read each thermocouple voltage and converted the voltage to temperatures. A single scan of the thermocouples was completed by the HP3852A in less than 0.3 seconds. Prior to making a temperature scan of the thermocouples, the external power supply which heats the turbine blade surface was momentarily shut off; otherwise, the current would short through the thermocouple leads into the FET multiplexer and damage the FET junction. After reading all thermocouples, the HP3852A turned the power supply back on. The entire process of turning the power off, reading the thermocouples, and turning the power supply back on, was completed in about 0.5 seconds. A change in the turbine blade surface temperature was not detectable until 1.3 seconds after the power supply was shut off; hence turning the power supply off momentarily had no effect on the temperature measurements.

The temperature readings for each test configuration listed in Tables 1.1 and 1.2 were stored on disk for post-processing. Subroutine *TRUN.BAS* of the main data acquisition code was used to control the HP3852A during temperature measurements. A source code listing of *TRUN.BAS* is given in Appendix E.

4.6.2 Stanton and Nussell Numbers on the Blade The Stanton number (St) and Nusselt number (Nu) for the turbine blade surface heat transfer are computed from a power balance on the turbine blade surface. The turbine blade surface is considered as a series of adjoining sections. The sum total of all the i surface sections make up the total surface area of the heat transfer surface of the turbine blade. At each i th section of the turbine blade surface, a specific power balance was applied as

$$q'_{electrical_i} = q'_{conduction_i} + q'_{convection_i} + q'_{radiation_i}$$ (4.30)

and

$$q'_{electrical_i} = I^2 R' \frac{A_i}{A_{tot}}$$

$$q'_{conduction_i} = \frac{k_{foam} A_i}{L_i}(T_{s_i} - T_{int_i})$$

$$q'_{convection_i} = h_i A_i (T_{s_i} - T_\infty)$$

$$q'_{radiation_i} = \sigma \epsilon A_i \left(T_{s_i}^4 - T_\infty^4\right)$$ (4.31)

where

$q'_{electrical_i}$	= electrical power input to each blade section
$q'_{conduction_i}$	= conductive heat loss at each section
$q'_{convection_i}$	= convective heat loss at each section
$q'_{radiation_i}$	= radiative heat loss at each section
I	= electrical current (amperes)
R'	= electrical resistance of the total foil surface area (ohms)
k_{foam}	= thermal conductivity for urethane foam ($0.026 \frac{W}{mK}$)
A_i	= area of the ith section of the turbine blade foil surface
L_i	= linear distance from the surface of the blade to the interior point in the turbine blade where the temperature is measured
T_{s_i}	= section surface temperature
T_{int_i}	= internal temperature of the turbine blade corresponding to each surface area section

h_i = convection heat transfer coefficient for each section

σ = Stefan-Boltzmann constant (5.67×10^{-8} W/m · K)

ϵ = emissivity of the stainless steel foil (0.17)

The thermal conductivity value is for rigid urethane foam at 300 K; the emissivity value is for highly polished stainless steel foil at 300 K (Incropera, 1985).

Substituting the set of Equations 4.31 into Equation 4.30, canceling the section area (A_i) from all terms, and solving for h_i gives

$$h_i = \frac{\frac{I^2 R'}{A_{tot}} + \frac{k_{foam}}{L}(T_{s_i} - T_{int_i}) - \sigma\epsilon\left(T_{s_i}^4 - T_\infty^4\right)}{T_{s_i} - T_\infty} \qquad (4.32)$$

Using h_i, the Nusselt number obtained for each blade section.

$$Nu_i = \frac{h_i s_i}{k_{air_i}} \qquad (4.33)$$

where

s_i = distance along the surface of the blade from the leading edge of the blade to the specific thermocouple location within area i

k_{air_i} = thermal conductivity of air evaluated at the mean fluid temperature (T_{mean})

$$T_{mean_i} = \frac{T_{s_i} - T_\infty}{2} \qquad (4.34)$$

The Stanton number (St) for each blade section is computed as

$$St_i = \frac{Nu_i}{Pr Re_{s_i}} \qquad (4.35)$$

where

Pr = Prandtl number of air

Re_{s_i} = Reynolds number based on surface distance s

Table 4.2. Experimental measurement uncertainties

Experimental Reading					
variable	range		variation		uncertainty (%)
length measurements	—	—	± 0.50	mm	0.50
manometer ($P_o - P_\infty$)	13.71	cm H_2O	± 0.13	cm	0.95
injection pressure	206.85	MPa	± 1.379	MPa	0.67
blade surface temperature (T)	38.50	°C	± 1.0	°C	2.60
T_∞	27.50	°C	± 1.0	°C	3.64
I	50.00	amp	± 0.2	amp	0.40
resistance (R')	0.13	Ω	0.001	Ω	0.70
emissivity (ϵ)	0.17		—		1.80
Pr	0.707		—		0.10
thermal conductivity (k_{air})	0.0263	W/mK	—		0.10
thermal conductivity (k_{foam})	0.026	W/mK	—		0.10

Stanton and Nusselt numbers were computed from the blade temperatures using subroutine *TRUN.BAS* of the main data acquisition program listed in Appendix E.

4.7 Experimental and Calculated Uncertainties

Measurement uncertainties are are listed in Table 4.2. An example of an uncertainty calculation for a measurement is shown for the turbine blade surface temperature (T).

$$uncertainty(T) = \frac{[(1.0)^2]^{\frac{1}{2}}}{38.5} = 2.60\%$$

Instrumentation accuracy is given in Table 4.3.

Table 4.3. Instrument accuracy specifications

Instrument Accuracy		
instrument	*range*	*uncertainty (%)*
HP44701 Voltmeter	30 mV	0.010
HP44701 Voltmeter	3 V	0.008
HP44702B Voltmeter	2.56 V	0.005
HP44713 Thermocouple (T)	30 °C	0.333
HP3852A Internal Clock	10 μs	0.75
TSI IFA-100	5.0 V	0.02
Scanivalve transducer	2500 kPa	0.86

Using the uncertainties listed above, the uncertainties of calculated variables were computed. Table 4.4 lists the uncertainties of the calculated variables. An example of a calculated uncertainty is given for the exit Reynolds number (Re_e).

$$\Delta Re_e = \left[(1.0)^2 + (1.31)^2 + (0.5)^2\right]^{\frac{1}{2}} = 1.72\%$$

Table 4.4. Uncertainty of calculated variables

Calculated Uncertainties	
variable	uncertainty (%)
ρ	1.0
ν	1.0
U_∞	1.31
$\overline{u}$	1.50
u'	1.91
$\frac{x}{L}$	0.7
$\frac{y}{L}$	0.7
Re_e	1.72
Tu	2.85
St	4.85
Nu	4.51
Cp	1.28
$q_{electrical}$	1.58
$q_{conductive}$	4.58
$q_{radiation}$	9.02
h	4.37

V. RESULTS AND DISCUSSION

5.1 Effect of the Jet-Grid on Turbine Blade Surface Pressures

The effect of the jet-grid on the surface pressure distributions was examined for co-flow, cross-flow, and counterflow injection of the secondary flow over a range of injection pressures.

A baseline case was established with the surface pressures measured on the turbine blade without any turbulence grid installed in the free-stream flow. The surface pressures are presented as nondimensional coefficients of pressure (C_p) along the nondimensionalized chord (x/c) of the turbine blade.

Figure 5.1 shows the pressure distribution on the turbine blade surface over a range of the wind tunnel exit Reynolds numbers. The surface pressure distribution determined by Langston (Langston, 1977) on an identical turbine blade profile is included for comparison. Figure 5.1 demonstrates the independence of the pressure coefficient from the exit Reynolds number. The pressure side of the turbine blade exhibits a stagnation point $(C_p = 1)$ at the 0.7 percent chord. Along the pressure surface of the turbine blade, the pressure coefficients measured compared favorably with Langston's data except near the trailing edge of the turbine blade. The suction surface pressure coefficients exhibited significant deviations from Langston's results, most noticeably in the pressure distribution measured near the leading edge of the suction surface. The free-stream incidence angle was the same for both studies; therefore, this difference in pressure distribution between the present study and Langston's results is attributed to the secondary flow effects within the cascade, and the actual location of the pressure port taps on the turbine blade.

Studies of others (Moore, 1984c, Langston, 1977) indicate strong secondary flow effects are present within linear turbine cascades. A strong passageway vortex impinges on the suction surface and tends to decrease the pressures measured on the suction surface. The secondary flow effects are more pronounced for low aspect ratio turbine cascade wind tunnels. The present study used a turbine cascade with a unity aspect ratio, thus secondary flow effects are expected. Also, because the turbine blade used in the present study was less than half the size of Langston's model, the secondary flow within a linear turbine
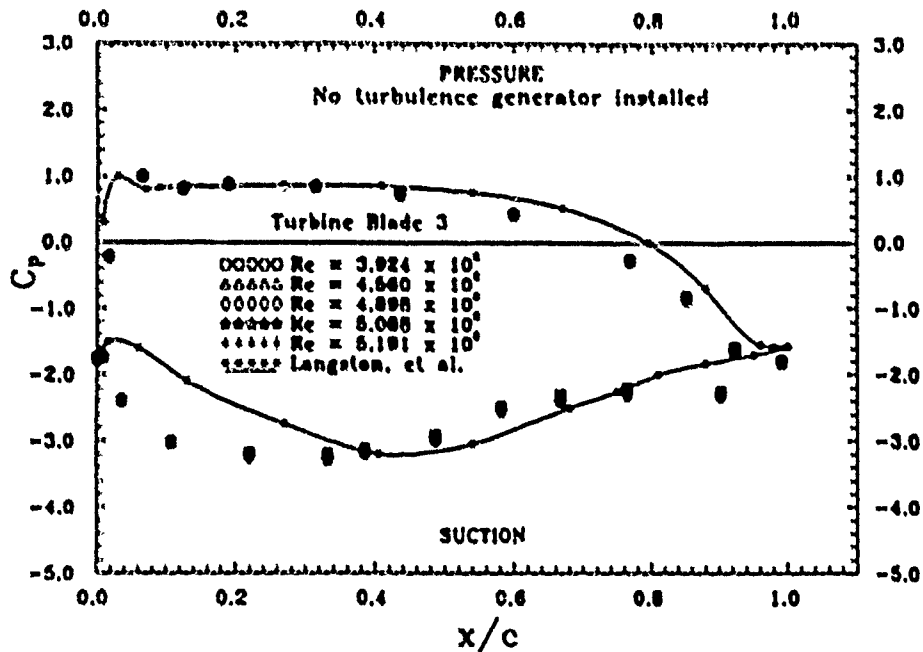
Figure 5.1. Pressure distributions on the turbine blade for several exit Reynolds numbers. No turbulence grid installed

cascade is expected to have a more pronounced effect on the smaller scale turbine cascade and the turbine blade surface pressures would be affected.

For all remaining turbine blade surface pressure measurements and pressure coefficient calculations, the free-stream total pressure and dynamic pressure were measured with the pitot tube in a different position in the wind tunnel than the position used to measure the free-stream total and static pressures for the results shown in Figure 5.1. Relocation of the pitot probe was necessary in order to accommodate the jet-grid device. The new position of the pitot probe was midway between turbine blades Number 2 and Number 3, 15.0 mm upstream of the reference plane, and midway between the two tunnel endwalls. Since the free-stream accelerated as it entered the cascade passageway, the measured free-stream dynamic pressure (q_∞) was greater at this pitot probe location than the free-stream dynamic pressure measured at the previous location where the results shown in Figure 5.1 were obtained. Due to the different dynamic pressures associated with the two different pitot probe locations in the wind tunnel, the no-grid baseline pressure distribution shown in Figures 5.2 - 5.8 is not the same as the no-grid baseline pressure distribution shown in

Figure 5.1. However, the results shown in Figures 5.1 - 5.8 have the same exit Reynolds number.

The pressure distribution on the turbine blade with the turbulence grid installed at two upstream locations, with no blowing, is shown in Figure 5.2. The pressure distribution on the turbine blade surface, without the turbulence grid installed, is included for comparison. On the pressure surface, the pressure coefficient remained constant. The suction surface pressure coefficients decreased with the jet-grid installed, especially near the trailing edge of the blade. Subsequent heat transfer tests and comparison to laminar boundary layer heat transfer theory and turbulent boundary layer heat transfer theory indicated the higher turbulence intensity generated by the turbulence grid in the free-stream flow induced a turbulent boundary layer on the suction side which was better able to negotiate the curvature of the suction surface.

The free-stream incidence angles were measured with the jet-grid installed in the flow. For the no injection cases shown in Figure 5.2 there was a possibility of some small incidence angle change; however, it was too small of a change to accurately measure. Incidence angle changes less than 0.75 degrees were within the uncertainty of the incidence angle measurements.

Figures 5.3, 5.4, and 5.5 show the effect on surface pressure distributions on the turbine blade with jet-grid injection in different directions, over a range of injection pressures ($\approx$ 75-300 kPa). The same location upstream of the cascade was used for the results of these three figures ($\frac{x}{c} = 15.75$).

Both co-flow and cross-flow exhibited very little effect on the pressure distributions on the turbine blade compared to the case with no injection. However, the counter-flow injection case, shown in Figure 5.5, had a significant effect overall on the turbine blade pressure distribution. With counter-flow injection, the pressure coefficient increased slightly over most of the turbine blade pressure surface as compared to the no injection case (solid line). The pressure coefficient seems to approach stagnation levels around $\frac{x}{c}$ = 0.2-0.3. A slight decrease in C_p occurred near the trailing edge of the pressure surface which indicates the flow was accelerated in this region. Conversely, counter-flow injection
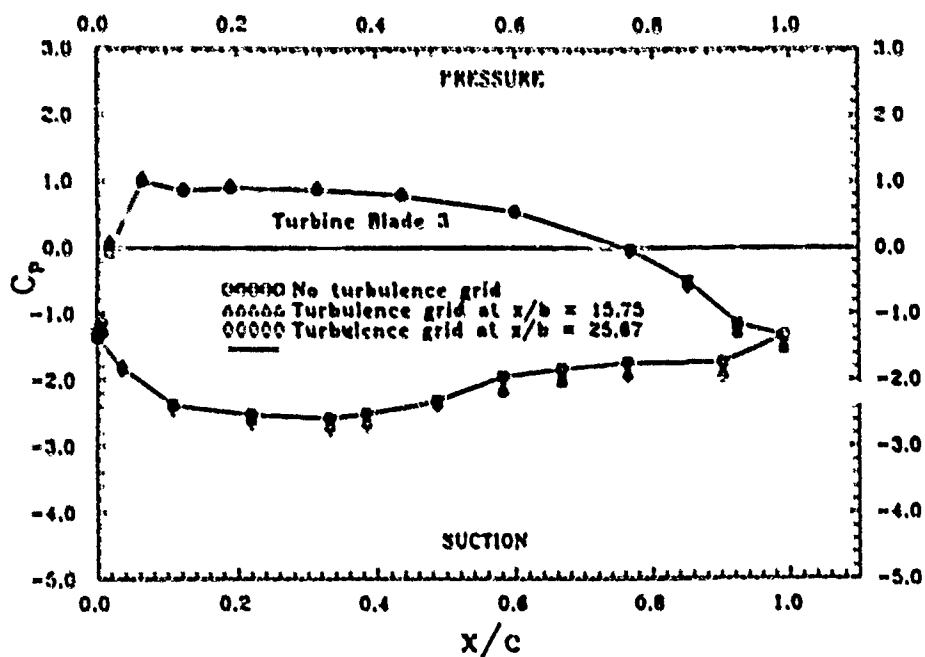
Figure 5.2. Pressure distribution on the turbine blade with the jet-grid installed at two upstream locations. No secondary flow injected. $Re_c = 5.0 \times 10^5$
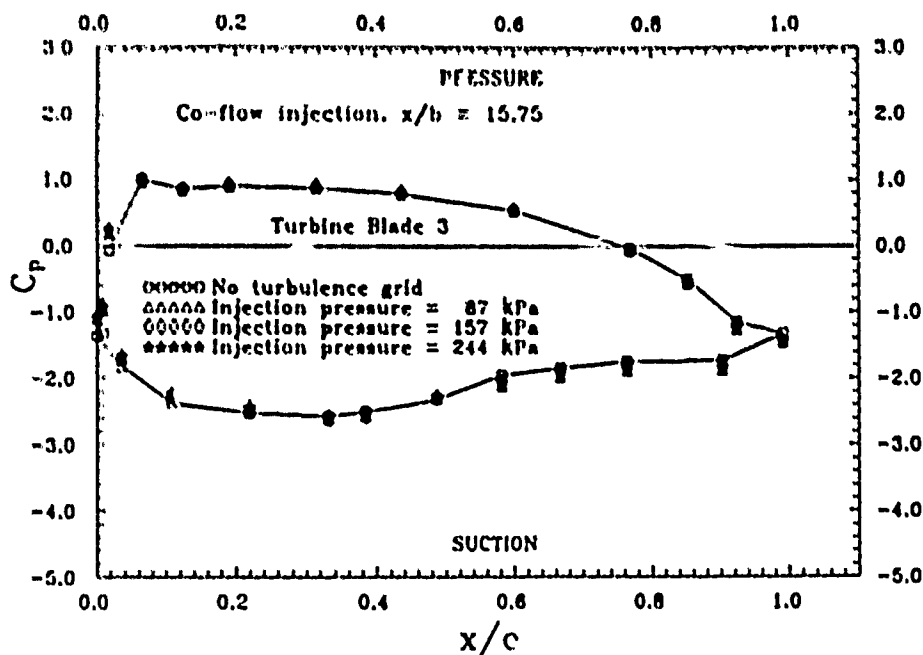
Figure 5.3. Pressure distribution on the turbine blade with co-flow injection at the near-upstream location. $Re_c = 5.0 \times 10^5$
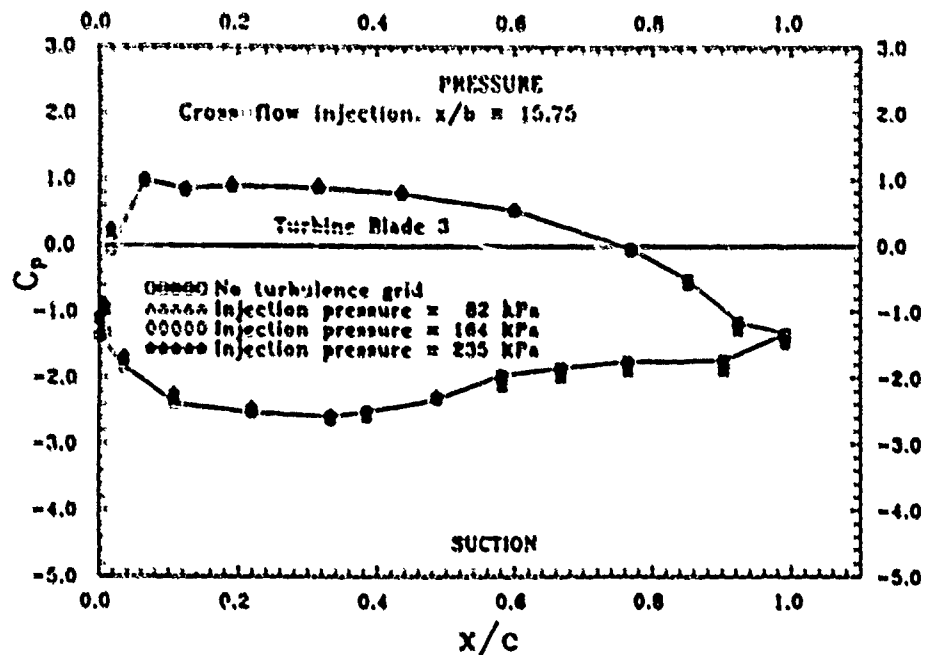
Figure 5.4. Pressure distribution on the turbine blade with cross-flow injection at the near-upstream location. $Re_c = 5.0 \times 10^5$
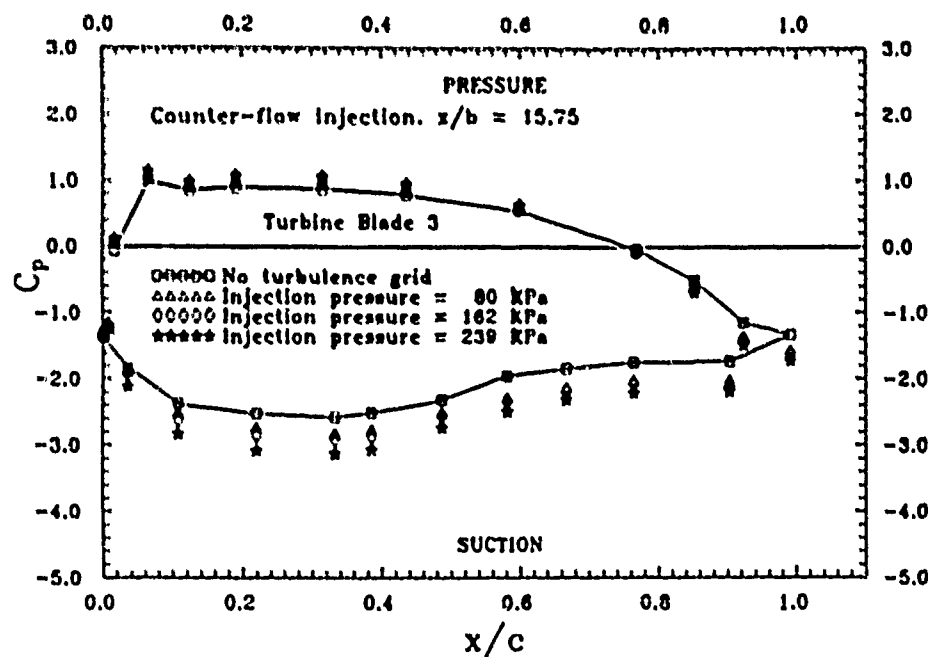
Figure 5.5. Pressure distribution on the turbine blade with counter-flow injection at the near-upstream location. $Re_c = 5.0 \times 10^5$

decreased the pressure coefficient on the blade suction surface dramatically. The injection direction was the dominant factor in changing the turbine blade pressure distribution. The injection pressure had less effect on the pressure distribution on the turbine blade than the injection direction. The flow incidence angle was measured for this counter-flow case and found to have changed from 44.7 degrees to 43.0 degrees which might account for the decrease in pressure coefficients on the suction surface. The flow incidence angle for the other two injection directions remained at 44.7 degrees. The effect of counter-flow injection on the secondary vortex core within the cascade passageway is not known, but some effect is suspected. This area deserves further study.

With the jet-grid placed at the far-upstream location ($\frac{x}{b} = 25.67$), the pressure distributions on the turbine blad. were similar to the pressure distributions on the turbine blade with the jet-grid placed at station 0. The effect on the blade pressure distribution for co-flow, cross-flow, and counterflow injection at this upstream location is displayed in Figures 5.6, 5.7, and 5.8, respectively. For all three injection directions tested at station 02, the effect of jet-grid injection on the pressure coefficient was confined to the suction surface only. The pressure distributions shown in Figures 5.6, 5.7, and 5.8 are nearly identical. At this jet-grid position, counter-flow injection shown in Figure 5.8 did not have a same effect as counter-flow injection at station 0 shown in Figure 5.5. This result became very important during subsequent turbine blade heat transfer measurements.

5.2 Turbulence Intensity and Decay

The turbulence intensity of the free-stream flow was measured for all test configurations. Equations 4.23, 4.24, and 4.25 were used to compute the X-component, Y-component, and the consolidated turbulence intensity, respectively. The turbulence integral length scales (Λ_u, Λ_v) and turbulence microscales (λ_u, λ_v) were computed from the turbulence energy spectrum of the free-stream flow. Figure 5.9 shows the turbulence energy spectrum ($E_{u'}$) as a function of turbulence frequency for the free-stream turbulence measured along the X-axis without the jet-grid installed (Test XXX). Figure 5.10 shows the Y-axis component of the spectrum of turbulence energy ($E_{v'}$) for the same test. The vonKarman spectrum (Batchelor, 1953) of turbulence predicts a -5/3 slope of the turbu-
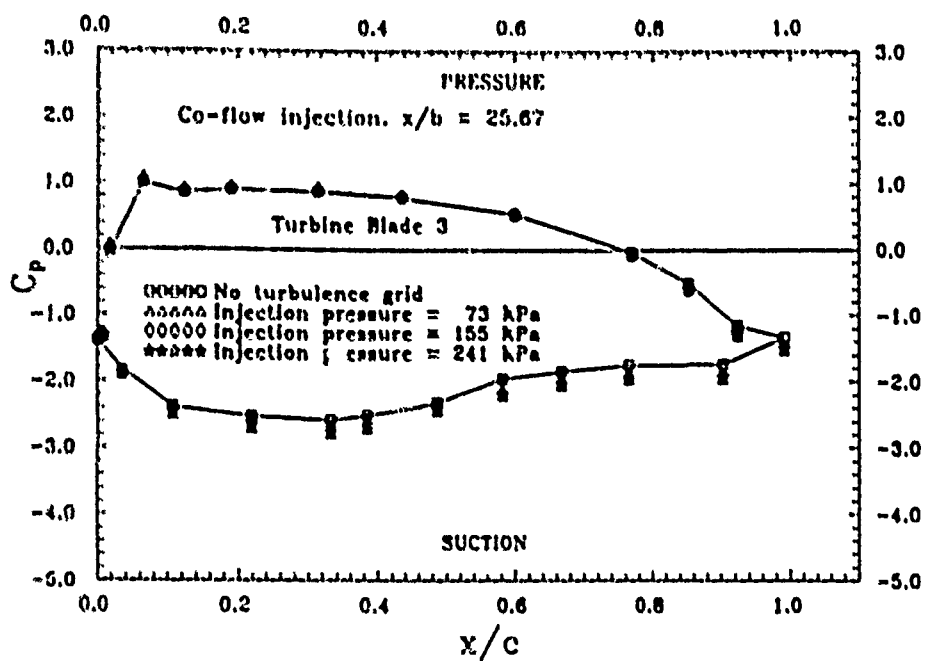
Figure 5.6. Pressure distribution on the turbine blade with co-flow injection at the far-upstream location. $Re_c = 5.0 \times 10^5$
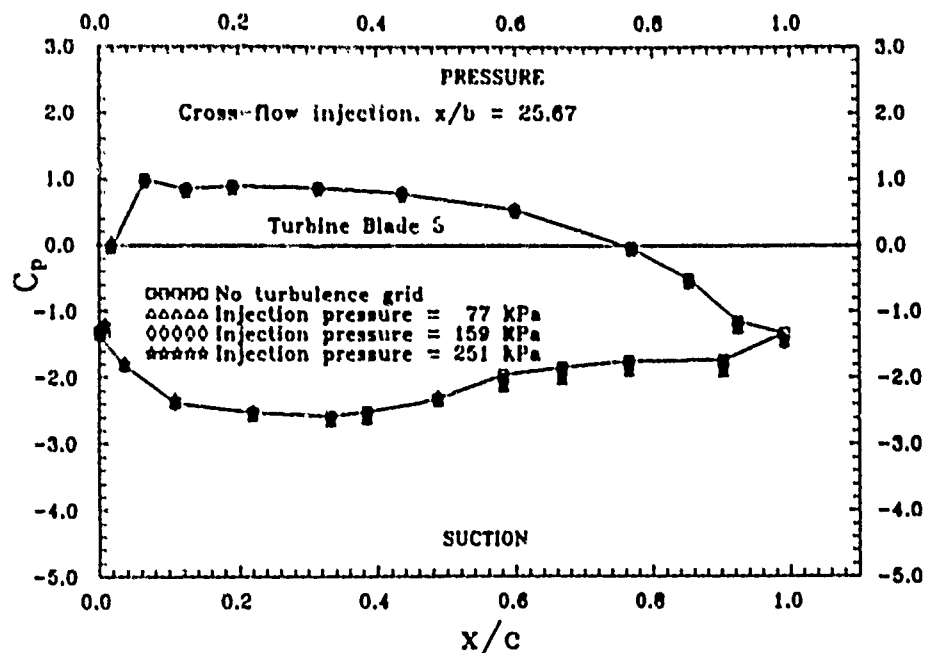
Figure 5.7. Pressure distribution on the turbine blade with cross-flow injection at the far-upstream location. $Re_c = 5.0 \times 10^5$
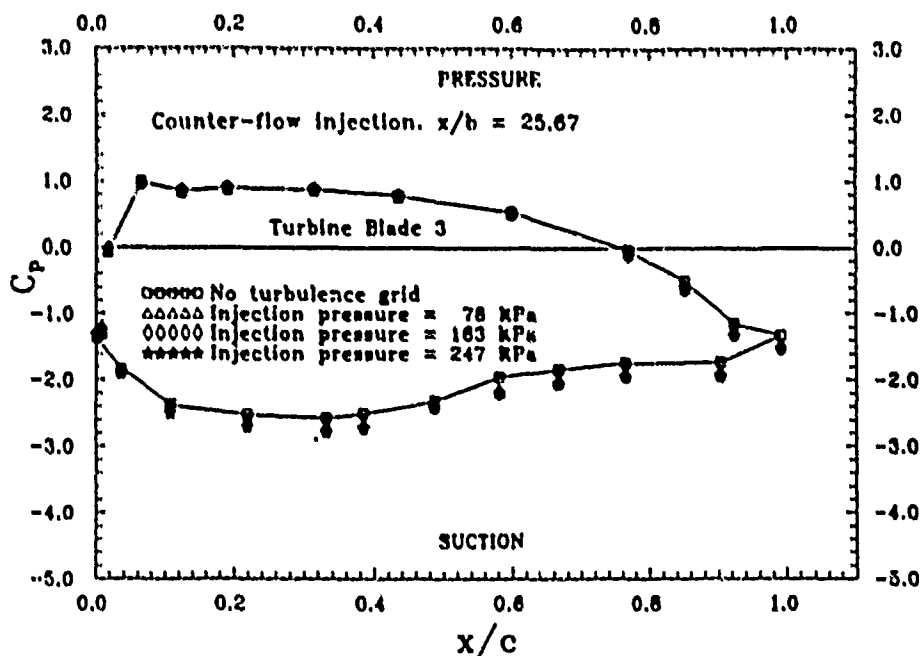
Figure 5.8. Pressure distribution on the turbine blade with counter-flow injection at the far-upstream location. $Re_c = 5.0 \times 10^5$

lence energy spectrum if the free-stream turbulence is homogeneous. The -5/3 slope is shown as a solid line in Figure 5.9. Both the X-axis and the Y-axis component of the turbulence energy spectrum, Figures 5.9 and 5.10, respectively, were too scattered to draw any conclusions as to the fit of the theoretical prediction. This is an indication that the turbulence was not uniform when the jet grid was not placed into the free-stream.

The turbulence energy spectrum for the jet-grid at station 0 ($\frac{x}{b} = 15.75$) , without secondary injection (Test 000), is shown in Figures 5.11 and 5.12. The turbulence energy spectrum for the jet-grid placed at station 02 ($\frac{x}{b} = 25.67$), without secondary injection (Test 002), is shown in Figures 5.13 and 5.14. With the jet-grid in place at either station, the slope of the turbulence energy spectrum matched the -5/3 slope very well, which indicated homogeneous free-stream turbulence was achieved.

5-8
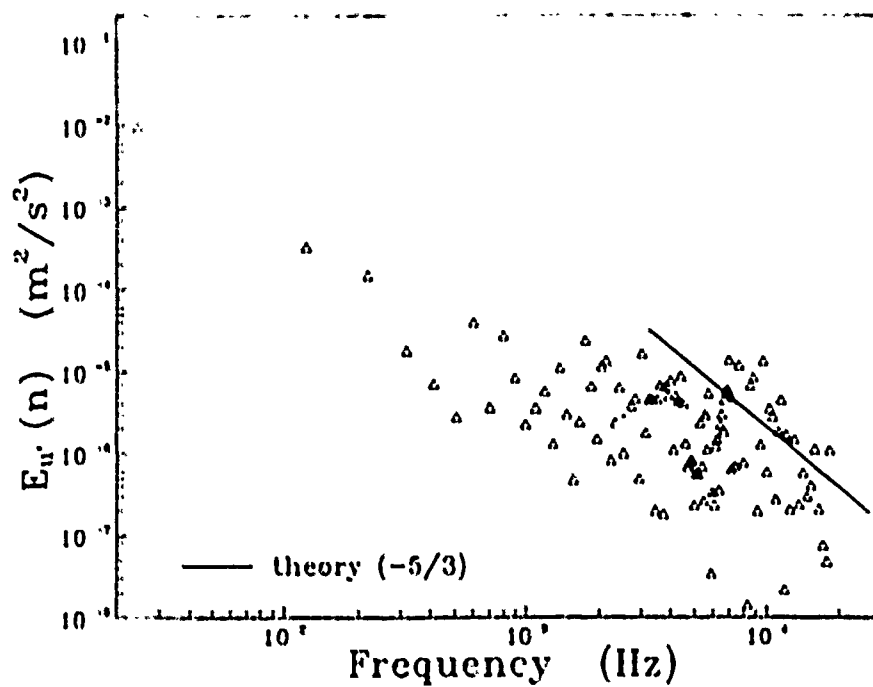
Figure 5.9. u'-turbulence energy spectrum—Test XXX. Theory (Batchelor, 1953)
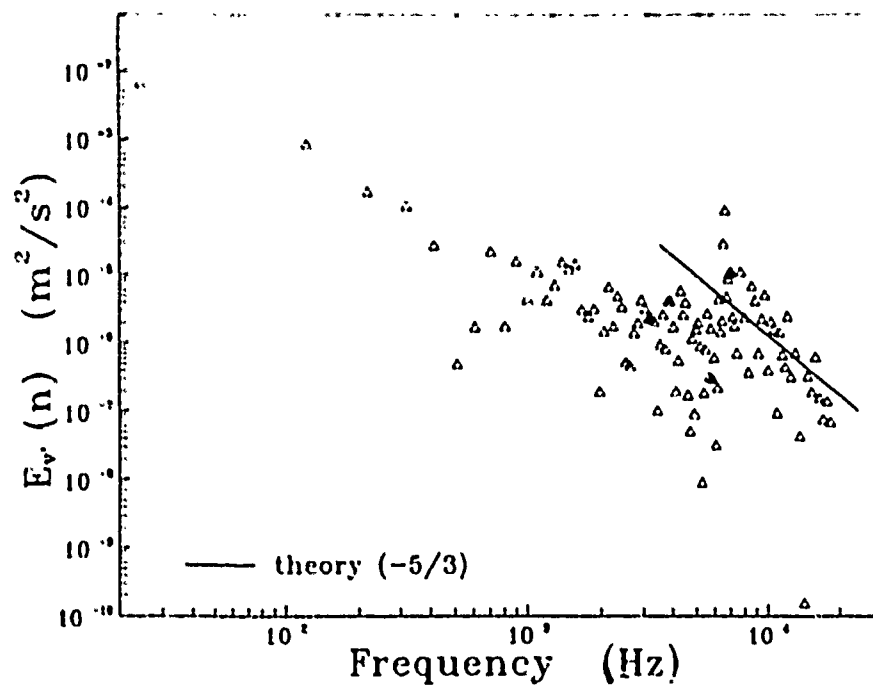
Figure 5.10. v'-turbulence energy spectrum—Test XXX. Theory (Batchelor, 1953)
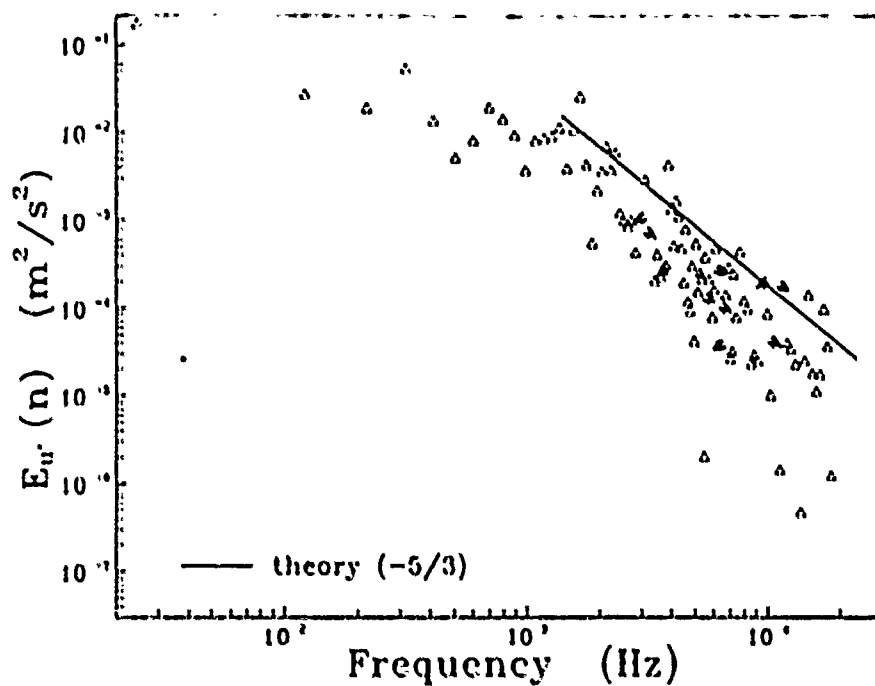
Figure 5.11. u'-turbulence energy spectrum—Test 000. Theory (Batchelor, 1953)
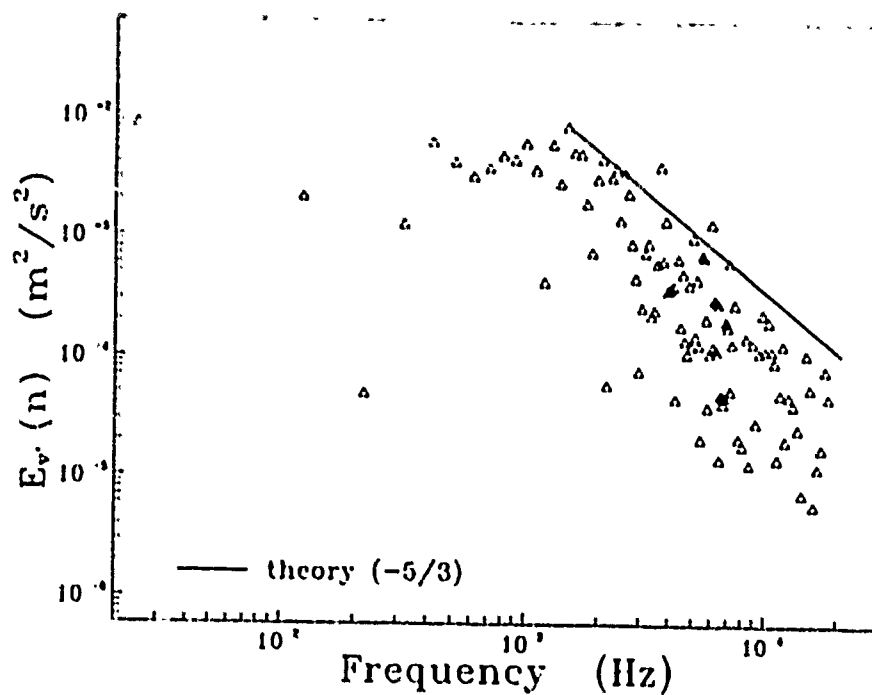
Figure 5.12. v'-turbulence energy spectrum—Test 000. Theory (Batchelor, 1953)
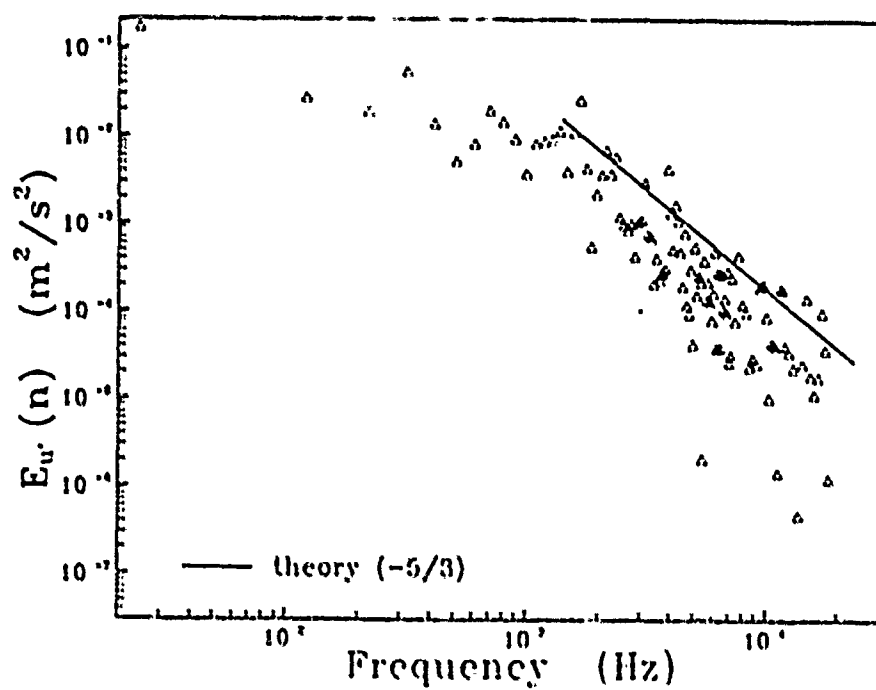
Figure 5.13. u'-turbulence energy spectrum—Test 002. Theory (Batchelor, 1953)
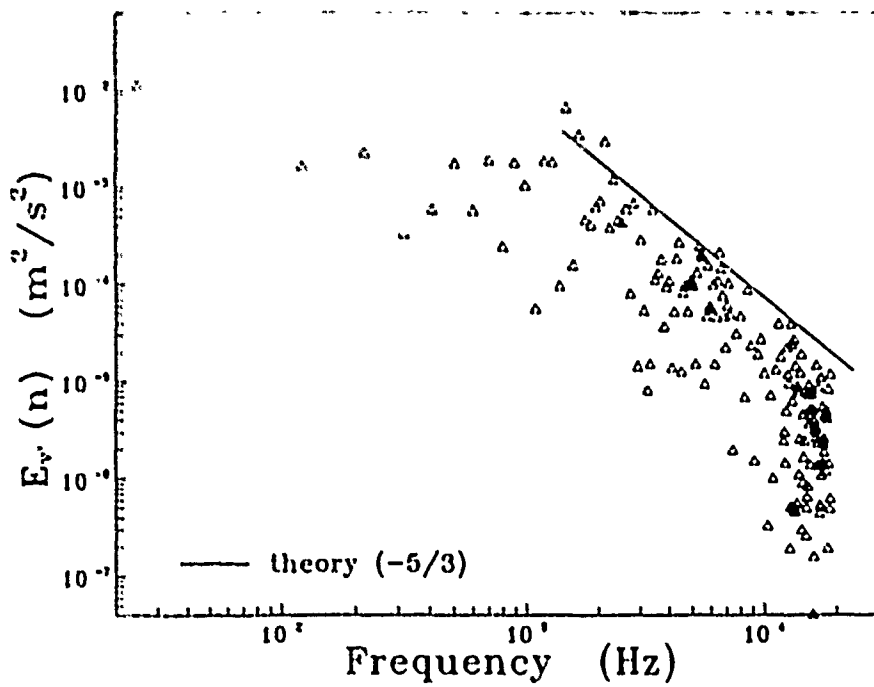
Figure 5.14. v'-turbulence energy spectrum—Test 002. Theory (Batchelor, 1953)

Plots of turbulence energy spectrum for all other test configurations are given in Appendix B. For all other test configurations, the turbulence energy spectrum was well correlated to the theoretical prediction. This is an indication of consistency of the turbulence measurement process and the uniformity of the turbulence in the free-stream.

The results of the turbulence measurements are tabulated in Tables 5.1 and 5.2. In Table 5.1, the test designators A, B, and C indicate co-flow, cross-flow, and counter-flow injection at station 0, respectively. In Table 5.2, test designators D, E, and F indicate co-flow, cross-flow, and counter-flow injection at station 02, respectively. Note the extremely low turbulence level measured during test A14 as compared to other tests at the same station and the very large value of A_v as compared to the value of A_u. The results of Test A14 are not included in the following discussion of turbulence intensity since subsequent testing indicated the hot-wire probe was not measuring free-stream conditions, but was being impinged upon directly by a jet of injected flow. Also, for Tests F21, F22, and F23; the Y-component integral scales and Y-component microscales were virtually indistinguishable.

The turbulence intensity was plotted against the jet-grid injection pressure for co-flow, cross-flow, and counter-flow injection at both stations. Figure 5.15 shows the variation of turbulence intensity for co-flow injection at both jet-grid locations in the free-stream flow. The higher levels of turbulence intensity were measured for the jet grid at station 0 and the lower turbulence levels were measured at station 02. Two conclusions are made from Figure 5.15. First, the turbulence intensity was relatively constant over the range of injection pressures tested for co-flow injection for all three jet-grid orifice diameters. Second, the greatest variation in turbulence intensity was due to the location of the jet-grid in the free-stream flow with respect to the leading edge of the turbine cascade.

The turbulence intensity variation for cross-flow and counter-flow test configurations are shown in Figure 5.16 and Figure 5.17, respectively. From Figures 5.15, 5.16, and 5.17, the most noticable trend is that secondary injection did not have a large effect on the free-stream turbulence, with cross-flow injection (Figure 5.16) having the least effect on the free-stream turbulence of all the injection directions tested. The results of cross-flow injection are extremely important in that the same turbulence level is maintained over the

5-12

Table 5.1. Turbulence intensity and turbulence scale results for turbine cascade wind tunnel test configurations—station 0

test	Tu %	Tu_x %	Tu_y %	Λ_u mm	Λ_v mm	λ_u μm	λ_v μm
XXX	1.26	1.25	1.26	—	—	—	—
000	11.8	13.8	9.5	5.578	0.6398	9.056	49.63
A11	10.5	11.5	9.4	5.324	0.4494	9.125	45.67
A12	9.2	10.5	7.7	4.911	0.5024	12.89	71.57
A13	8.9	9.7	8.0	5.472	0.8310	13.58	61.74
A14	3.7	3.8	3.5	8.002	4.1610	38.25	82.76
A15	10.3	11.5	9.1	5.033	0.4987	8.183	43.99
A21	9.3	10.6	9.0	5.919	0.4833	5.355	30.65
A22	10.3	11.2	8.6	6.275	0.4612	3.727	29.00
A23	10.5	11.5	9.4	6.317	0.4017	3.301	29.15
A24	11.8	13.9	9.2	5.989	0.3381	2.920	28.07
A31	9.6	10.4	8.4	4.426	0.6823	6.147	38.31
A32	9.5	10.4	8.5	6.163	0.4911	5.149	29.40
A33	10.5	12.0	8.8	6.346	0.4792	3.061	24.86
A34	11.2	13.0	9.0	8.116	0.3616	2.649	24.59
B11	10.4	11.4	8.5	5.376	0.5660	12.86	63.88
B12	10.3	11.7	8.5		0.5966	9.097	51.48
B13	10.4	11.8	8.7	5.809	0.6432	11.92	63.87
B14	10.2	11.4	8.9	5.430	0.7921	11.84	63.40
B21	10.7	11.6	9.0	5.831	0.5610	8.307	61.03
B22	10.5	11.7	9.2	5.452	0.5737	8.036	46.84
B23	10.6	11.6	9.4	6.394	0.6251	6.713	37.47
B24	11.1	11.7	10.5	5.537	0.5571	6.347	32.93
B31	11.2	12.3	9.0	5.731	0.5912	8.200	46.51
B32	10.9	12.9	8.3	5.900	0.6204	9.318	61.79
B33	11.3	12.8	9.6	6.191	0.7573	8.183	46.88
C11	9.4	10.6	7.8	5.268	0.7858	6.283	36.77
C12	9.1	10.3	7.8	5.744	0.6295	6.986	40.74
C13	9.3	10.7	7.6	5.918	0.7264	7.306	43.35
C14	9.3	11.0	7.2	6.998	0.7670	8.640	55.04
C21	9.4	10.8	7.9	6.176	0.6540	6.540	39.78
C22	9.7	11.0	8.2	6.685	0.7680	6.805	38.51
C23	10.6	12.2	8.7	7.625	0.8916	6.984	45.80
C24	10.8	12.4	9.0	6.909	0.6196	7.914	55.16
C31	9.5	10.4	8.5	6.681	0.8390	5.845	32.66
C32	10.0	11.6	8.2	7.416	0.5433	5.005	32.53
C33	11.6	13.9	8.7	7.390	0.7372	5.433	41.06
C34	11.6	13.9	8.7	7.651	0.7677	6.852	51.46

Table 5.2. Turbulence intensity and turbulence scale results for turbine cascade wind tunnel test configurations—station 02

test	Tu %	Tu_x %	Tu_y %	Λ_u mm	Λ_v mm	λ_u μm	λ_v μm
002	6.5	7.4	5.5	6.532	0.7782	39.97	343.2
D11	6.6	7.8	5.3	6.098	0.6608	36.70	338.5
D12	5.5	6.1	4.8	5.197	0.6405	54.34	436.9
D13	5.3	6.0	4.5	5.449	0.9349	54.28	449.4
D21	5.4	6.2	4.6	6.323	0.7437	51.34	406.1
D22	5.4	6.4	4.0	6.691	0.7235	41.60	399.1
D23	5.6	6.7	4.4	6.192	0.6393	36.05	357.5
D31	4.9	5.5	4.3	5.328	0.6072	55.78	437.1
D32	5.6	6.1	4.9	5.659	0.7433	39.92	291.0
D33	6.4	7.2	5.5	7.140	0.7524	26.36	215.0
E11	6.0	6.7	5.3	5.691	0.5718	47.10	377.6
E12	6.5	7.5	5.2	6.860	0.7455	43.77	428.9
E13	5.5	6.3	4.6	6.455	0.7255	52.61	463.4
E21	5.8	6.4	5.2	5.896	0.6757	54.72	429.3
E22	5.5	6.3	4.7	6.003	0.7173	50.37	436.3
E23	6.1	6.8	5.3	6.000	0.7470	42.18	374.2
E31	5.9	6.7	4.9	6.589	0.7172	52.98	455.8
E32	5.5	6.3	4.5	6.453	0.7180	66.23	606.8
E33	6.2	6.7	5.6	6.193	0.7261	51.12	441.5
F11	5.6	6.6	4.4	6.603	0.7470	47.86	462.0
F12	5.1	5.8	4.4	5.888	0.7720	58.86	481.8
F13	4.9	5.6	4.1	6.083	0.7561	59.25	500.8
F21	4.8	5.2	3.6	6.727	0.7016	78.26	867.0
F22	5.9	6.9	4.6	6.771	0.6218	94.75	1137.7
F23	5.5	6.0	4.9	5.915	0.7085	103.43	964.6
F31	5.3	5.7	4.8	6.295	0.8283	60.48	433.0
F32	5.6	6.2	5.0	6.727	0.8433	63.10	526.8
F33	5.8	6.5	4.9	6.697	0.7985	74.20	620.0
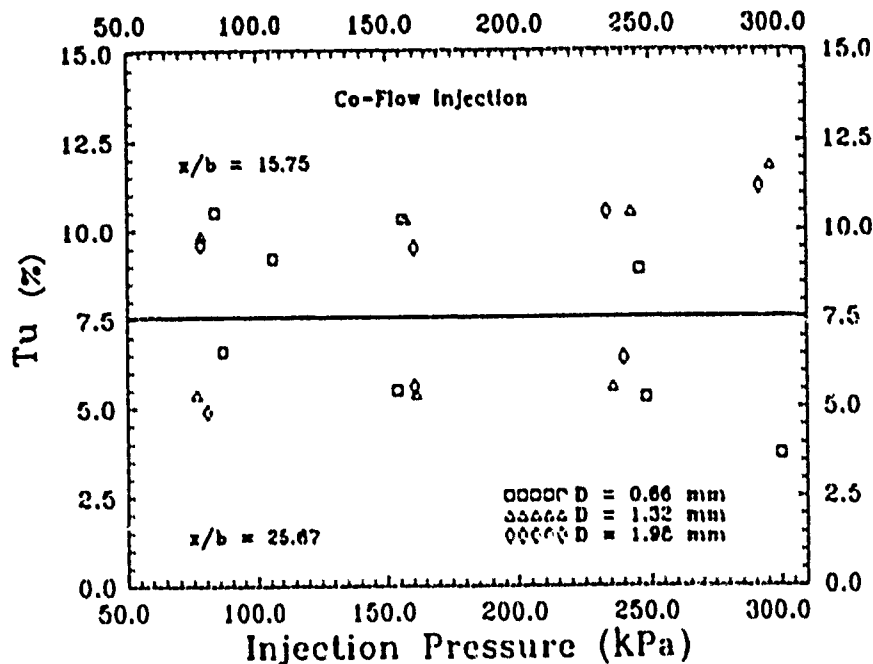
Figure 5.15. Effect of jet-grid injection pressure on free-stream turbulence intensity for co-flow injection

range of injection pressures, but from Tables 5.1 and 5.2, for tests designated with either a B or an E (cross-flow injection), the turbulence microscale lengths are not the same and to a lesser degree, the turbulence integral scale lengths are not the same. Hence cross-flow injection allows one to observe the effect of turbulence scale lengths on turbine blade heat transfer measurements at a constant turbulence level. Further discussion on this effect is delayed until heat transfer results are discussed.

The variation of turbulence intensity with injection pressure is shown in Figures 5.15, 5.16, and 5.17 for co-flow, cross-flow, and counter-flow injection, respectively. The lower turbulence levels are the result of jet-grid injection at station 02, while the higher levels of turbulence are the result of injection at station 0. From Figures 5.15 and 5.16, the turbulence intensity was relatively constant for all injection pressures, and for all injection orifice diameters, using co-flow and cross-flow injection. However, Figure 5.17 shows the free-stream turbulence intensity increased 1-2 percent with increasing injection pressure for both 1.32 mm and 1.98 mm injection orifice diameters, but only with the jet-grid at station 0. A 1-2 percent change in turbulence intensity represents a small change in the
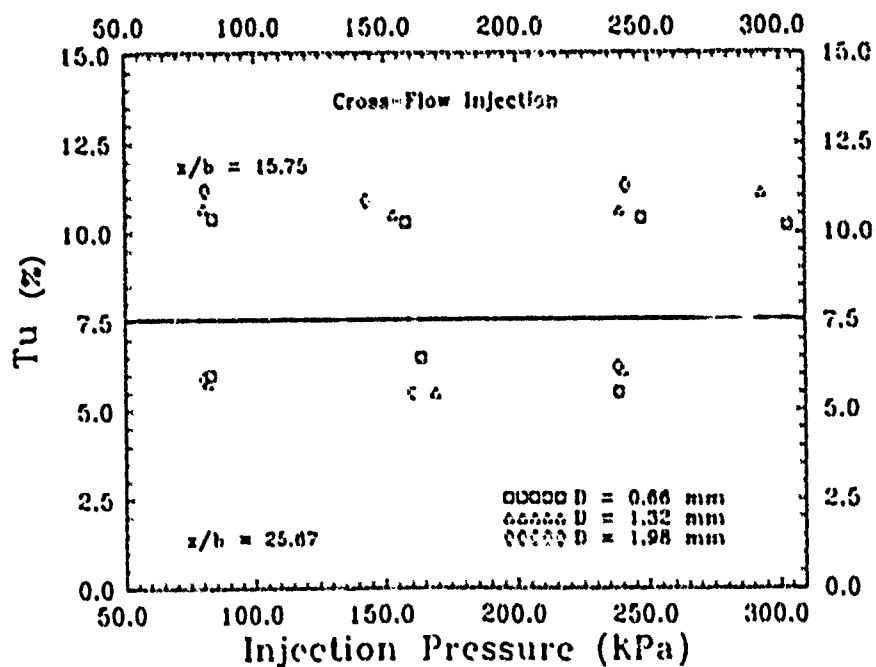
Figure 5.16. Effect of jet-grid injection pressure on free-stream turbulence intensity for cross-flow injection
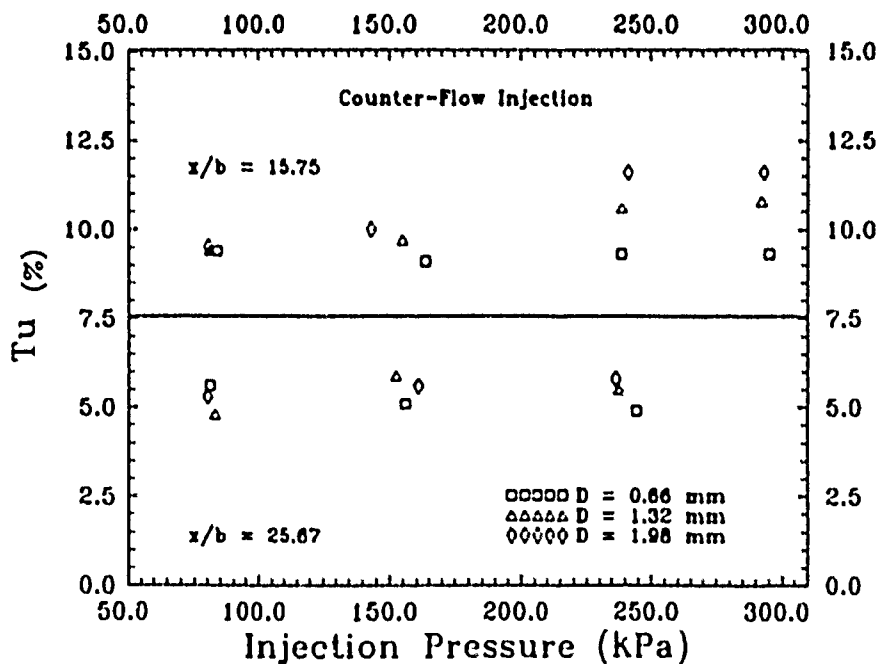

Figure 5.17. Effect of jet-grid injection pressure on free-stream turbulence intensity for counter-flow injection

overall turbulence level, and for the most part, the injection pressure seemed to have a small effect on turbulence intensity. This result is in contrast to the results of Young and Han (Young, 1989) where they determined jet-grid injection increased the turbulence intensity of the free-stream flow by an amount of up to 45 percent over the non-injection case. The difference in results may be due to several factors. Young and Han used supersonic jet-grid injection, while this study was limited to sonic injection, except during test A13, where sonic injection is thought to have occurred. Young and Han (Young, 1989) found that the turbulence level remained relatively constant until they used supersonic injection. Only with supersonic injection were they able to obtain the large increase in turbulence intensity.

An analysis of the free-stream turbulence decay is presented. The turbulence intensity decay behind the jet-grid at station 0 ($\frac{x}{b} = 15.75$) compares favorably with the turbulence decay correlation used by Blair (Blair, 1983a). The free-stream turbulence level varied from 8.9 percent using the 0.66 mm diameter injection orifice and co-flow injection (Test A13), up to 11.8 percent with the jet-grid at station 0 with no jet-grid injection (Test 000). The correlation used by Blair (Blair, 1983a) is given by Equation 2.12. Using Equation 2.12, the free-stream turbulence level at a non-dimensional distance of $\frac{x}{b} = 25.67$ behind the jet-grid is computed as 10.9 percent which closely matched the results of the present study.

At station 02 ($\frac{x}{b} = 25.67$), the free-stream turbulence level varied from 4.8 percent using the 1.32 mm injection orifice and cross-flow injection (Test F21), up to 6.6 percent using the 0.66 mm injection orifice and co-flow injection (Test D11). Equation 2.12 predicts a 7.7 percent turbulence level. This represents a 16 percent difference between computed and measured turbulence levels. One reason for the difference between the computed and measured turbulence levels may be different test conditions existed between Blair's experiment and the present experiment. Blair's correlation was developed from tests on a flat plate where the wind tunnel free-stream velocity was constant along the length of the tunnel. In contrast, in the linear turbine cascade wind tunnel of this study, the free-stream accelerated as the flow approached the leading edge of the turbine cascade where the turbulence intensity was measured with a hot-wire probe.

Turbulence is proportional to the fluctating component of velocity (u', v'). As the

free-stream velocity increases, the fluctuating component of that velocity remains relatively constant or even decreases under accelerating flow conditions, while the mean velocity increases and the measured turbulence intensity decreases. The difference between accelerating free-stream and steady free-stream conditions may account for the difference in the predicted turbulence level from Equation 2.12 and the actual turbulence level measured with the jet-grid at station 02.

5.2.1   Turbulence Integral Scale The X-component integral scale (Λ_u) length was on the same order as the outside diameter of the jet-grid injection tube ($b = 0.635$ mm) (See Figures 5.18, 5.19, and 5.20. As seen in Figures 5.21, 5.22, and 5.23, the Y-component integral scale (Λ_v) was an order of magnitude smaller than the X-component integral scale, except for the case where it is thought that a jet of injected flow impinged directly on the hot-wire anemometer and distorted the test results (Test A14).

The variation of integral scale length was examined for dependence on jet-grid orifice diameter, injection pressure, and injection direction. Figures 5.18, 5.19, and 5.20 show effect on the X-component integral scale for the three orifice diameters tested over the same range of injection pressures for co-flow, cross-flow, and counter-injection, respectively, at station 0 ($\frac{x}{b} = 15.75$). The results of Figures 5.18, 5.19, and 5.20 were repeatable for similar free-stream conditions. Uncertainty in defining the zero frequency turbulence energy ($E_u'(n)$ as $n \to 0$) was minimimized by averaging all turbulence energies between 0 and 1000 Hz frequencies; this method provided consistent results for the computation of the turbulence integral scale lengths listed in Tables 5.1 and 5.2. The turbulence scale measurements (both integral scale and microscale) had a calculated uncertainty of 2 percent.

Comparing the results given in Figures 5.18, 5.19, and 5.20, the X-component integral scale remained nearly constant over the range of injection pressures. The only exception was a 30 percent increase in integral scale length which occurred for co-flow injection at an injection pressure of approximately 300 Pa, Figure 5.18. From Figure 5.20, counter-flow injection increased slightly the X-component integral scale over the case with the jet-grid in place, but without injection. The larger diameter injection orifices, generally produced the larger X-component integral scales. Young and Han (Young, 1989) propose counter-flow

5-18

injection increases the effective diameter of the jet-grid tube that the free-stream sees as it flows through the grid. These results support this proposal since the larger X-component integral scale lengths were obtained for the counter-flow configuration.

Figures 5.21, 5.22, and 5.23 show the effect on the Y-component integral scale for the three orifice diameters tested over the same range of injection pressures for co-flow, cross-flow, and counter-injection, respectively, at station 0. The Y-component integral scales were nearly independent of injection orifice diameter. The Y-component integral scale also seemed insensitive to injection pressure except for one case. Figure 5.21 shows a dramatic increase (800 percent) of integral scale size for the 0.66 mm diameter injection orifice at about 300 kPa. As discussed previously, this datum represents the results of Test A14 where supersonic injection velocities may have occurred. Since injection pressures were measured and not flow rates, it is not possible to accurately determine the exit velocity. However, the high jet-grid injection pressures make it highly probable that the flow was supersonic during Test A14.

Similar to the results for the X-component and Y-component integral scales with the jet-grid at station 0, results of the X-component and Y-component integral scales were obtained for the jet-grid located at station 02 ($\xi = 25.67$). Plots of the X-component integral scale versus injection pressure for all three diameters are given in Figures 5.24, 5.25, and 5.26 for co-flow, cross-flow, and counter-flow, respectively. The Y-component of integral scales measured over the injection pressure range, with the jet-grid at station 02, are shown in Figures 5.27, 5.28, and 5.29 for co-flow, cross-flow, and counter-flow injection directions, respectively.

Most noticeable from Figures 5.24, 5.25, and 5.26 is the result that the X-component integral scale length was on the order as the jet-grid tube diameter (0.635 mm). This is the same result obtained with the jet-grid at station 0. Hence, the turbulence integral scale did not decay downstream of the jet-grid. In contrast to the results obtained for the integral scale length with the jet-grid at station 0, Figure 5.20, counter-flow injection at station 02, shown in Figure 5.26, did not increase the X-component integral scale length. The effect of injection orifice diameter on X-component integral scale length was the same as for the jet-grid placed at either station. On the other hand, the Y-component integral

scale length became more dependent on injection orifice diameter than with the jet-grid at station 0. A larger variation of the Y-component integral scale corresponding to each orifice diameter is visible in Figures 5.27, 5.28, and 5.29 as compared to the variation of the Y-component integral scale obtained with the jet-grid at station 02 shown in Figures 5.21, 5.22 and 5.23.
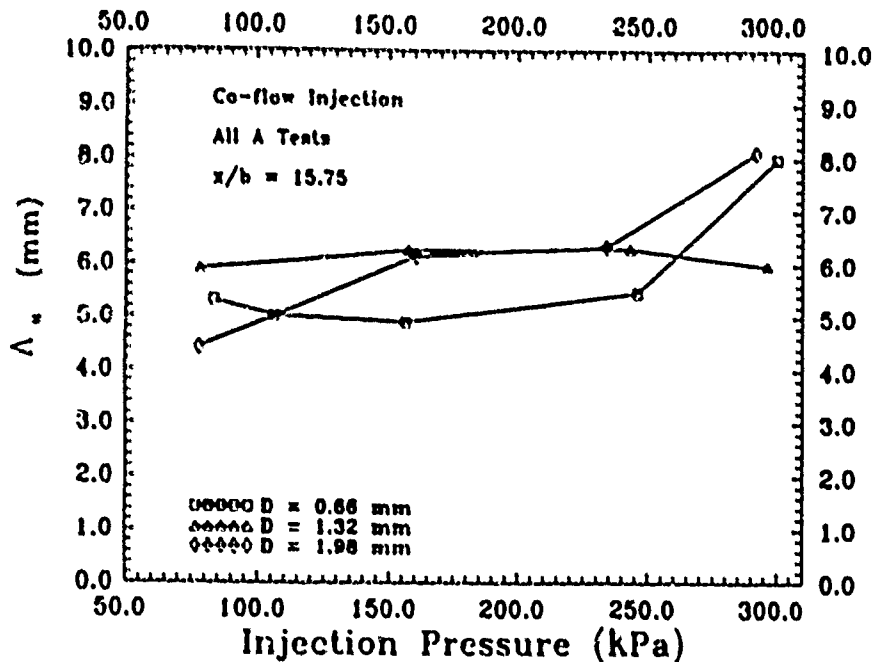
Figure 5.18. Effect of injection pressure and orifice diameter on X-component integral scale length for co-flow injection at $\xi = 15.75$

The effects of jet-grid injection orifice diameter on the X-component and Y-component integral scale were cross-plotted against their respective free-stream turbulence level component. Figures 5.30–5.32 present the X-component turbulence integral scale lengths as a function of the respective X-component of turbulence intensity (Tu_x) for each of the three jet-grid injection diameters. Each plot shows the integral scale for all injection pressures, for the jet-grid at both locations in the free-stream flow. The injection directions are denoted by either a solid symbol for co-flow injection, a hatched symbol for cross-flow injection, or a open symbol for counter-flow injection. The X-component integral scale remained relatively independent of the free-stream turbulence intensity. Figures 5.30–5.32 show the same integral length scale was obtained throughout the range of turbulence levels tested (5–13.9 percent), except in the case of co-flow injection, at the 10–12 percent turbulence level, shown in Figure 5.32. In this case, the solid star symbol represents the datum obtained from Test A14, where it is thought supersonic injection through the jet-grid occured. All other results are for subsonic injection through the jet-grid. Comparison between each of these three figures shows the injection orifice diameter had no distinct

5-21

Figure 5.19. Effect of injection pressure and orifice diameter on X-component integral scale length for cross-flow injection at $\frac{x}{b} = 15.75$

Figure 5.20. Effect of injection pressure and orifice diameter on X-component integral scale length for counter-flow injection at $\frac{x}{b} = 15.75$

Figure 5.21. Effect of injection pressure and orifice diameter on Y-component integral
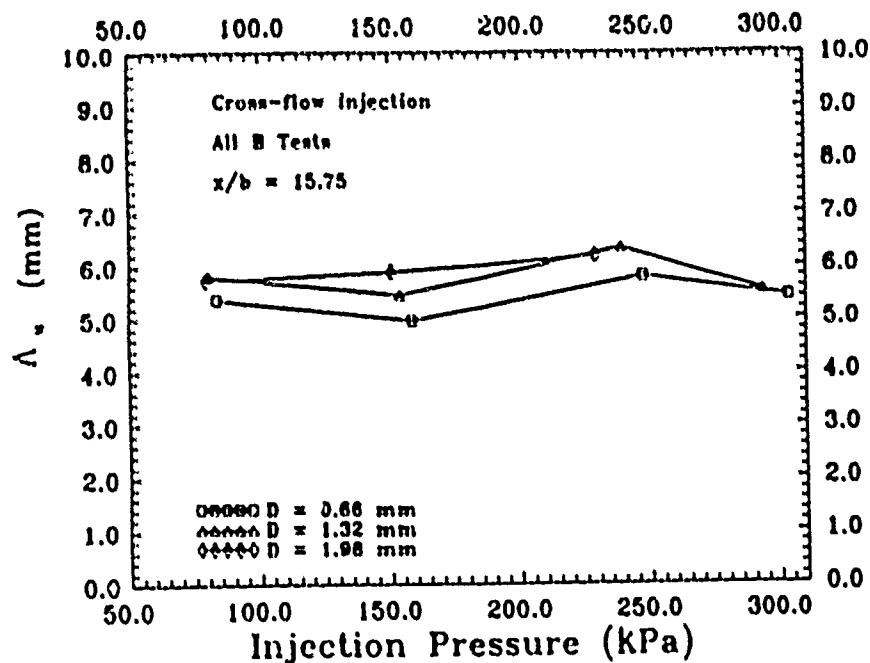scale length for co-flow injection at $\frac{x}{b} = 15.75$

Figure 5.22. Effect of injection pressure and orifice diameter on Y-component integral
scale length for cross-flow injection at $\frac{x}{b} = 15.75$

Figure 5.23. Effect of injection pressure and orifice diameter on Y-component integral scale length for counter-flow injection at $\frac{x}{b} = 15.75$

Figure 5.24. Effect of injection pressure and orifice diameter on X-component integral scale length for co-flow injection at $\frac{x}{b} = 25.67$

Figure 5.25. Effect of injection pressure and orifice diameter on X-component integral scale length for cross-flow injection at $\frac{x}{b} = 25.67$
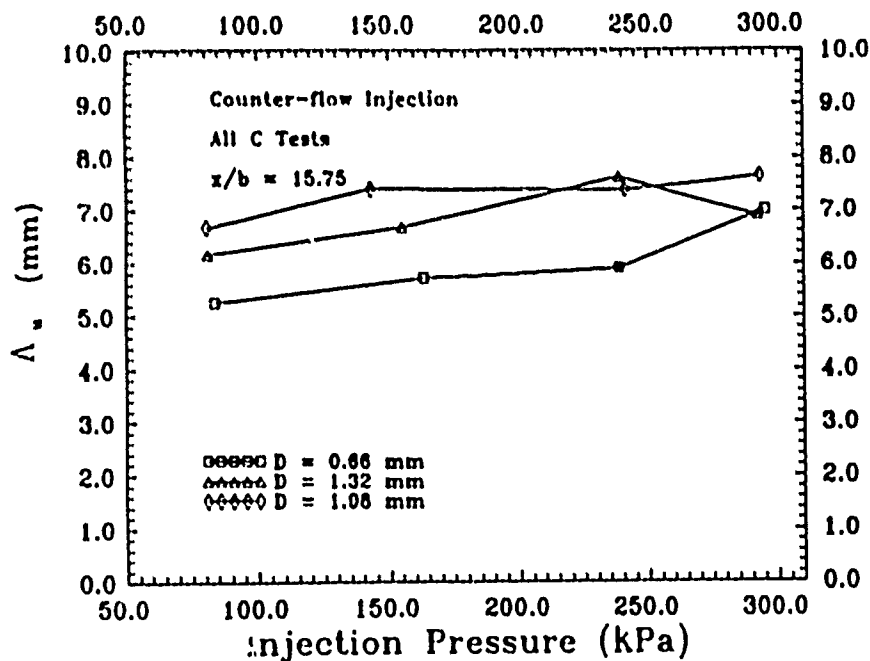

Figure 5.26. Effect of injection pressure and orifice diameter on X-component integral scale length for counter-flow injection at $\frac{x}{b} = 25.67$
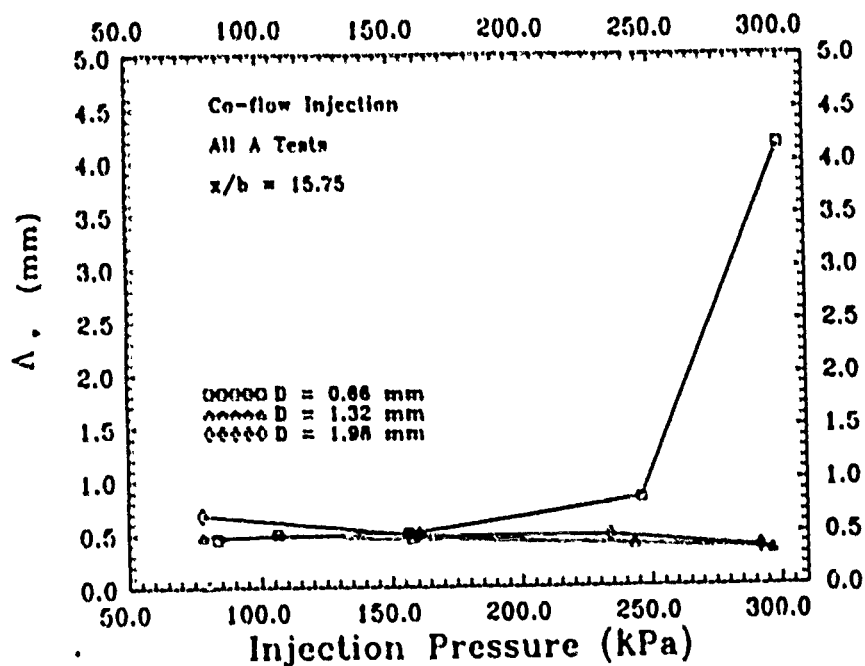
Figure 5.27. Effect of injection pressure and orifice diameter on Y-component integral scale length for co-flow injection at $\frac{x}{b} = 25.67$
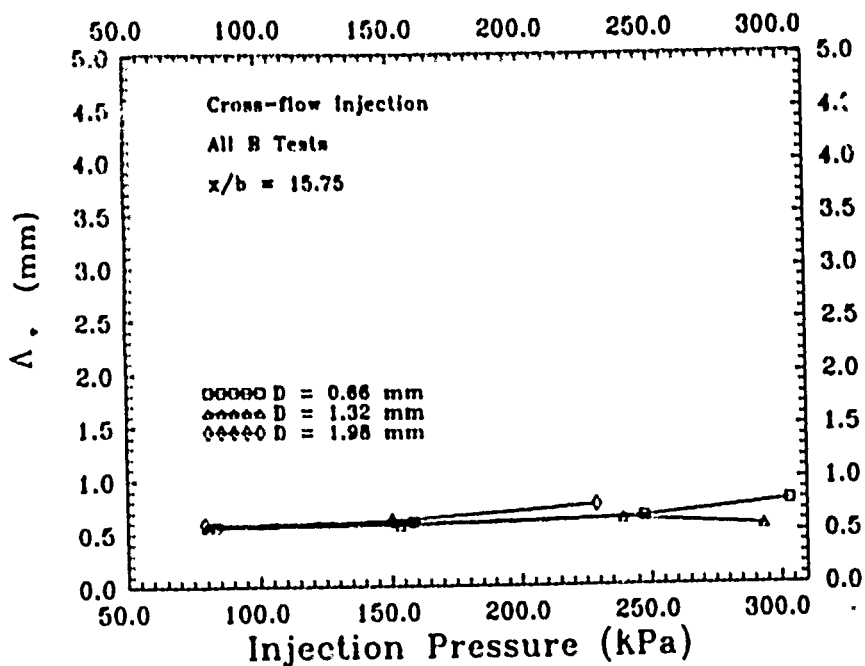

Figure 5.28. Effect of injection pressure and orifice diameter on Y-component integral scale length for cross-flow injection at $\frac{x}{b} = 25.67$
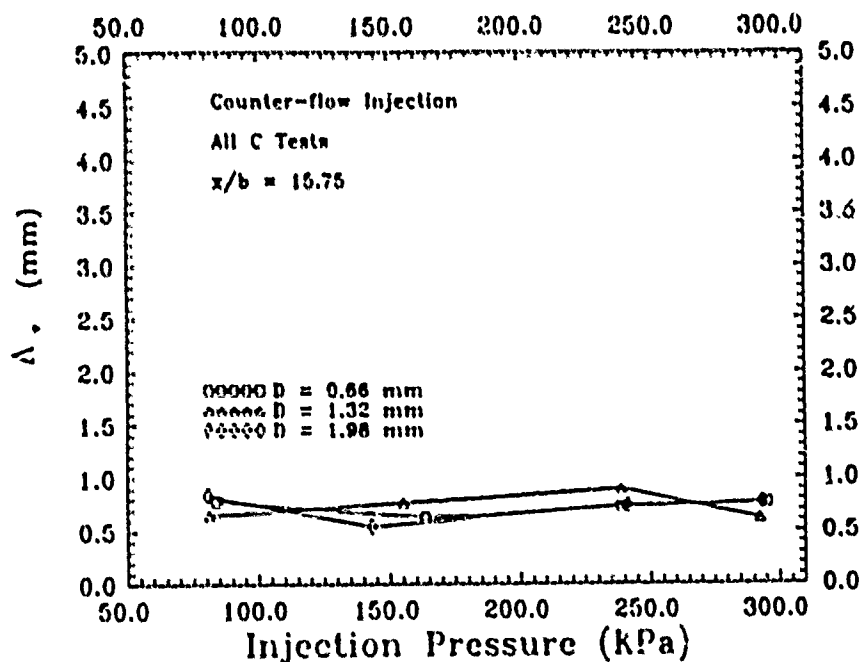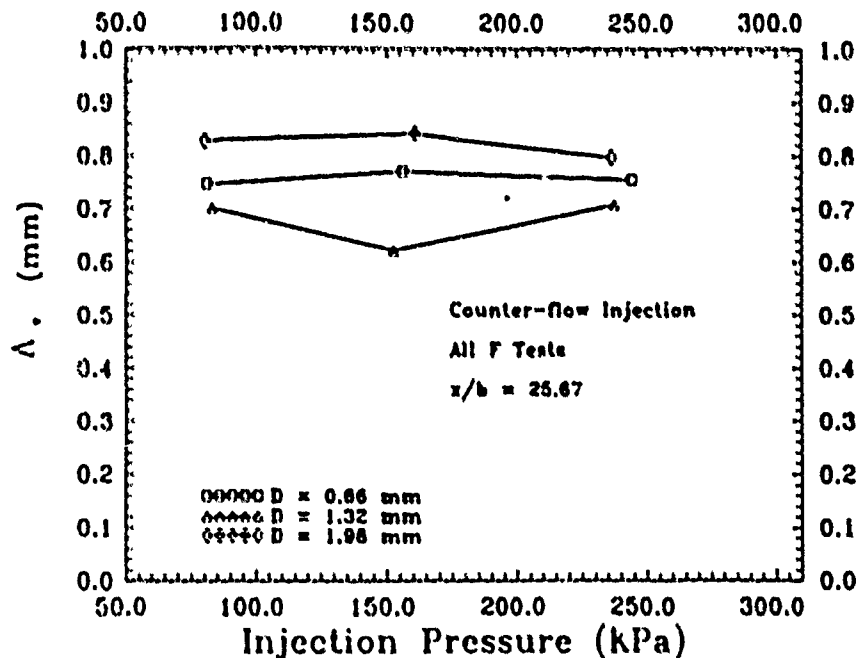
Figure 5.29. Effect of injection pressure and orifice diameter on Y-component integral scale length for counter-flow injection at $\frac{x}{b} = 25.67$
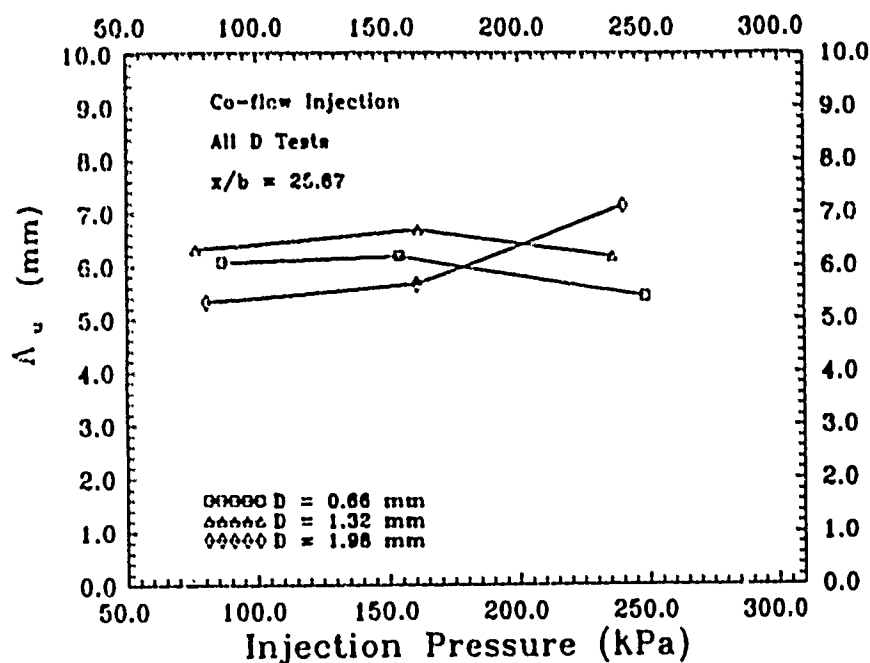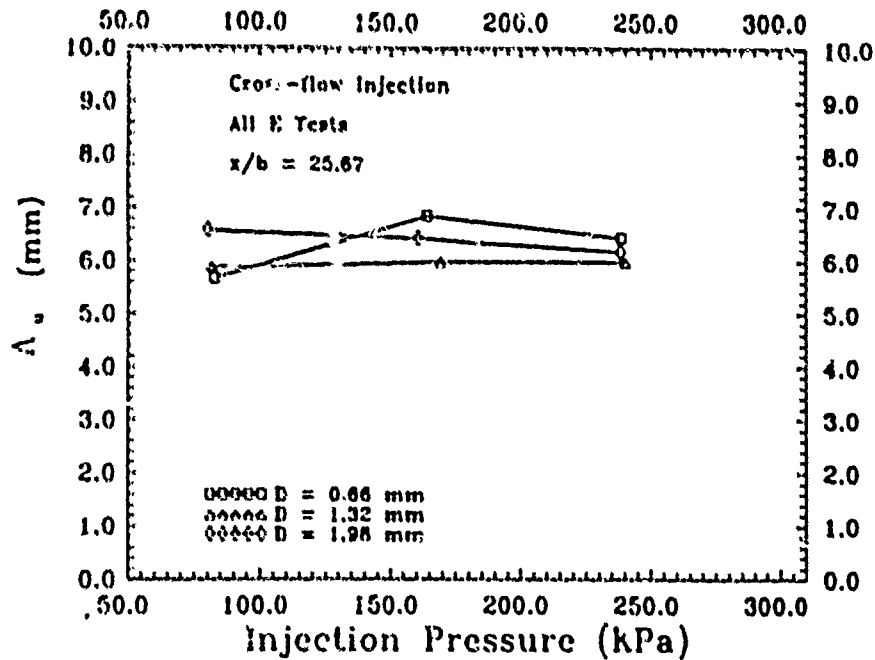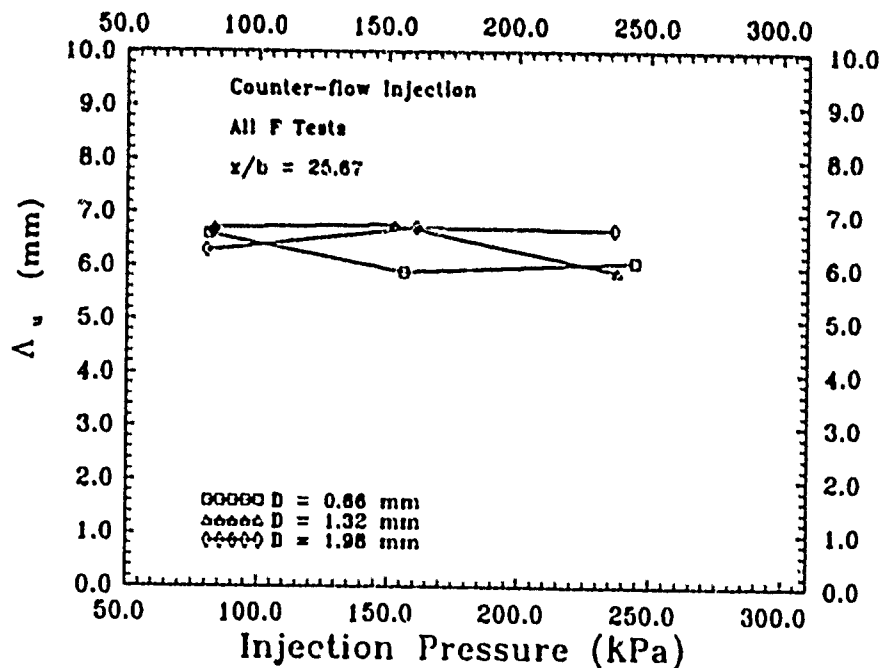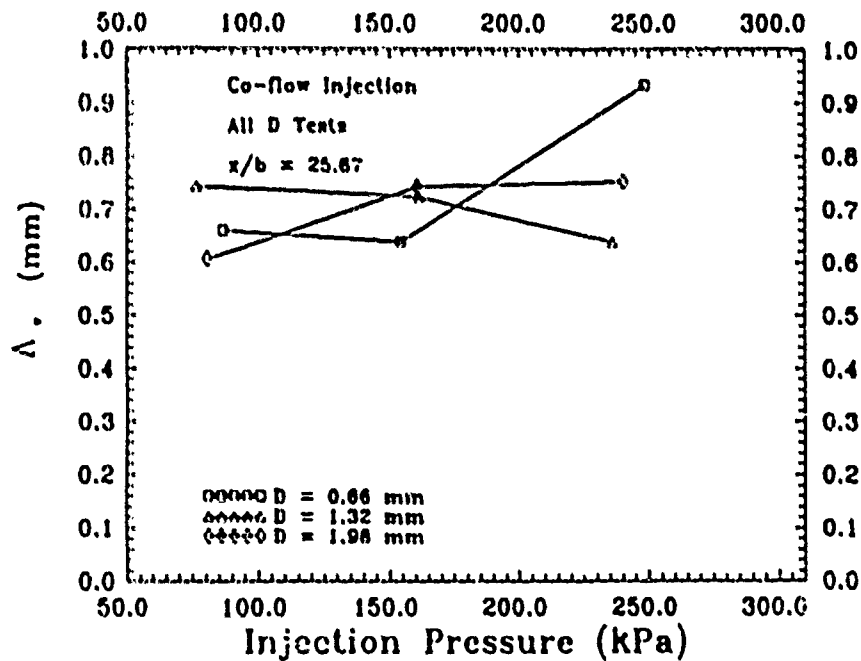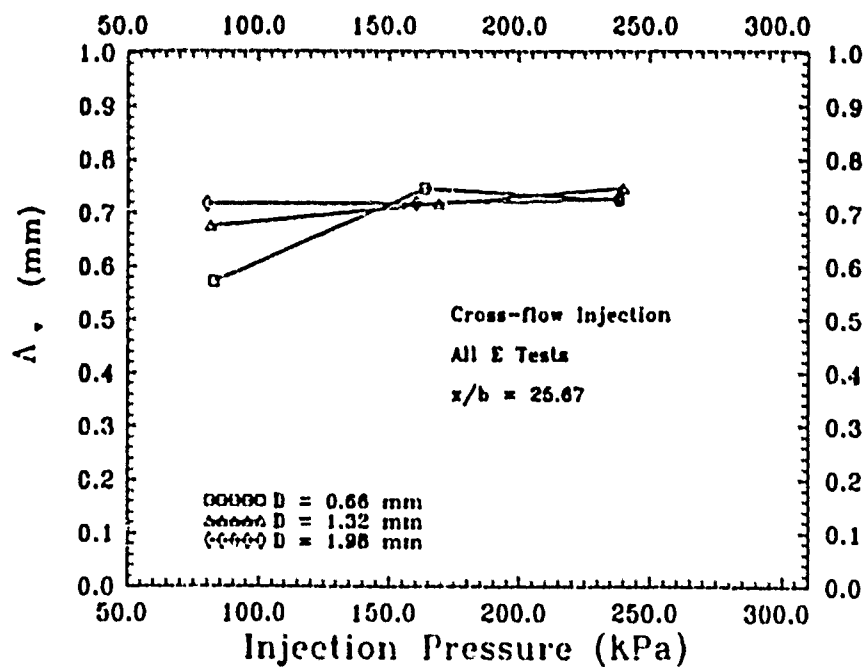
effect on the X-component integral scale length. This reinforces the observation that the X-component turbulence integral scale length is primarily a function of the jet-grid tube diameter and does not dissipate downstream of the jet-grid.

Lastly, from Figures 5.30-5.32, the different injection orientations produced integral scales that are grouped together for particular turbulence levels. As an example, Figure 5.31 shows the X-component integral scales for cross-flow injection (hatched symbols), are all plotted in the same region at both the 5-6 percent turbulence level and the 10-12 turbulence level. This phenomena may prove to be useful for selecting a precise turbulence level once the overall range turbulence intensity for all types of jet-grid injection has been obtained.

Figures 5.33-5.35 show the Y-component integral scale as a function of the Y-component turbulence intensity for each of the three jet-grid injection orifice diameters. These figures show the Y-component integral scale data was more randomly distributed than the X-component integral scales shown in Figures 5.30 - 5.32. For example, this randomness of data is readily apparent when one compares Figure 5.30 with Figure 5.33.

Figure 5.30. Effect of X-component turbulence intensity on the X-component integral scale length for $D = 0.66$ mm

Figure 5.31. Effect of X-component turbulence intensity on the X-component integral scale length for $D = 1.32$ mm
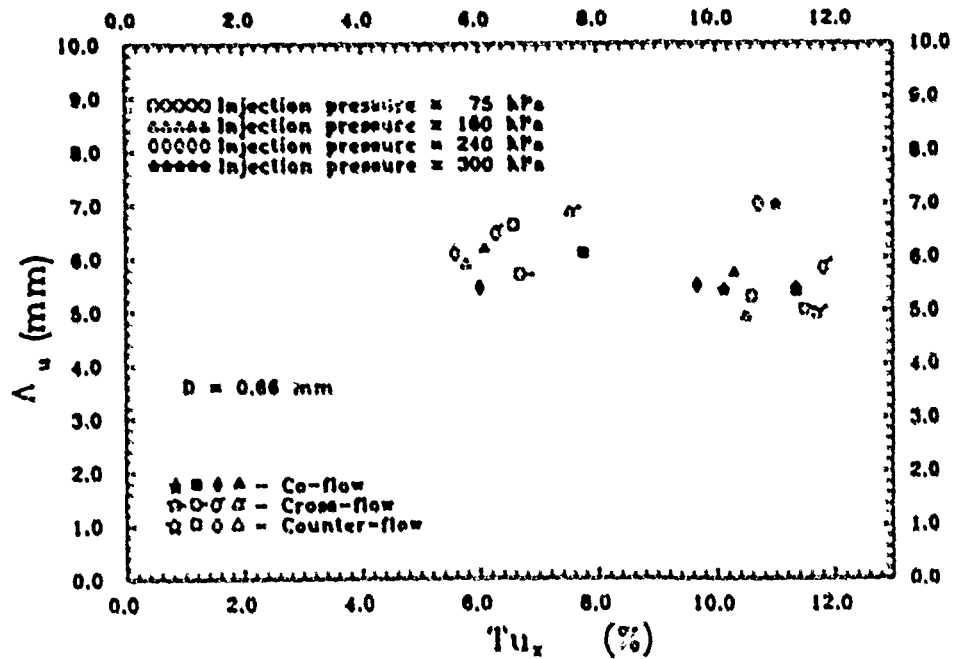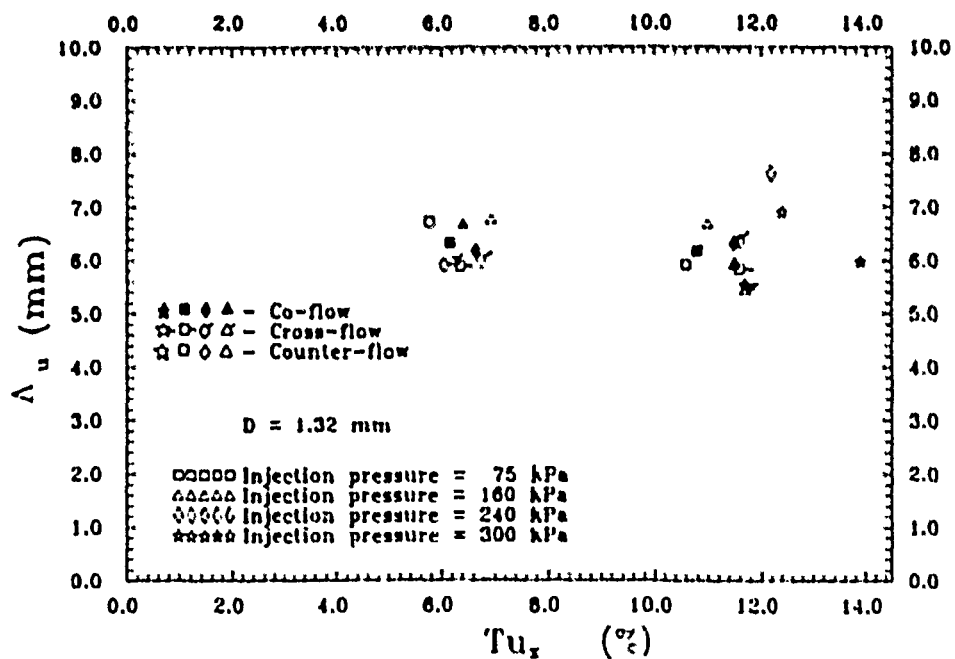
Figure 5.32. Effect of X-component turbulence intensity on the X-component integral scale length for 1.98 mm

which represent the X and Y components of turbulence integral scale for the same tests. Also, as the injection orifice diameter increased, the overall range of values possible for the Y-component turbulence integral scale length increased. The grouping of results obtained for the Y-component integral scale lengths from co-flow, cross-flow, and counter-flow is not as readily apparent from these plots as it was in Figures 5.30 - 5.32.

5.2.2 Turbulence Microscale The turbulence microscale size was affected by jet-grid location, injection pressure, and injection orifice diameter. The location of the jet-grid had the most effect on the microscale size and the injection orifice diameter had the least effect on the microscale size. Comparing the results tabulated in Table 5.1 with those results of Table 5.2 for the turbulence microscales, the X-component microscale was on the order of 5-10 μm with jet-grid injection at station 0 ($\frac{x}{b} = 15.75$) and 4.2-9.9 times larger with jet-grid injection at station 02 ($\frac{x}{b} = 25.67$) and the Y-component microscale was on the order of 30-60 μm with jet-grid injection at $\frac{x}{b} = 15.75$ and 9.4-10.3 times larger with the jet-grid injection at station 02.

From Tables 5.1 and 5.2, the X-component turbulence microscale is much smaller

Figure 5.33. Effect of Y-component turbulence intensity on the Y-component integral scale length for $D = 0.66$ mm
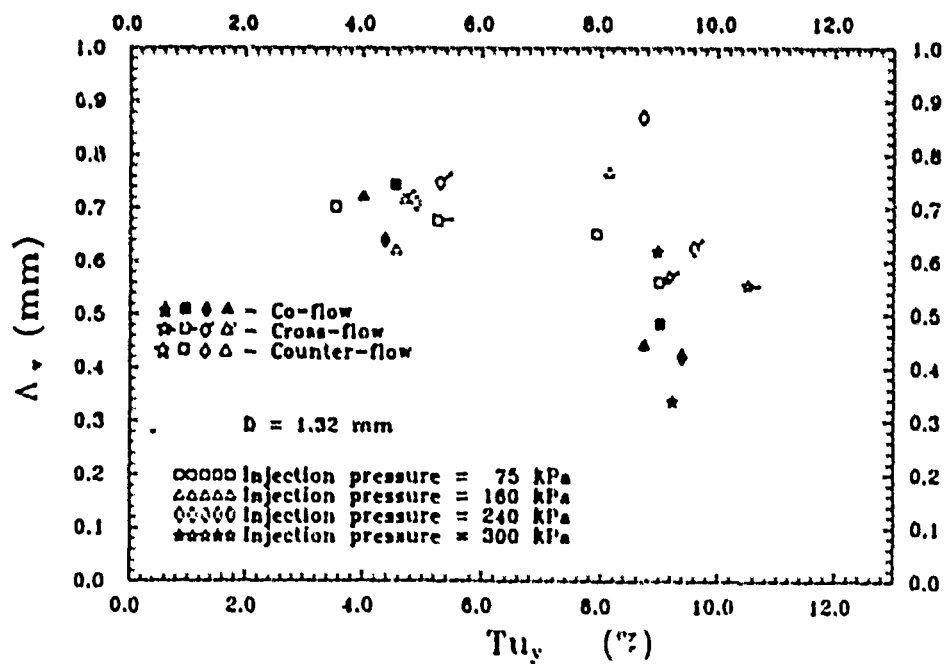
Figure 5.34. Effect of Y-component turbulence intensity on the Y-component integral scale length for $D = 1.32$ mm
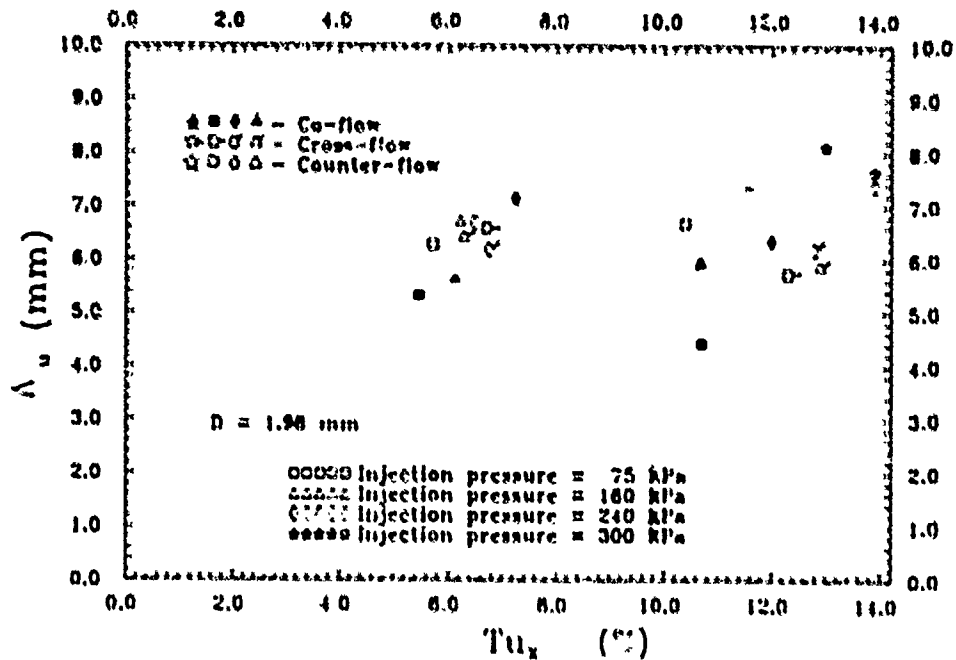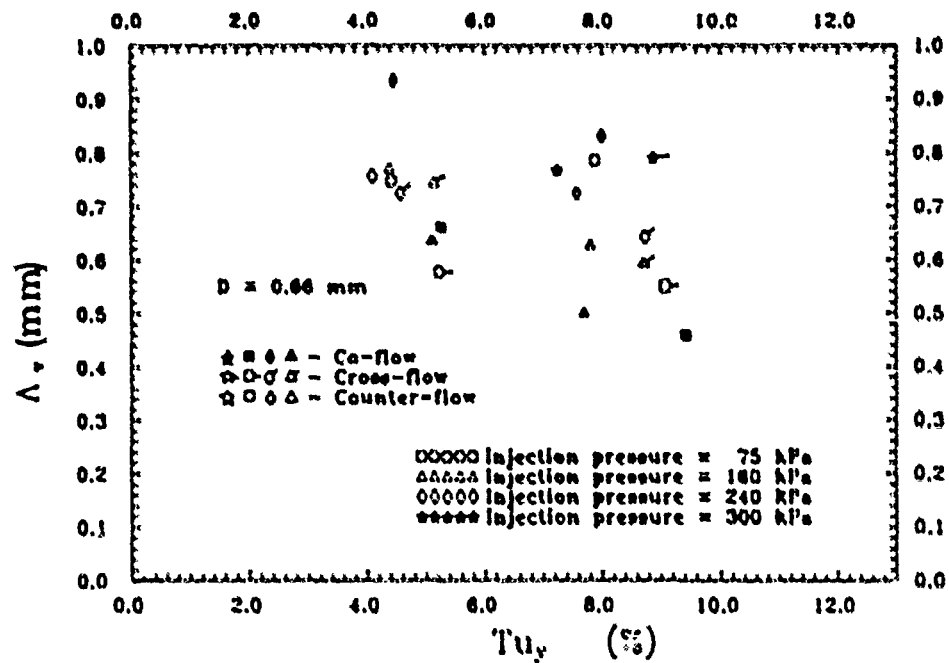
Figure 5.35. Effect of Y-component turbulence intensity on the Y-component integral scale length for 1.98 mm

than the Y-component turbulence microscale, whereas the the results of the previous section show the X-component integral scale length was greater than the Y-component integral scale length. This result is expected since the smallest fluctuations in the free-stream, as it passes through the jet-grid, are in the X direction. Shearing of the wake behind each jet-grid tube creates a high frequency disturbance in the free-stream, in the X-direction. The high frequency disturbances due to shearing between the wake and the free-stream produce small turbulence microscales. The Y-component microscale is due to Y-direction fluctuations of the flow in the wake of the jet-grid tubes. The Y-direction fluctuations are primarily dependent on the oscillating components of the wake, which occur at a much lower frequencies than the frequencies associated with shearing of the flow in the X-direction. As a result of the low frequency disturbances to the free-stream, the Y-component turbulence microscales are relatively large compared to the X-component turbulence microscales.

The X-component turbulence microscale size (λ_u) and Y-component turbulence microscale size (λ_v) are tabulated for each test in Tables 5.1 and 5.2. The X-component

microscale size for co-flow, cross-flow, and counter-flow jet-grid injection at both jet-grid locations, as a function of jet-grid injection pressures, is presented in Figures 5.36-5.41. The Y-component microscale size for co-flow, cross-flow, and counter-flow jet-grid injection at both jet-grid locations, as a function of jet-grid injection pressures, is presented in Figures 5.42-5.47.

Figure 5.36 shows a pronounced variation of the X-component microscale for co-flow injection with the smallest diameter orifice (0.66 mm) at station 0, especially at the higher injection pressures. Again, similar to the related effect on integral scale for this test, this increase in turbulence microscale to over 4 times its nominal value for lower injection pressures was probably due to supersonic injection. Young and Han (Young, 1989) experienced similar results in their tests where supersonic injection pressures were used to increase the microscale length. As seen in Figure 5.37 for cross-flow injection and Figure 5.38 for counter-flow injection, the microscale was relatively constant over a 75-300 kPa injection pressure range.

At station 02, co-flow injection shown in Figure 5.39 produced up to a 81 percent variation in X-component microscale size for the 1.98 mm injection orifice. Cross-flow injection at station 02, Figure 5.40, and the X-component microscales for counter-flow injection at station 02 are shown in Figure 5.41. Both cross-flow and counter-flow injection produced a variety of X-component microscale sizes, depending on injection pressure and orifice diameter.

The Y-component microscales for co-flow injection at station 0 are shown in Figure 5.42. The large increase in Y-component microscale size for the 0.66 mm diameter injection orifice is attributed to supersonic injection conditions that may have been present. Y-component microscales as a result of cross-flow injection at station 0, Figure 5.43, varied in size depending on the injection pressure and orifice diameter. Counter-flow injection at station 0 increased the Y-component microscale as the injection pressure increased, as shown in Figure 5.44.

The variation of the Y-component microscale as a function of injection pressure, with the jet-grid at station 02 is shown for co-flow injection in Figure 5.45. With the
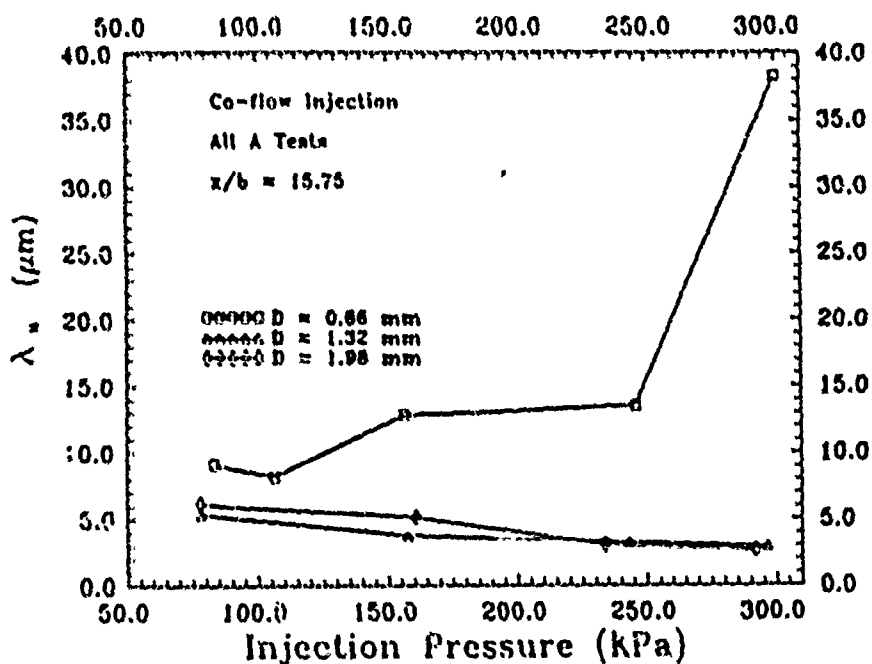
Figure 5.36. Effect of injection pressure and orifice diameter on X-component microscale length for co-flow injection at $\frac{x}{b} = 15.75$
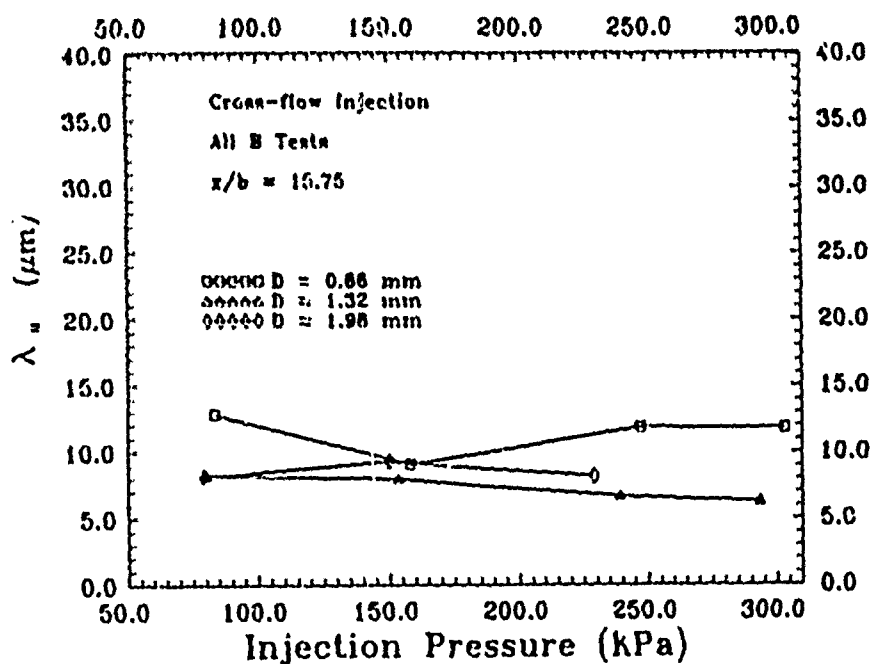

Figure 5.37. Effect of injection pressure and orifice diameter on X-component microscale length for cross-flow injection at $\frac{x}{b} = 15.75$
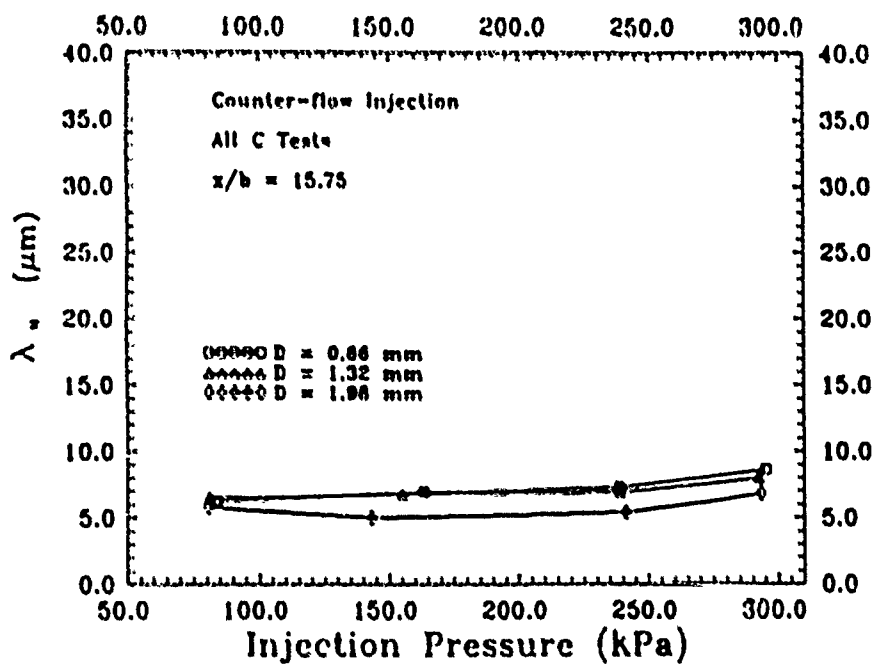
Figure 5.38. Effect of injection pressure and orifice diameter on X-component microscale length for counter-flow injection at $\frac{x}{b} = 15.75$
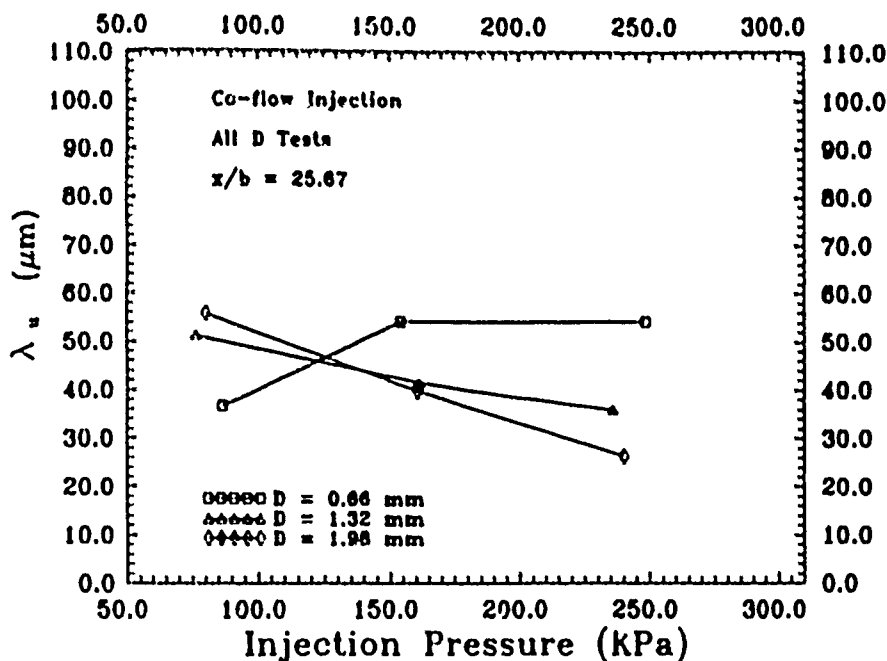

Figure 5.39. Effect of injection pressure and orifice diameter on X-component microscale length for co-flow injection at $\frac{x}{b} = 25.67$
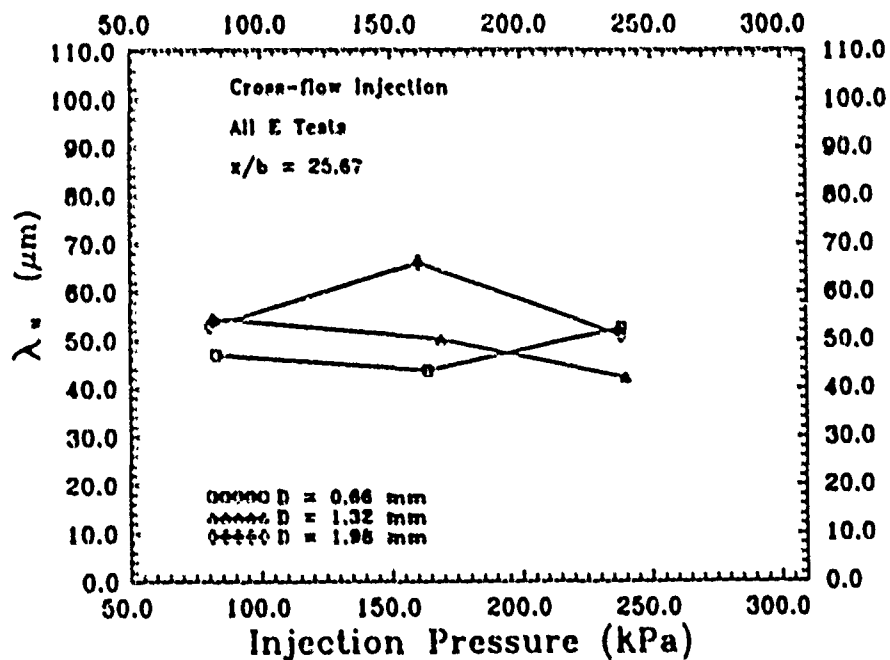
Figure 5.40. Effect of injection pressure and orifice diameter on X-component microscale length for cross-flow injection at $\frac{x}{b} = 25.67$
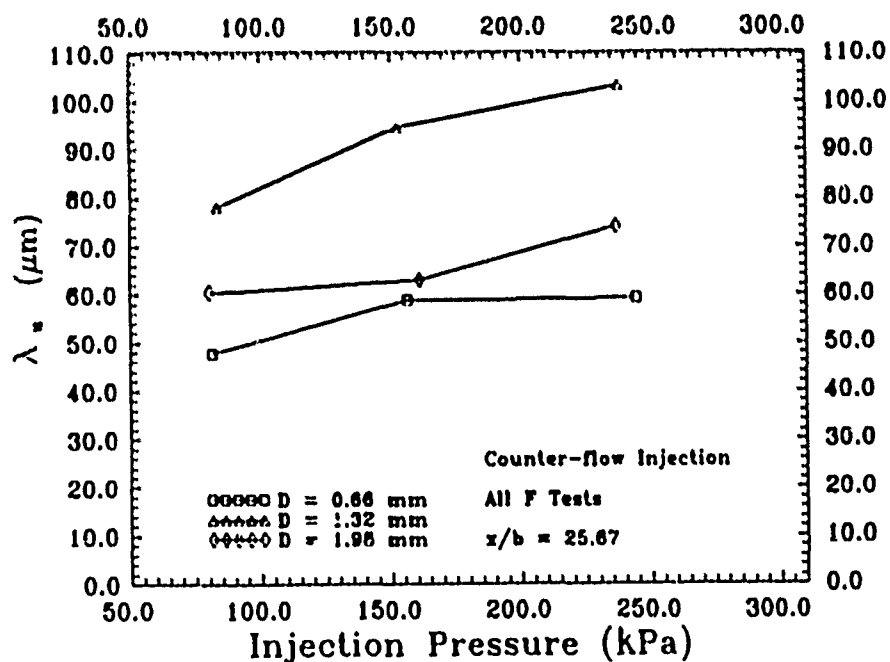

Figure 5.41. Effect of injection pressure and orifice diameter on X-component microscale length for counter-flow injection at $\frac{x}{b} = 25.67$
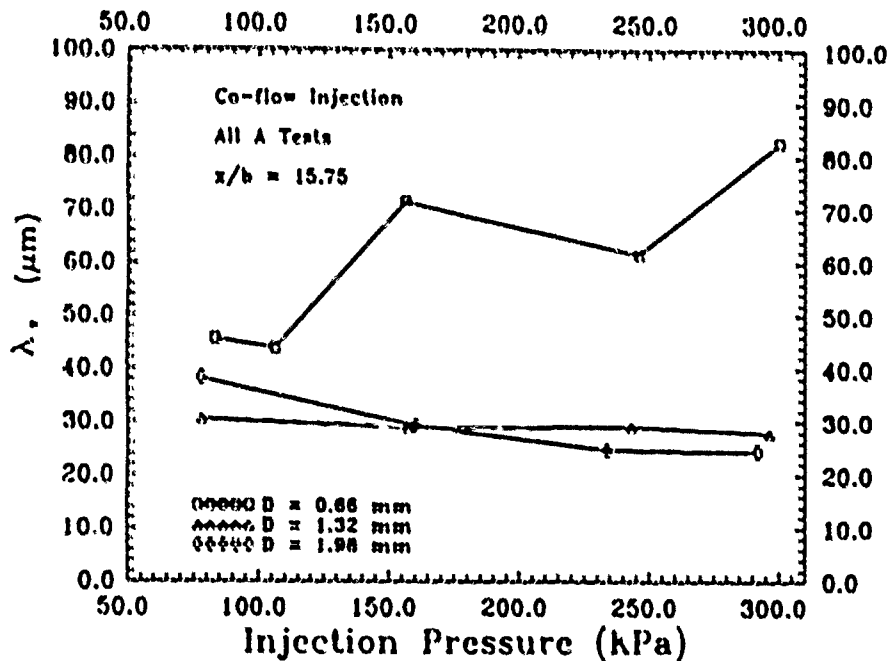
Figure 5.42. Effect of injection pressure and orifice diameter on Y-component microscale length for co-flow injection at $\frac{x}{b} = 15.75$

jet-grid at station 02, no supersonic injection occurred and there was no accompanying large increase in the Y-component turbulence microscale as seen in Figures 5.36 and 5.42. Figure 5.46 indicates cross-flow injection produced a relatively small change in the Y-component microscale size for the two smallest injection orifices with a small increase in the Y-component microscale size for the largest injection orifice at a 150 kPa injection pressure. For counter-flow injection at station 02, Figure 5.47, the Y-component microscale length varied significantly depending on the injection orifice diameter. In this case, the 1.32 mm injection orifice diameter produced microscales twice the size of the microscale sizes produced by other injection orifice diameters for the same injection pressure and injection direction. The reason for the large increase of the Y-component microscale size for the 1.32 mm orifice using counter-flow injection is not known.

Cross-plots of turbulence microscale as a function of their respective component of turbulence, for each injection orifice diameter, are presented in Figures 5.48–5.53. The jet-grid injection pressure and orientation are designated on each figure accordingly. As seen in each of these six figures, there was a large variation in the turbulence microscale
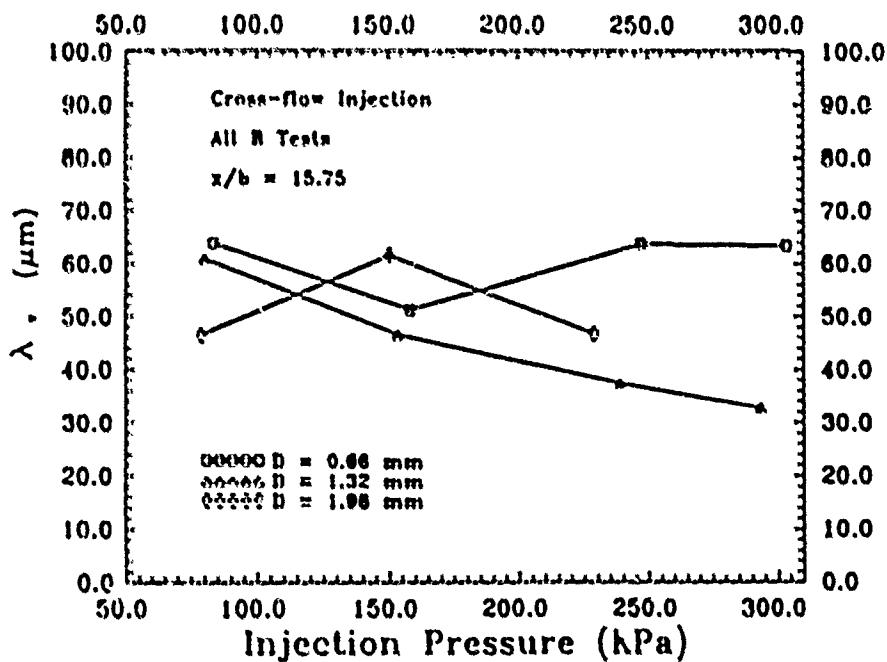
Figure 5.43. Effect of injection pressure and orifice diameter on Y-component microscale length for cross-flow injection at $\frac{x}{b} = 15.75$
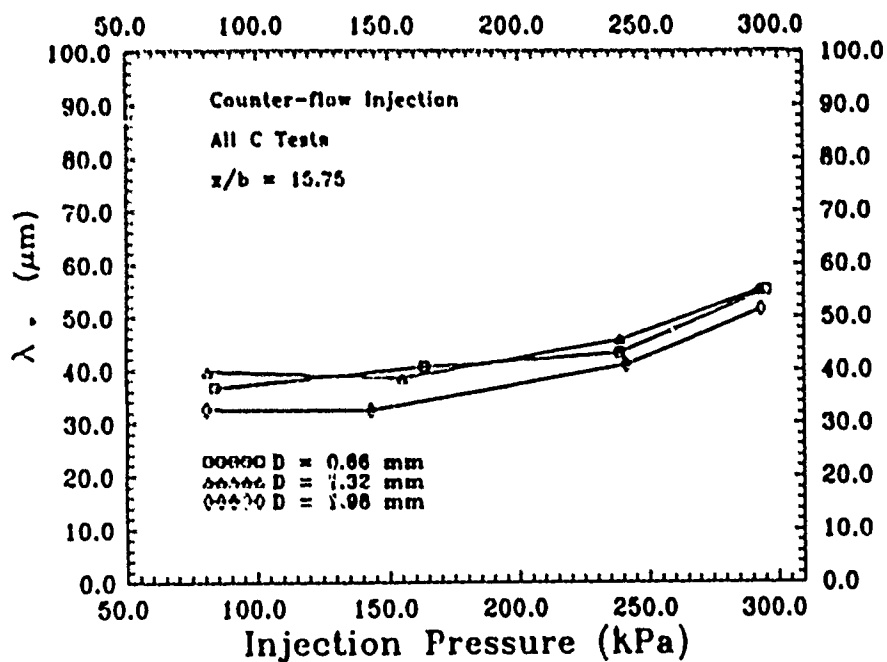

Figure 5.44. Effect of injection pressure and orifice diameter on Y-component microscale length for counter-flow injection at $\frac{x}{b} = 15.75$
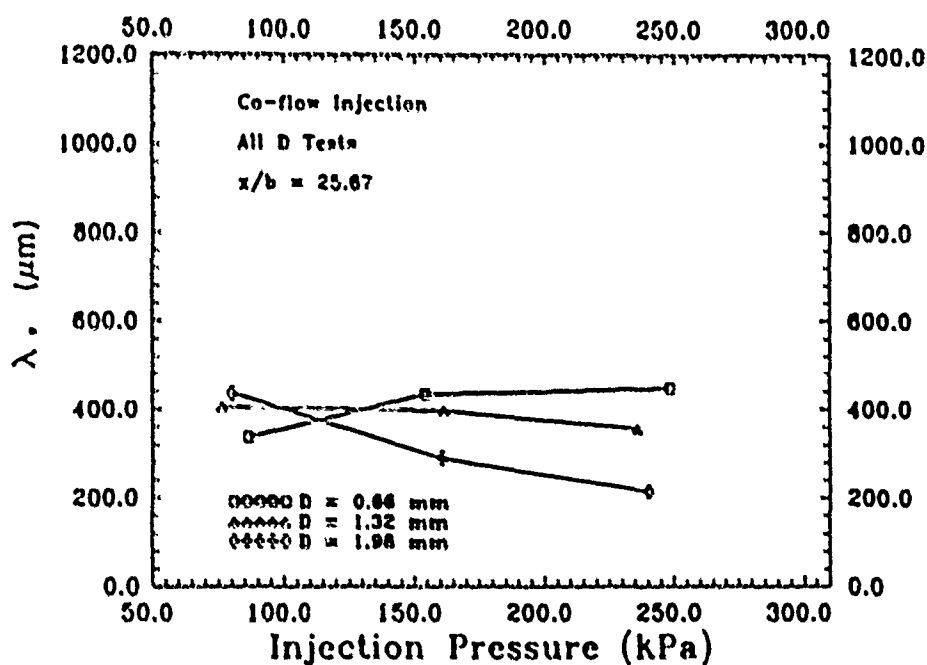
Figure 5.45. Effect of injection pressure and orifice diameter on Y-component microscale length for co-flow injection at $\frac{x}{b} = 25.67$
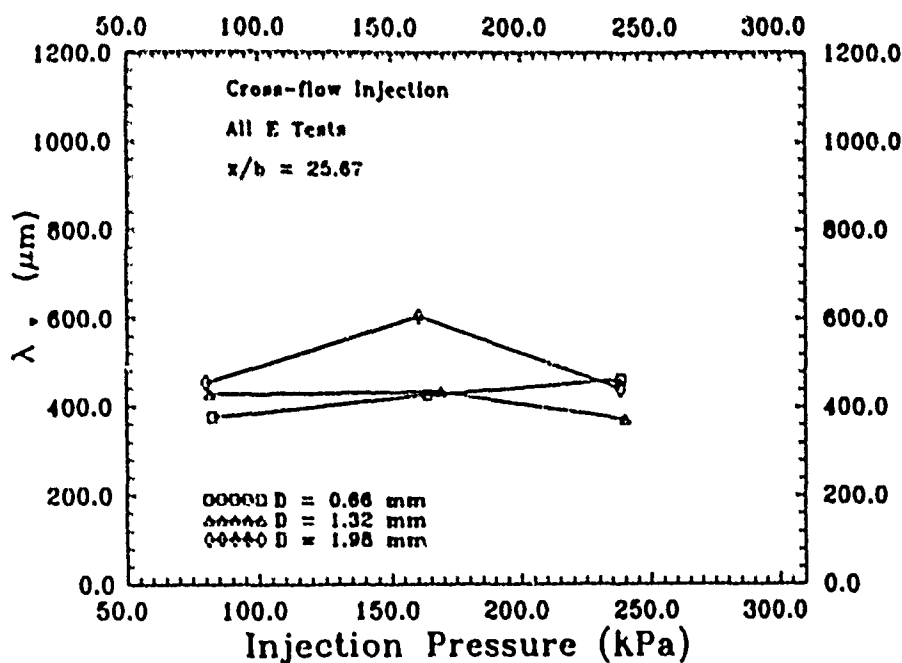

Figure 5.46. Effect of injection pressure and orifice diameter on Y-component microscale length for cross-flow injection at $\frac{x}{b} = 25.67$
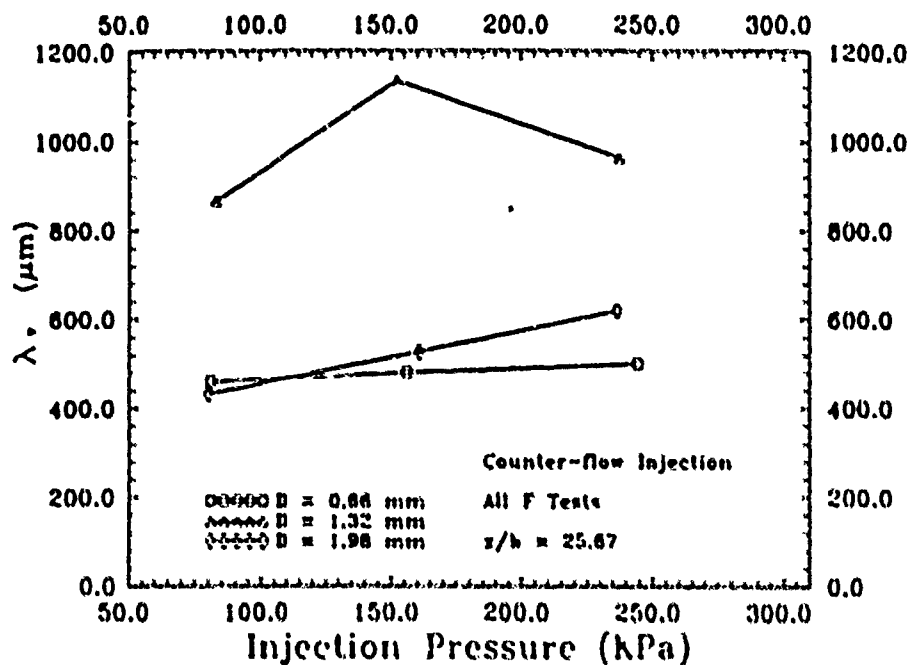
Figure 5.47. Effect of injection pressure and orifice diameter on Y-component microscale length for counter-flow injection at $\xi = 25.67$

at the low turbulence levels and a small variation of the turbulence scales at the high turbulence levels. (This result indicates that in the study of turbulence microscale effects on heat transfer, the jet-grid should be placed far upstream of the turbine cascade in order to get the largest variation of the microscale length.) Also seen in these figures, both the X-component and Y-component microscale lengths are inversely proportional to the turbulence intensity. This is in contrast to the results shown in the cross-plots of the turbulence integral scale length with their respective component of turbulence intensity (Figures 5.30 - 5.35). These particular figures also serve to highiight the differences in injection orientation. For example, from Figure 5.48, co-flow injection produced nearly the same size X-component microscales centered around the 10 percent turbulence level, cross-flow injection produced similar microscale sizes in the region of 11 percent turbulence level, and counterflow produced similar size microscales at 12 percent turbulence level. The same trend is observed for the X-component microscale plots of Figure 5.49 and Figure 5.50. Injection pressure seems to have a more random effect on the turbulence microscale size than the turbulence integral scale length in that the microscales are not the same size
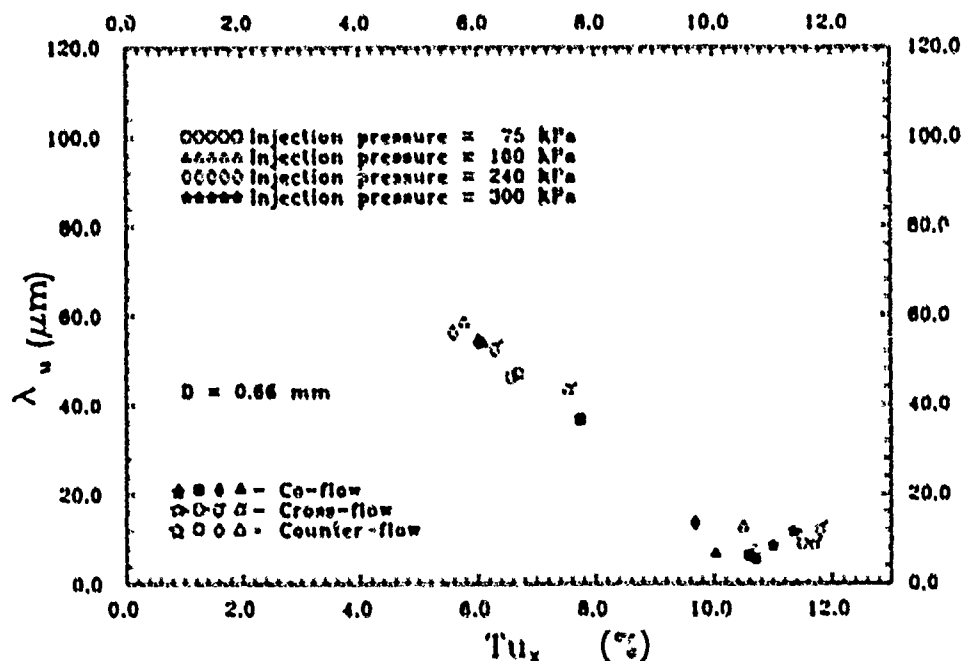
Figure 5.48. Variation of the X-component turbulence microscale with the X-component of turbulence: $D = 0.66$ mm

for a injection direction at a particular level of free-stream turbulence. This was not the case for the turbulence integral scale lengths (See Figures 5.30 - 5.32).

At the lower turbulence level (4-6 percent), counterflow injection produced the largest size microscales; Figures 5.49 and 5.52 demonstrate the effect of counterflow injection for an orifice diameter of 1.32 mm. One possible explanation for the effect of counter-flow injection on the turbulence microscale size is that although counter-flow injection may have a large shearing effect on the free-stream, any increased turbulence level that one might get from an increased shearing due to counter-flow injection decays as the free-stream passes through the jet-grid. Further study in the area of turbulence scale production and dissipation is necessary before firm conclusions may be formulated.

5.3 Turbine Blade Heat Transfer

5.3.1 Baseline Turbine Blade Heat Transfer Tests
Heat transfer on the turbine blade was measured for all test configurations given in Tables 1.1 and 1.2, except test numbers A14, A15, A24, A34, B14, B24, C14, C24, and C34. The results of these tests
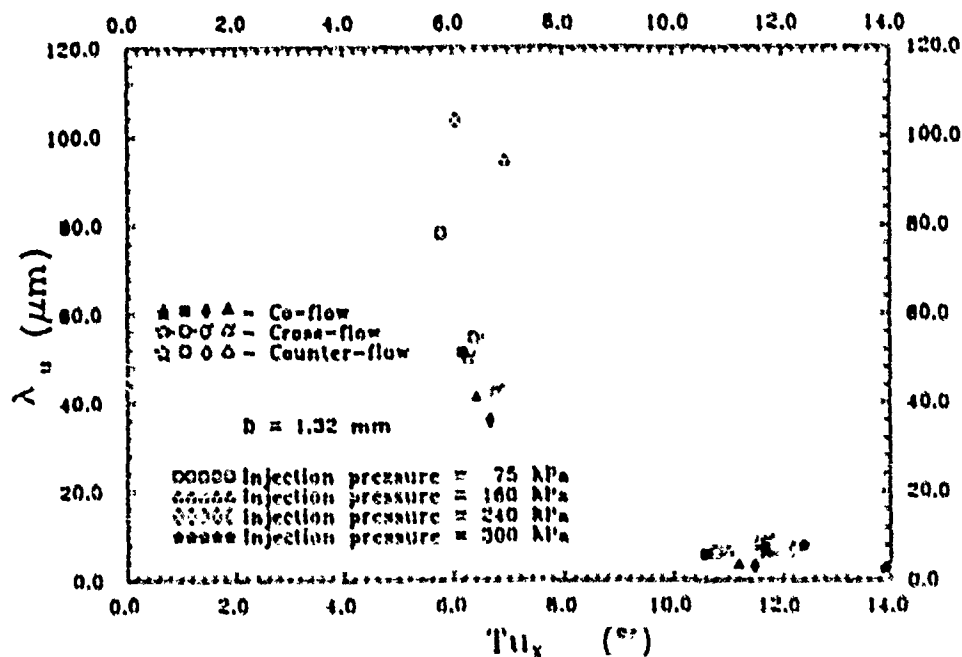
Figure 5.49. Variation of the X-component turbulence microscale with the X-component of turbulence: $D = 1.32$ mm

Figure 5.50. Variation of the X-component turbulence microscale with the X-component of turbulence: $D = 1.98$ mm

Figure 5.51. Variation of the Y-component turbulence microscale with the Y-component of turbulence: $D = 0.66$ mm
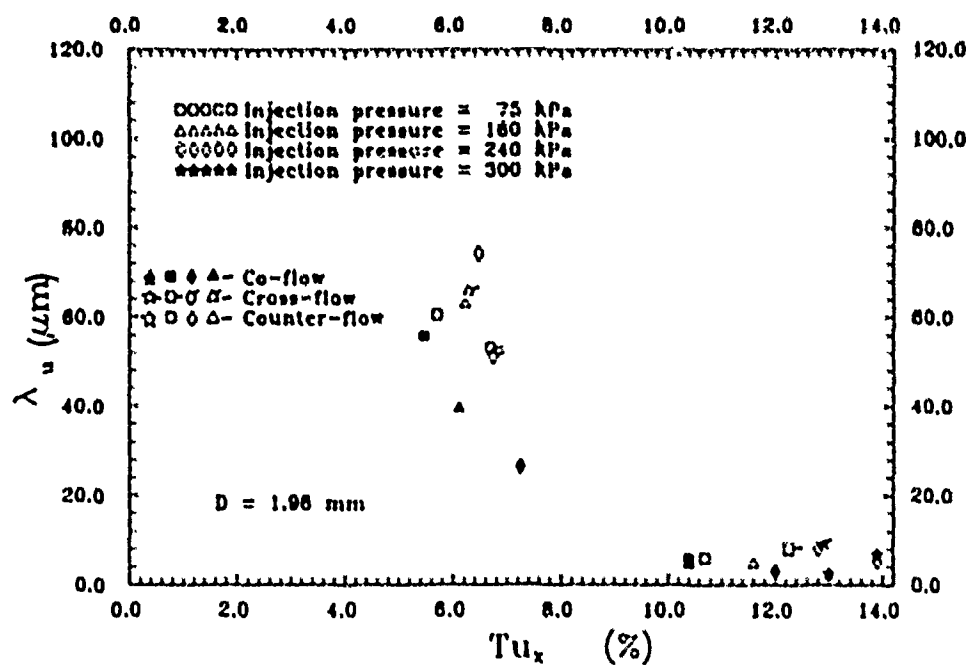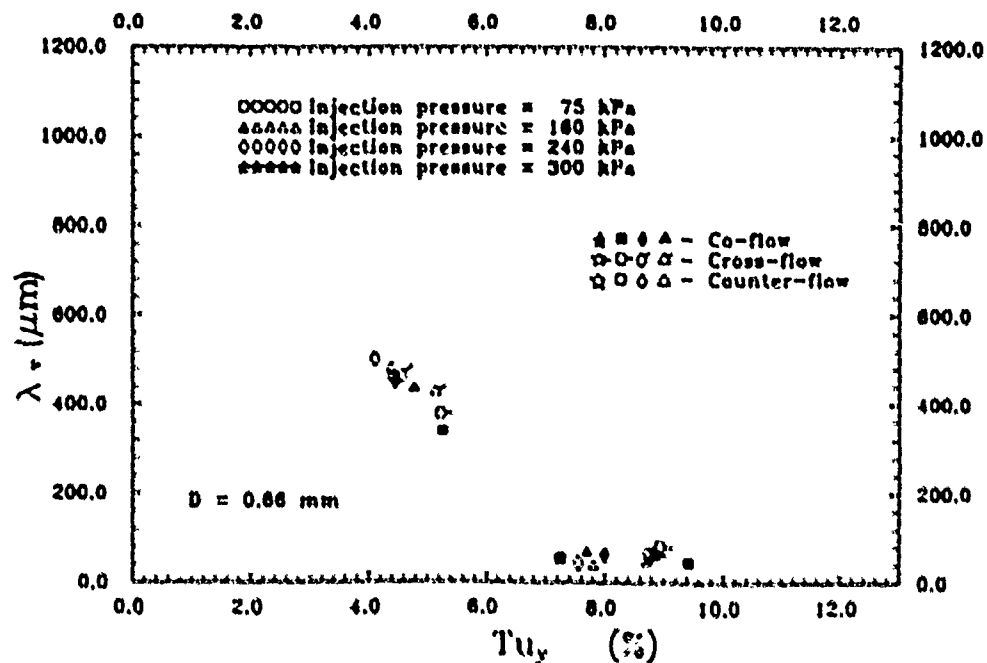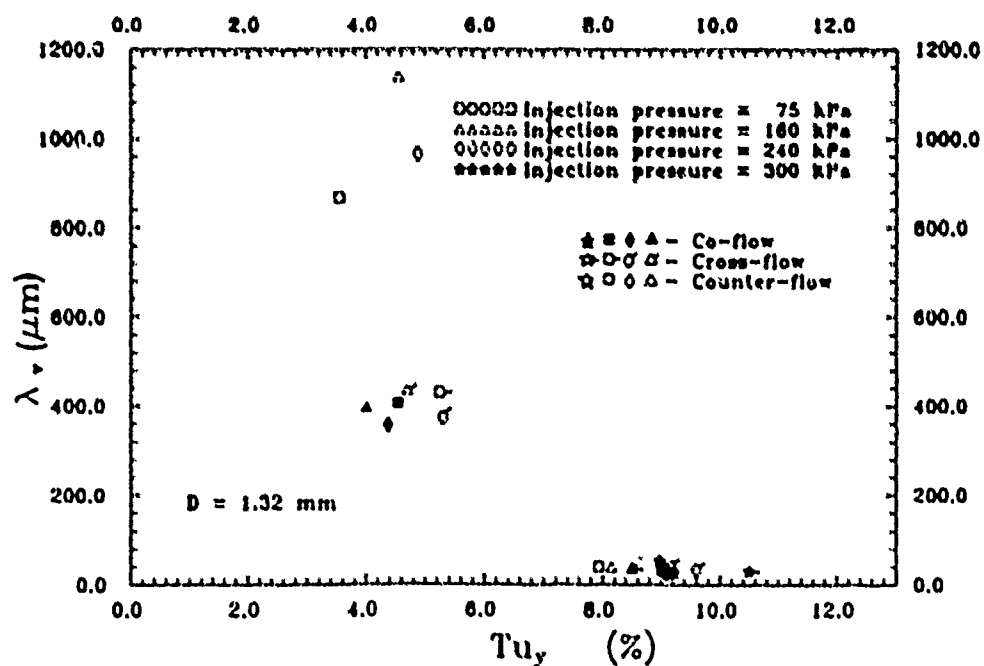

Figure 5.52. Variation of the Y-component turbulence microscale with the Y-component of turbulence: $D = 1.32$ mm
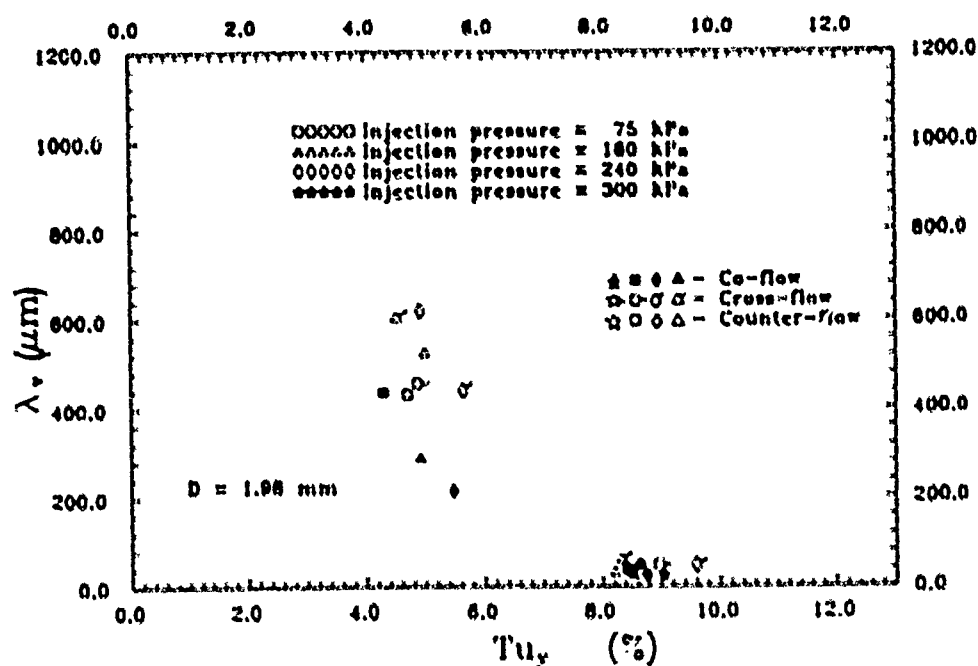
Figure 5.53. Variation of the Y-component turbulence microscale with the Y-component of turbulence: $D = 1.98$ mm

were confined to turbulence measurements only. The results are presented in the form of Stanton number (St) and Nusselt number (Nu) on the turbine blade. The Stanton number and Nusselt number on the turbine blade without the jet-grid in the free-stream flow are designated by subscript x. With the jet-grid at station 0 ($\xi = 15.75$), the Stanton number and Nusselt number are designated with a subsript 0. Lastly, with the jet-grid at station 02 ($\xi = 25.67$), the Stanton number and Nusselt number are designated by subscript 02.

The Stanton and Nusselt numbers on the turbine blade with no jet-grid in the free-stream flow are presented in Figures 5.54 and 5.55, respectively. The Stanton and Nusselt numbers with the jet-grid at station 0 are presented in Figures 5.56 and 5.57, respectively. The Stanton and Nusselt numbers with the jet-grid at station 02 are presented in Figures 5.58 and 5.59. These three heat transfer tests form a baseline for comparison with all other heat transfer tests.

The results of all other tests are presented as the ratio of the Stanton numbers on the blade to the Stanton number on the blade for a baseline test configuration. Nusselt numbers for all other tests are presented as a ratio of Nusselt numbers in the same manner

as the Stanton number ratios were formed. This method of presentation gives a graphical comparison for each heat transfer test to the baseline heat transfer tests. True values for Stanton and Nusselt numbers may be calculated by multiplying the Stanton number ratio or Nusselt number with the respective baseline Stanton or Nusselt number.

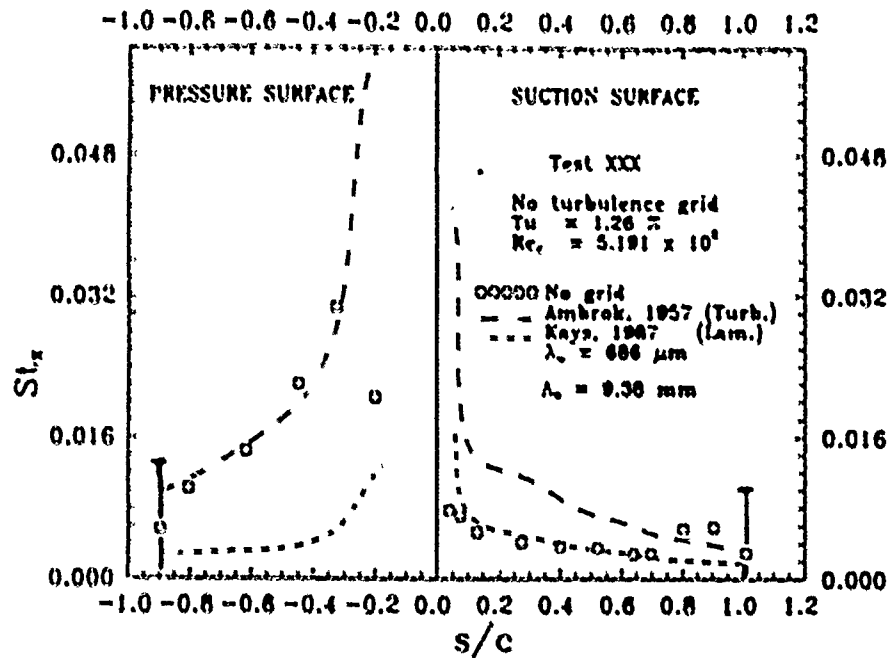Figure 5.54. Stanton number on the turbine blade surface with no jet-grid installed. Test XXX
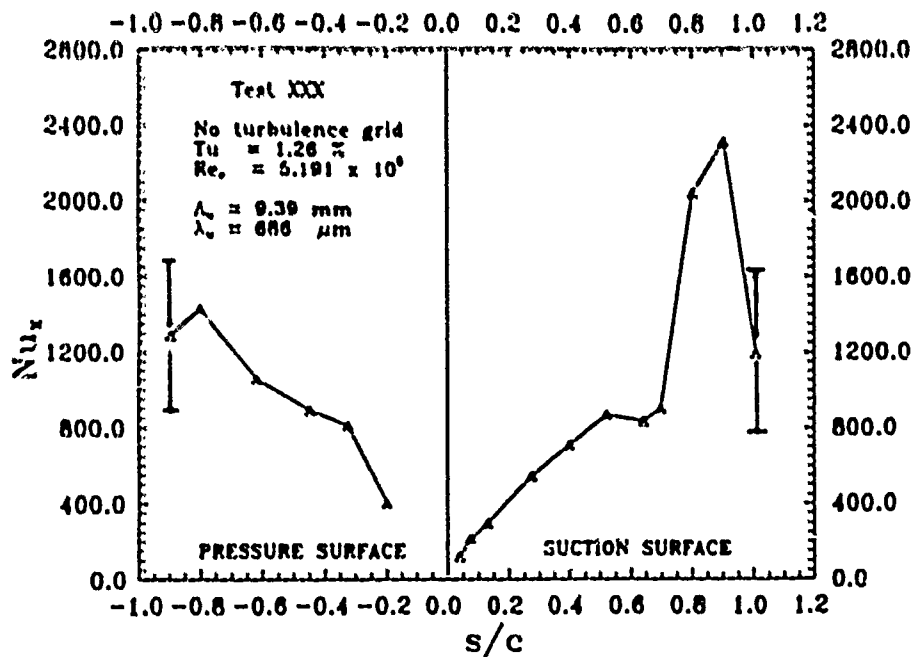
Figure 5.55. Nusselt number on the turbine blade surface with no jet-grid installed. Test XXX
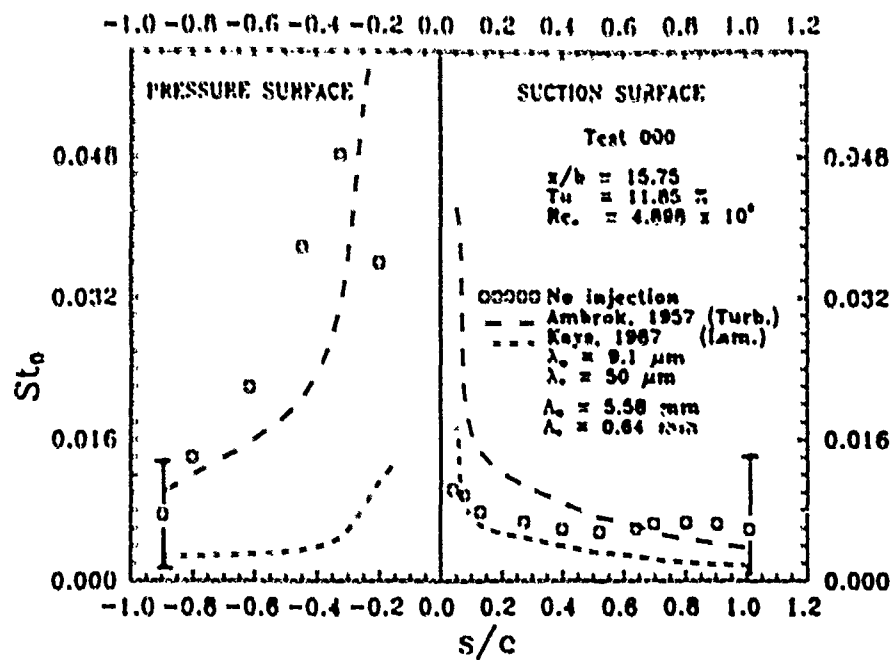
Figure 5.56. Stanton number on the turbine blade surface with the jet-grid at station 0 ($\frac{\xi}{t} = 15.75$). Test 000
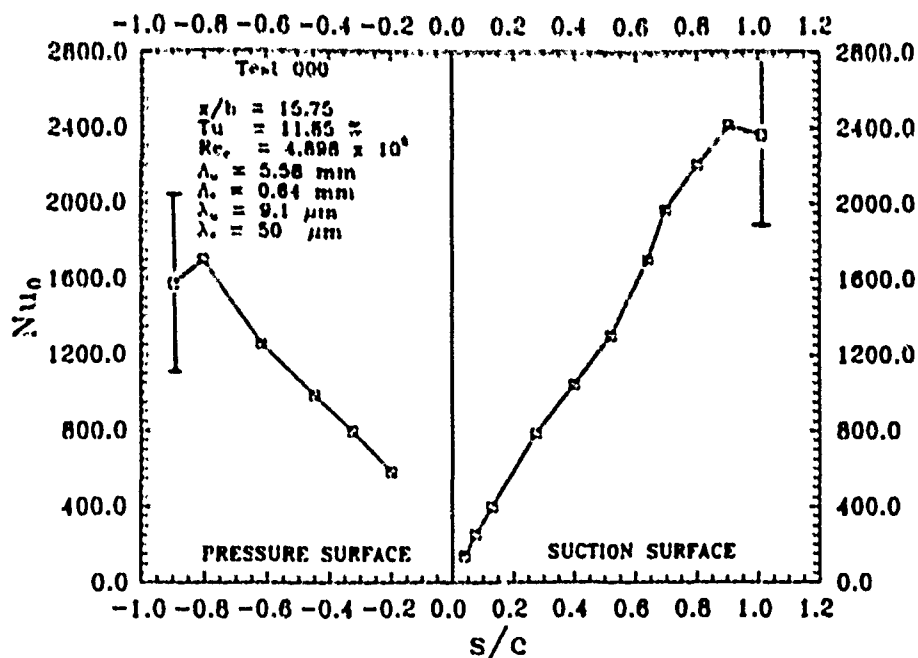
Figure 5.57. Nusselt number on the turbine blade surface the jet-grid at station 02 ($\frac{\xi}{t} = 15.75$). Test 000
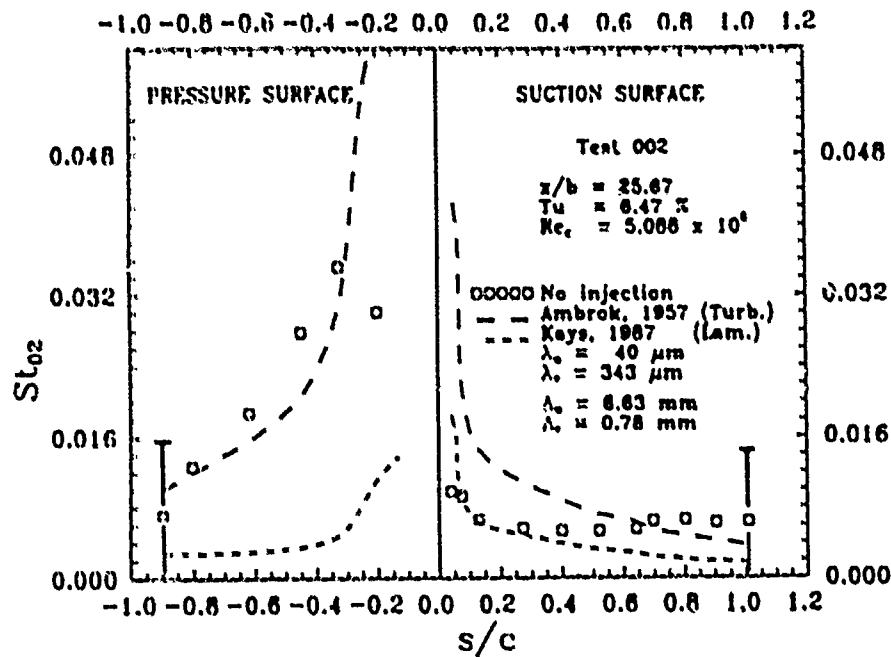
Figure 5.58. Stanton number on the turbine blade surface with the jet-grid at station 02 ($\frac{x}{b} = 25.67$). Test 002
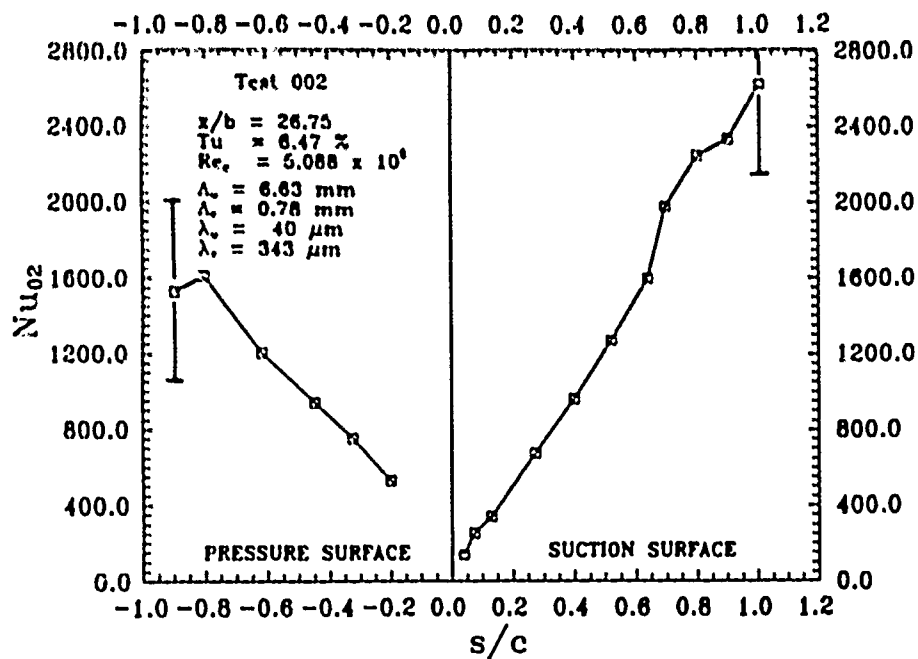
Figure 5.59. Nusselt number on the turbine blade surface the jet-grid at station 02 ($\frac{x}{b} = 25.67$). Test 002

All plots of the Stanton number and Nusselt number are presented as a function of the nondimensional distance ($\frac{s}{c}$) along the surface of the turbine blade. The results from the pressure surface are given on the left side of each plot and results from the suction surface are given on the right side of each plot. The negative $\frac{s}{c}$ values have no physical significance, but are a result of the plotting package used to create the plots.

5.3.2 Comparison to Theoretical Predictions for Heat Transfer Figure 5.54 shows the Stanton number for the turbine blade surface without the jet-grid installed. The free-stream turbulence level was 1.26 percent and the turbulence microscale in the X-direction was computed as 686 μm. The turbulence integral scale length was 9.4 mm. Computation of the Y-direction turbulence microscale and integral scale failed to produce a valid result for the turbulence microscale. This was a direct result of the turbulent energy spectrum for the Y-direction, which was highly scatterred. Recall that a spectrum that does not approach a -5/3 slope indicates a condition of non-uniform turbulence.

The laminar boundary layer heat transfer prediction of the Stanton number (Kays, 1987) is included on Figure 5.54 as well as the turbulent turbulent boundary layer prediction for Stanton number on the turbine blade (Ambrok, 1957).

The Stanton number measured on the pressure surface matches well with the turbulent boundary layer prediction of Stanton number except near the leading edge of the turbine blade at about $\frac{s}{c} = -0.2$. In this region, it has been suggested (Consigny, 1982) that on the pressure suface, immediately downstream of the leading edge, the flow is strongly decelerated over a short distance which results in a laminar separation bubble and a lower heat transfer. The low level heating rate was followed immediately by a high heating rate due to the reattaching turbulent boundary layer. The surface pressure distribution shown in Figure 5.2 indicates the flow was highly stagnated, hence, a laminar boundary layer exists in this region . Figure 5.55 shows the Nusselt number was approximately 400 for this region, hence heat transfer was low compared to the theoretical Nusselt number computed from the turbulent boundary layer theoretical prediction of the Stanton number. The turbulent boundary layer prediction assumes a fully turbulent, attached boundary layer and is unable to predict the Stanton number in the region of the pressure surface leading edge.

In the region of the trailing edge on the pressure side, Figure 5.54, the measured Stanton number is low. Other studies on turbine blade heat transfer (Blair, 1989a), (Consigny, 1982) indicate the Stanton number measured in this region should be as high or higher than the turbulent boundary layer prediction of the Stanton number. One possible reason for the low value of Stanton number in this region is because of inaccuracies in accounting for heat conduction losses near the trailing edge. The proximity of the copper bus bars and the thinness of the blade section contribute to the heat conduction losses in this region. Near the trailing edge, no interior thermocouple was placed directly under the surface thermocouples. The interior blade temperature in this region was estimated using a thermocouple 1 cm ahead (towards the turbine blade leading edge) of this position which might have overestimated the actual conduction losses. An estimate of the heat conduction loss was computed using the opposing suction surface thermocouple. Results of this calculation indicate the Stanton number in this area may actually be as high as 0.0015. This being the case, an error bar is indicated as shown to account for the uncertainty of the conductive heat losses in this region. This same argument applies to the trailing edge region of the suction surface where $\frac{s}{c} = 1.0$. Elsewhere on the blade, the blade was thick enough to allow interior thermocouples to be placed, and there were no heat sink masses present, like the bus bars. The results of the remaining tests are presented as a ratio of Stanton numbers and as a ratio of Nusselt numbers. The Stanton number ratio and the Nusselt number ratio are valid over the entire surface except in the region of the trailing edge of the turbine blade, for both surfaces, where a there is larger uncertainty in the Stanton or Nusselt number ratio due to the uncertainty associated with the heat conduction losses. The uncertainty of the Stanton number in the region of the trailing edge is shown as an error bar in Figure 5.54.

On the suction surface presented in Figure 5.54, the measured Stanton number was best correlated by the laminar boundary layer heat transfer prediction for the majority of the surface. Near the trailing edge of the suction surface ($\frac{s}{c} \approx 0.7$), the laminar boundary layer transitioned to a turbulent boundary layer and the Stanton number was best predicted by the Ambrok (Ambrok, 1957) turbulent boundary layer prediction of the Stanton number. The decrease in Stanton number in the region of $\frac{s}{c} = 1.0$, on the trailing edge of

the suction surface, is related to the uncertainty of computing the heat conduction in this region.

With the jet-grid introduced at station 0, the free-stream turbulence increased to 11.85 percent and the turbulence microscales decreased dramatically for the low-turbulence case. This was the second baseline case for heat transfer on the turbine blade. The results of this test (Test 000) are illustrated in Figure 5.56 and Figure 5.57. On the pressure surface, the Stanton number increased above the zero free-stream turbulence, turbulent boundary layer prediction, except at the leading edge where a laminar bubble separated the flow and lowered the heat transfer rate. On the suction surface, the boundary layer on the blade was initially laminar, but started transitioning to a turbulent boundary layer immediately ($\frac{s}{c} \approx 0.1$). With transition to a turbulent boundary layer, the Stanton number increased accordingly.

Figure 5.57 gives the Nusselt number on the turbine blade. On the suction surface, the Nusselt number increases linearly towards the trailing edge in contrast to Figure 5.55, where at $\frac{s}{c} = 0.5$ there was a leveling of the Nusselt number followed by a rapid increase of the Nusselt number at $\frac{s}{c} = 0.7$.

The Stanton number for the turbine blade with the jet-grid at station 02 ($\frac{x}{b} = 25.67$) is shown in Figure 5.58. The free-stream turbulence level was 6.47 percent and the turbulence microscale lengths increased five times over Test 000 microscale sizes. The turbulent boundary layer heat transfer prediction underestimated the Stanton number over much of the pressure surface.

On the suction surface shown in Figure 5.58, the Stanton number increased from the laminar boundary layer levels of Stanton number to Stanton number levels predicted by turbulent boundary layer heat transfer. The transition from laminar to turbulent boundary layer seems to have begun at $\frac{s}{c} \approx 0.3$. In this case, transition from laminar to turbulent boundary layer was delayed compared to the case with the jet-grid at station 0 where transition started at $\frac{s}{c} = 0.1$. The delayed transition was due to the lower free-stream turbulence level associted with the jet-grid placed at station 02. Comparing Figures 5.54,

5.56, and 5.58, the laminar-to-turbulent boundary layer transition point advanced toward the leading edge as the free-stream turbulence level increased.

The Nusselt numbers for this configuration are given in Figure 5.59. Similar values of Nusselt number on the turbine blade surface were obtained with the jet-grid at station 0. This result was expected since the free-stream was moderately turbulent for both Test 000 and Test 002, and no other test conditions were changed.

The ratio of Stanton numbers and Nusselt numbers for the jet-grid in at station 0 compared to the no jet-grid in the flow is shown in Figures 5.60 and 5.61, respectively. From Figure 5.60, the Stanton number increased on the pressure surface as much as 70 percent at the leading edge over the low-turbulence test (no jet-grid). The largest effect was on the suction surface where the Stanton number increase by as much as 120 percent due to the ratio of the turbulent boundary layer Stanton number to the laminar boundary layer Stanton number. The ratio of the Nusselt numbers shown in Figure 5.61 demonstrate the same increase in heat transfer rate on the turbine blade surface. This large increase in Stanton and Nusselt numbers was due largely to the increased free-stream turbulence level. Simonich and Bradshaw concluded in their study of turbulence effects on heat transfer on a flat plate, that the Stanton number increases with free-stream turbulence at a rate of about five percent for each percent increase in turbulence intensity (Simonich, 1978). Based on this estimate, a free-stream turbulence level of 11.85 percent should produce a 56 percent increase in Stanton number. The predicted increase in Stanton number was exceeded at several locations on both surfaces of the turbine blade.

From Figure 5.61, on the pressure surface, at $\frac{z}{c} = -0.3$, the rapid decrease of the Nusselt number ratio indiactes the heat transfer rate in this region decreased from the test without the jet-grid in the free-stream as compared to the test with the jet-grid at station 0. One possible expalanation for this rapid decrease in Nusselt number is the laminar to turbulent boundary layer transition point moved its position on the turbine blade surface between the two tests. The direction of movement of this transition point seems to be towards the turbine blade leading edge since at $\frac{z}{c} = -0.2$ the Nusselt number ratio in Figure 5.61 is 1.48 which was significantly greater than the Nusselt number ratios for the remaining pressure surface.
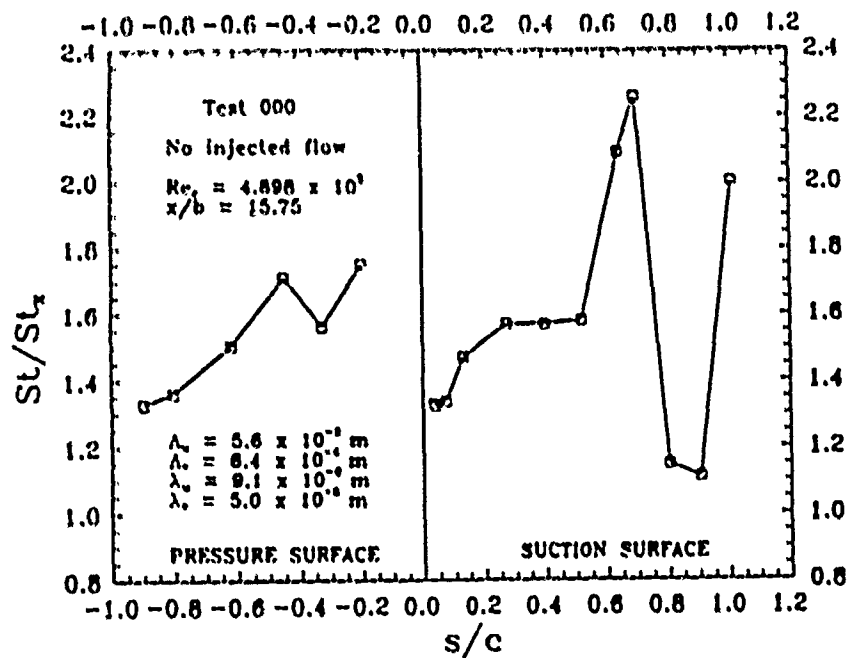
Figure 5.60. Effect of the jet-grid at station 0 ($\frac{x}{b} = 15.75$) on the Stanton number—
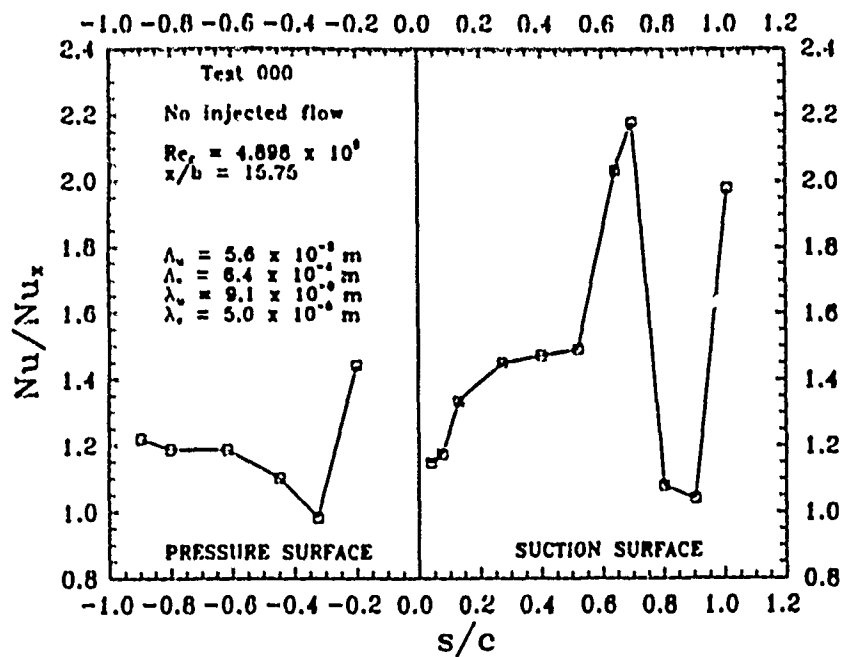Stanton number ratio. Test 000

Figure 5.61. Effect of the jet-grid at station 0 ($\frac{x}{b} = 15.75$) on the Nusselt number—
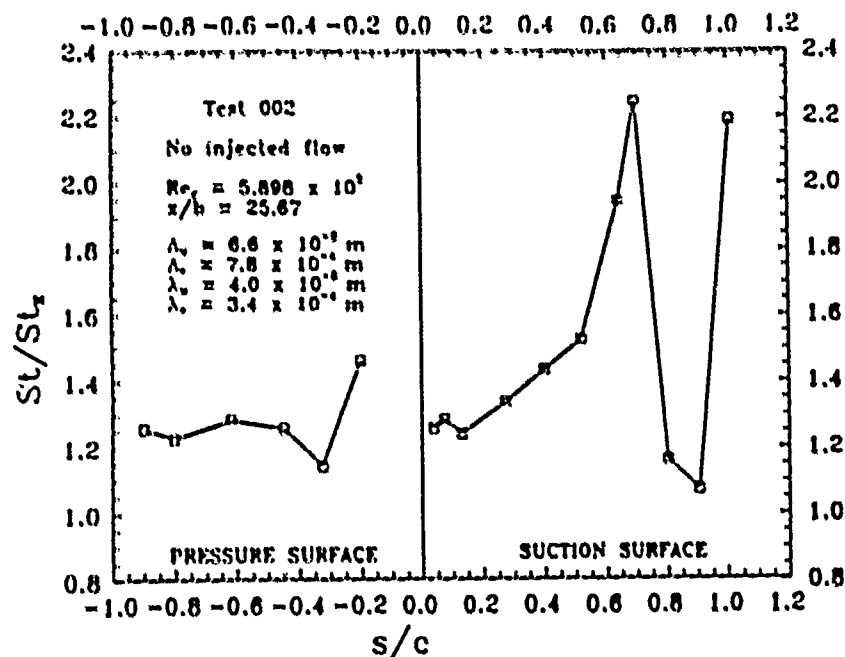Nusselt number ratio. Test 000

Figure 5.62. Effect of the jet-grid at station 02 ($\frac{\xi}{\xi} = 25.67$) on the Stanton number Stanton number ratio. Test 002

Comparison of the Stanton and Nusselt numbers for this test to the Stanton and Nusselt numbers for the test with no jet-grid is presented in Figures 5.62 and 5.63. For this case, from Figure 5.62, the Stanton numbers on the pressure surface increased about 20 percent over the no jet-grid Stanton number levels except at $\frac{s}{c} = -0.2$, where the laminar to turbulent boundary layer transition point shifted towards the leading edge from its position during Test 000, hence increasing the heat transfer rate at this poision on the turbine blade surface. Figure 5.63 confirms the shift in laminar to turbulent boundary layer transition towards the leading edge at $\frac{s}{c} = -0.3$ occurred with Test 002. The ratio of the Stanton numbers, shown in Figure 5.62, and the ratio of Nusselt numbers, shown in Figure 5.63, on the suction surface remained about the same value in this case (Test 002) as with the jet-grid located at station 0 (Test 000).

5.3.2.1 Heat Tranfer on the Turbine Blade with Jet-Grid Injection The effect of jet-grid injection on heat transfer is now considered. In all figures pertaining to this section, multiple test results are shown on a single figure. On each figure, the injection orifice diameter and injection direction are identical for all tests; however, the injection
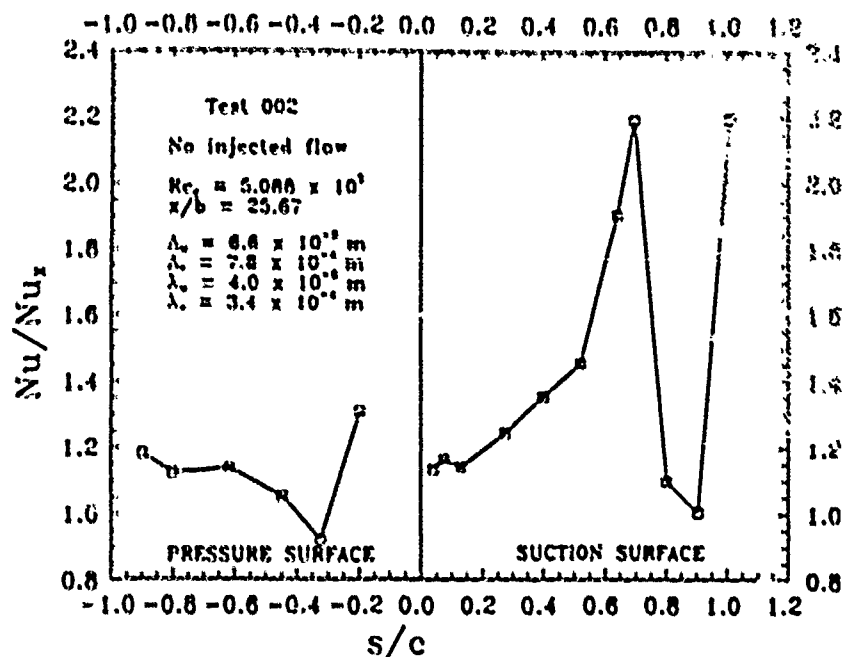
Figure 5.63. Effect of the jet-grid at station 0 ($\xi = 25.67$) on the Nusselt number Nusselt number ratio. Test 002

pressure was varied. The Stanton and Nusselt numbers for the lowest jet-grid injection pressure is designated by square symbols. The results from next highest injection pressure are designated with triangle symbols, and the results from the highest injection pressure are designated with diamond symbols. Actual injection pressures for each test are given in Tables 1.1 and 1.2.

Figures shown in this section gi   the Stanton number ratios and the Nusselt number ratios measured on the turbine blade surface with the jet-grid at station 0 ($\xi = 15.75$). Only representative plots of heat transfer measurements in the form of Stanton and Nusselt number ratios are given in this section. All other plots of the Stanton and Nusselt number ratios are shown in Appendix D.

First, co-flow with jet-grid injection shown in Figure 5.64 had the least effect on the Stanton number on the turbine blade pressure surface. As may be seen in Figures 5.65, 5.67, and 5.69, counter-flow injection increased the Stanton number on the pressure surface up to five times the nominal value (with no jet-grid injection). This would suggest an enormous heat transfer rate, but the corresponding figures for Nusselt number ratios for
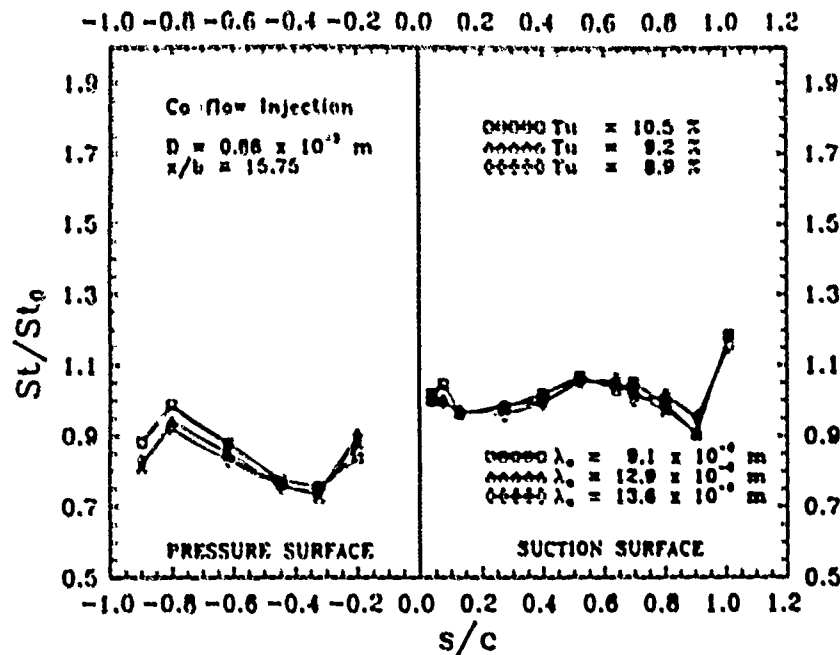
Figure 5.64. Stanton number on the turbine blade for co-flow injection. $D = 0.66$ mm. Test A11, A12 and A13. Jet-grid at station 0

counter-flow injection , Figures 5.66, 5.68, and 5.70, show the Nusselt number ratios are unity or less. There seems to be a dichotomy of results; however this is not the case, rather the turbine blade surface velocity distribution changed as jet-grid injection was introduced which changed the Stanton number. The Stanton number is inversely proportional to the local Reynolds number, Re_s, on the blade surface. Counter-flow injection changed the velocity distribution on the turbine blade pressure surface by stagnating the flow. Pressure distributions on the turbine blade surface measured for counter-flow injection support this conclusion (see Figures 5.5 and 5.8). Since the Reynolds number is proportional to the local velocity, any change in velocity would result in a change in Reynold number which gives an equally large change in Stanton number. The heat transfer coefficient did not change and the Nusselt number for this configuration confirms this fact. Rather the local velocity on the turbine blade surface changed, which affected the Stanton numbers.

The dependence of the Stanton number on the turbulence microscale is more difficult to determine because of the Stanton number's inherent dependence on the local velocity distribution, however from Figures 5.71 and 5.72, where the free-stream turbulence was
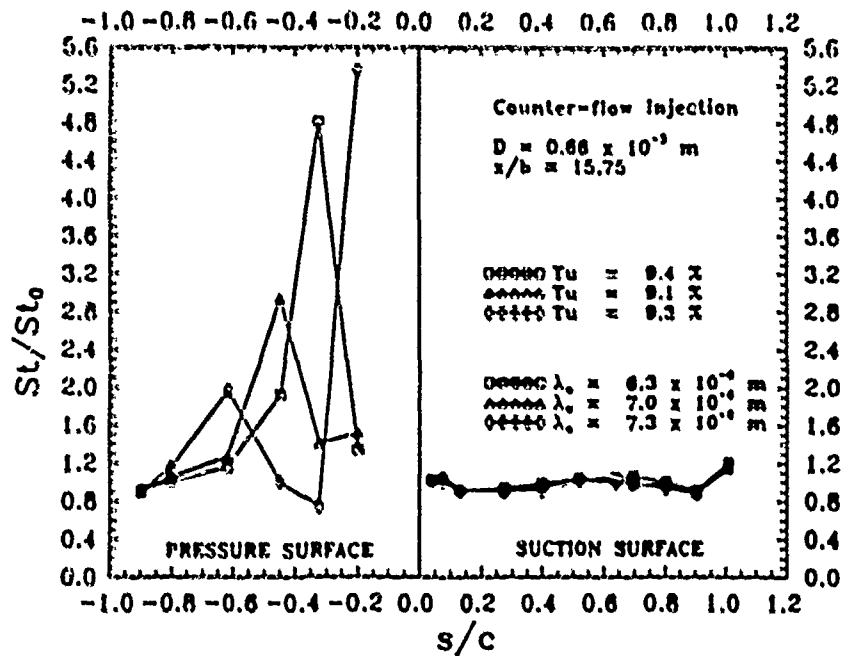
Figure 5.65. Stanton number on the turbine blade for counter-flow injection. $D = 0.66$ mm. Test C11, C12 and C13. Jet-grid at station 0
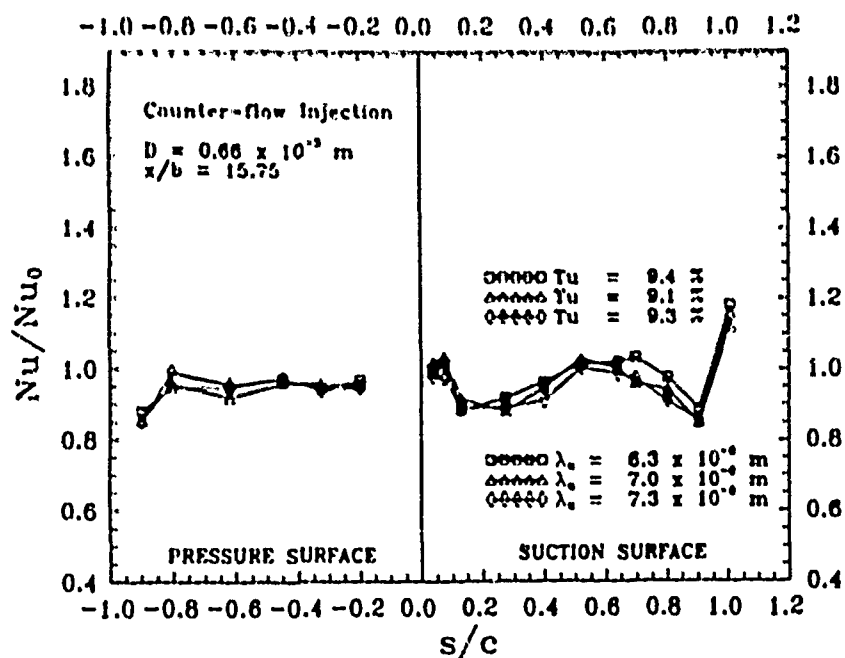

Figure 5.66. Nusselt number on the turbine blade for counter-flow injection. $D = 0.66$ mm. Test C11, C12 and C13. Jet-grid at station 0
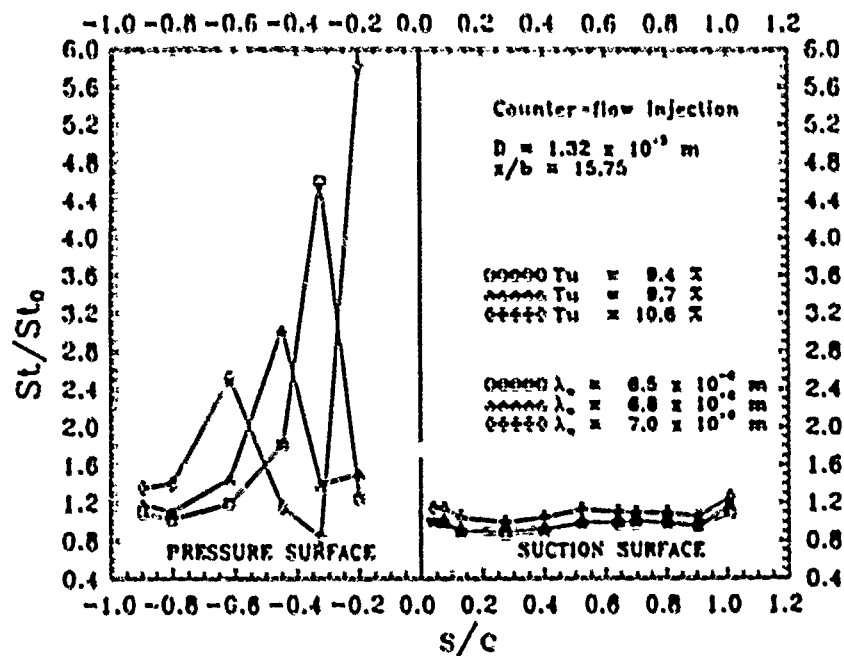
Figure 5.67. Stanton number on the turbine blade for counter-flow injection. $D = 1.32$ mm. Test C21, C22 and C23. Jet-grid at station 0
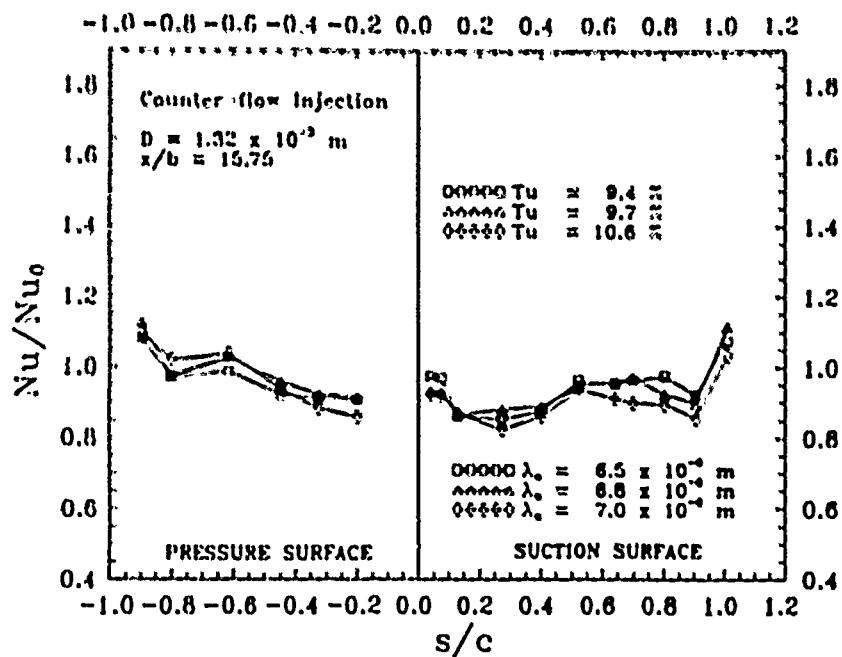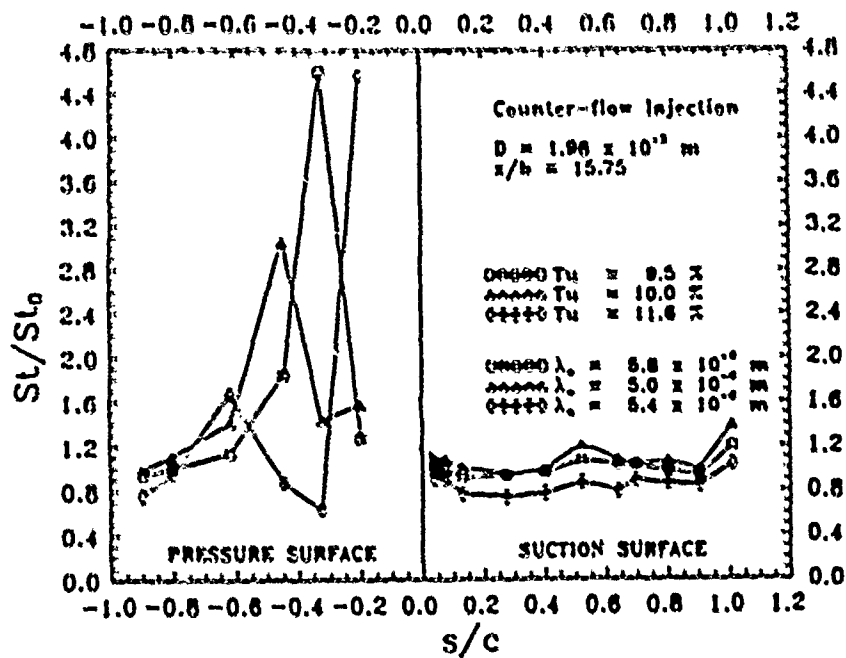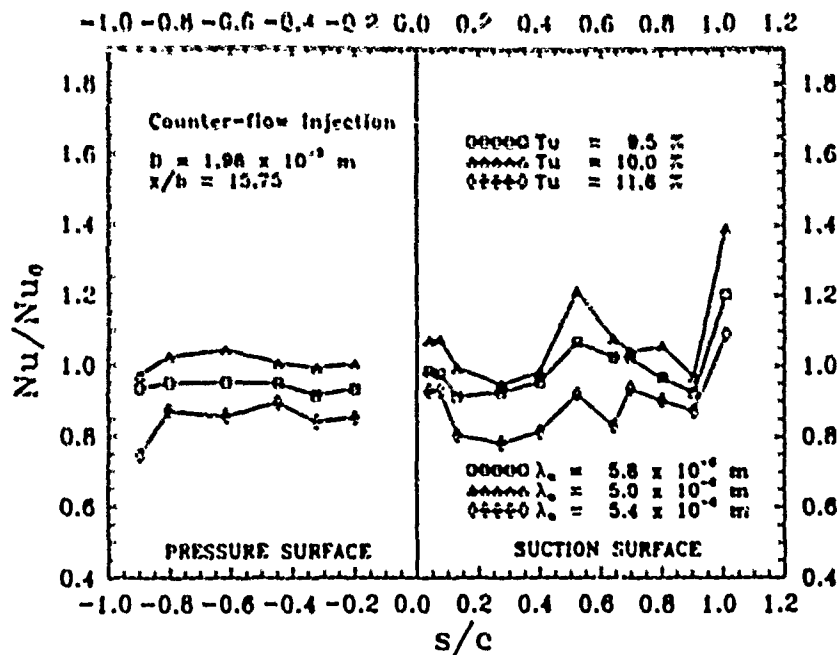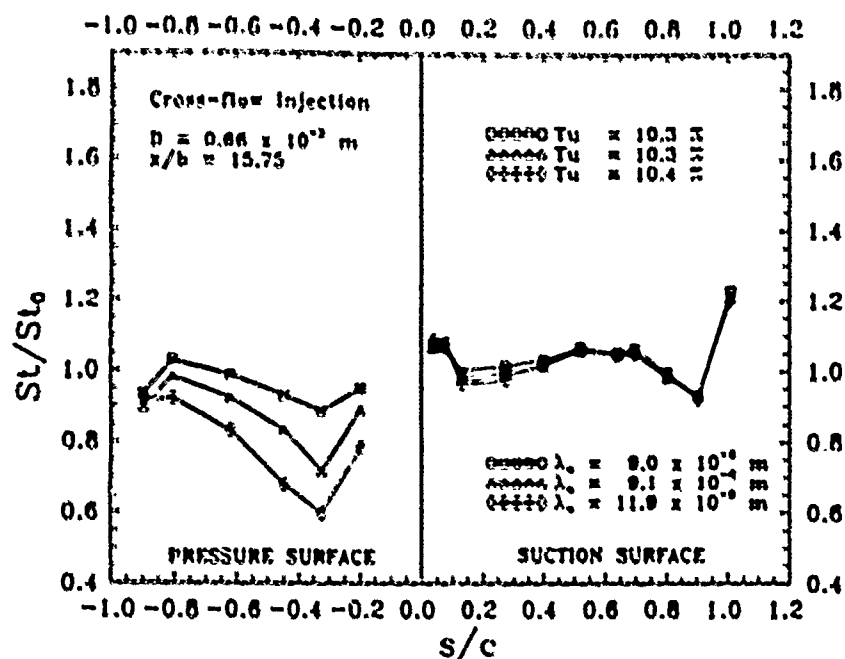

Figure 5.68. Nusselt number on the turbine blade for counter-flow injection. $D = 1.32$ mm. Test C21, C22 and C23. Jet-grid at station 0

Figure 5.69. Stanton number on the turbine blade for counter-flow injection. $D = 1.98$ mm. Test C31, C32 and C33. Jet-grid at station 0

Figure 5.70. Nusselt number on the turbine blade for counter-flow injection. $D = 1.98$ mm. Test C31, C32 and C33. Jet-grid at station 0

Figure 5.71. Stanton number on the turbine blade for cross-flow injection. $D = 0.66$ mm. Test B11, B12 and B13. Jet-grid at station 0

matched for all three tests shown in this figure, and where the turbine blade surface pressure distribution from Figure 5.4 was constant for all three tests, the increase in Stanton number ratio is attributable to the respective decrease in X-component microscale. Note, due to room restrictions on the plot, only the X-component microscales have been listed, however the corresponding Y-component microscales for the X-component microscales listed in Figures 5.71 and 5.72 similarly decreased in size for these three tests.

The effect of turbulence microscale on the turbine blade Nusselt number is seen when the free-stream turbulence was matched for different tests. Cross-flow injection pre ..uced measureable variations in the turbulence microscale for the same turbulence level. Figures 5.73, 5.74, and 5.75 indicate the Nusselt number increased on the pressure surface as the turbulence microscale length decreased for the same turbulence level. The suction surface Nusselt number ratios were unaffected by the variation in the microscale size, which was expected since the microscale, which is a measure of turbulence intensity and only affects the turbulent boundary layer. but the suction surface boundary layer was laminar or in
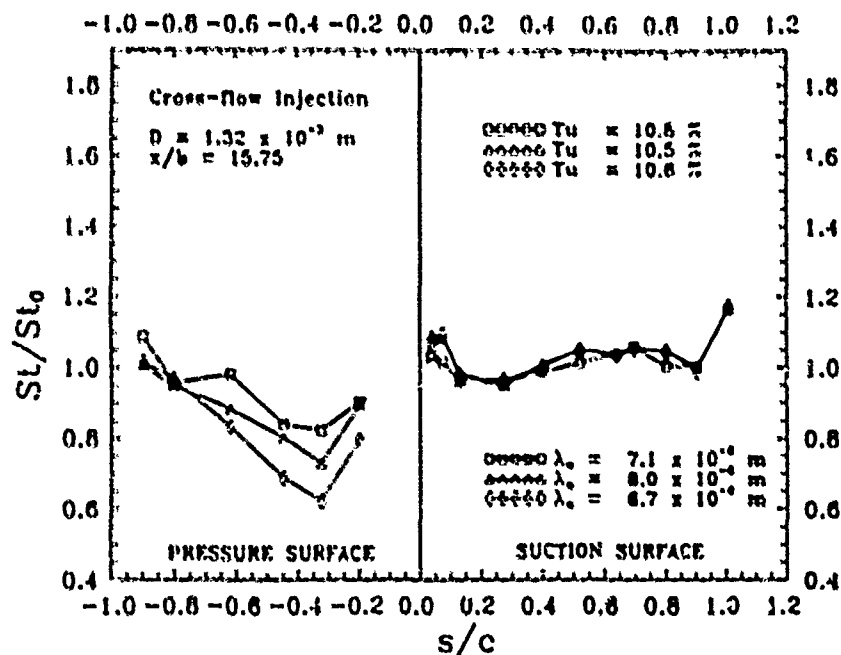
Figure 5.72. Stanton number on the turbine blade for cross-flow injection. $D = 1.32$ mm. Test B21, B22 and B23. Jet-grid at station 0

transition from a laminar to a turbulent boundary layer and was; therefore, unaffected by the variation in the turbulence microscale size.

Figure 5.76 shows the Nusselt number for both the pressure surface and the suction surface was different for all three tests in this figure, but the free-stream turbulence was only matched for the two lower injection pressures shown in this figure. For the two tests of Figure 5.76 where the turbulence level was matched, only a small increase in the Nusselt number ratio is noticeable near the leading edge of the pressure surface. On the suction surface, there is no discernable difference between the two test results. The noticeable increase of the Nusselt number ratio for the test with the highest injection pressure may or may not be attributible to the decrease in microscale length since the free-stream turbulence level was roughly 1 percent higher than the free-stream turbulence level of the other two tests.

Representative plots of the Stanton number and Nusselt number ratios for the turbine blade with the jet-grid at station 02 ($\frac{x}{b} = 25.67$) are now presented.

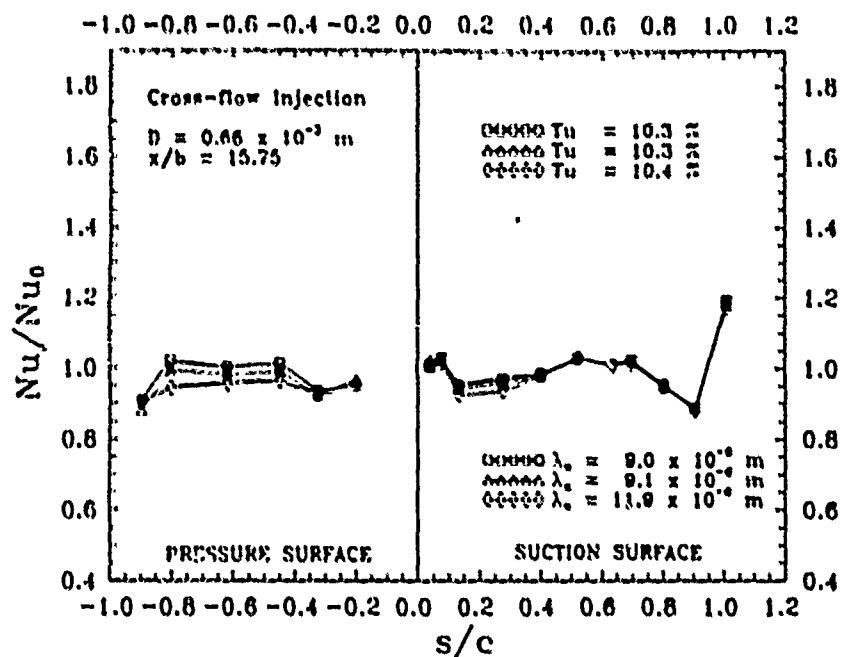In general, the Stanton numbers ratios measured on the turbine blade were on the

Figure 5.73. Nusselt number on the turbine blade for cross-flow injection. $D = 0.66$ mm. Test B11, B12 and B13. Jet-grid at station 0
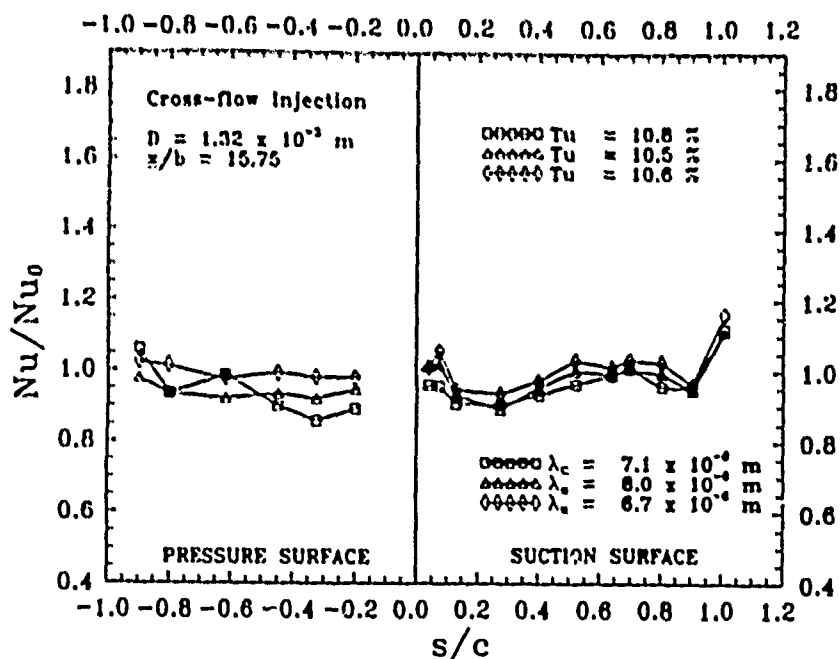

Figure 5.74. Nusselt number on the turbine blade for cross-flow injection. $D = 1.32$ mm. Test B21, B22 and B23. Jet-grid at station 0
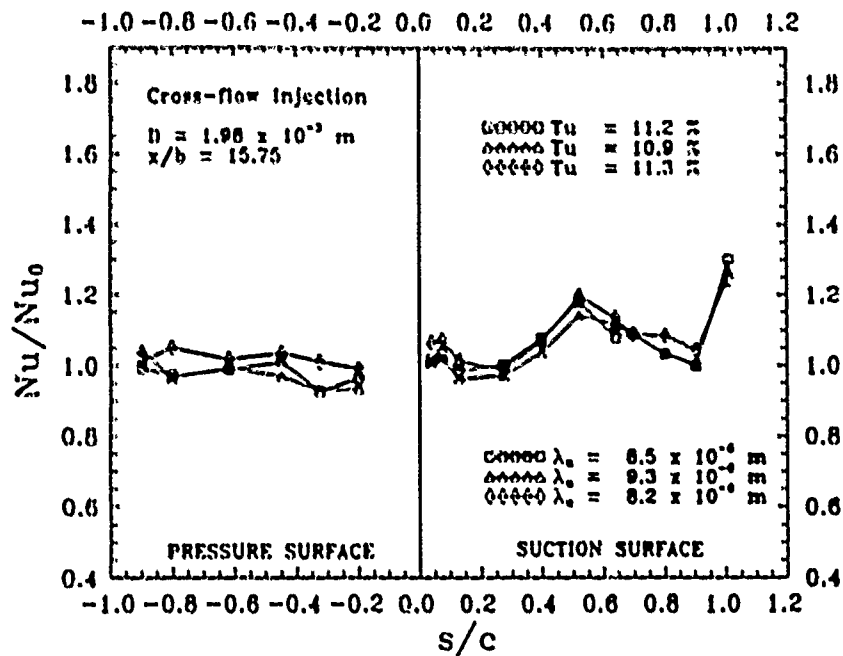
Figure 5.75. Nusselt number on the turbine blade for cross-flow injection. $D = 1.98$ mm. Test B31, B32 and B33. Jet-grid at station 0
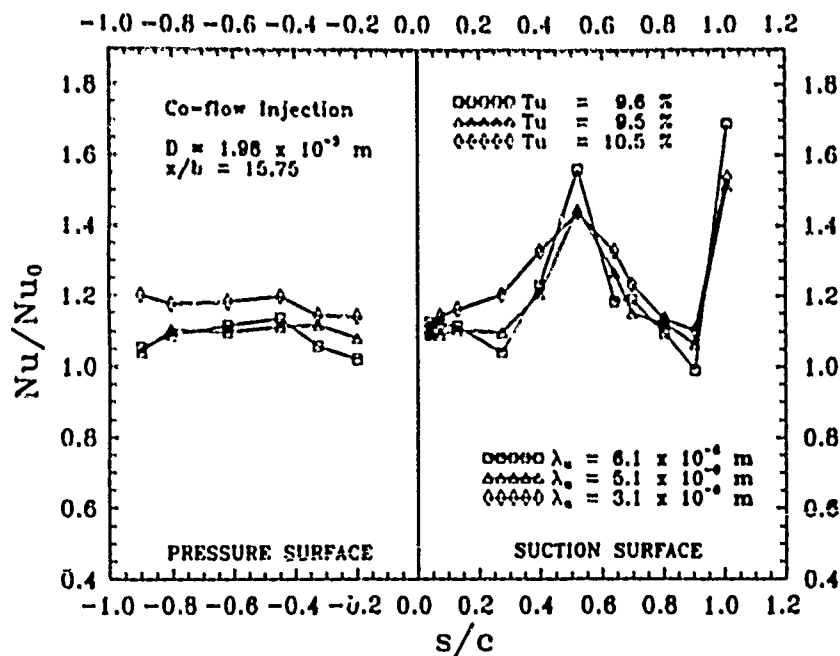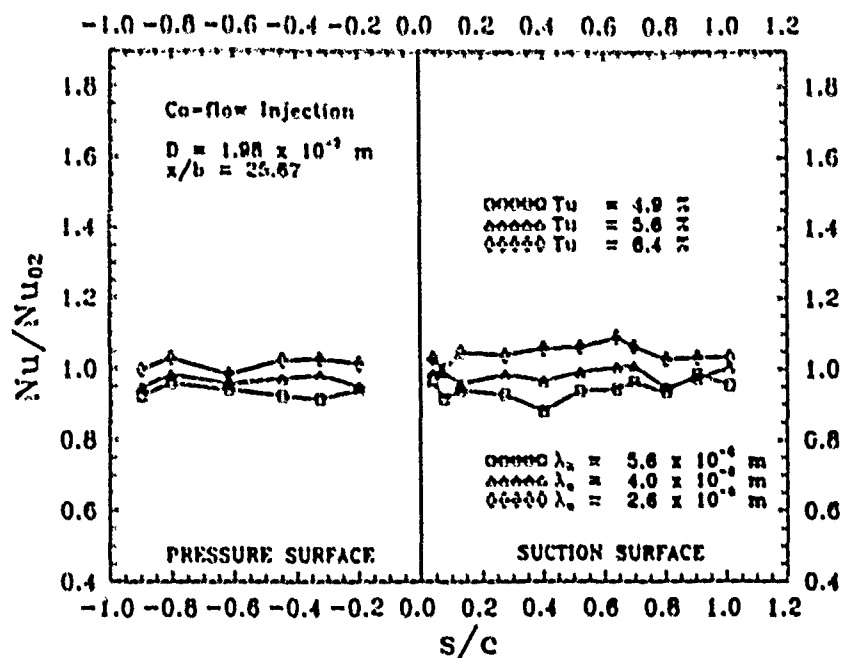

Figure 5.76. Nusselt number on the turbine blade for co-flow injection. $D = 1.98$ mm. Test A31, A32 and A33. Jet-grid at station 0

Figure 5.77. Nusselt number on the turbine blade for co-flow injection. $D = 1.98$ mm. Test D31, D32 and D33. Jet-grid at station 02

order of unity or slightly less than unity over the pressure and suction surfaces of the turbine blade. The Nusselt number ratios were also on the order of unity, except in the case of co-flow injection through the 1.98 mm diameter orifice shown in Figure 5.77. In this plot, the Nusselt number varied widely, and especially along the presure surface. The effect of the turbulence microscale on the Nusselt number is not clear in this plot since the turbulence intensity was not held constant for all tests shown in this figure.

Again, the ratios refer to Test 002, not Test XXX. Although the ratio may be unity or less, the actual Stanton or Nusselt numbers are generally much higher than the Stanton and Nusselt numbers on the turbine blade without the jet-grid installed in the free-stream flow.

The most noticeable trend for this set of figures is that no large increase in the Stanton number occurred for counter-flow injection, Figures 5.78, 5.79, and 5.80, as it did at station 0 (Compare to Figures 5.65, 5.67, and 5.69). The local surface velocities on the pressure surface of the turbine blade remained relatively unaffected which is visible from Figure 5.8. But counter-flow injection did cause the largest variation of the Stanton
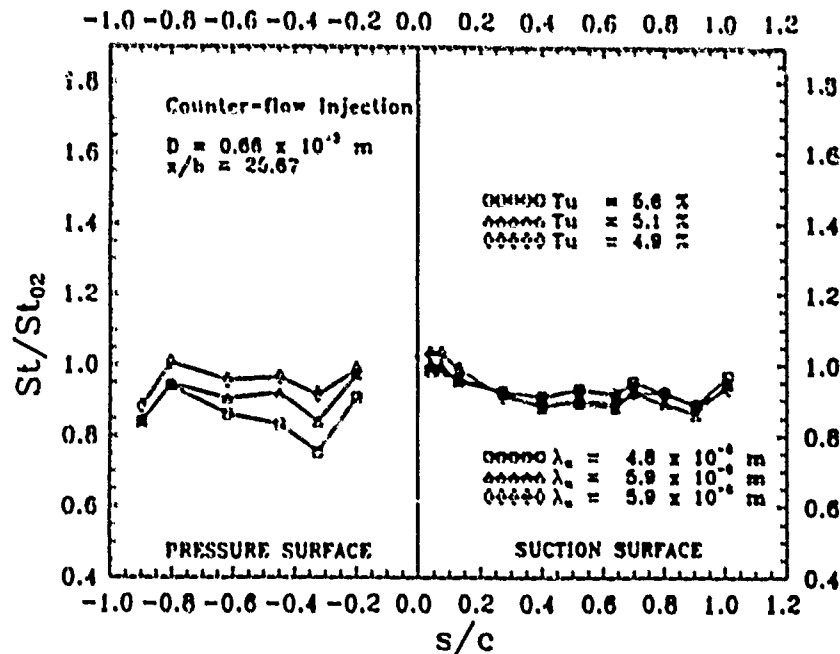
Figure 5.78. Stanton number on the turbine blade for counter-flow injection. $D = 0.66$ mm. Test F11, F12 and F13. Jet-grid at station 02

number as compared to the other injection directions tested with the jet-grid at station 02. For example, compare Figure 5.79 with Figure 5.81.

For all heat transfer tests made at station 02, the free-stream turbulence and surface velocity distribution were matched only in a two cases. Figure 5.81 and Figure 5.82 show a small increase in the Stanton number ratio and the Nusselt number ratio, respectively, of each test as the turbulence microscale size decreased. It is not known why the increase in the Stanton number ratios and the Nusselt number ratios was so small for a 27 percent decrease in the tubulence X-component microscale size.

Figure 5.80 represents the second case where both the free-stream turbulence and surface velocities on the pressure surface of the turbine blade were matched for the two tests shown. In this case, the Stanton number ratio increased as the turbulence microscale decreased. the Nusselt number ratio shown for this case in Figure 5.83 remained relatively constant for both tests.
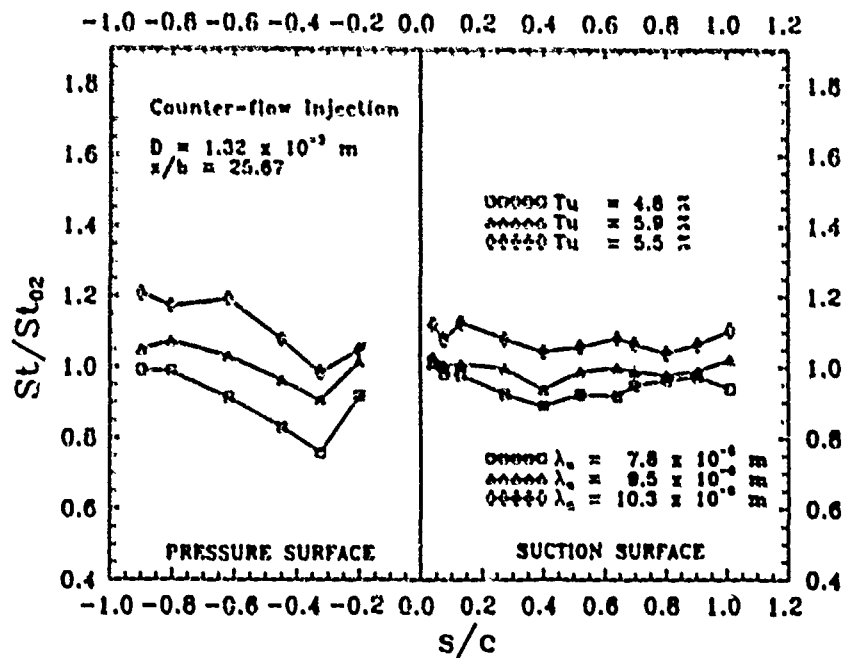
Figure 5.79. Stanton number on the turbine blade for counter-flow injection. $D = 1.32$ mm. Test F21, F22 and F23. Jet-grid at station 02
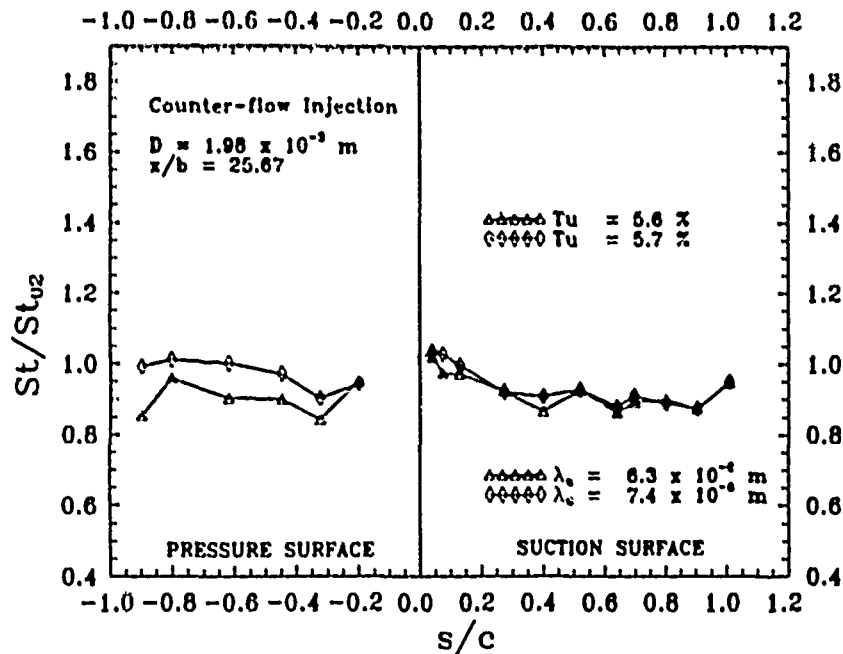

Figure 5.80. Stanton number on the turbine blade for counter-flow injection. $D = 1.98$ mm. Test F31, F32 and F33. Jet-grid at station 02
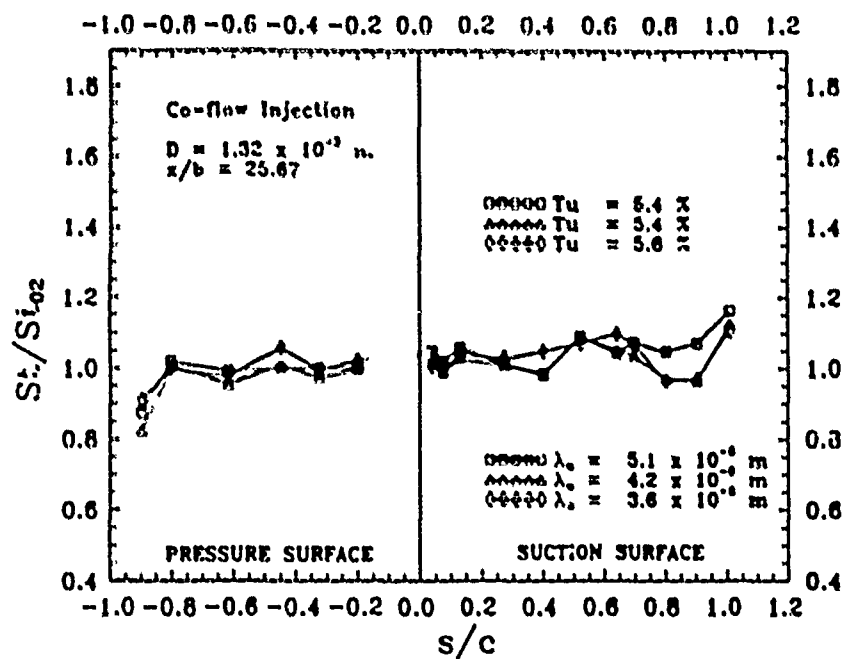
Figure 5.81.   Stanton number on the turbine blade for co-flow injection. $D = 1.32$ mm. Test D21, D22 and D23. Jet-grid at station 02
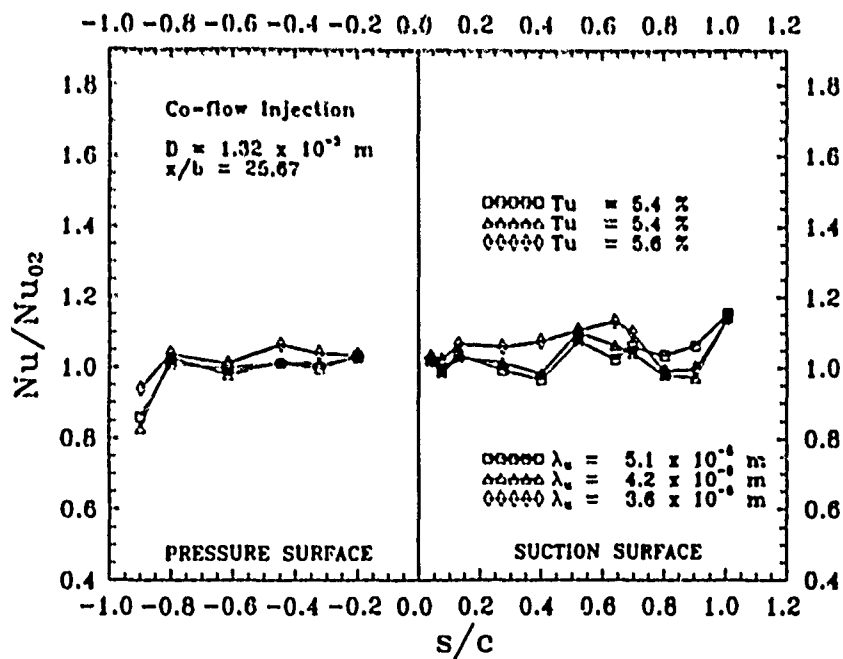

Figure 5.82.   Nusselt number on the turbine blade for co-flow injection. $D = 1.32$ mm. Test D21, D22 and D23. Jet-grid at station 02
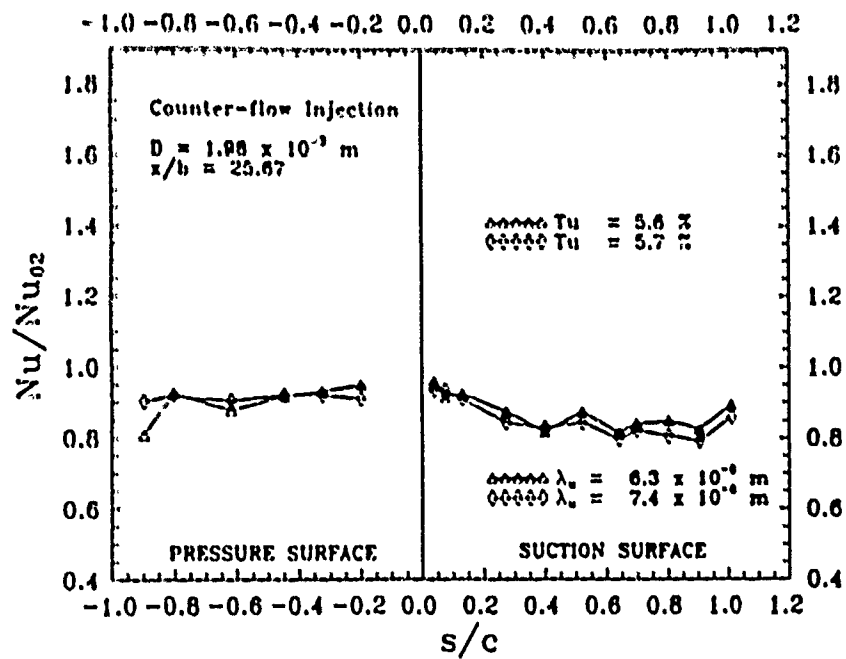
Figure 5.83. Nusselt number on the turbine blade for counter-flow injection. $D = 1.98$ mm. Test F31, F32 and F33. Jet-grid at station 02

VI. CONCLUSIONS AND RECOMMENDATIONS

6.1 Conclusions

The effect of turbulence scale lengths on heat transfer in a linear turbine cascade was studied. Of equal importance, methods were developed to control the turbulence integral scale and microscale lengths at a given free-stream turbulence level. The overall results of this experiment are presented as turbulence scale generation and turbulence scale effects on the Stanton and Nusselt numbers for the turbine blade.

The following conclusions are given for the turbulence scale results:

1. The turbulence integral scale length (Λ) was primarily dependent on the physical dimensions of the turbulence generating grid tube. The streamwise component of integral scale were on the order on 0.6 mm, which corresponds closely with the outside diameter of the jet-grid tube inserted into the free-stream. In this study, secondary flow injection through a jet-grid placed in the free-stream increased the integral scale length by as much as 45 percent. Co-flow injection increased and decreased the integral scale lengths depending on injection pressure and injection orifice diameter. Cross-flow injection has negligible effect on the size of the integral scales. Counter-flow injection increased the effective jet-grid tube diameter.

2. Turbulence integral scales did not decay downstream of the turbulence generating grid.

3. The turbulence microscale length (λ) was primarily determined by the location of the jet-grid in the free-stream with respect to the position of the turbulence measurement device. A large variation of the microscales occurred for the jet-grid location when the injection direction was changed. Co-flow injection through the jet-grid tended to decrease the microscale lengths. Cross-flow injection produced a variety of microscale lengths. Counter-flow injection had a relatively minor affect on the microscale lengths. The largest variation of the turbulence microscales due to injection occurred with the jet-grid placed at the far upstream location ($\frac{x}{b} = 25.67$).

4. Turbulence microscales grew in size as the free-stream flow moved downstream of the turbulence generating device. Turbulence microscales measured at a nondimensional distance of $\frac{z}{b} = 25.67$ were 5-8 times the size of turbulence microscales measured at $\frac{z}{b} = 15.75$.

5. Turbulence intensity varied inversely with turbulence microscale size. The higher free-stream turblence levels contained the smallest microscale sizes. Turbulence decay matched turbulence decay correlations provided by Blair (Blair, 1983a) for the jet-grid at $\frac{z}{b} = 15.75$. Blair's correlation underestimated the turbulence decay by 16 percent with the jet-grid at $\frac{z}{b} = 25.67$. In this case, the effect on the turbulence intensity of the free-stream accelerating as it approached the turbine cascade is thought to have caused the measured free-stream turbulence level to decrease beyond Blair's correlation.

Conclusions on the heat transfer results are listed as follows:

1. The Stanton number measured on the turbine blade pressure surface matches the turbulent boundary layer heat transfer prediction presented by Ambrok (Ambrok, 1957) for low-turbulence (1.26 percent) free-stream conditions. Near the leading edge of the pressure surface, a laminar bubble is thought to have caused a signigficantly lower Stanton number than what is predicted by Ambrok's theory.

2. The Stanton number measured on the suction surface is best correlated by laminar boundary heat transfer predictions (Kays, 1987) for low-turbulence free-stream flow. An abrubt increase in Stanton number on the suction surface occured around the non-dimensional surface distance of $\frac{s}{c} = 0.6$, at which point, the Stanton number matched the turbulent boundary layer prediction. It is thought laminar to turbulent boundary layer transition occured at this location on the suction surface.

3. Introduction of the jet-grid device produced significantly higher levels of free-stream turbulence, which caused a higher heat transfer rate and a higher Stanton number than predicted by Ambrok's theory on the pressure surface. Higher free-stream turbulence advanced the laminar-to-turbulent boundary layer transition point on the suction surface. For a 11.8 percent free-stream turbulence level, the boundary

layer on the suction surface was almost entirely in a transition state or fully turbulent and the Stanton number approached turbulent boundary layer predictions.

4. With the free-stream turbulence level held constant and for a constant turbine blade surface velocity, the Stanton number increased as the turbulence microscale length decreased in repeated heat transfer tests. However, the jet-grid introduced a variation of the local velocity along the turbine blade surface, which had a large effect on the measured Stanton number and made it difficult to correlate the turbulence microscale lengths with the Stanton number for many of the heat transfer tests performed in this study.

5. The effect of the turbulence microscale length on the Nusselt number was best observed with cross-flow injection with the jet-grid at station 0, where it was observed that the free-stream turbulence level remained constant, the turbine blade surface velocities remained constant, the turbulence microscales decreased with increasing injection pressure, and the Nusselt number increased.

6.2 *Recommendations*

In light of the results of this report, the following recommendations are made for advanced study of turbulence scale effects on heat transfer in a linear turbine cascade:

Instrumentation improvements:

1. The turbine blade heat transfer test model and pressure surface model should be integrated as one test model. This would allow the experimenter to simultaneously measure pressure distributions and heat transfer on the turbine blade surface.

2. An additional Hewlett-Packard 44713, 24-Channel FET Multiplexer should be incorporated with the present data acquisition system. This improvement would allow more thermocouples to be used with the test model and allow a more detailed measurement of the turbine blade surface temperatures.

3. Improved the jet-grid device by attaching high-pressure air lines, rather than the low pressure air lines presently used. This would allow higher injection pressures to be used and supersonic injection effects may be studied.

4. The test section endwall should be modified to allow easier access to the test section for introduction and removal of the test models.

Areas of further research:

1. Investigate the free-stream turbulence decay and microscale decay through the cascade passageway.

2. Measure the effect of free-stream turbulence level and turbulence microscale length on the turbine blade boundary layer.

3. Model turbine blade surface degradation with a rough surface model and study the effects on surface heat transfer and the location of transition to from laminar to turbulent boundary layers on both the pressure surface and the suction surface. Riblets on the blade surface may also be incorporated into the study.

4. Lastly, perform a flow visualization study in order to determine the three-dimensional effects of the low-aspect ratio test section. Use the flow visualization to study the effects of jet-grid injection on the local velocities on the surface of the turbine blade.

Ambrok, 1957. Ambrok, G. S., *Soviet Physics-Technical Physics*, vol. 2, p. 1979 (1957).

Batchelor, 1953. Batchelor, G. K., *The Theory of Homogeneous Turbulence*. London and New York: Cambridge University Press, 1953.

Brigham, 1986. Bingham, D. A. *The Fast Fourier Transform*. New York: McGraw-Hill, 1986.

Blair, 1989a. Blair, M. F., et al. "The Effects of Turbulence and Stator/Rotor Interactions on Turbulence Heat Transfer: Part I - Design Operating Conditions,"*Journal of Turbomachinery* , *111*: 87-96 (January 1989a).

Blair, 1989b. Blair, M. F., et al. "The Effects of Turbulence and Stator/Rotor Interactions on Turbulence Heat Transfer: Part II - Effects of Reynolds Number and Incidence," *Journal of Turbomachinery*, *111*: 97-103 (January 1989b).

Blair, 1983a. Blair, M. F., et al. "Influence of Free-Stream Turbulence on Turbulent Boundary Layer Heat Transfer and Mean Profile Development, Part II—Analysis of Results,"*Journal of Heat Transfer*, *105*:33-40 (February 1983a).

Blair, 1983b. Blair, M. F., et al. "Influence of Free-Stream Turbulence on Turbulent Boundary Layer Heat Transfer and Mean Profile Development, Part I—Experimental Data,"*Journal of Heat Transfer*, *105*:41-47 (February 1983b).

Cebeci, 1974. Cebeci, T., and A. O. Smith. *Analysis of Turbulent Boundary Layers*. New York: Academic Press, 1974.

Consigny, 1982. Consigny, H., and B. E. Richards, " Short Duration Measurements of Heat-Transfer Rate to a Gas Turbine Rotor Blade," *Journal of Engineers for Power,104*: 542-551 (July 1982).

Eckert, 1942. Eckert, E. R. G.," ," *VDI—Forschungsh,416*: 1-24 (1942).

Hinze, 1959. Hinze, J. O.. *Turbulence, an Introduction to its Mechanism and Theory*. New York: McGraw-Hill, 1959.

Incropera, 1985. Incropera, F. P., and D. P. DeWitt. *Introduction to Heat Transfer*. New York: John Wiley and Sons, 1985.

Kays, 1987. Kays, W. M., and M. E. Crawford. *Convective Heat and Mass Transfer*. 2nd ed. New York: McGraw-Hill Book Company, 1987.

Kays, 1970. Kays, W. M., et al., *Journal of Heat Tansfer*, Vol. 92, p. 499-505 (1970).

Langston, 1977. Langston, L. S., M. L. Nice, and R. M. Hooper, " Three-Dimensional Flow Within a Turbine Cascade Passage," *Journal for Engineering for Power, 99*: 21-28 (January 1977).

MATHCAD Manual, 1987. *MathCad Manual*, Dealer documentation, Mathsoft, Inc., October 1987.

Moore, 1984c. Moore, J., and A. Ransmayr, "Flow in a Turbine Cascade: Part I – Losses and Leading-Edge Effects," *Journal for Engineering for Gas Turbines and Power*, 106: 400-408 (April 1984).

Moore, 1984a. Moore, J., and R. Y. Adhye, "Secondary Flows and Losses Downstream of a Turbine Cascade," Paper Number 85 - GT - 64, *The American Society for Mechanical Engineers*. (December 1984a).

Moore, 1984b. Moore, J., and J. G. Moore, "Performance Evaluation of Linear Turbine Cascades Using Three-Dimensional Viscous Flow Calculations," Paper Number 85 - GT - 65, *The American Society for Mechanical Engineers*. (December 1984b).

Priddy, 1985. Priddy, W. J., and F. J. Bayley, " Effects of Free Stream Turbulence on the Distribution of Heat Transfer Around Turbine Blade Sections," *International Journal of Heat and Fluid Flow*, 6: 181-192 (September 1985).

Simonich, 1978. Simonich, J. C. and P. Bradshaw, *Journal of Heat Transfer*, 100: 671-677 (1978).

Smith, 1958. Smith, A. G. and D. B. Spaulding, *Journal of the Royal Aeronautical Society*, 62: 60 (1958).

TSI Manual, 1983. *Intelligent Flow Analyzer Instruction Manual*, Dealer Operating Manual, TSI Part Number 1990237, TSI Incorporated, June 1983.

Young, 1989. Young, C. D., and J. C. Han, "The Influence of Jet-Grid Turbulence on Turbulent Boundary Layer Flow and Heat Transfer," Contractor Report -RF 5734 to Wright-Patterson AFB, March 1988.

Heat transfer data for the turbine cascade with no jet-grid installed: Test XXX

```
File: xxx
Secondary flow pressure =    0   KPa
Electrical energy input =  325   Watts
```

x/c	Re no.	Nusselt	Stanton
1.73910E-02	0.00000E+00	0.00000E+00	0.00000E+00
6.52170E-02	1.33630E+03	0.00000E+00	0.00000E+00
1.24349E-01	2.77358E+04	4.03821E+02	2.05935E-02
1.91304E-01	3.74176E+04	8.13716E+02	3.07594E-02
3.15652E-01	5.73666E+04	8.95459E+02	2.20784E-02
4.36522E-01	1.03032E+05	1.05932E+03	1.45424E-02
6.00000E-01	1.96877E+05	1.42988E+03	1.02727E-02
7.68696E-01	3.21277E+05	1.29002E+03	5.67935E-03
8.52174E-01	4.66597E+05	0.00000E+00	0.00000E+00
9.23478E-01	5.87590E+05	0.00000E+00	0.00000E+00
9.91304E-01	7.00919E+05	0.00000E+00	0.00000E+00
9.02609E-01	7.17577E+05	0.00000E+00	0.00000E+00
7.64348E-01	5.77157E+05	1.19522E+03	2.92909E-03
6.66957E-01	5.59542E+05	2.31694E+03	5.85682E-03
5.81739E-01	5.07137E+05	2.04288E+03	5.69768E-03
4.86957E-01	4.42468E+05	9.04001E+02	2.88980E-03
3.85217E-01	4.18384E+05	8.40041E+02	2.83992E-03
3.32174E-01	3.51226E+05	8.73489E+02	3.51764E-03
2.19130E-01	2.68639E+05	7.11123E+02	3.74417E-03
1.07826E-01	1.81815E+05	5.44172E+02	4.23338E-03
3.56520E-02	7.98340E+04	2.99230E+02	5.30149E-03
0.00000E+00	4.24161E+04	2.17413E+02	7.24998E-03
8.69565E-03	2.23173E+04	1.22888E+02	7.78844E-03

Heat t   .. for the turbine cascade jet-grid installed , no blowing . $\frac{z}{b} = 15.75$:

Test 000

```
File: 000
Secondary flow pressure =    0   KPa
Electrical energy input =   325  Watts
x/c              Re no.          Nusselt         Stanton
1.73910E-02     0.00000E+00     0.00000E+00     0.00000E+00
6.52170E-02     5.28691E+03     0.00000E+00     0.00000E+00
1.24349E-01     2.28461E+04     5.83206E+02     3.61070E-02
1.91304E-01     2.34950E+04     8.00154E+02     4.81702E-02
3.15652E-01     3.70269E+04     9.89404E+02     3.77952E-02
4.36522E-01     8.12465E+04     1.25927E+03     2.19226E-02
6.00000E-01     1.71917E+05     1.70049E+03     1.39907E-02
7.68696E-01     2.94917E+05     1.57382E+03     7.54809E-03
8.52174E-01     4.28749E+05     0.00000E+00     0.00000E+00
9.23478E-01     5.48295E+05     0.00000E+00     0.00000E+00
9.91304E-01     6.59944E+05     0.00000E+00     0.00000E+00
9.02609E-01     6.70384E+05     0.00000E+00     0.00000E+00
7.64348E-01     5.70136E+05     2.36502E+03     5.86728E-03
6.66957E-01     5.24245E+05     2.41284E+03     6.50990E-03
5.81739E-01     4.76330E+05     2.20921E+03     6.56003E-03
4.86957E-01     4.27040E+05     1.96938E+03     6.52292E-03
3.85217E-01     4.06611E+05     1.70647E+03     5.93609E-03
3.32174E-01     3.31049E+05     1.30467E+03     5.57428E-03
2.19130E-01     2.51700E+05     1.04757E+03     5.88682E-03
1.07826E-01     1.67939E+05     7.90401E+02     6.65696E-03
3.56520E-02     7.24332E+04     3.99754E+02     7.80613E-03
0.00000E+00     3.72762E+04     2.55815E+02     9.70678E-03
8.69565E-03     1.93108E+04     1.41271E+02     1.03474E-02
```

Heat transfer data for the turbine cascade jet-grid installed, no blowing. $\xi = 25.67$:
Test 002

```
File: 002
Secondary flow pressure =      0   KPa
Electrical energy input =    325   Watts
x/c              Re no.           Nusselt          Stanton
1.73910E-02    0.00000E+00      0.00000E+00      0.00000E+00
6.52170E-02    5.06586E+03      0.00000E+00      0.00000E+00
1.24349E-01    2.48590E+04      5.30052E+02      3.01589E-02
1.91304E-01    3.01694E+04      7.53089E+02      3.53070E-02
3.15652E-01    4.80176E+04      9.46641E+02      2.78847E-02
4.36522E-01    9.12736E+04      1.20913E+03      1.87373E-02
6.00000E-01    1.80266E+05      1.61313E+03      1.28571E-02
7.68696E-01    3.01917E+05      1.52730E+03      7.15513E-03
8.52174E-01    4.36054E+05      0.00000E+00      0.00000E+00
9.23478E-01    5.51019E+05      0.00000E+00      0.00000E+00
9.91304E-01    6.59929E+05      0.00000E+00      0.00000E+00
9.02609E-01    6.75457E+05      0.00000E+00      0.00000E+00
7.64348E-01    5.78900E+05      2.62639E+03      6.41705E-03
6.66957E-01    5.24732E+05      2.33533E+03      6.29494E-03
5.81739E-01    4.79838E+05      2.25002E+03      6.63242E-03
4.86957E-01    4.31781E+05      1.98047E+03      6.48762E-03
3.85217E-01    4.09825E+05      1.60245E+03      5.53053E-03
3.32174E-01    3.34915E+05      1.27357E+03      5.37859E-03
2.19130E-01    2.53604E+05      9.64510E+02      5.37937E-03
1.07826E-01    1.69121E+05      6.79014E+02      5.67888E-03
3.56520E-02    7.35434E+04      3.43152E+02      6.59969E-03
0.00000E+00    3.85336E+04      2.54121E+02      9.32784E-03
8.69565E-03    2.01419E+04      1.39989E+02      9.83048E-03
```

Appendix B. *TURBULENCE ENERGY*

This appendix contains plots of the turbulence energy spectrum used to calculate the turbulence integral scale lengths and turbulence microscale lengths for each test. The theoretical slope of the spectrum (Batchelor, 1953) is shown for comparison.
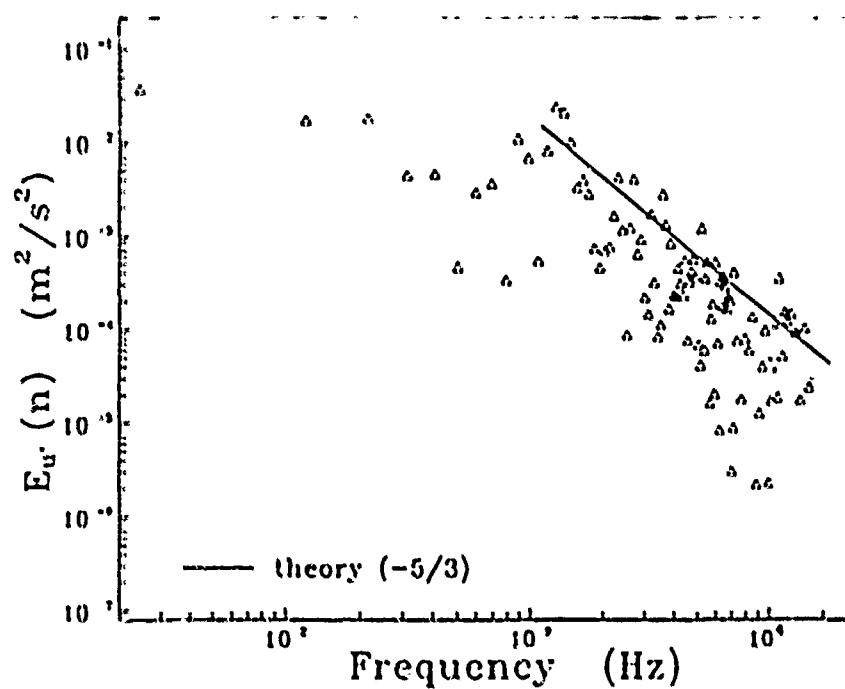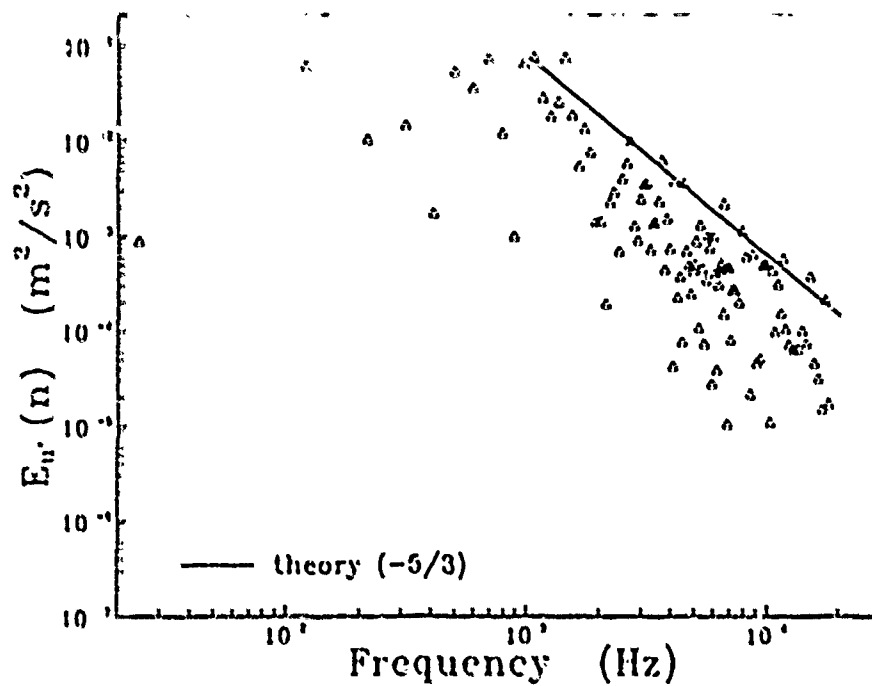
Figure B.1. Turbulence energy spectrum for u'^2: Test A11
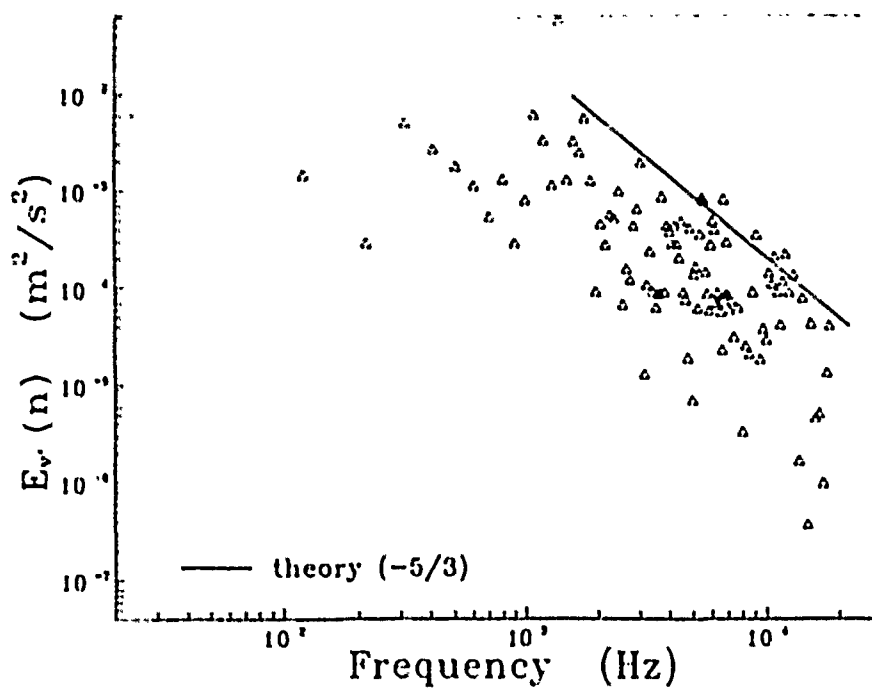
Figure B.2. Turbulence energy spectrum for v'^2: Test A11
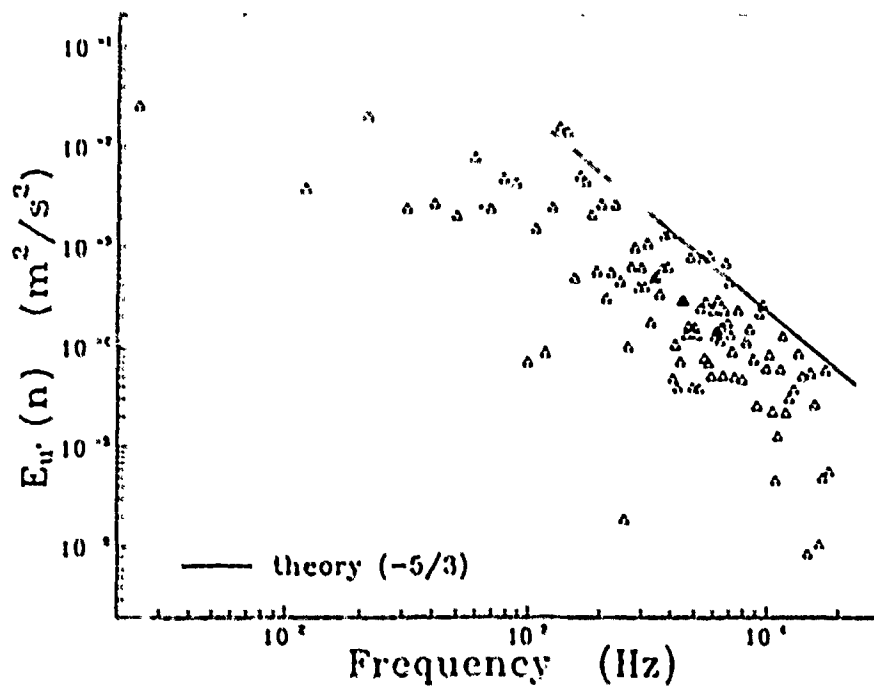
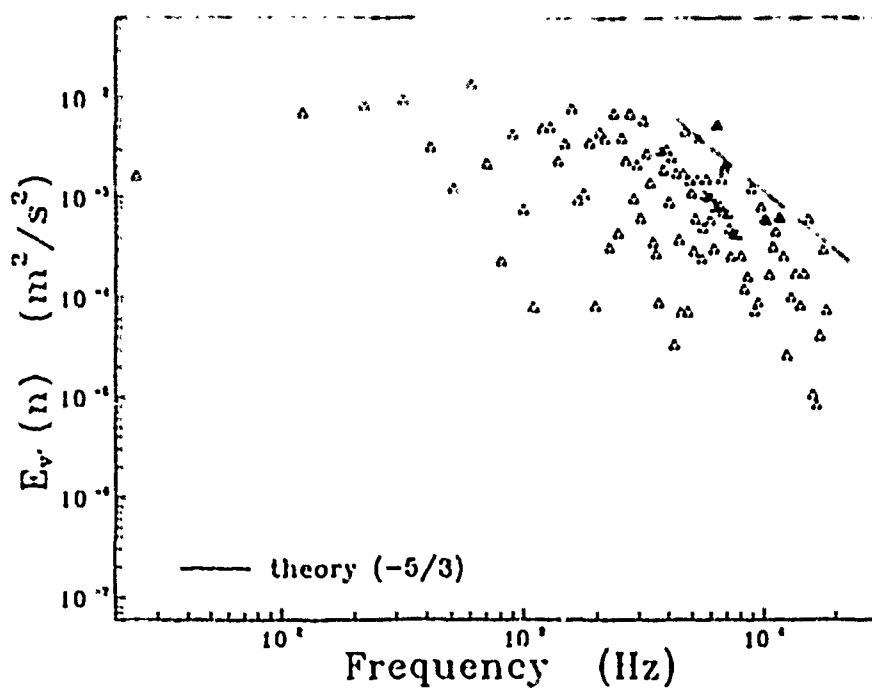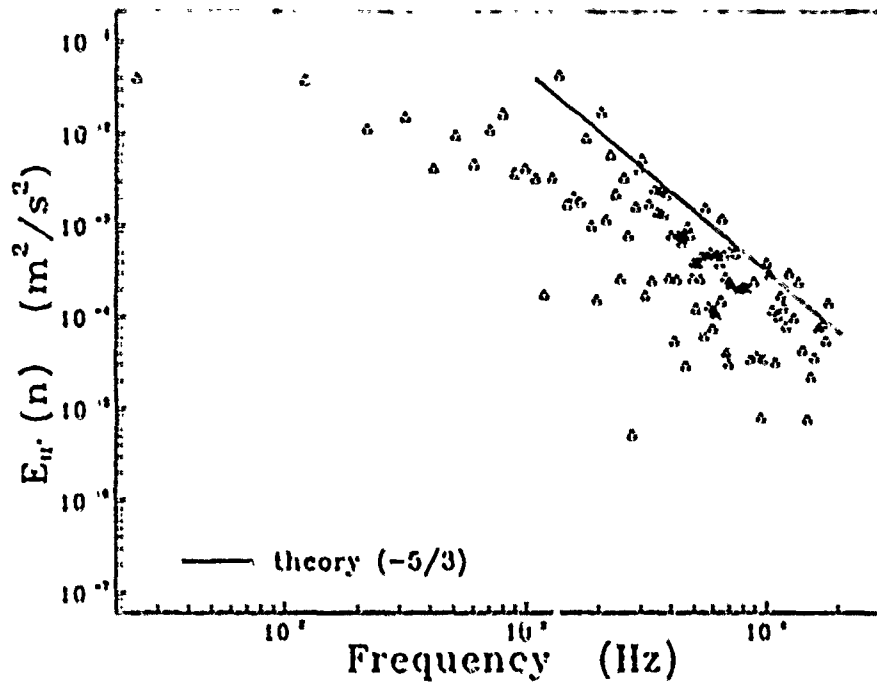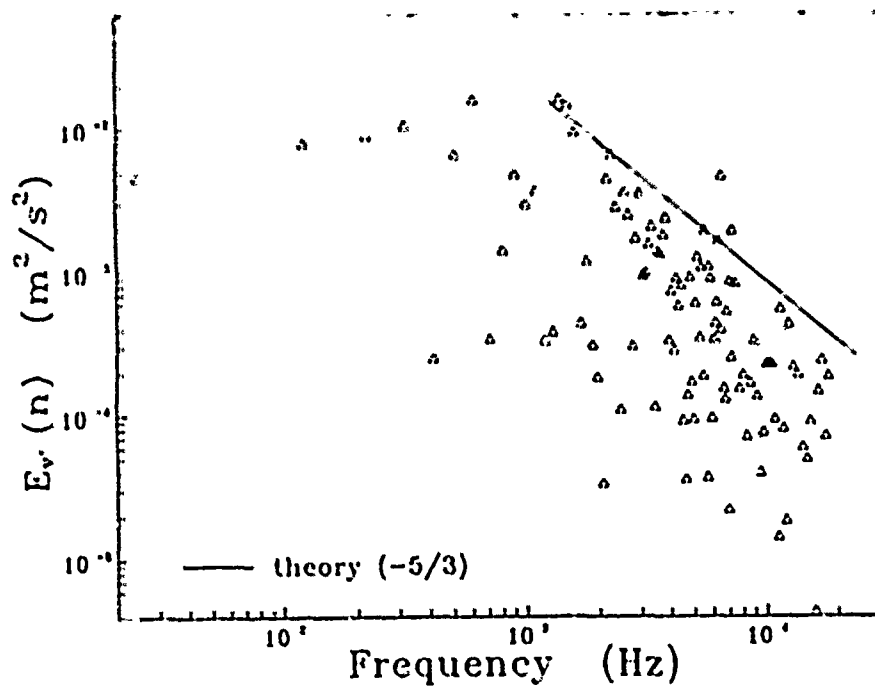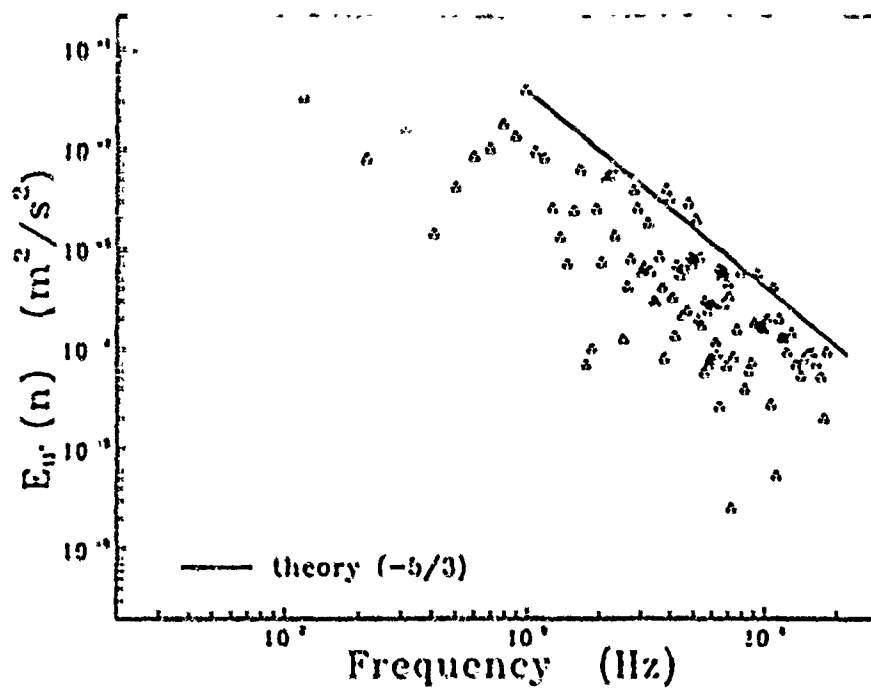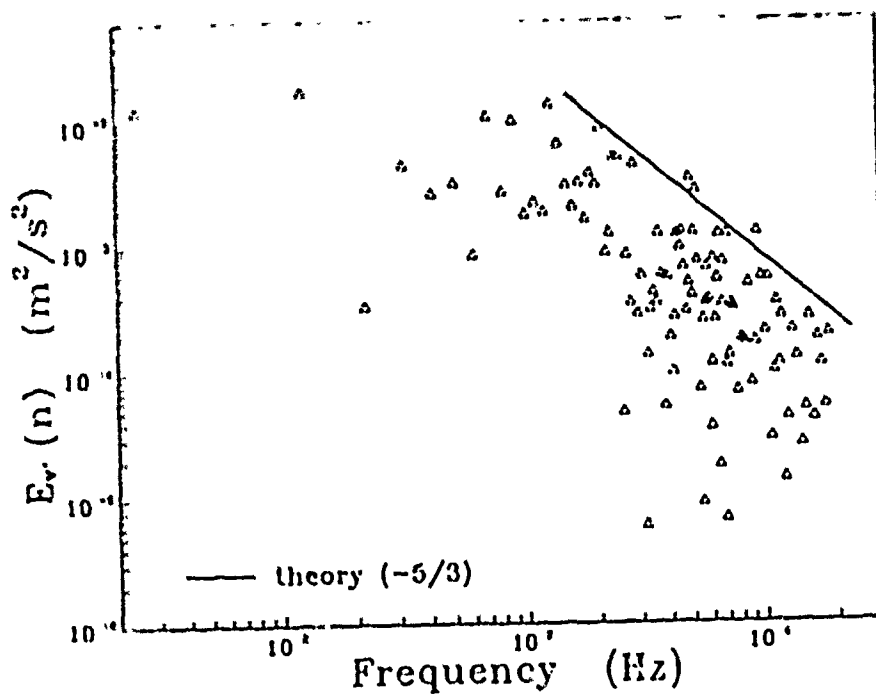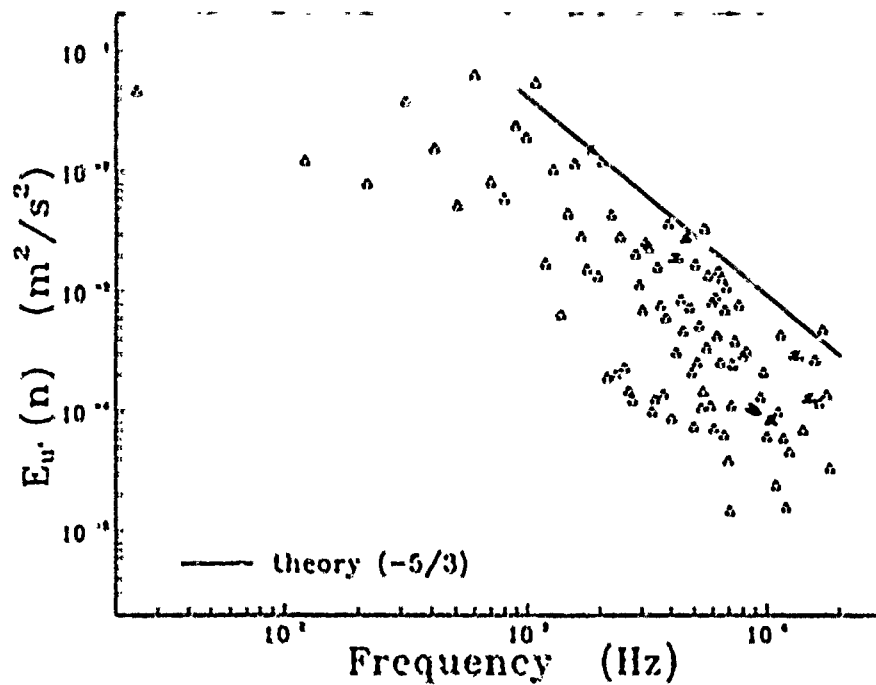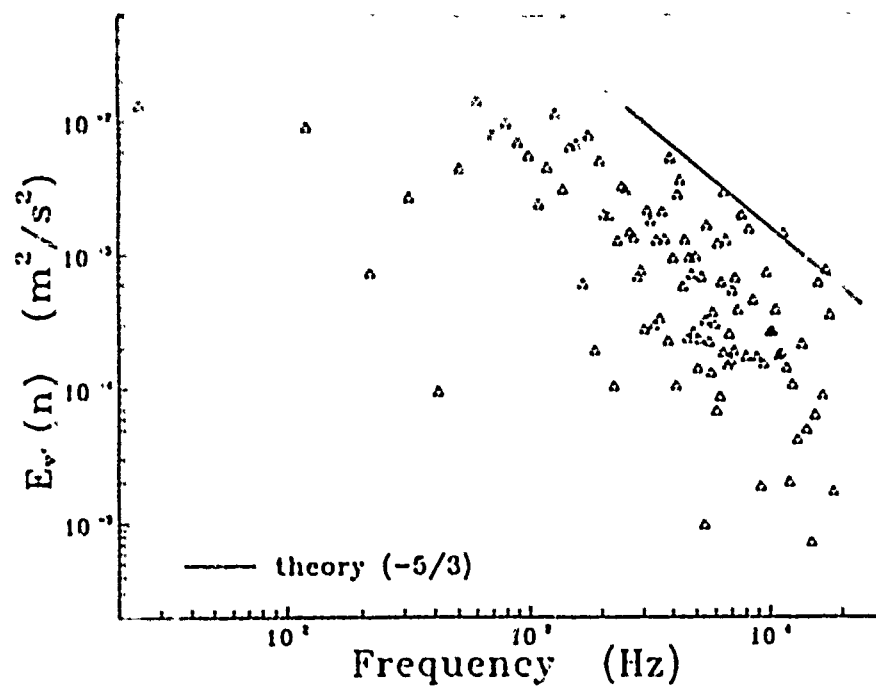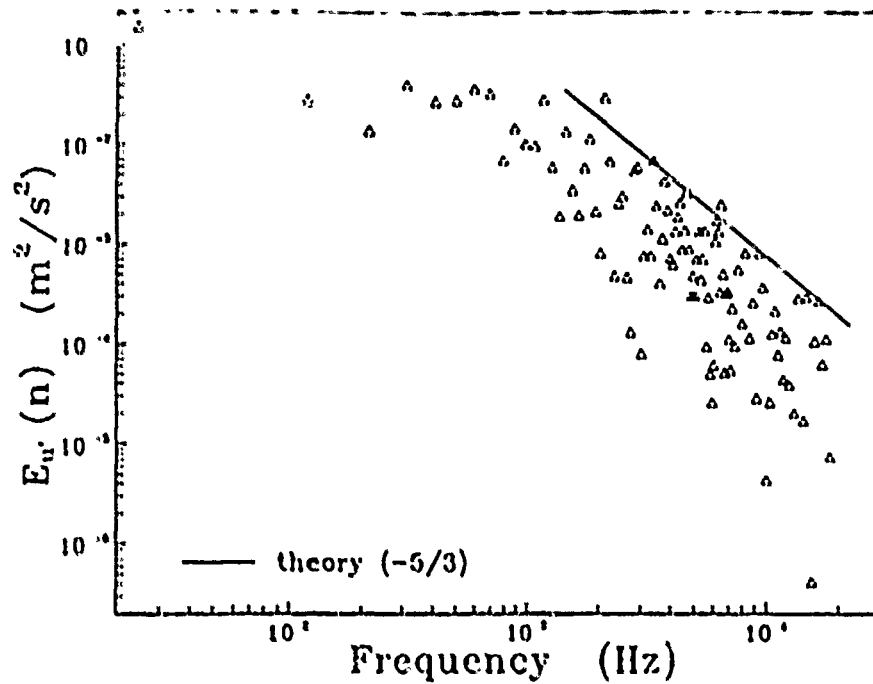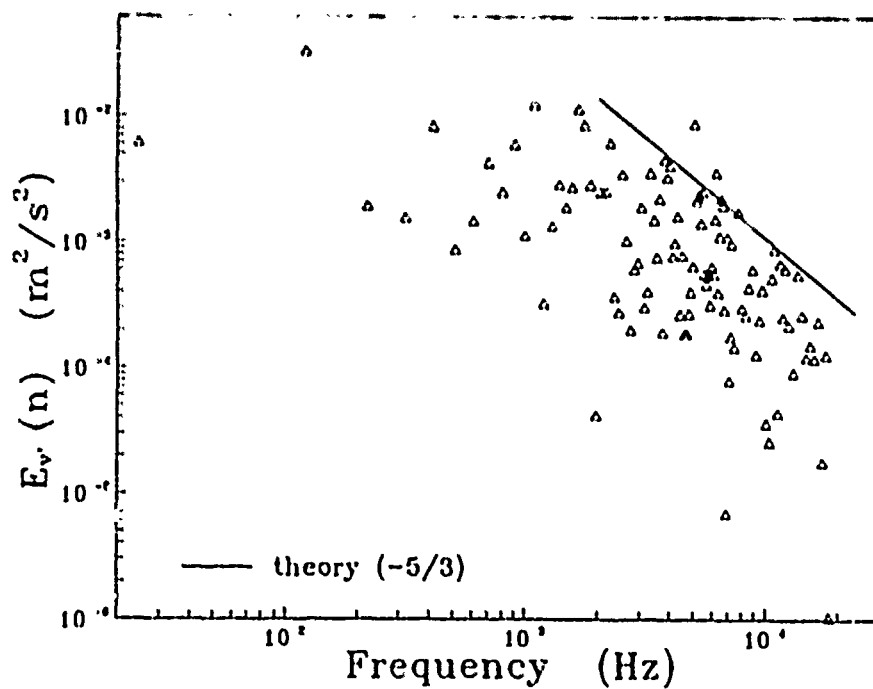Figure B.3. Turbulence energy spectrum for u'^2: Test A12
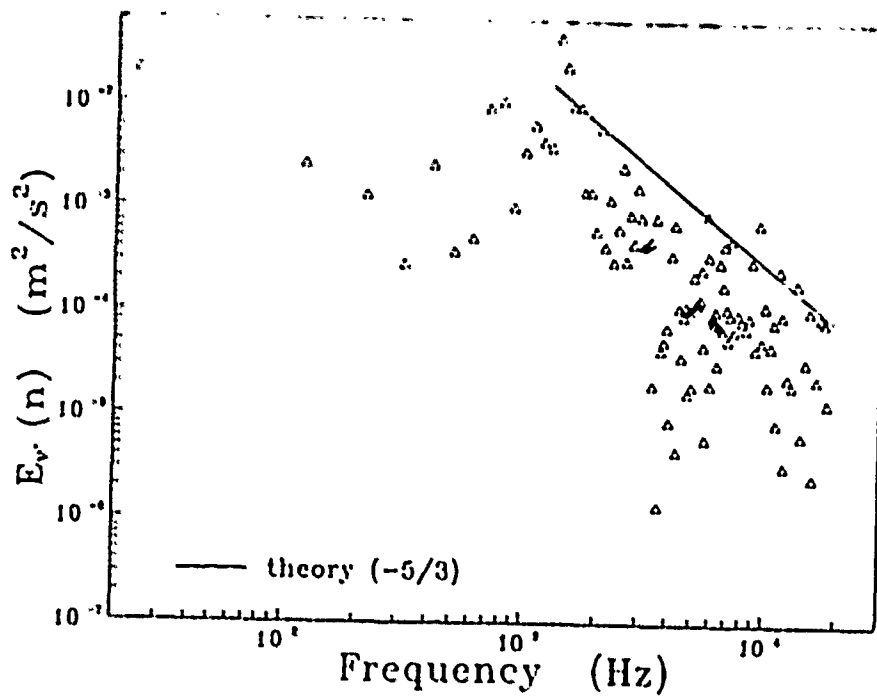
Figure B.4. Turbulence energy spectrum for v'^2: Test A12
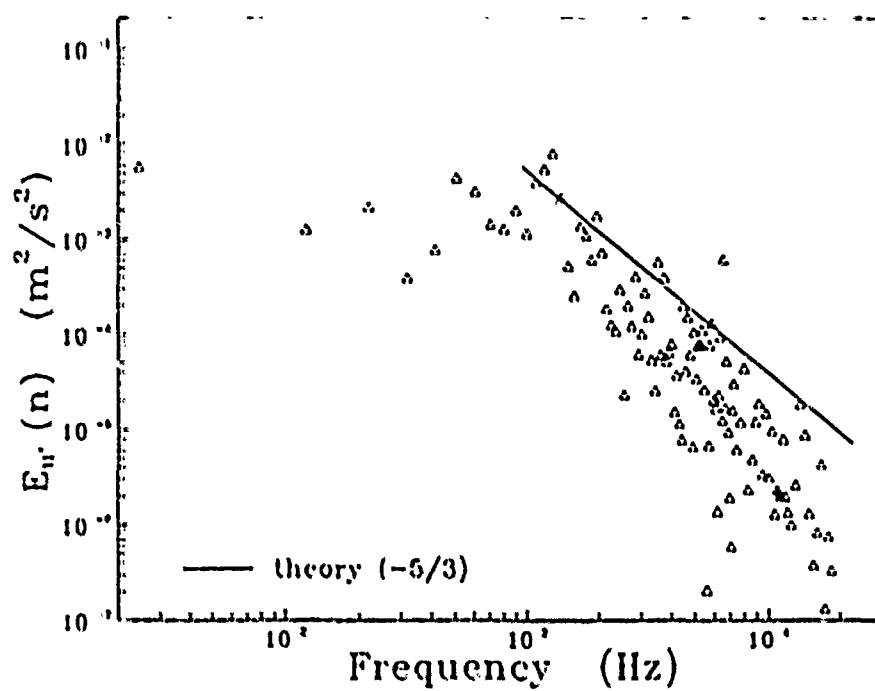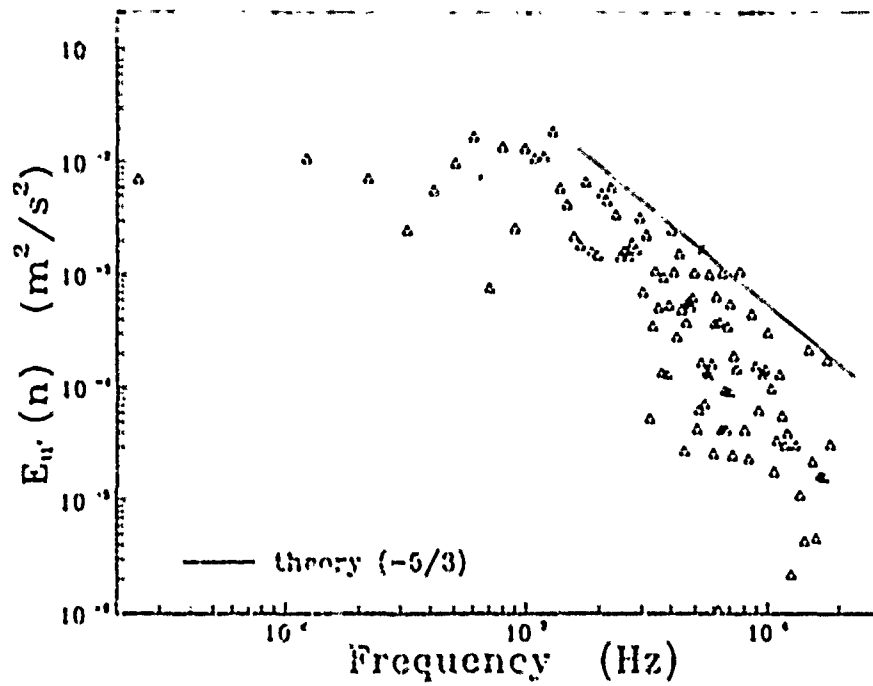
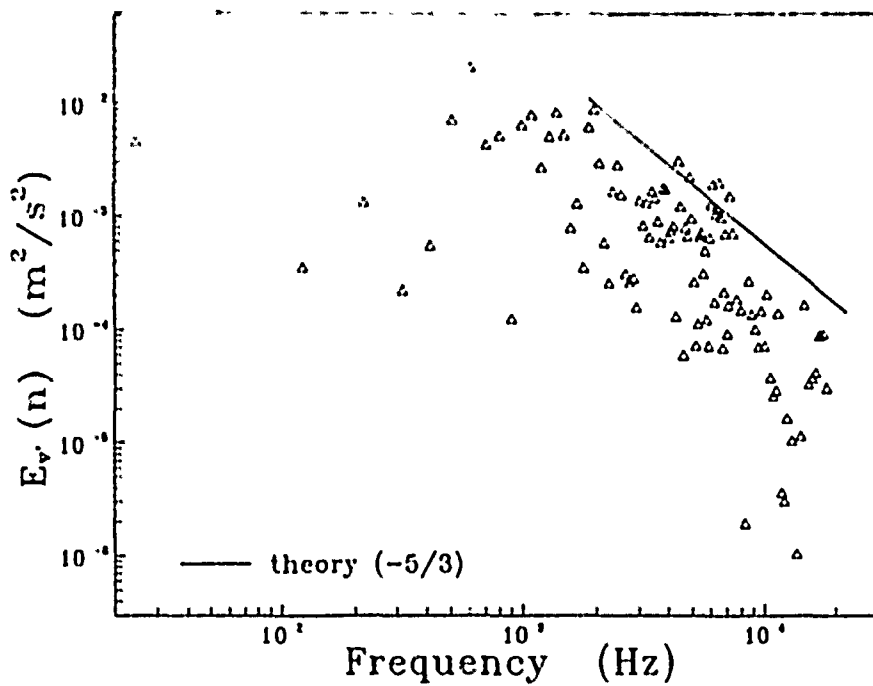Figure B.5. Turbulence energy spectrum for u'^2: Test A13
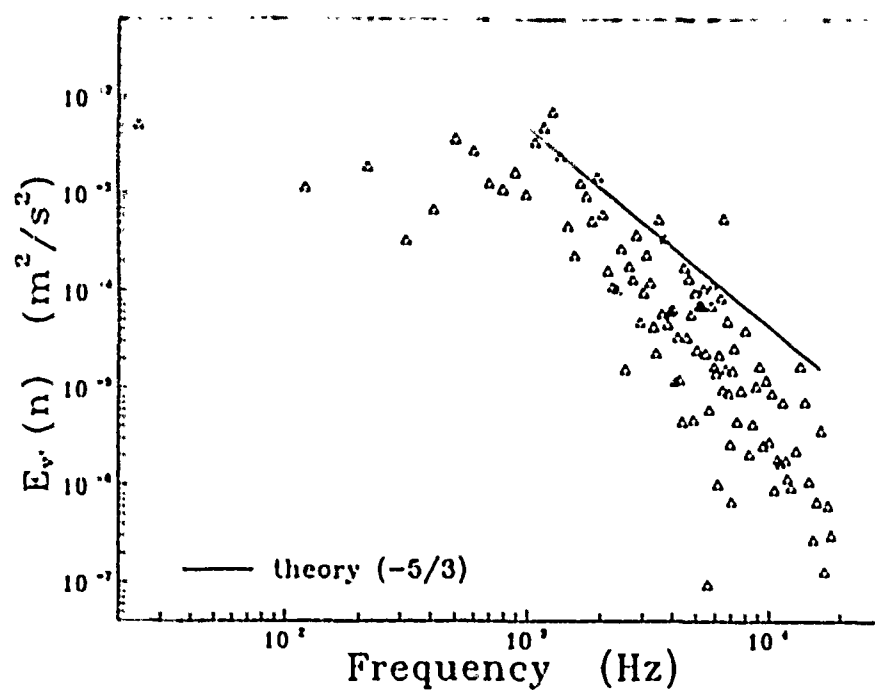
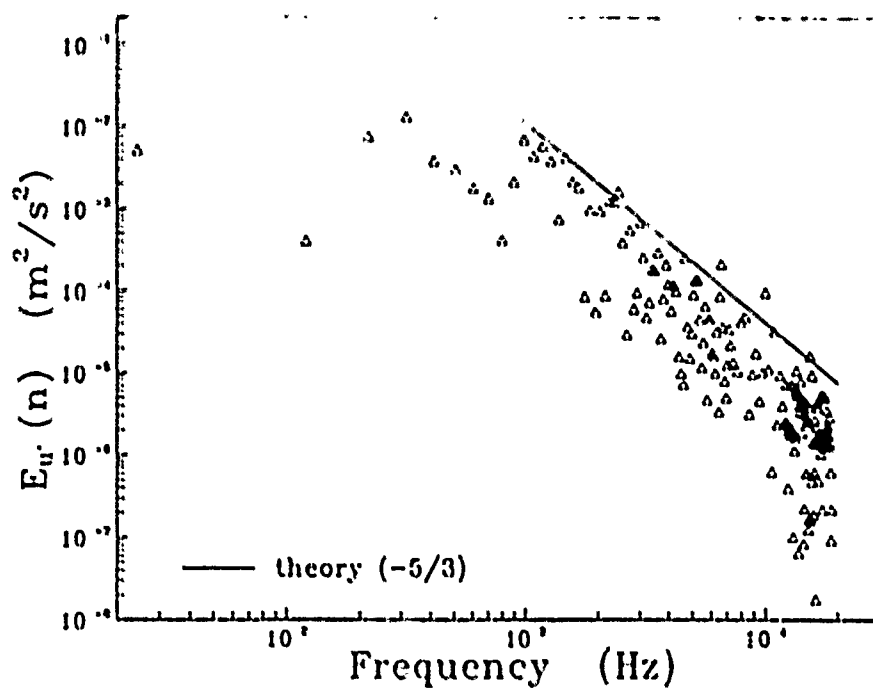Figure B.6. Turbulence energy spectrum for v'^2: Test A13
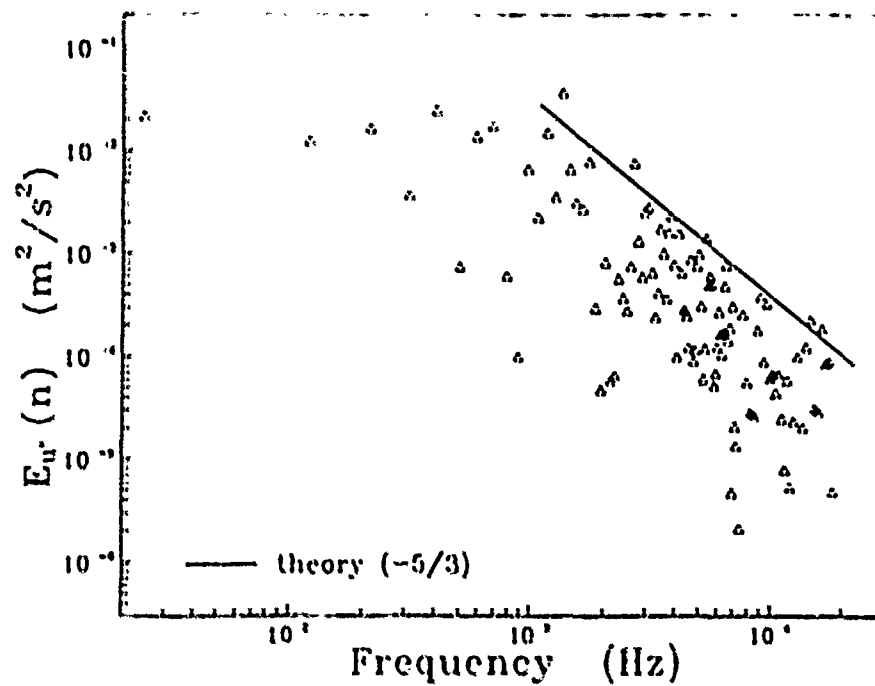
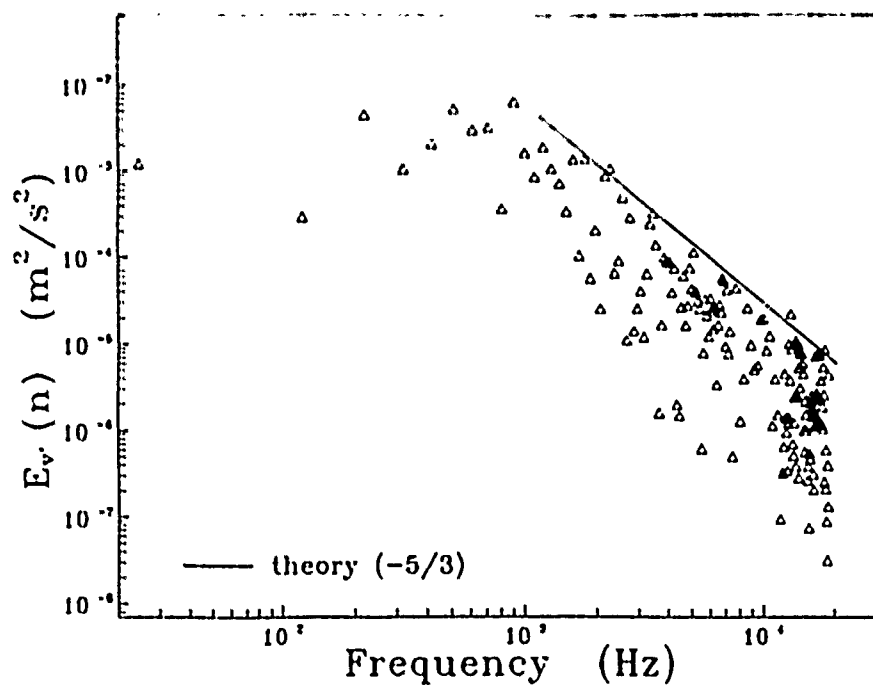Figure B.7. Turbulence energy spectrum for u'^2: Test A14
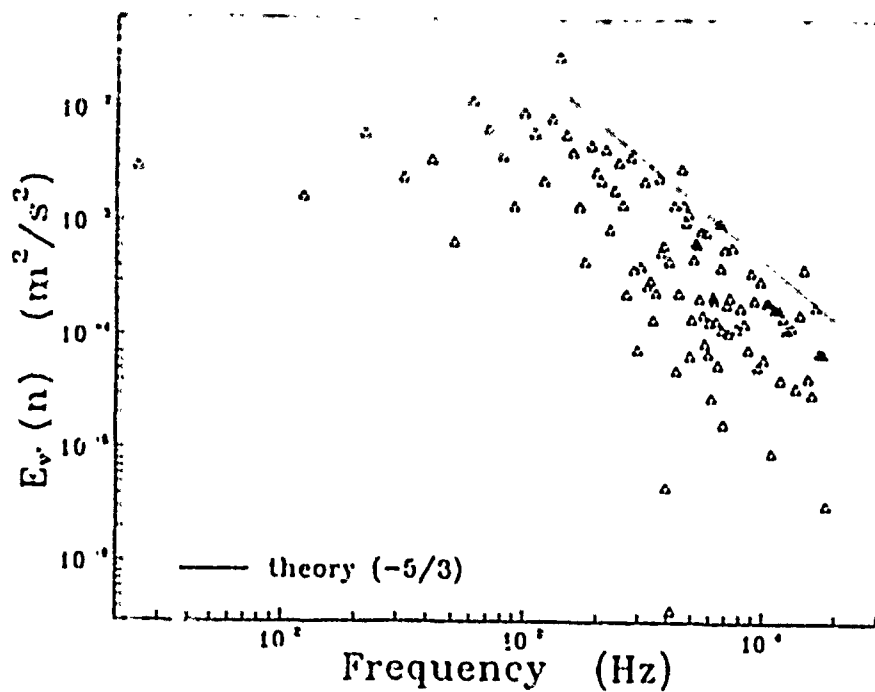
Figure B.8. Turbulence energy spectrum for v'^2: Test A14
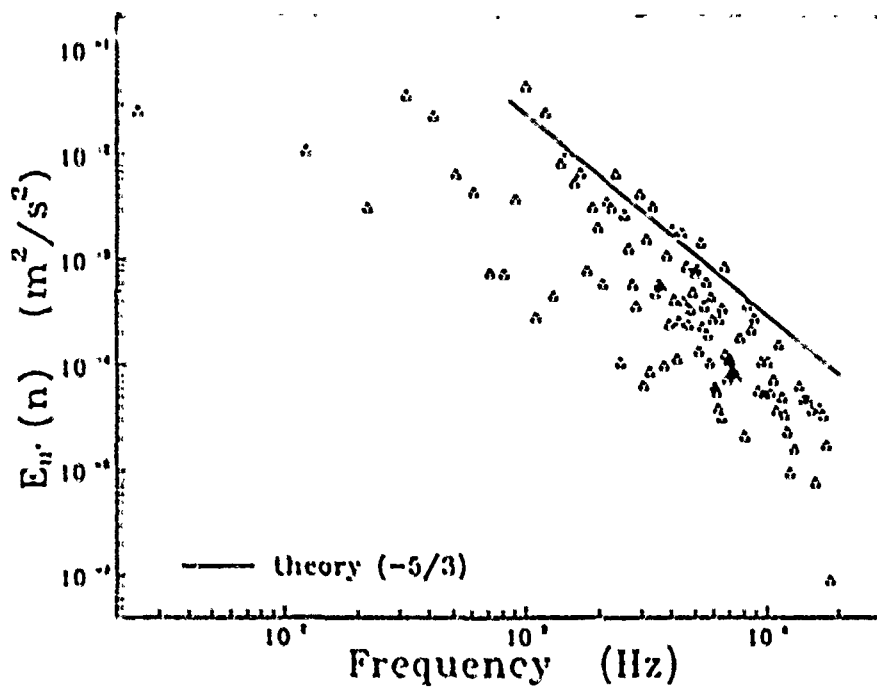
Figure B.9. Turbulence energy spectrum for u'^2: Test A15
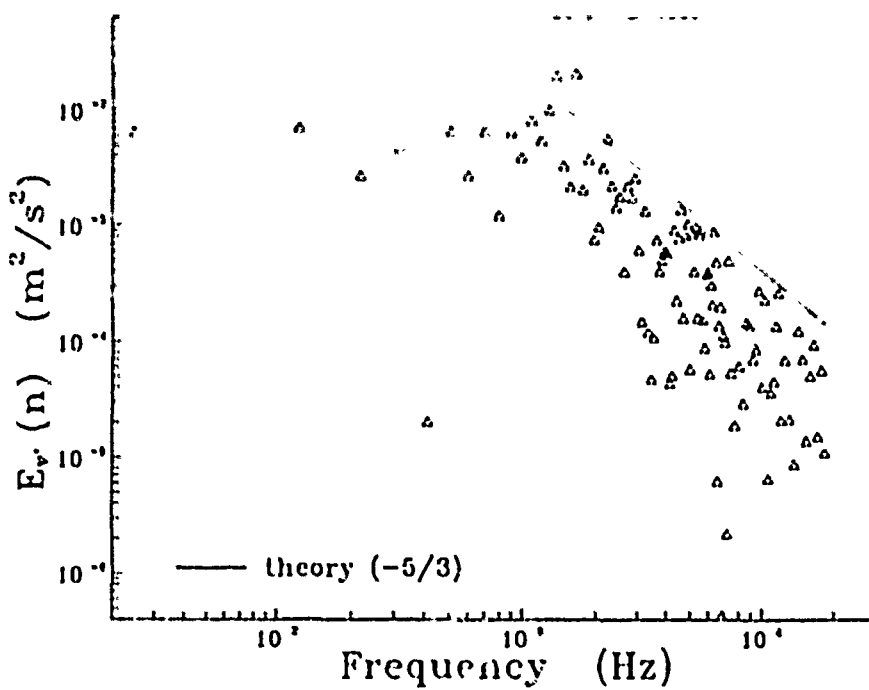
Figure B.10. Turbulence energy spectrum for v'^2: Test A15
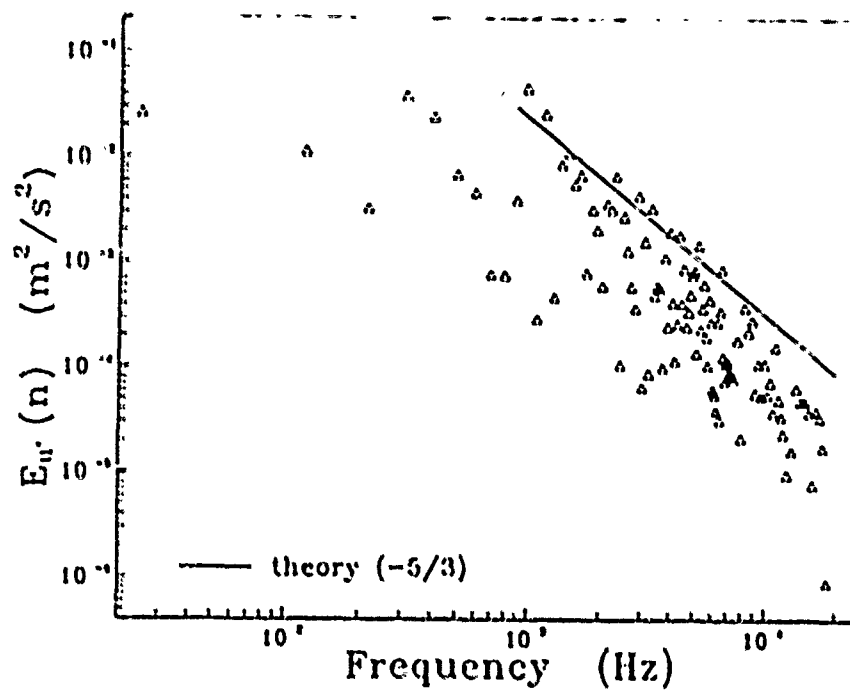
Figure B.11. Turbulence energy spectrum for u'^2: Test A21
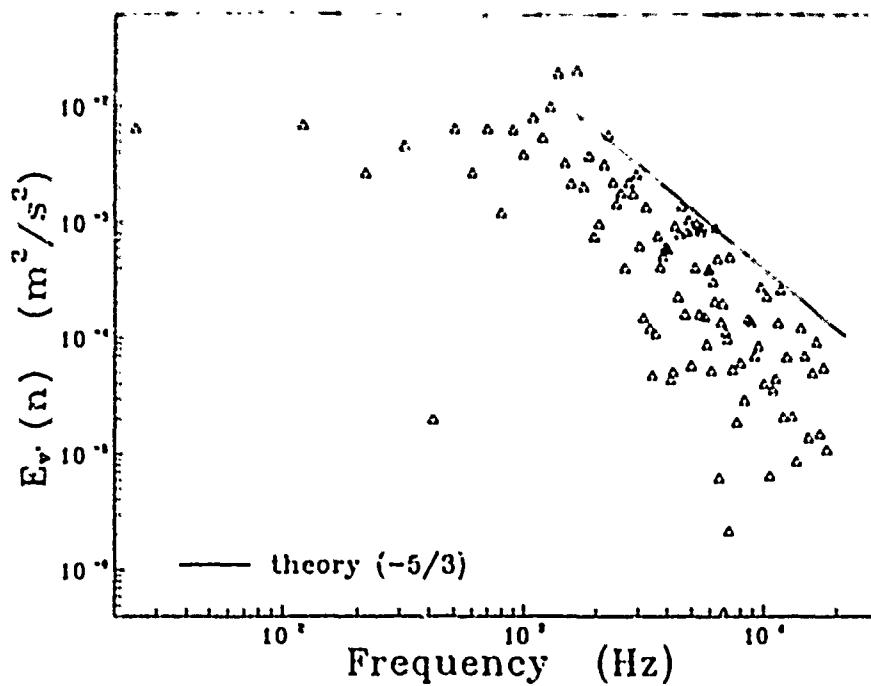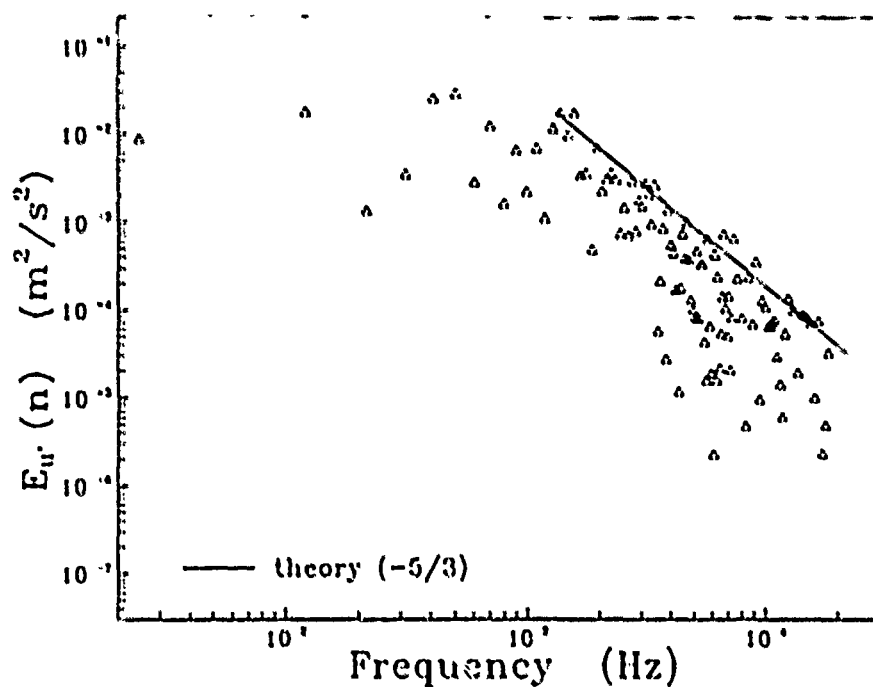

Figure B.12. Turbulence energy spectrum for v'^2: Test A21
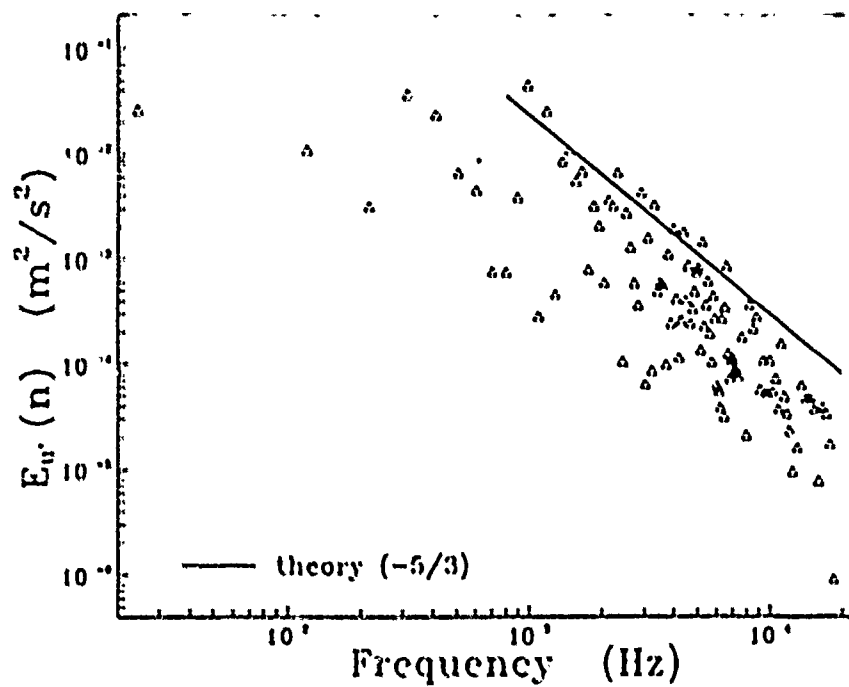
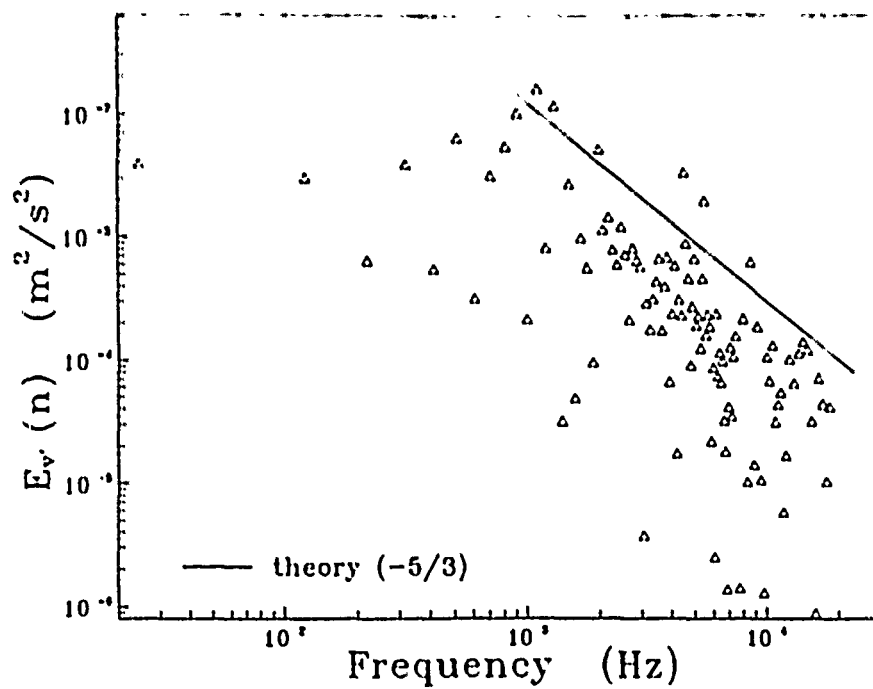Figure B.13. Turbulence energy spectrum for u'^2: Test A22
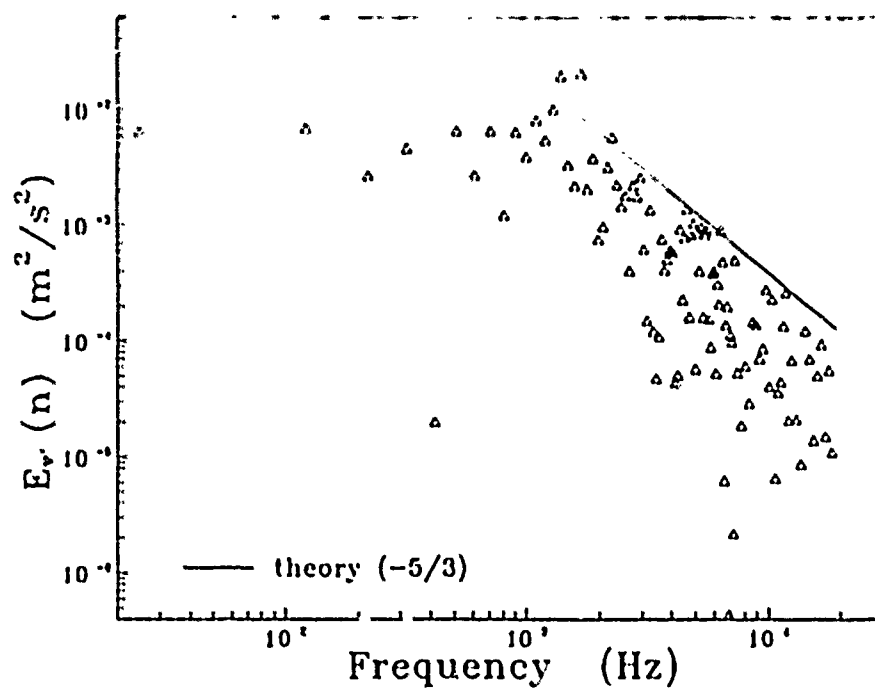
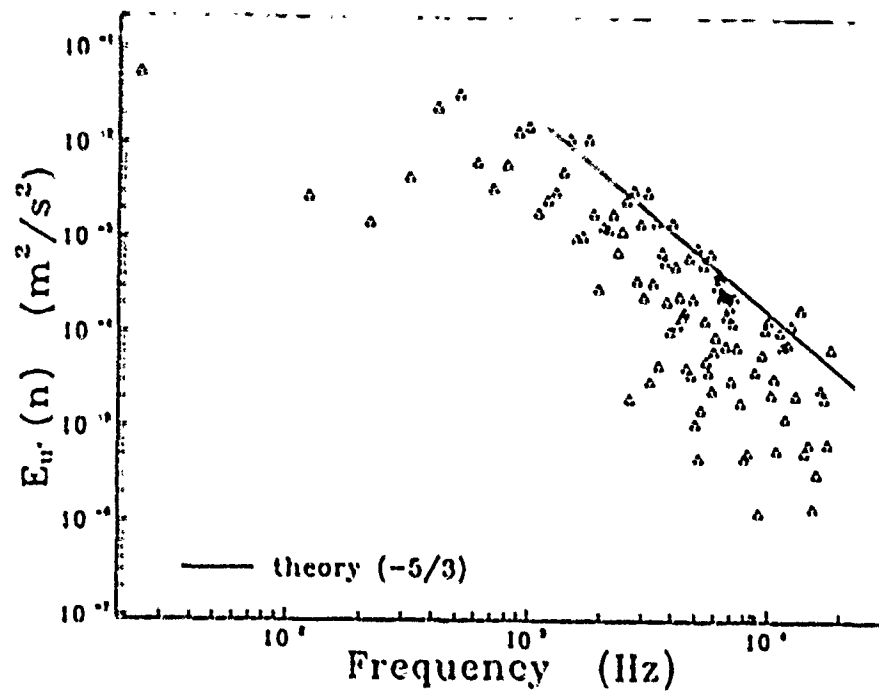Figure B.14. Turbulence energy spectrum for v'^2: Test A22

Figure B.15. Turbulence energy spectrum for u'^2: Test A23

Figure B.16. Turbulence energy spectrum for v'^2: Test A23

Figure B.17. Turbulence energy spectrum for u'^2: Test A24

Figure B.18. Turbulence energy spectrum for v'^2: Test A24

Figure B.19. Turbulence energy spectrum for u'^2: Test A31

Figure B.20. Turbulence energy spectrum for v'^2: Test A31

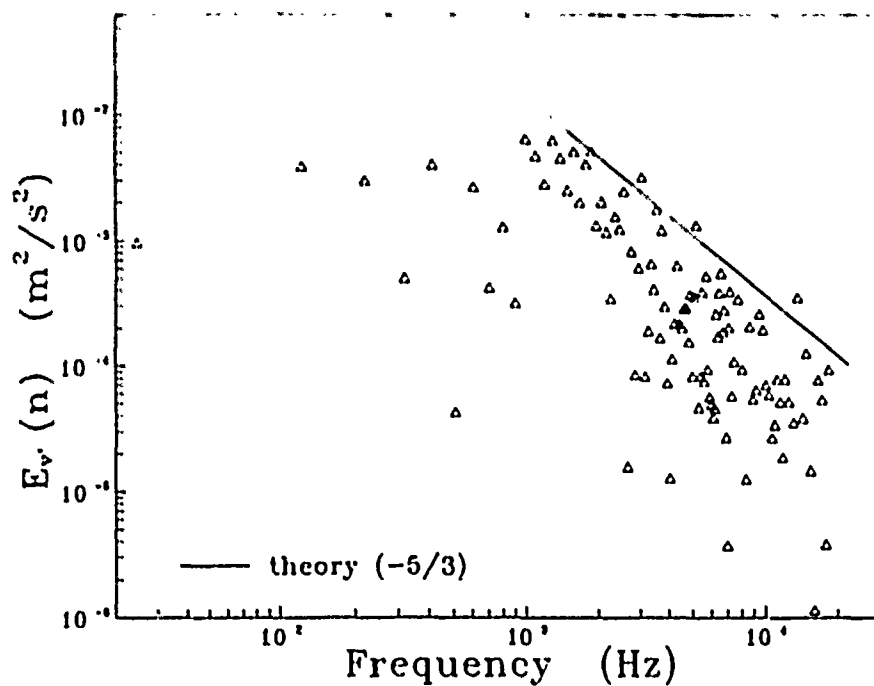Figure B.21. Turbulence energy spectrum for u'^2: Test A32

Figure B.22. Turbulence energy spectrum for v'^2: Test A32

Figure B.23. Turbulence energy spectrum for u'^2: Test A33

Figure B.24. Turbulence energy spectrum for v'^2: Test A33

B-13

Figure B.25. Turbulence energy spectrum for u'^2: Test A34

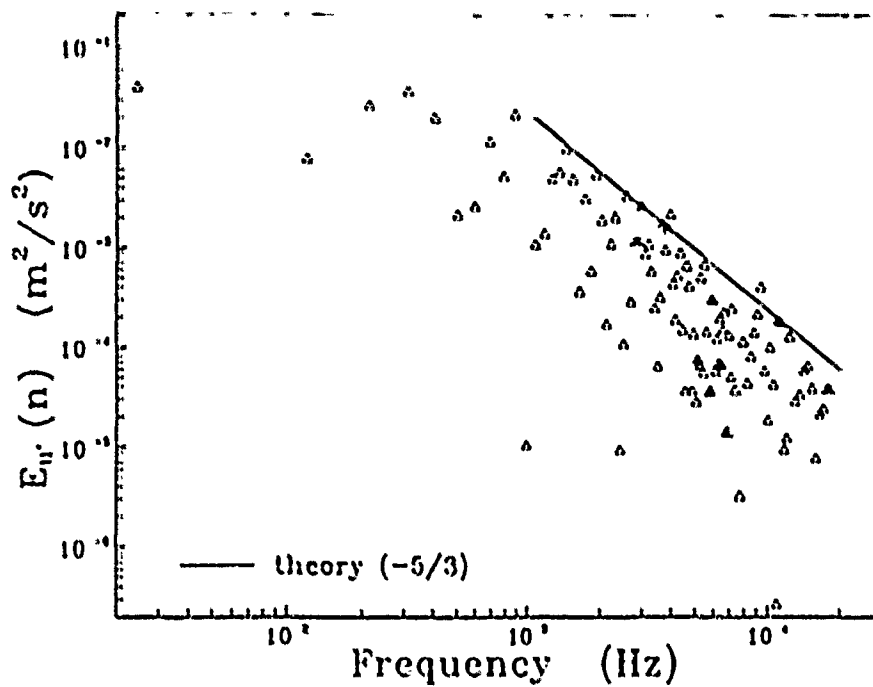Figure B.26. Turbulence energy spectrum for v'^2: Test A34

Figure B.27. Turbulence energy spectrum for u'^2: Test B11

Figure B.28. Turbulence energy spectrum for v'^2: Test B11

Figure B.29. Turbulence energy spectrum for u'^2: Test B12

Figure B.30. Turbulence energy spectrum for v'^2: Test B12

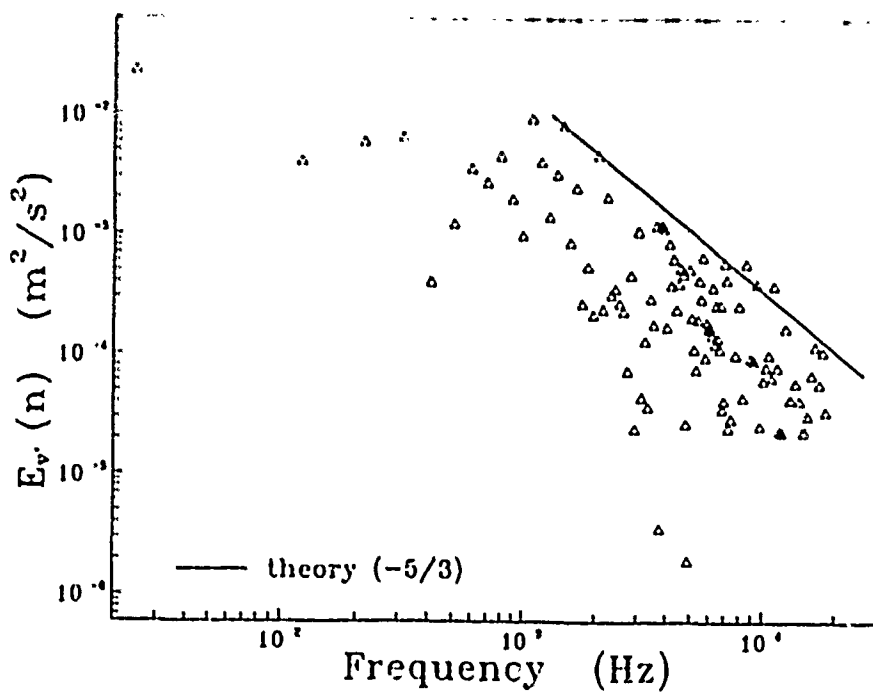Figure B.31. Turbulence energy spectrum for u'^2: Test B13

Figure B.32. Turbulence energy spectrum for v'^2: Test B13

Figure B.33. Turbulence energy spectrum for u'^2: Test B14

Figure B.34. Turbulence energy spectrum for v'^2: Test B14
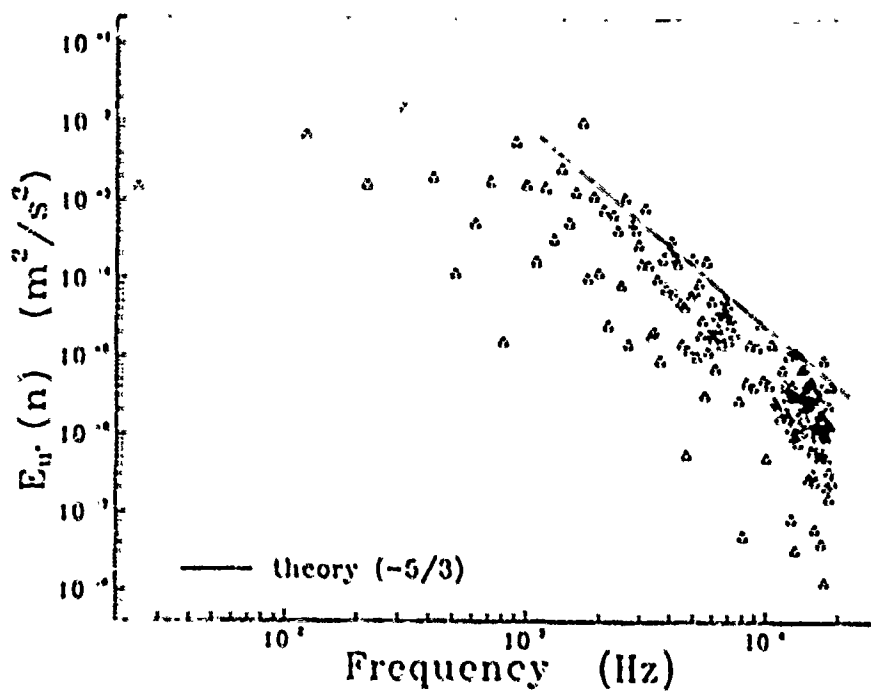
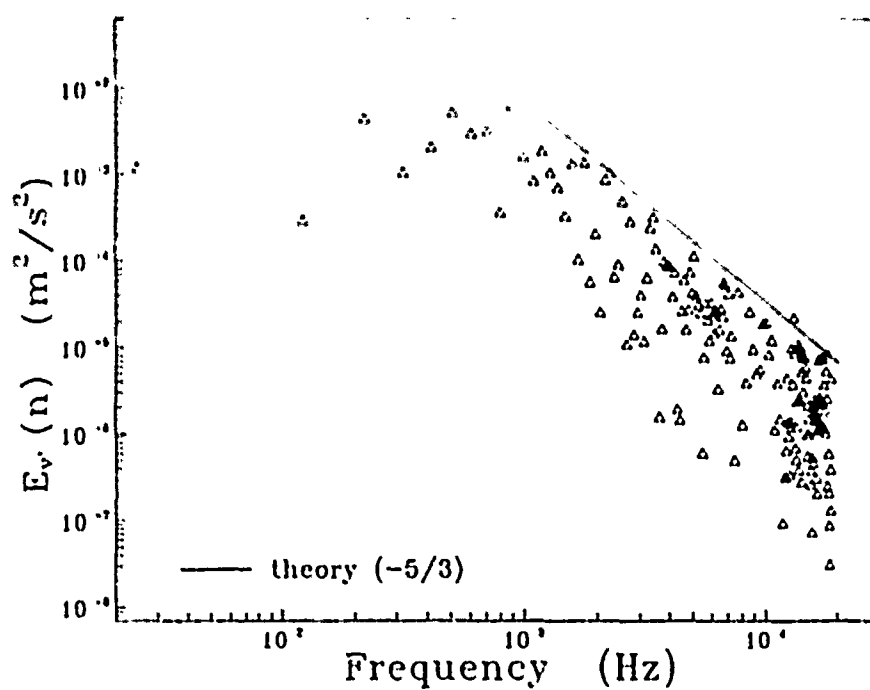Figure B.35. Turbulence energy spectrum for u'^2: Test B21

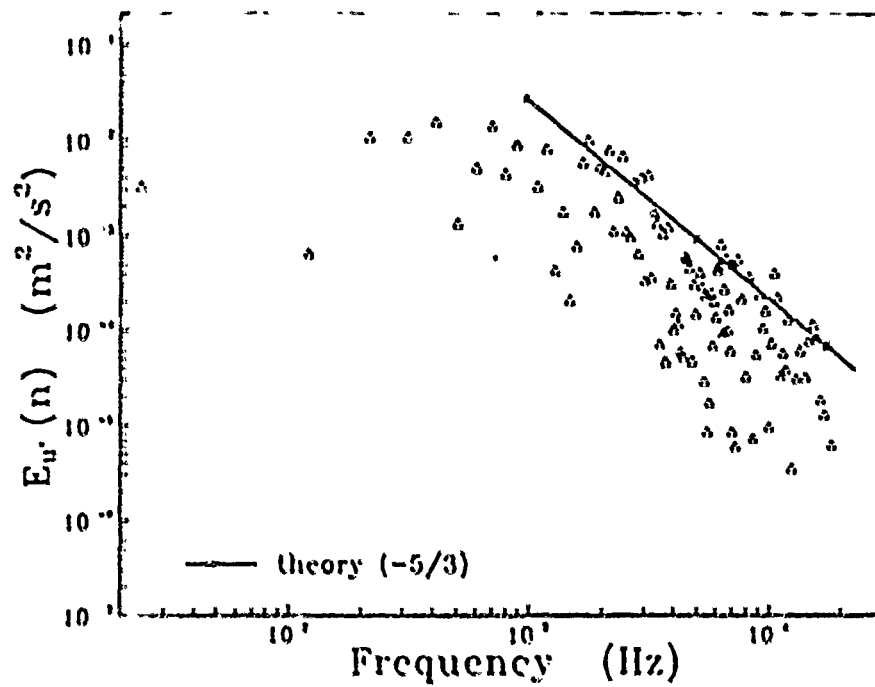Figure B.36. Turbulence energy spectrum for v'^2: Test B21

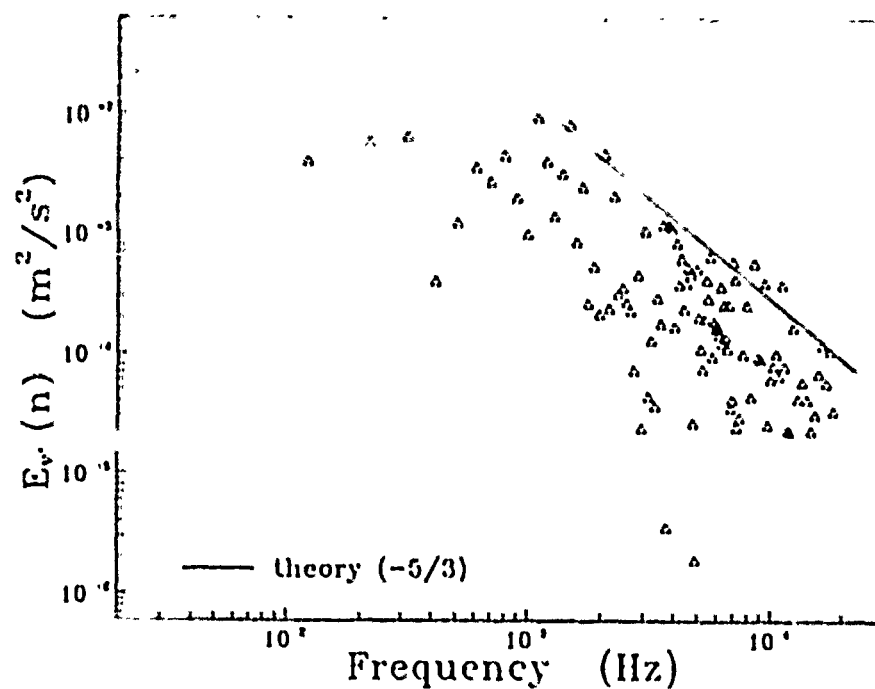Figure B.37. Turbulence energy spectrum for u'^2: Test B22

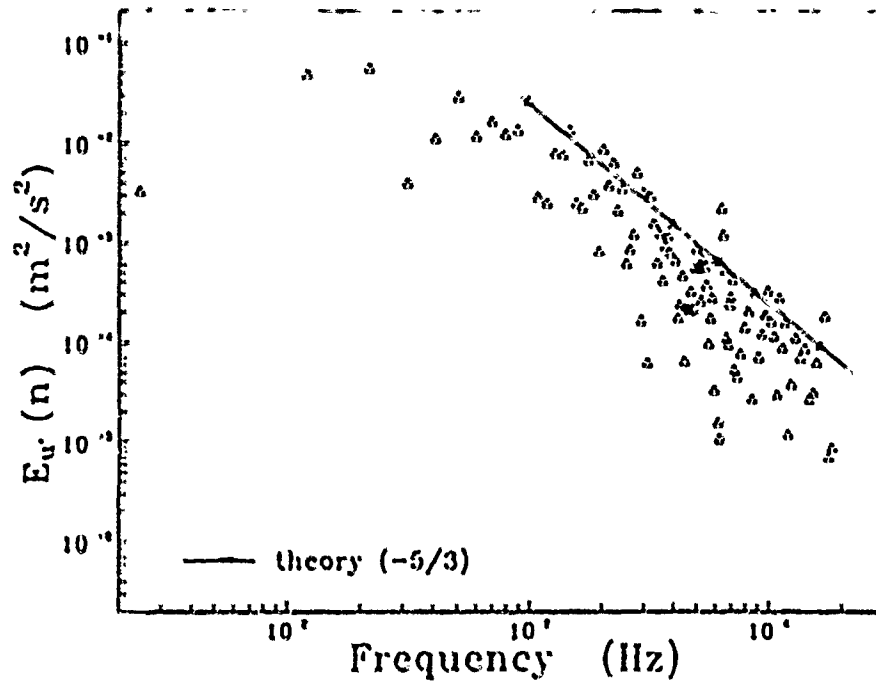Figure B.38. Turbulence energy spectrum for v'^2: Test B22

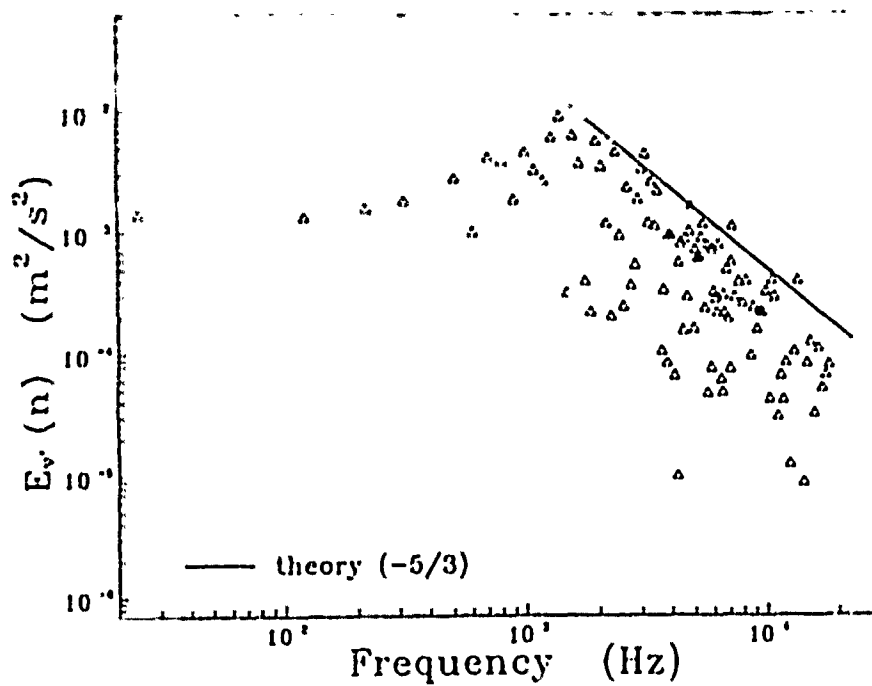Figure B.39. Turbulence energy spectrum for u'^2: Test B23

Figure B.40. Turbulence energy spectrum for v'^2: Test B23

B-21

Figure B.41. Turbulence energy spectrum for u'^2: Test B24

Figure B.42. Turbulence energy spectrum for v'^2: Test B24

Figure B.43. Turbulence energy spectrum for u'^2: Test B31

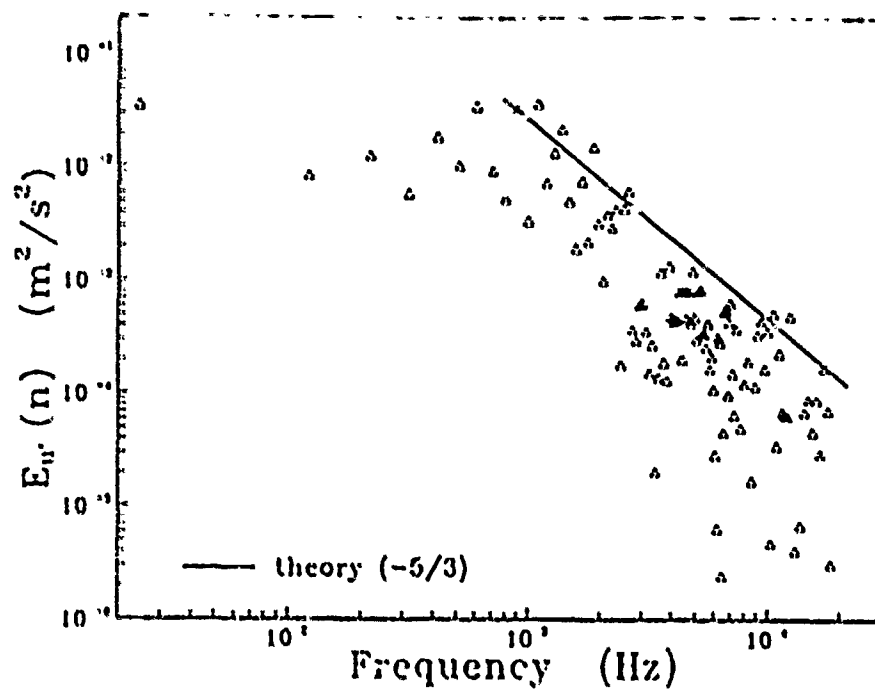Figure B.44. Turbulence energy spectrum for v'^2: Test B31

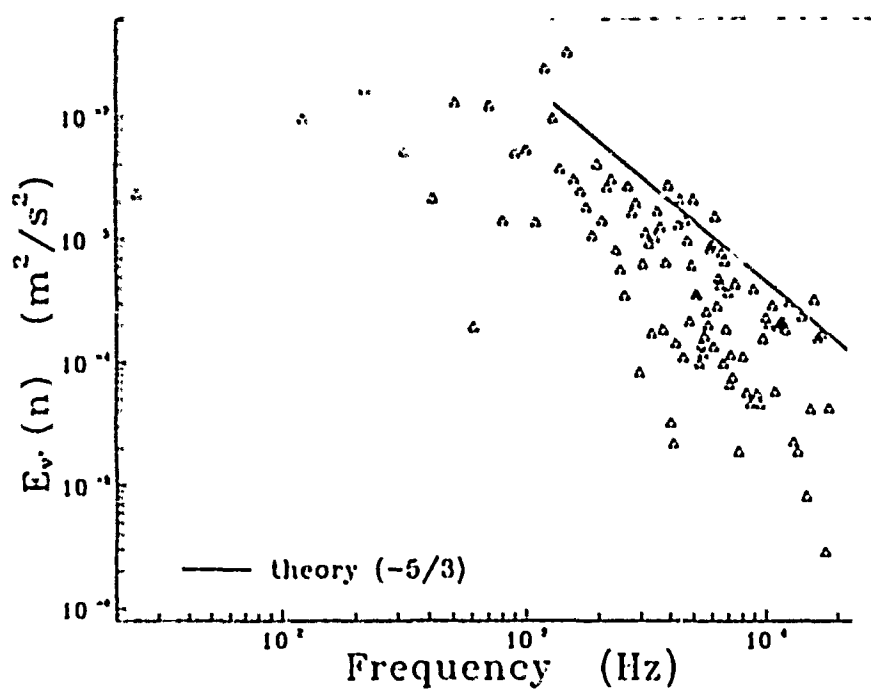Figure B.45. Turbulence energy spectrum for u'^2: Test B32

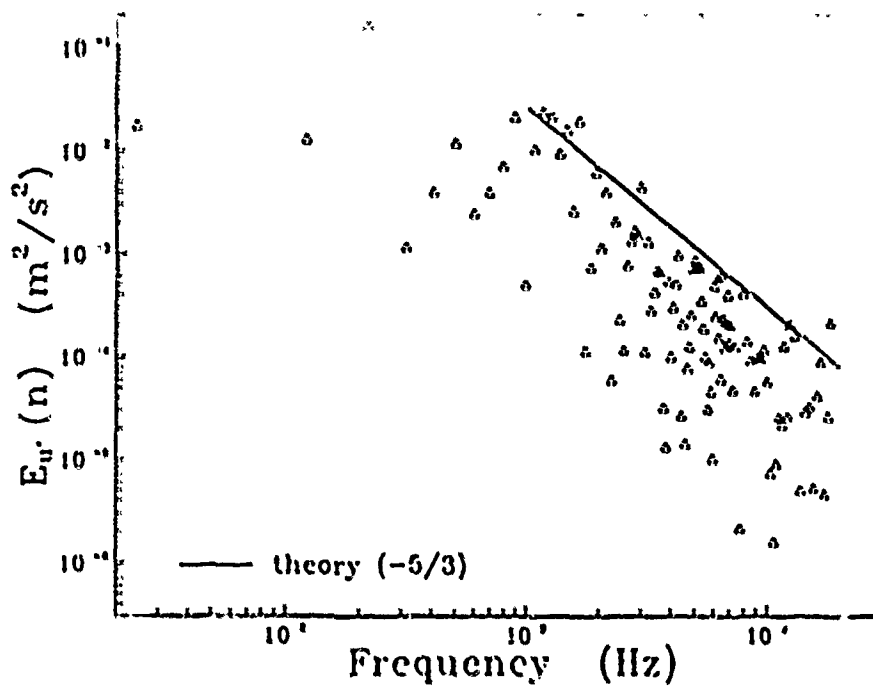Figure B.46. Turbulence energy spectrum for v'^2: Test B32

Figure B.47. Turbulence energy spectrum for u'^2: Test B33

Figure B.48. Turbulence energy spectrum for v'^2: Test B33

Figure B.49. Turbulence energy spectrum for u'^2: Test B34

Figure B.50. Turbulence energy spectrum for v'^2: Test B34

Figure B.51. Turbulence energy spectrum for u'^2: Test C11

Figure B.52. Turbulence energy spectrum for v'^2: Test C11

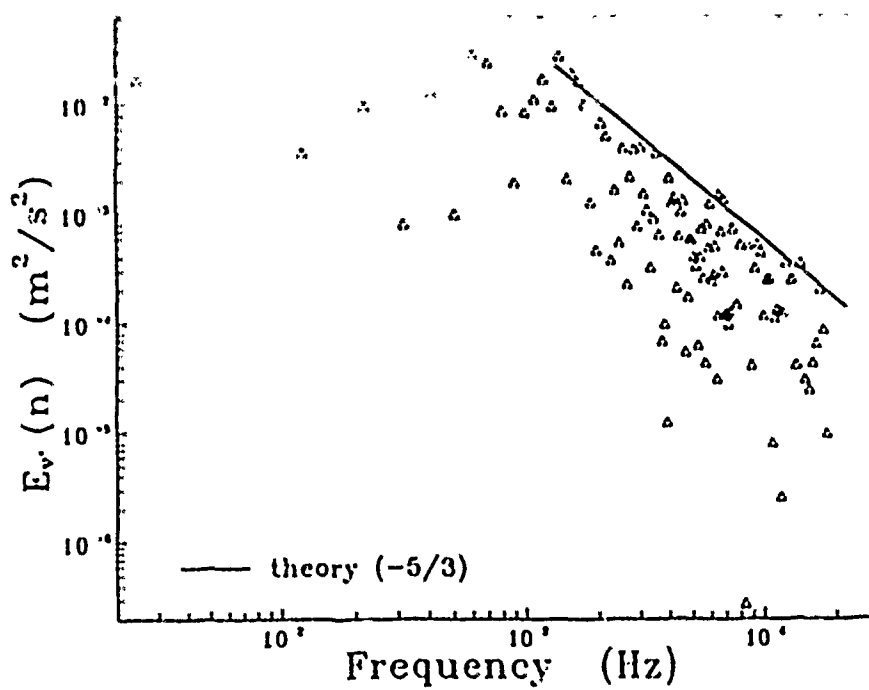Figure B.53. Turbulence energy spectrum for u'^2: Test C12

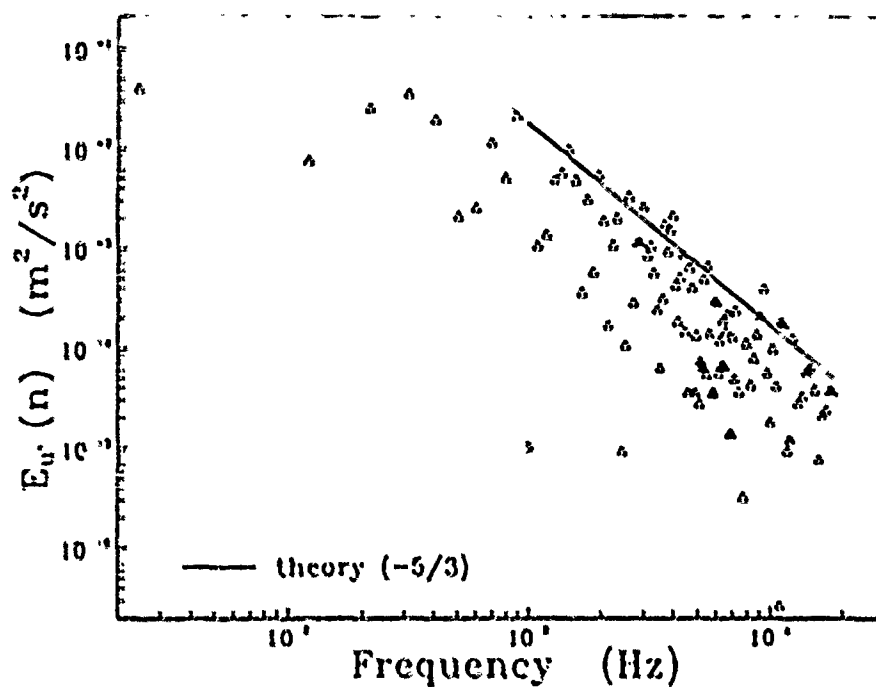Figure B.54. Turbulence energy spectrum for v'^2: Test C12

Figure B.55. Turbulence energy spectrum for u'^2: Test C13

Figure B.56. Turbulence energy spectrum for v'^2: Test C13

Figure B.57. Turbulence energy spectrum for u'^2: Test C14

Figure B.58. Turbulence energy spectrum for v'^2: Test C14

Figure B.59. Turbulence energy spectrum for u'^2: Test C21

Figure B.60. Turbulence energy spectrum for v'^2: Test C21

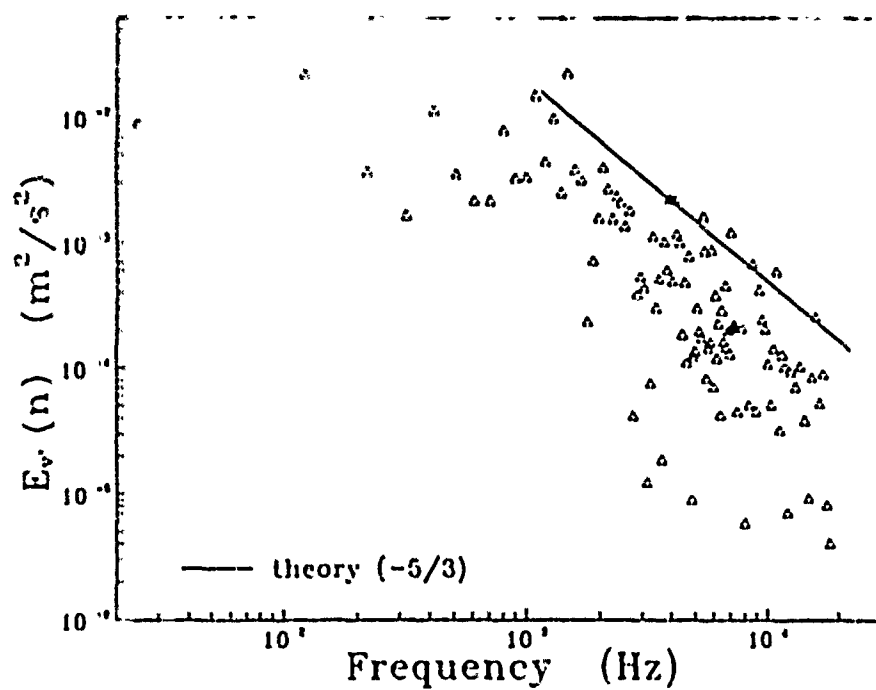Figure B.61. Turbulence energy spectrum for u'^2: Test C22

Figure B.62. Turbulence energy spectrum for v'^2: Test C22

Figure B.63. Turbulence energy spectrum for u'^2: Test C23

Figure B.64. Turbulence energy spectrum for v'^2: Test C23

Figure B.65. Turbulence energy spectrum for u'^2: Test C24

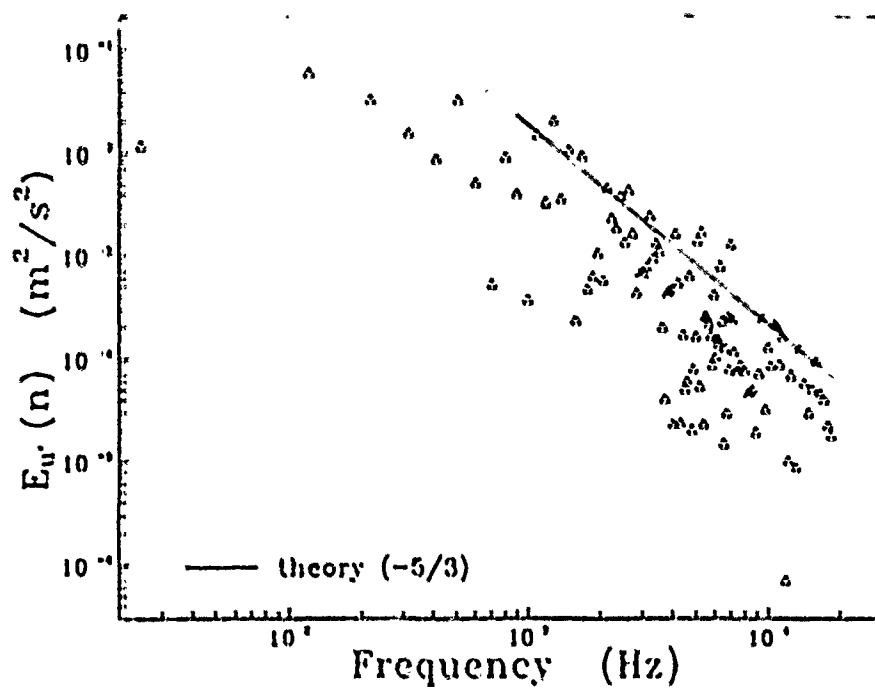Figure B.66. Turbulence energy spectrum for v'^2: Test C24

Figure B.67. Turbulence energy spectrum for u'^2: Test C31

Figure B.68. Turbulence energy spectrum for v'^2: Test C31

Figure B.69. Turbulence energy spectrum for u'^2: Test C32

Figure B.70. Turbulence energy spectrum for v'^2: Test C32

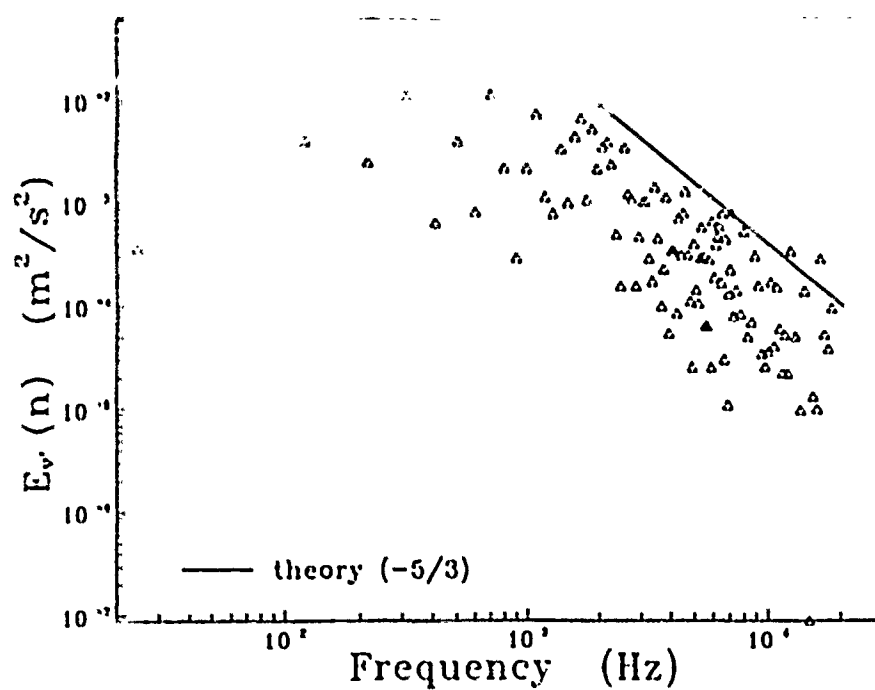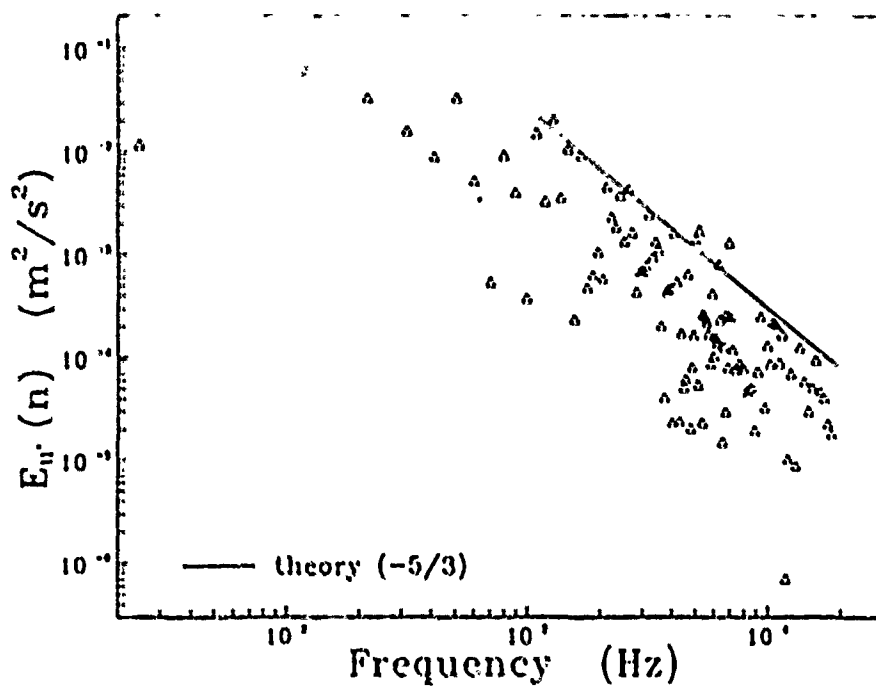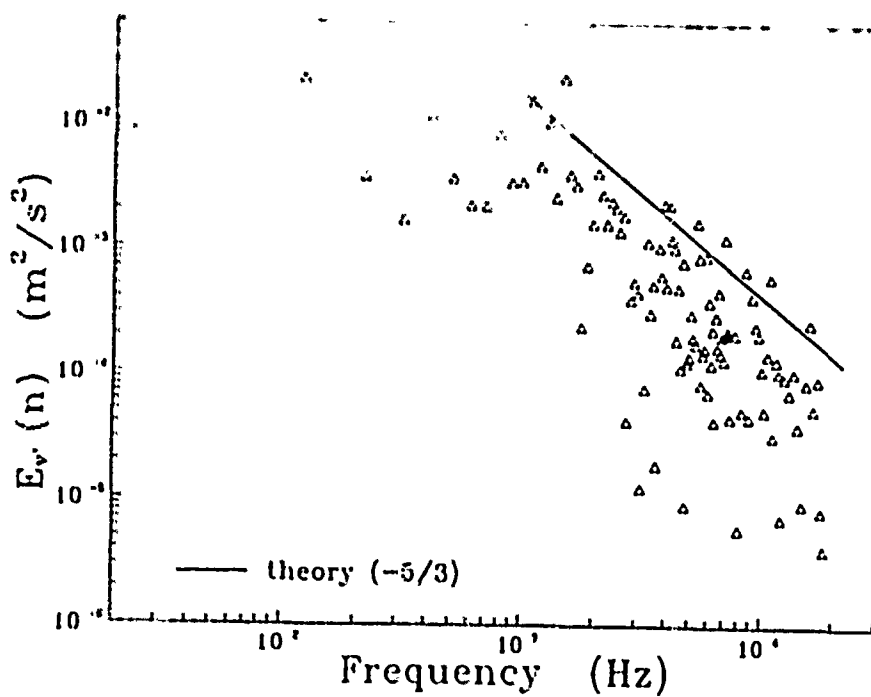Figure B.71. Turbulence energy spectrum for u'^2: Test C33

Figure B.72. Turbulence energy spectrum for v'^2: Test C33

Figure B.73. Turbulence energy spectrum for u'^2: Test C34

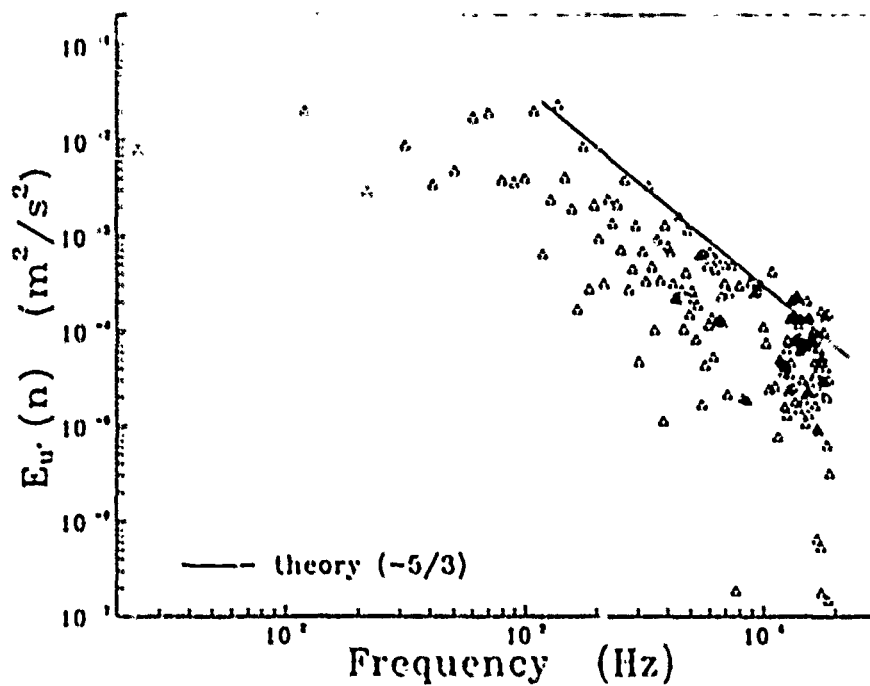Figure B.74. Turbulence energy spectrum for v'^2: Test C34

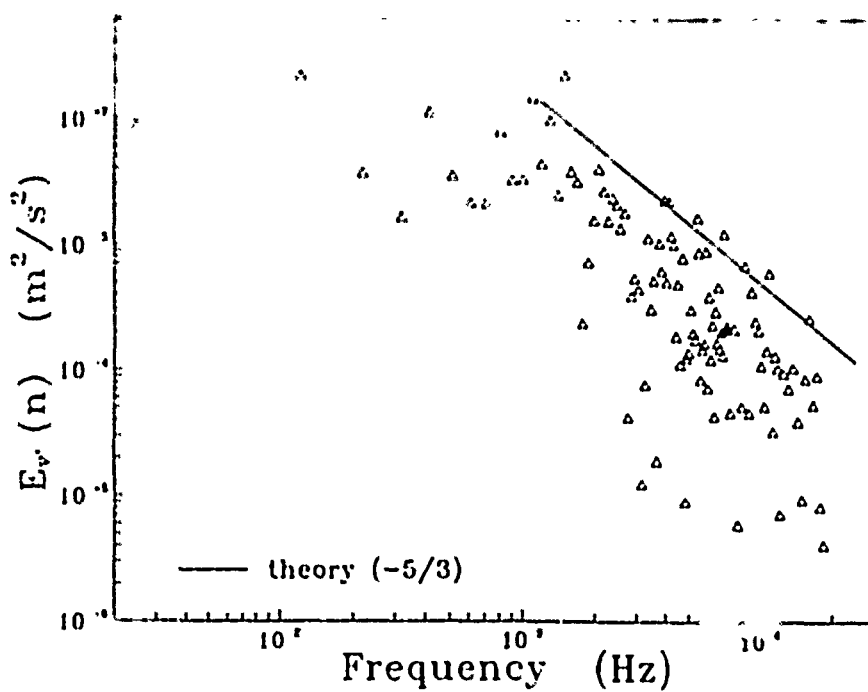Figure B.75. Turbulence energy spectrum for u'^2: Test D11

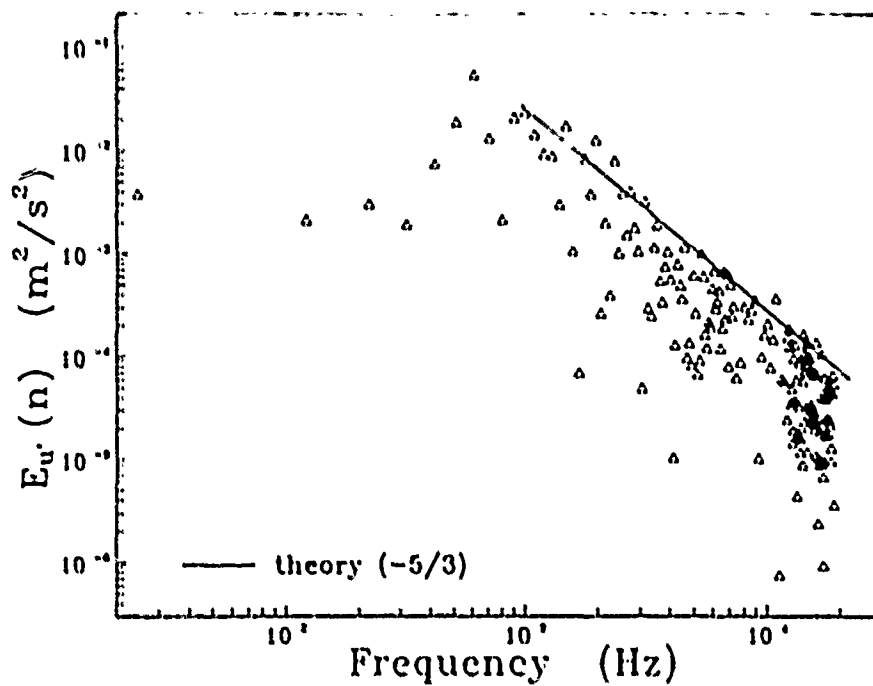Figure B.76. Turbulence energy spectrum for v'^2: Test D11

Figure B.77. Turbulence energy spectrum for u'^2: Test D12

Figure B.78. Turbulence energy spectrum for v'^2: Test D12

Figure B.79. Turbulence energy spectrum for u'^2: Test D13

Figure B.80. Turbulence energy spectrum for v'^2: Test D13
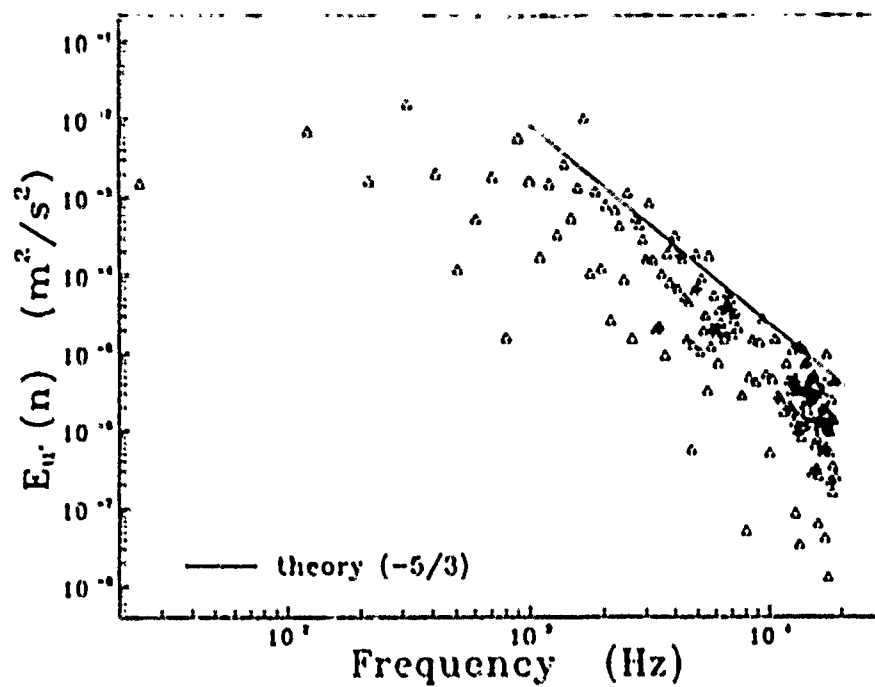
Figure B.81. Turbulence energy spectrum for u'^2: Test D21
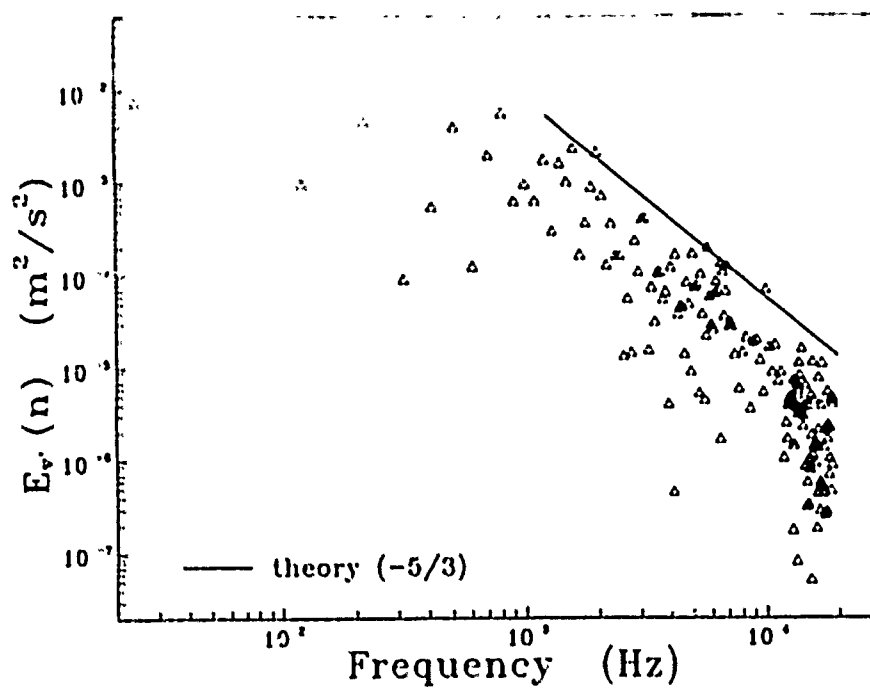
Figure B.82. Turbulence energy spectrum for v'^2: Test D21
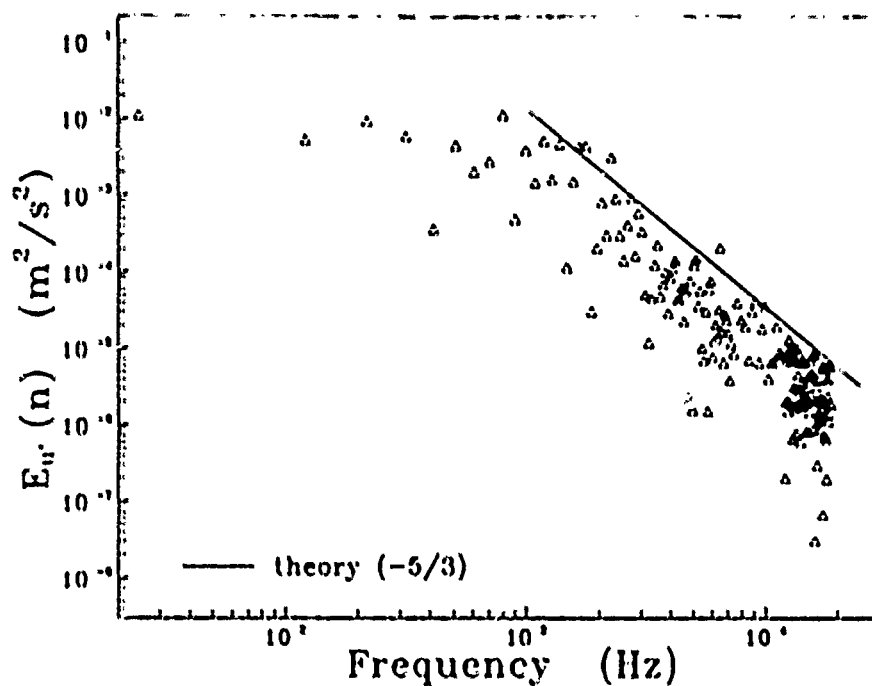
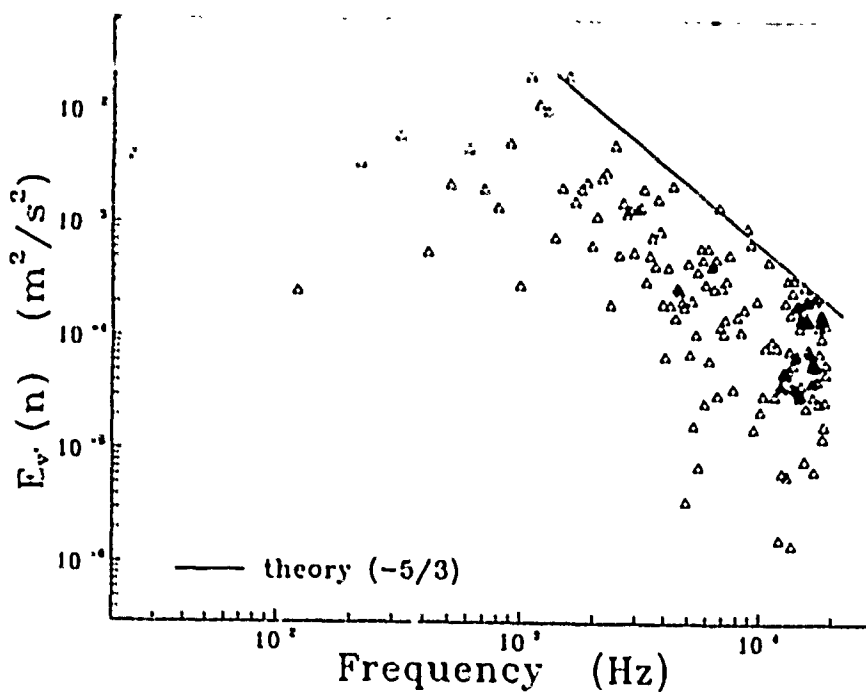Figure B.83. Turbulence energy spectrum for u'^2: Test D22
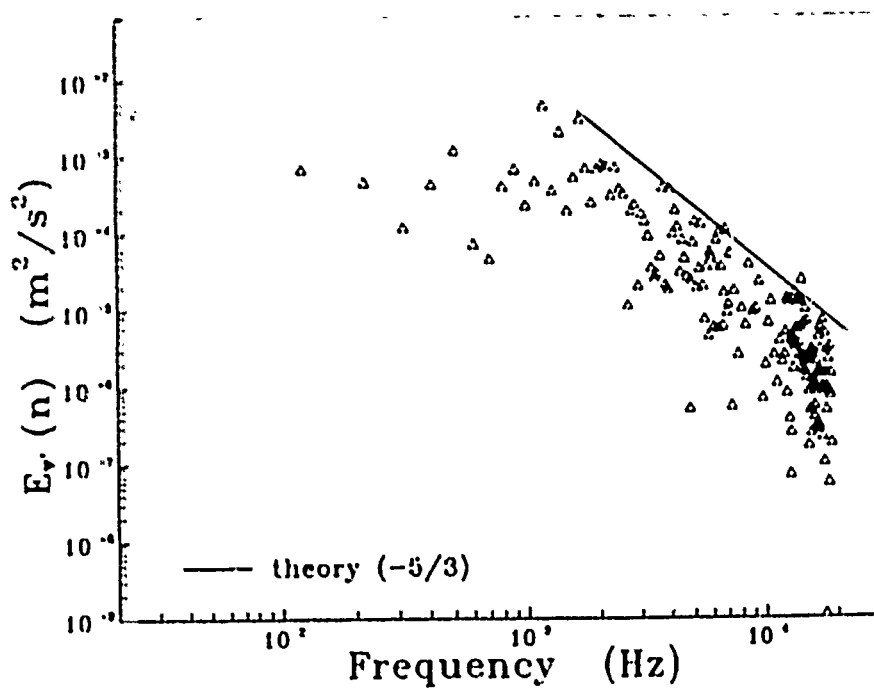
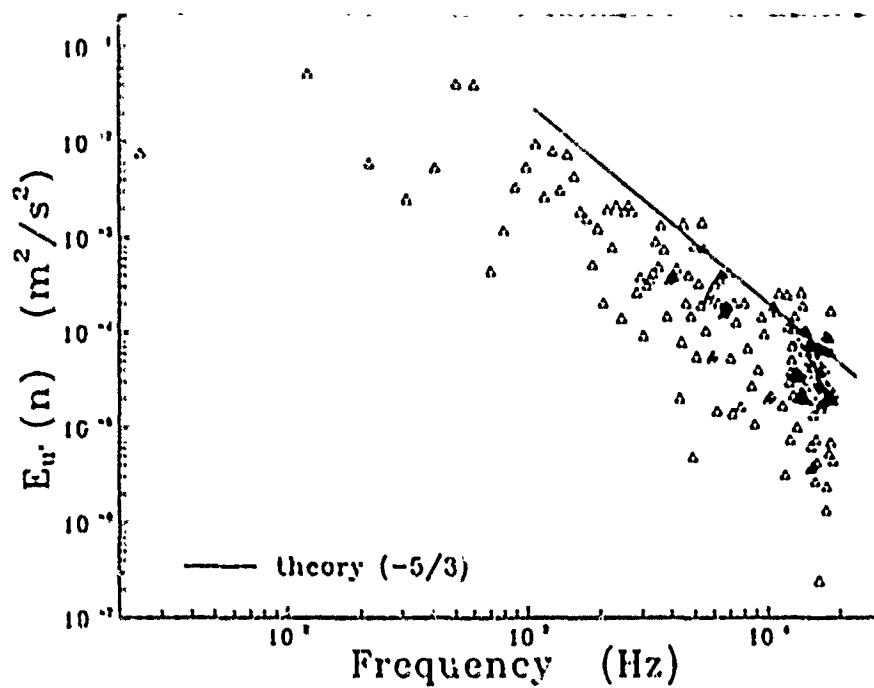Figure B.84. Turbulence energy spectrum for v'^2: Test D22
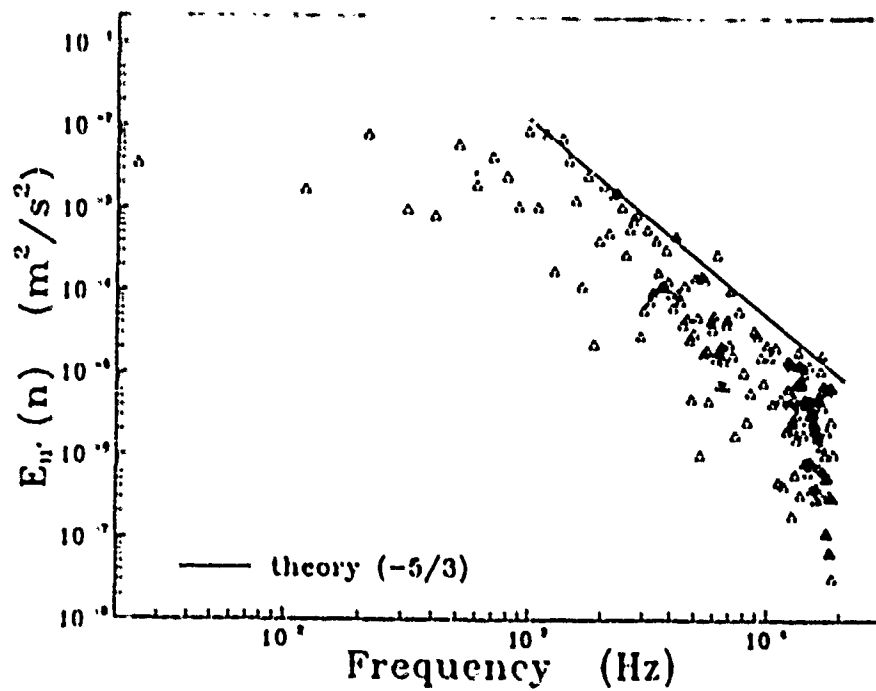
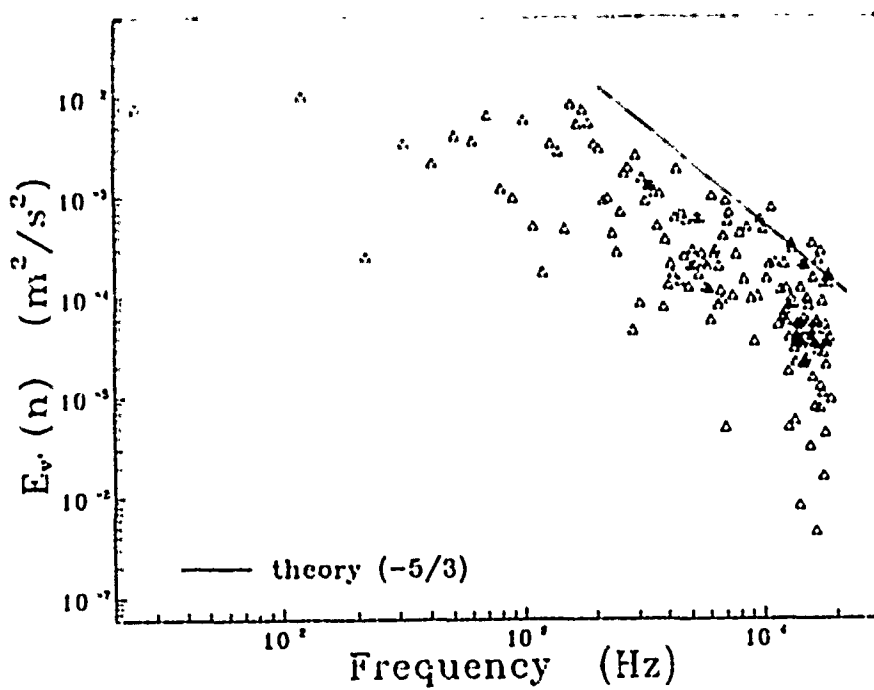Figure B.85. Turbulence energy spectrum for u'^2: Test D23
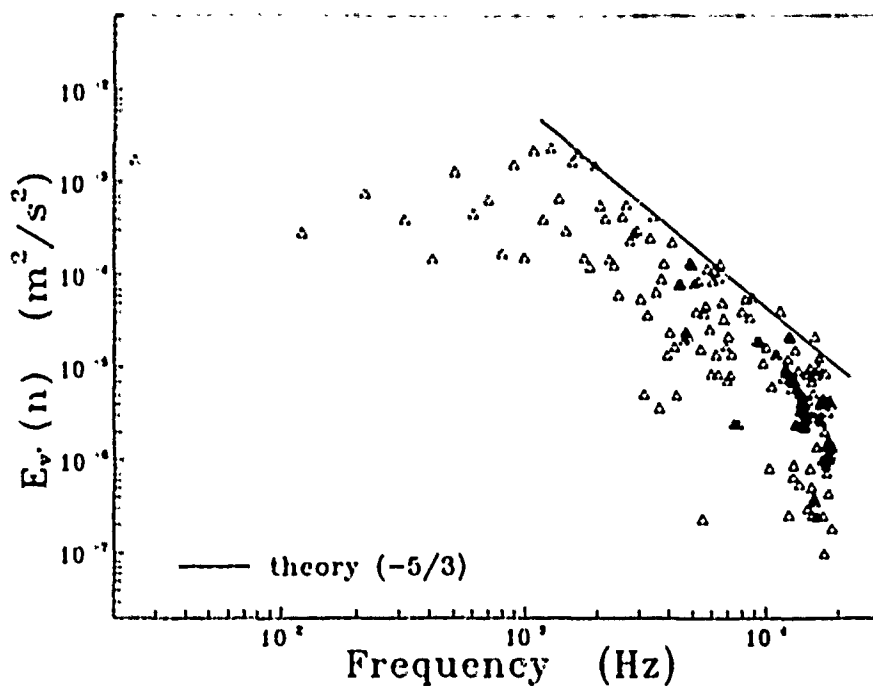
Figure B.86. Turbulence energy spectrum for v'^2: Test D23
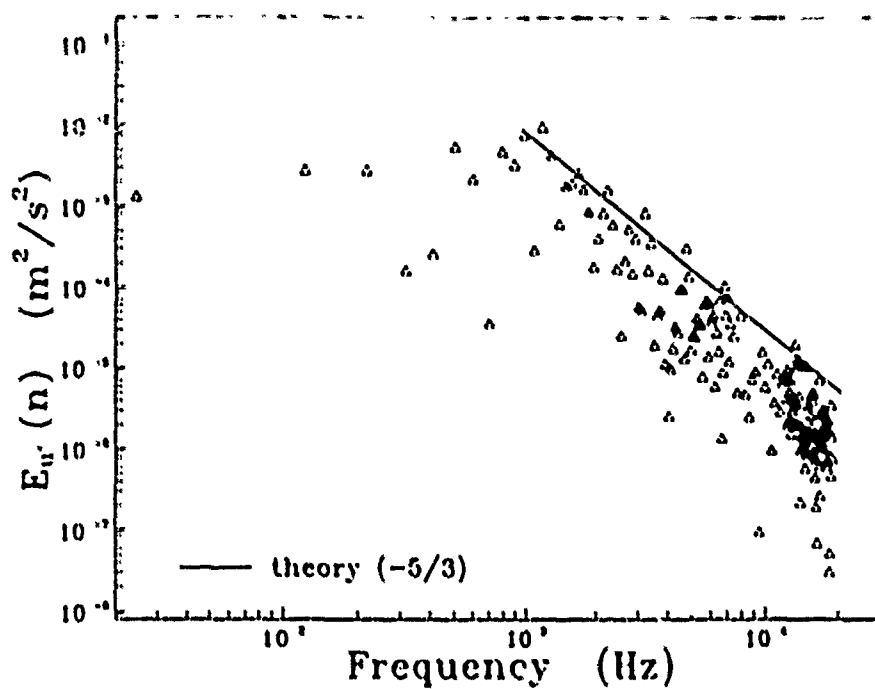
Figure B.87. Turbulence energy spectrum for u'^2: Test D31
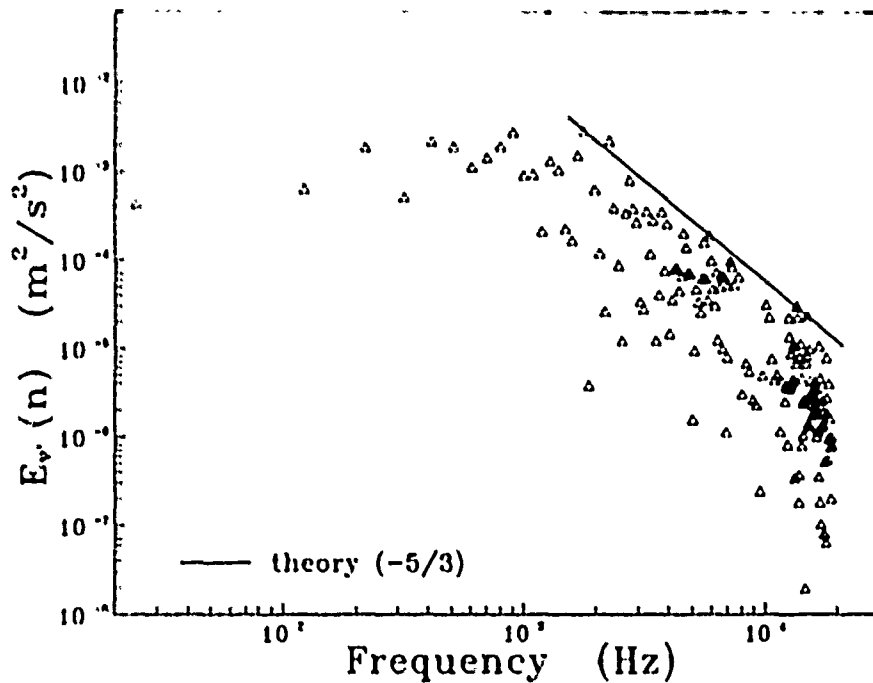
Figure B.88. Turbulence energy spectrum for v'^2: Test D31
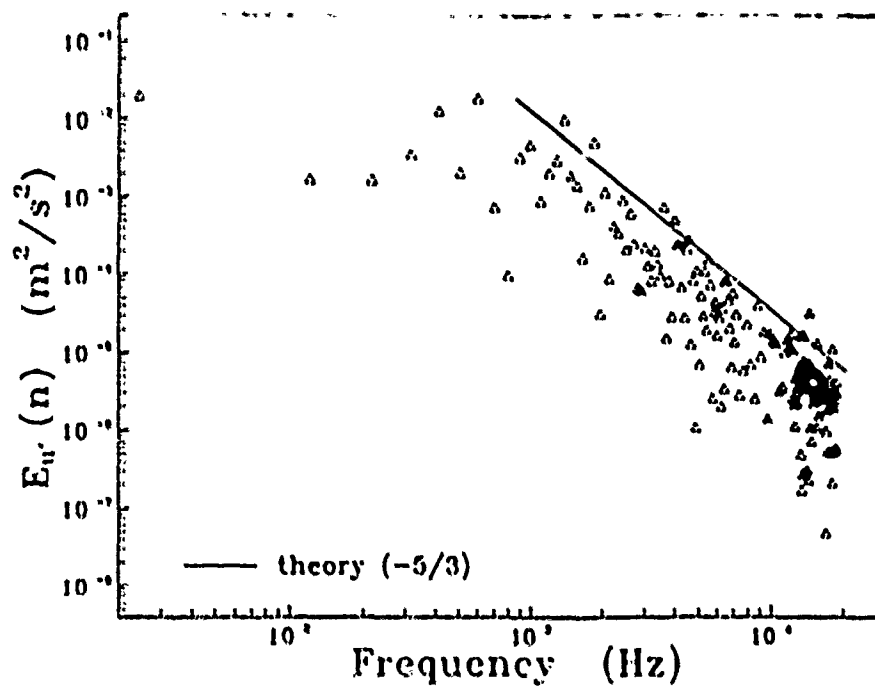
Figure B.89 Turbulence energy spectrum for u'^2: Test D32
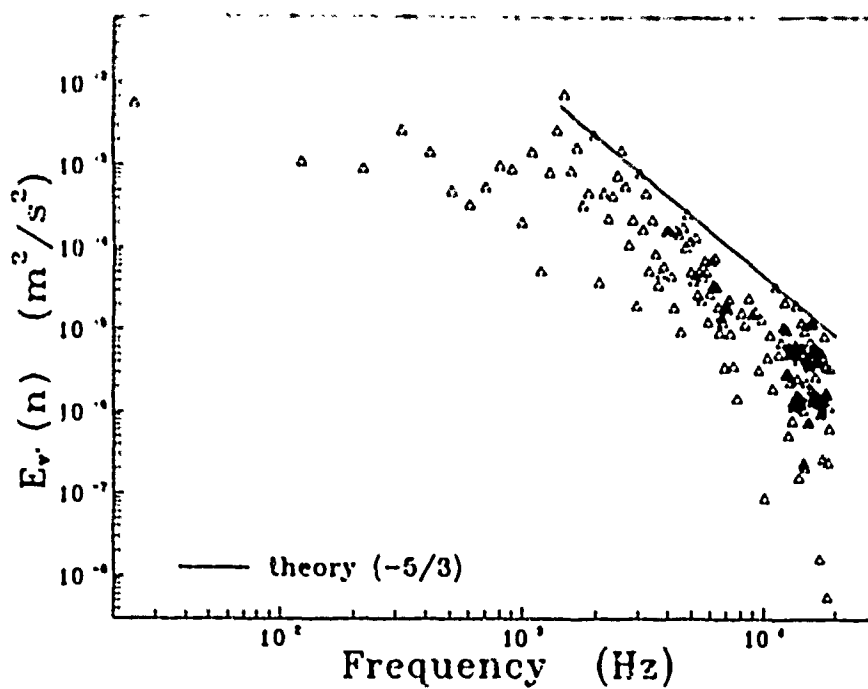
Figure B.90. Turbulence energy spectrum for v'^2: Test D32
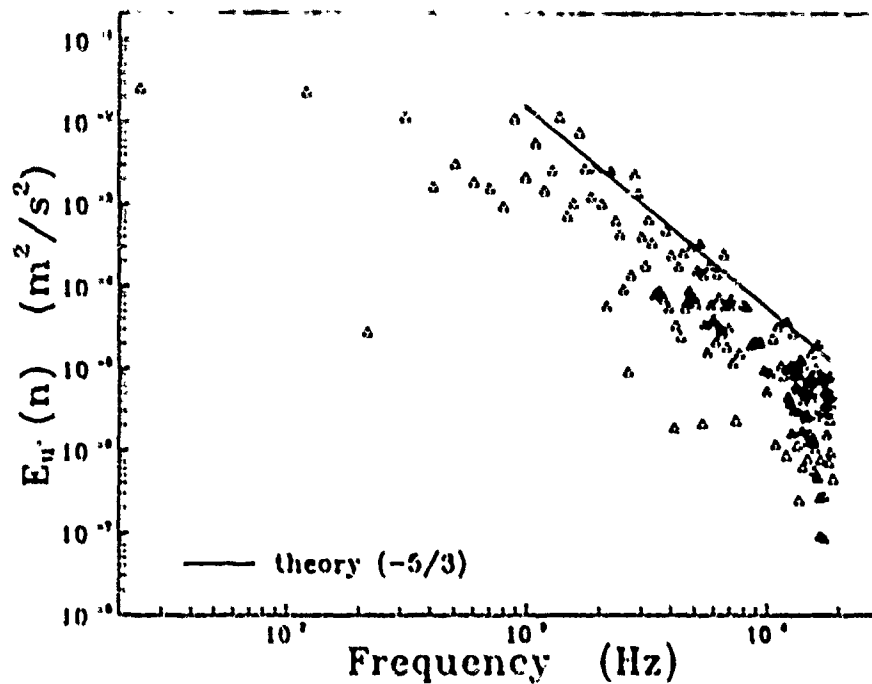
Figure B.91. Turbulence energy spectrum for u'^2: Test D33
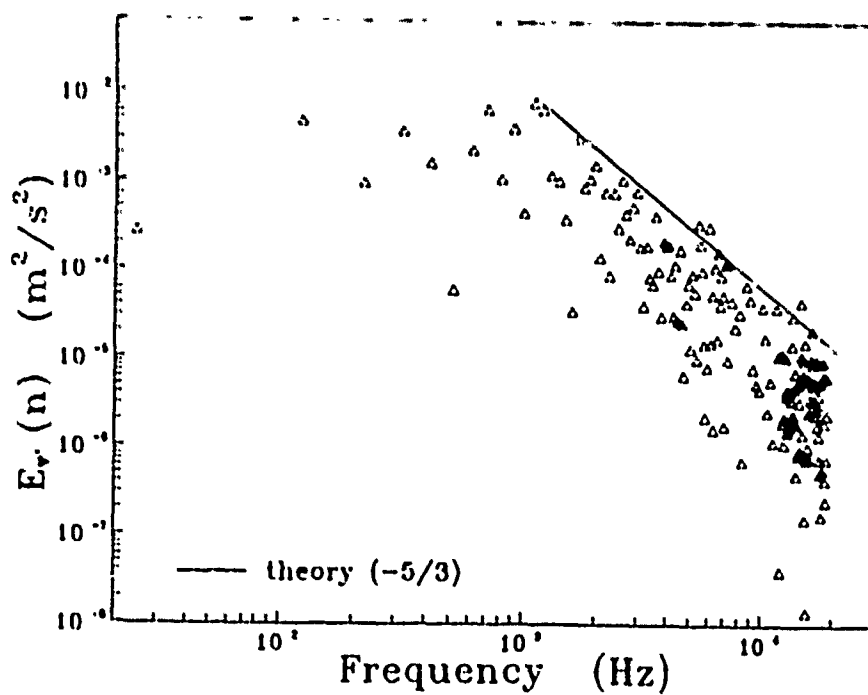
Figure B.92. Turbulence energy spectrum for v'^2: Test D33
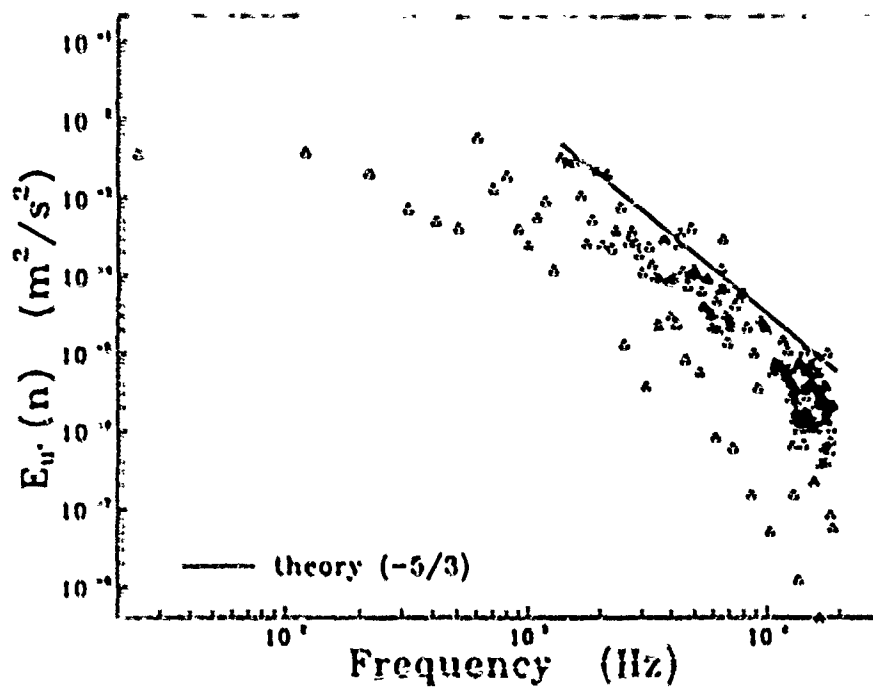
Figure B.93. Turbulence energy spectrum for u'^2: Test E11
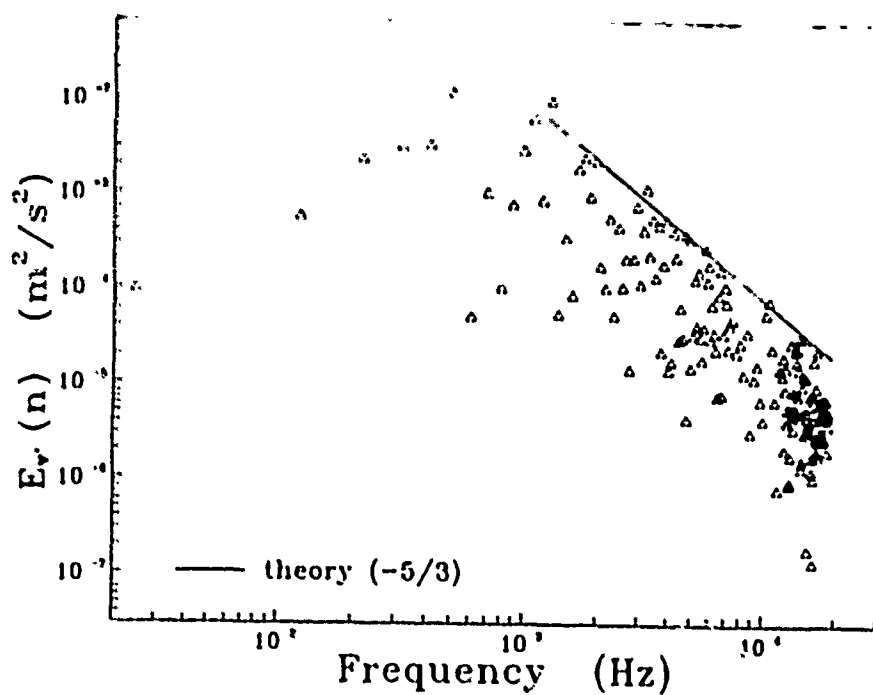
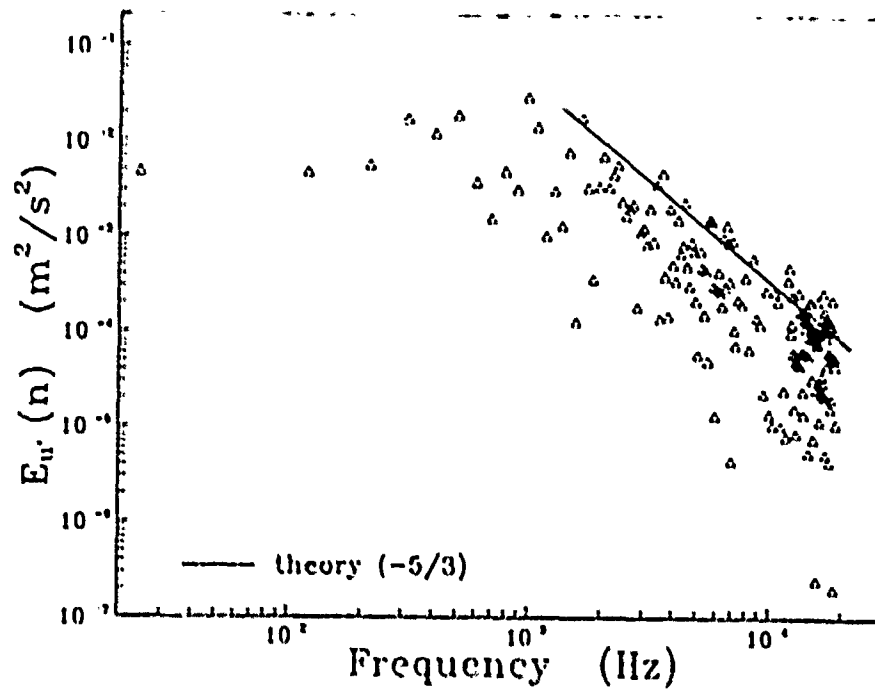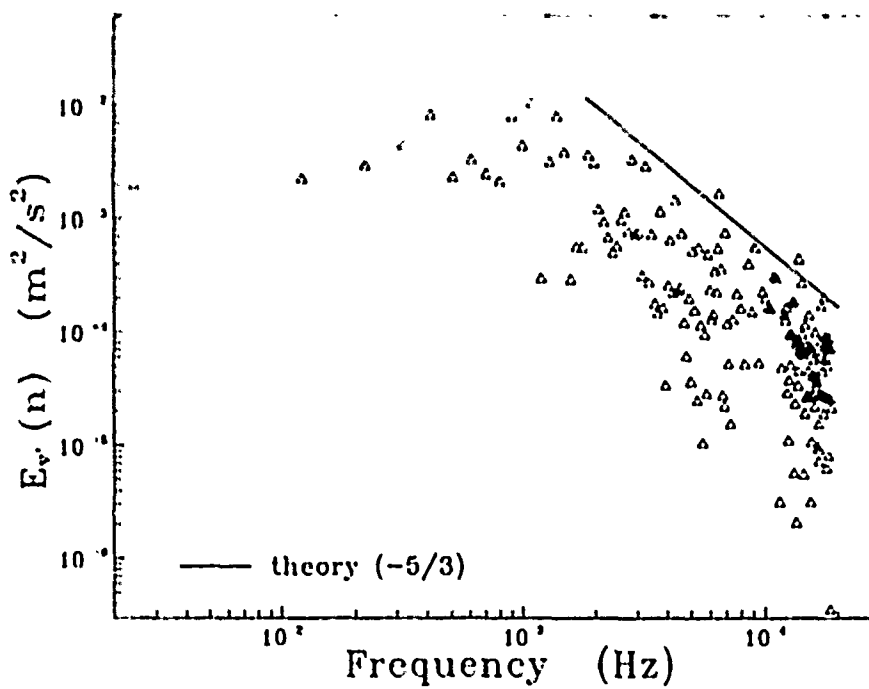Figure B.94. Turbulence energy spectrum for v'^2: Test E11
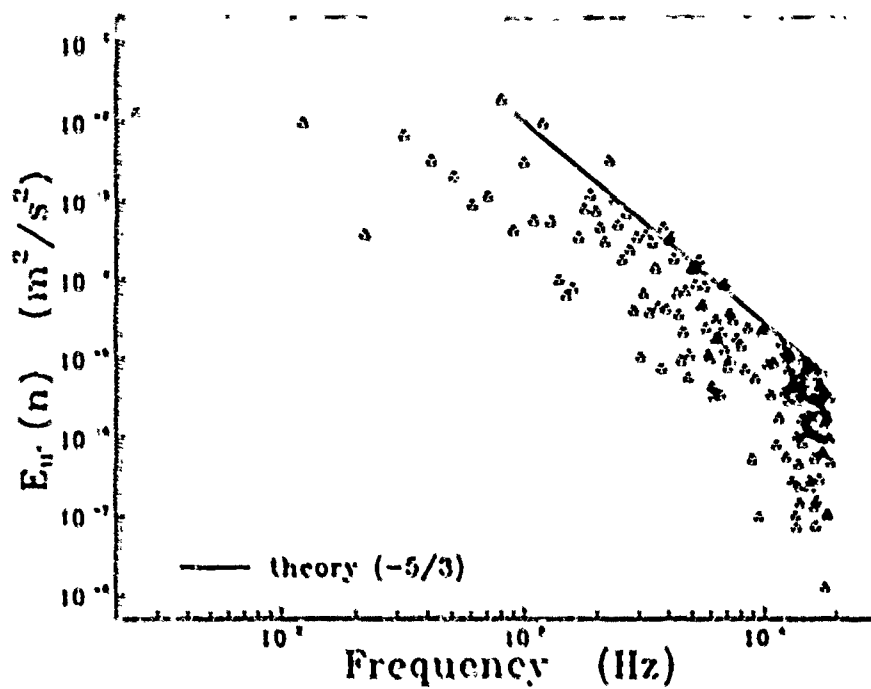
Figure B.95. Turbulence energy spectrum for u'^2: Test E12
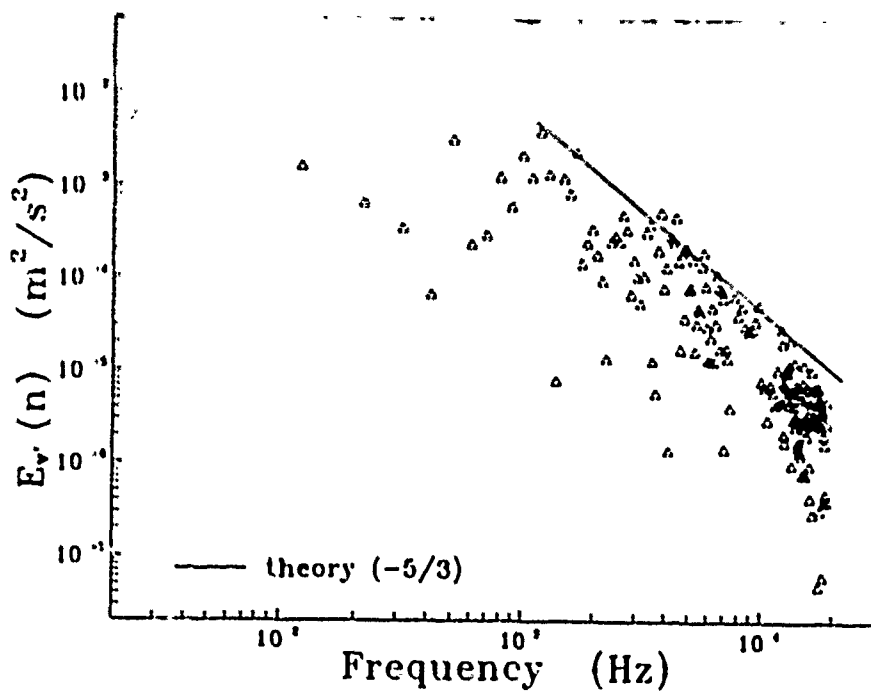
Figure B.96. Turbulence energy spectrum for v'^2: Test E12
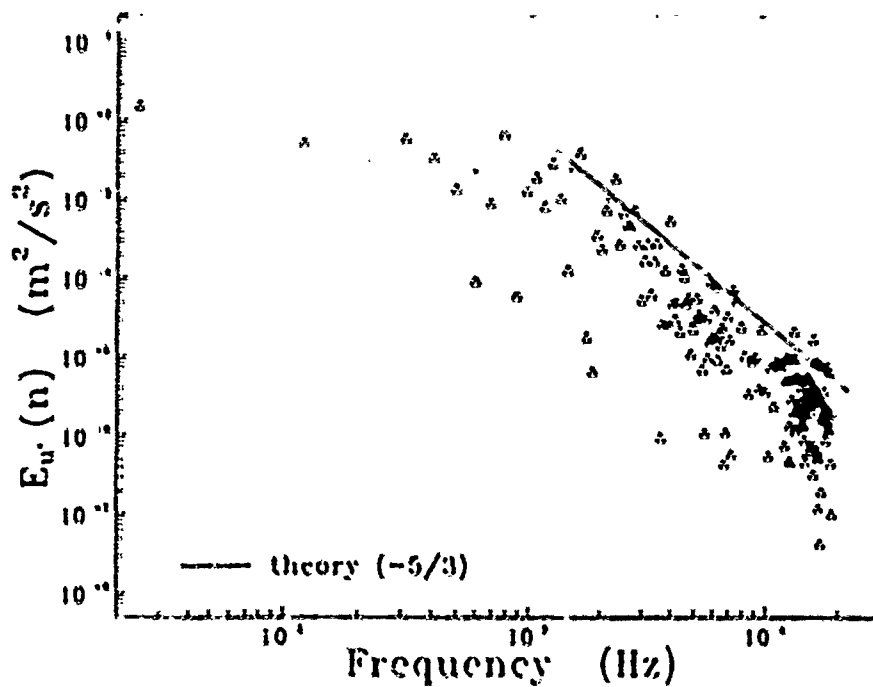
Figure B.97. Turbulence energy spectrum for u'^2: Test E13
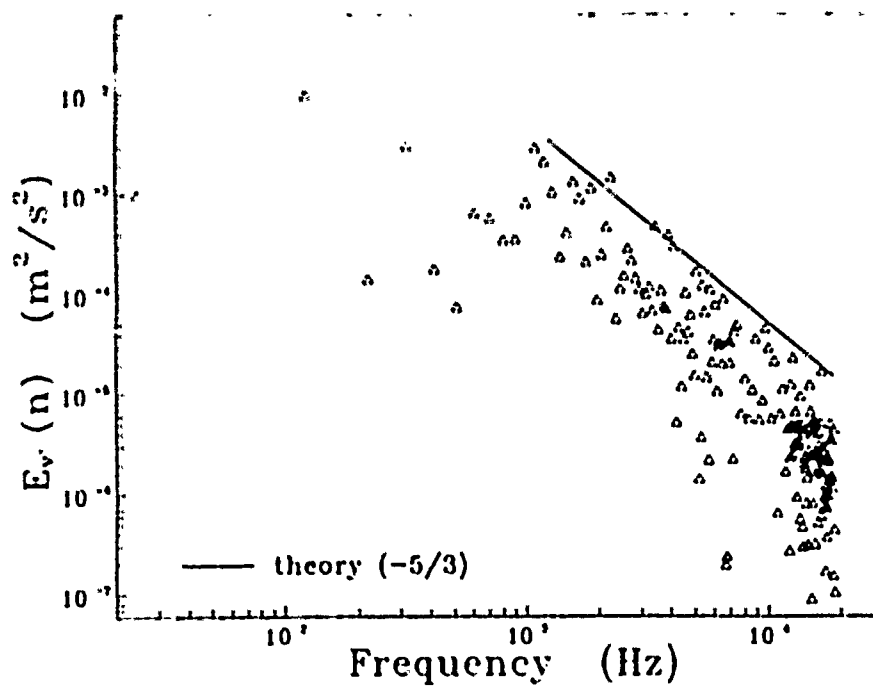
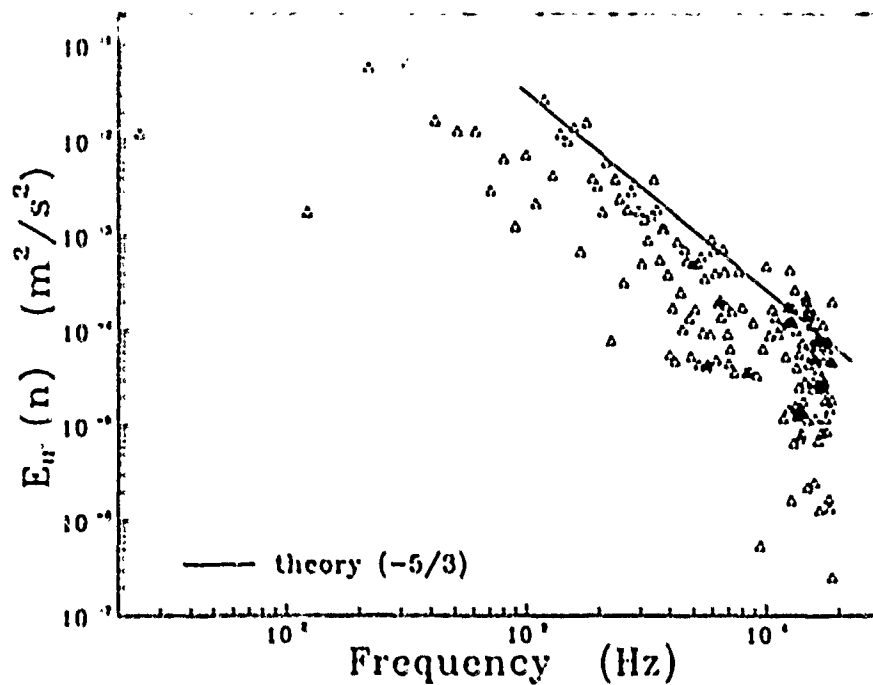Figure B.98. Turbulence energy spectrum for v'^2: Test E13
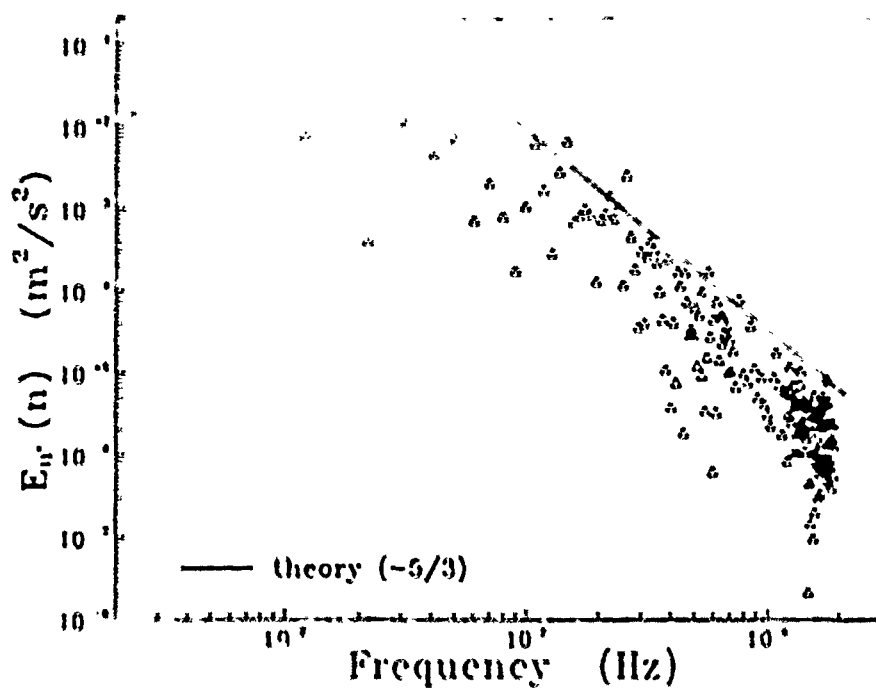
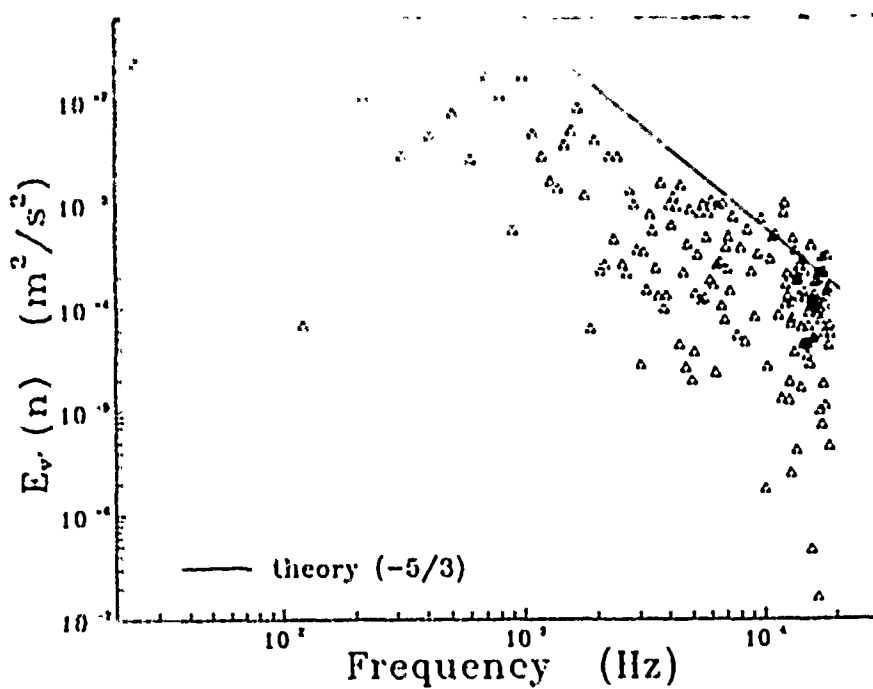Figure B.99. Turbulence energy spectrum for u'^2: Test E21
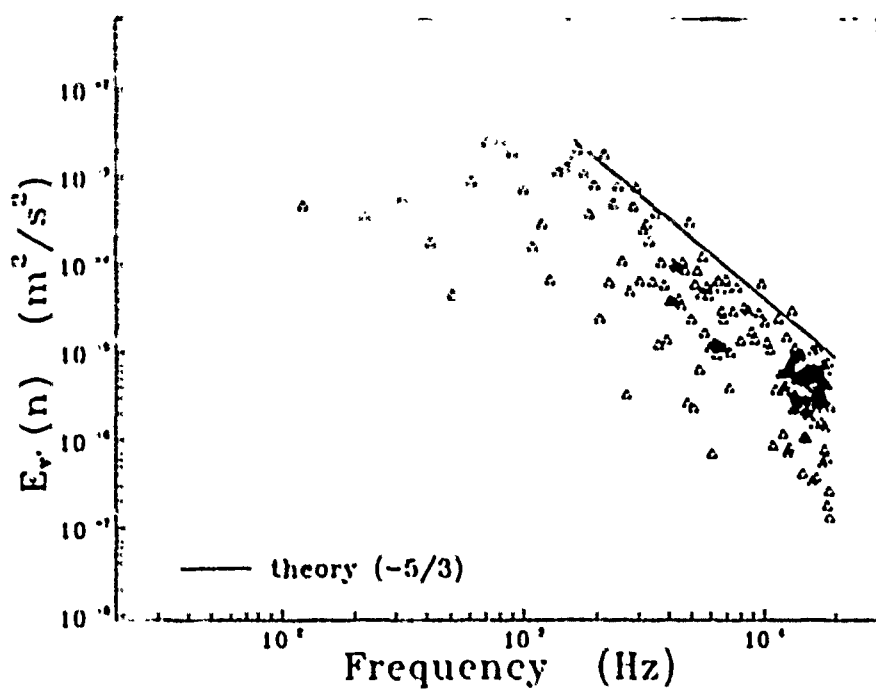
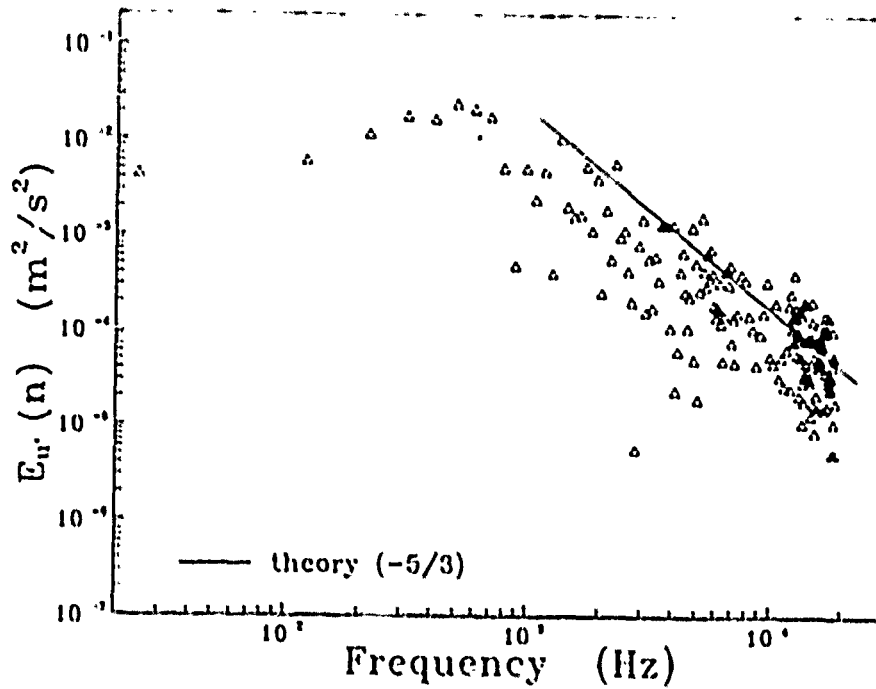Figure B.100. Turbulence energy spectrum for v'^2: Test E21
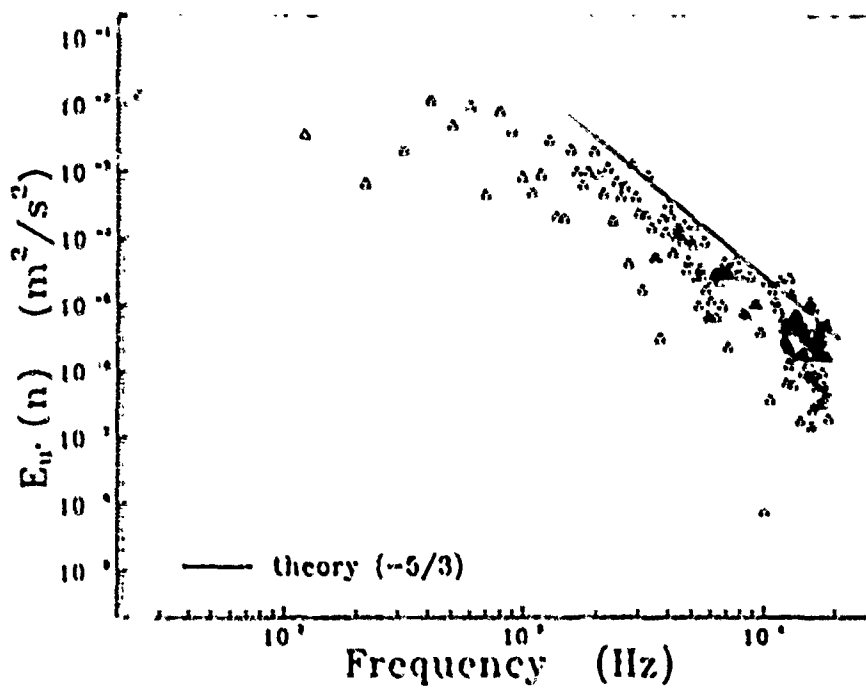
Figure B.101. Turbulence energy spectrum for u'^2: Test E22
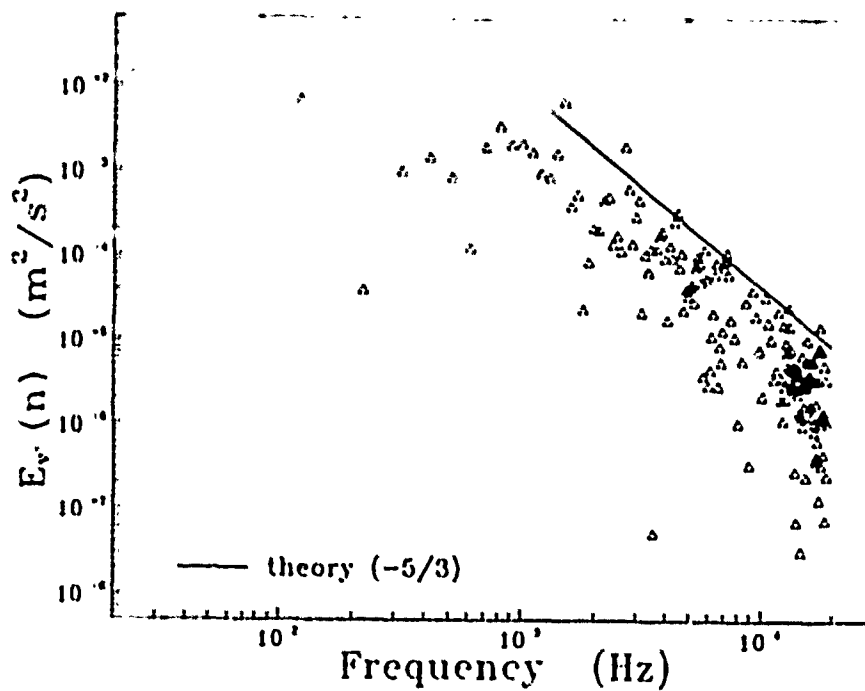
Figure B.102. Turbulence energy spectrum for v'^2: Test E22
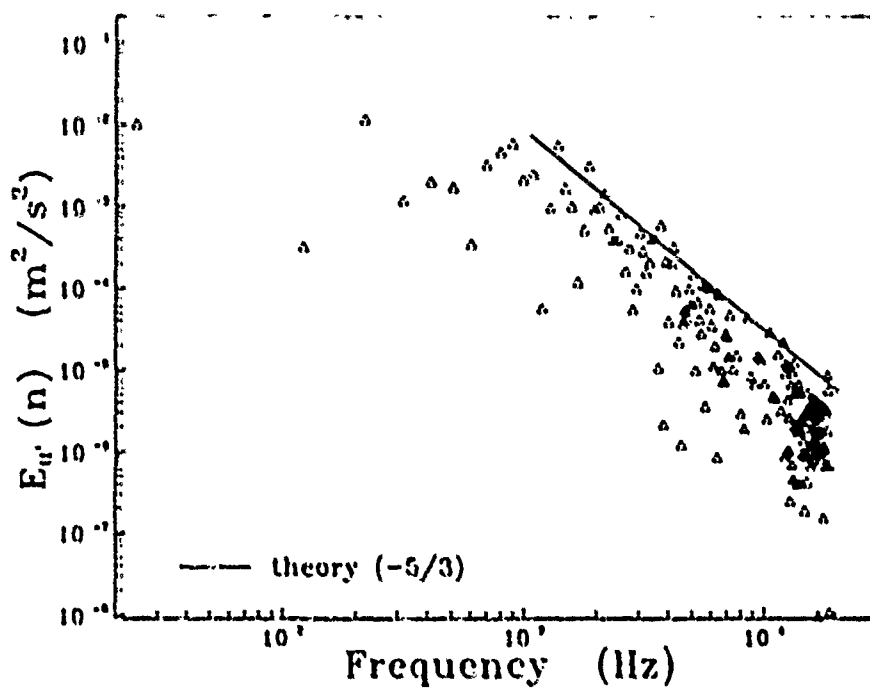
Figure B.103. Turbulence energy spectrum for u'^2: Test E23
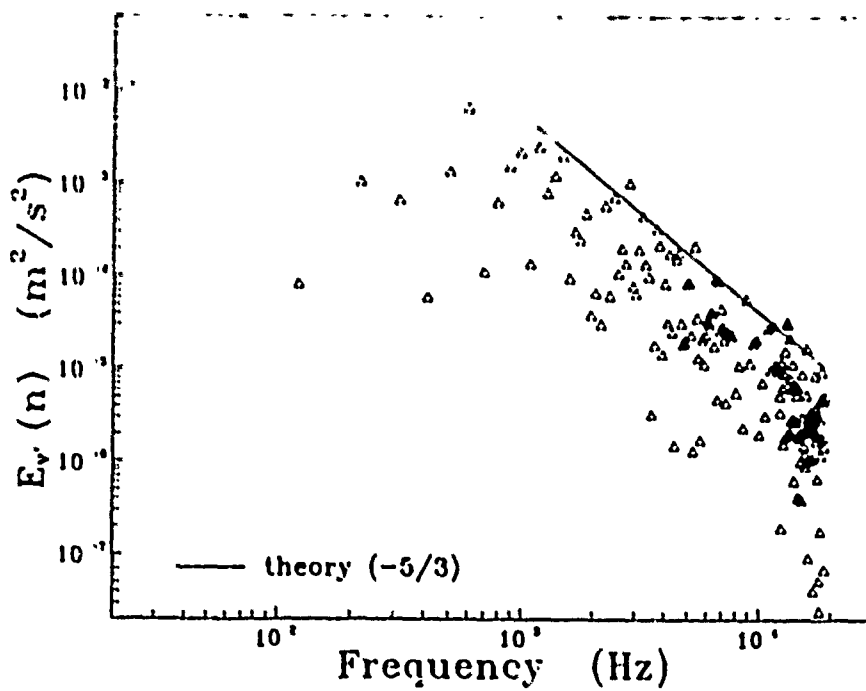
Figure B.104. Turbulence energy spectrum for v'^2: Test E23
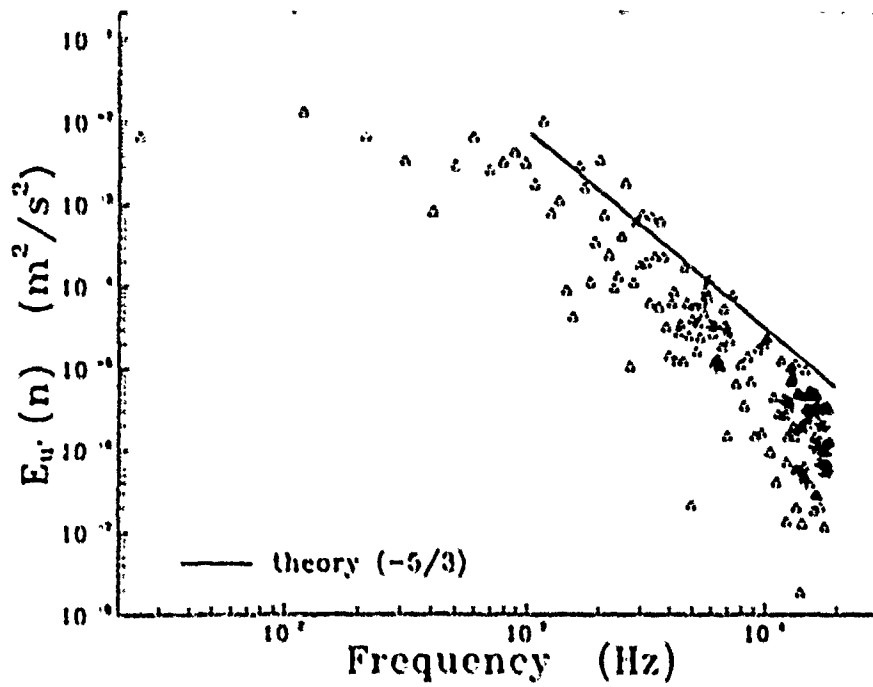
Figure B.105. Turbulence energy spectrum for u'^2: Test E31
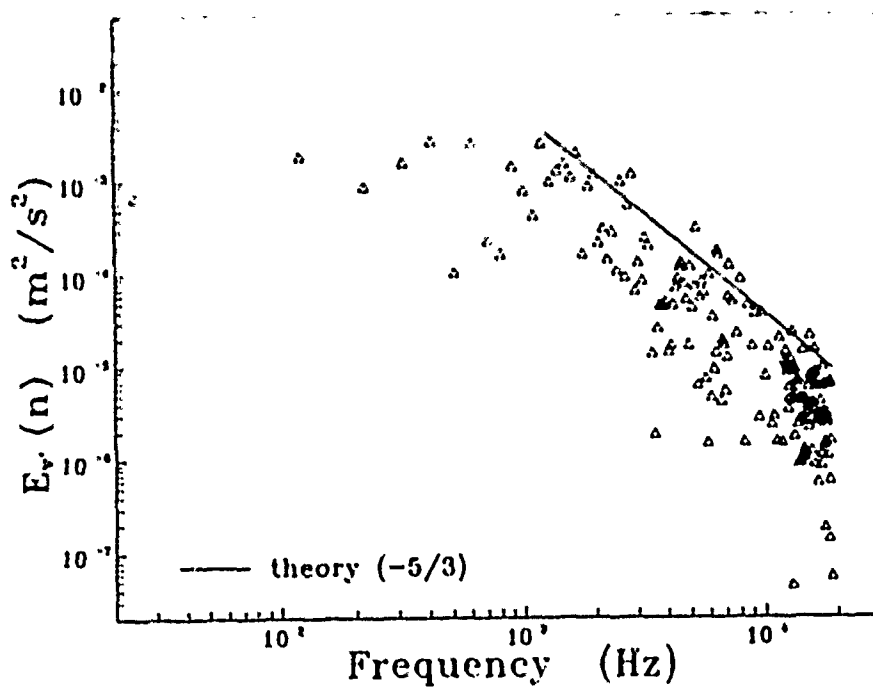
Figure B.106. Turbulence energy spectrum for v'^2: Test E31
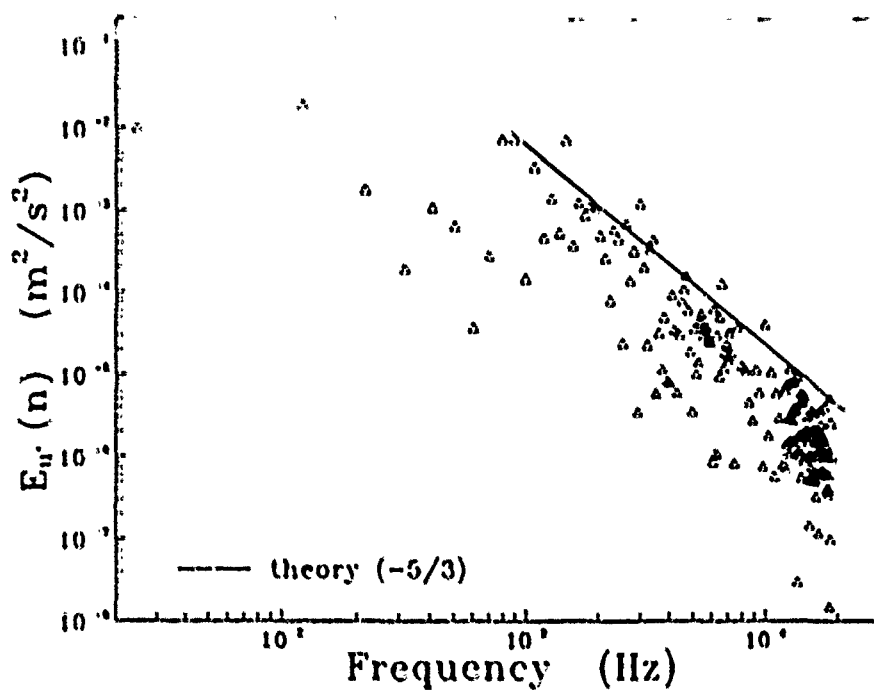
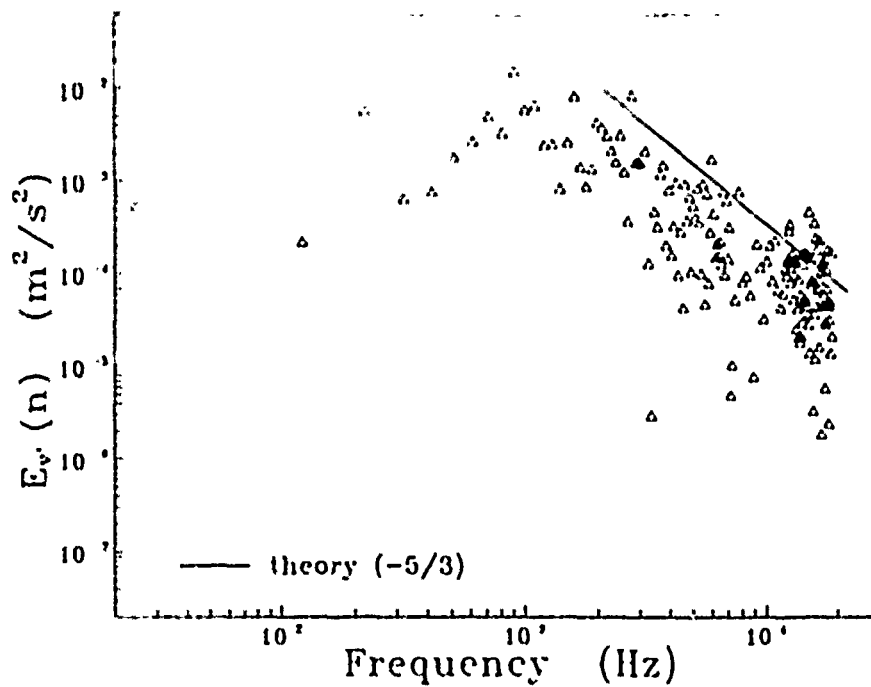Figure B.107. Turbulence energy spectrum for u'^2: Test E32
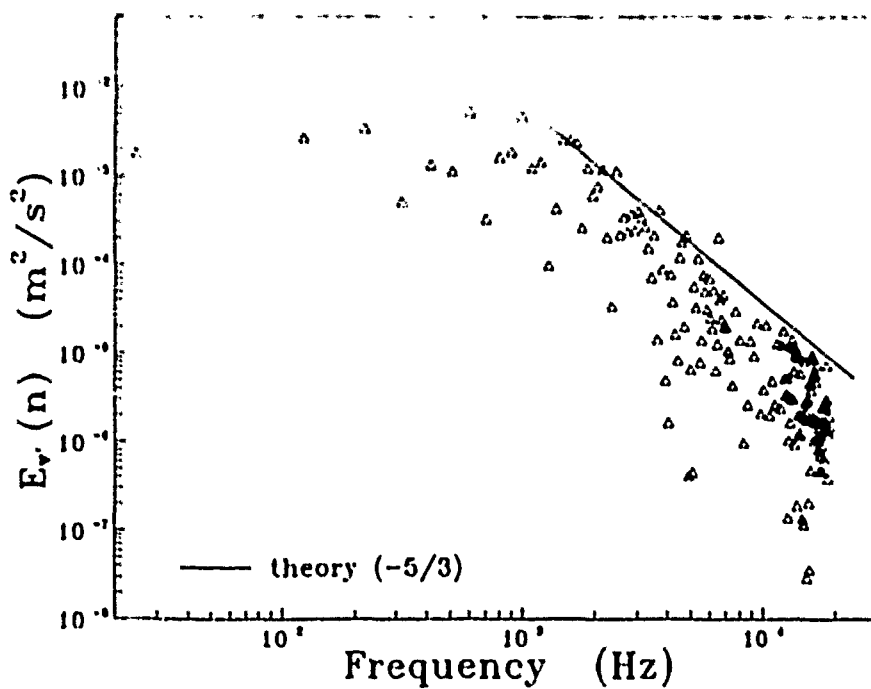
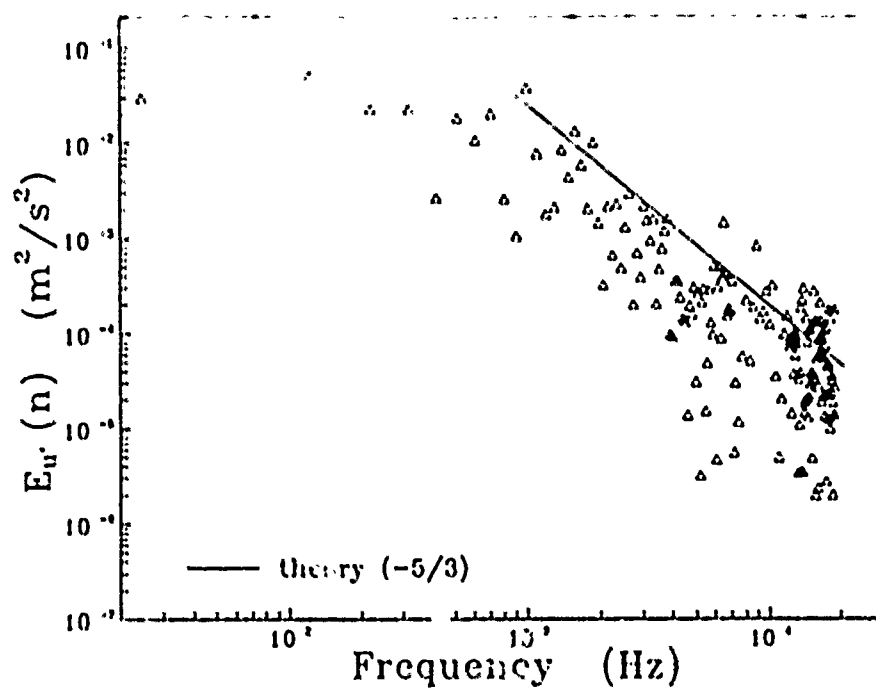Figure B.108. Turbulence energy spectrum for v'^2: Test E32
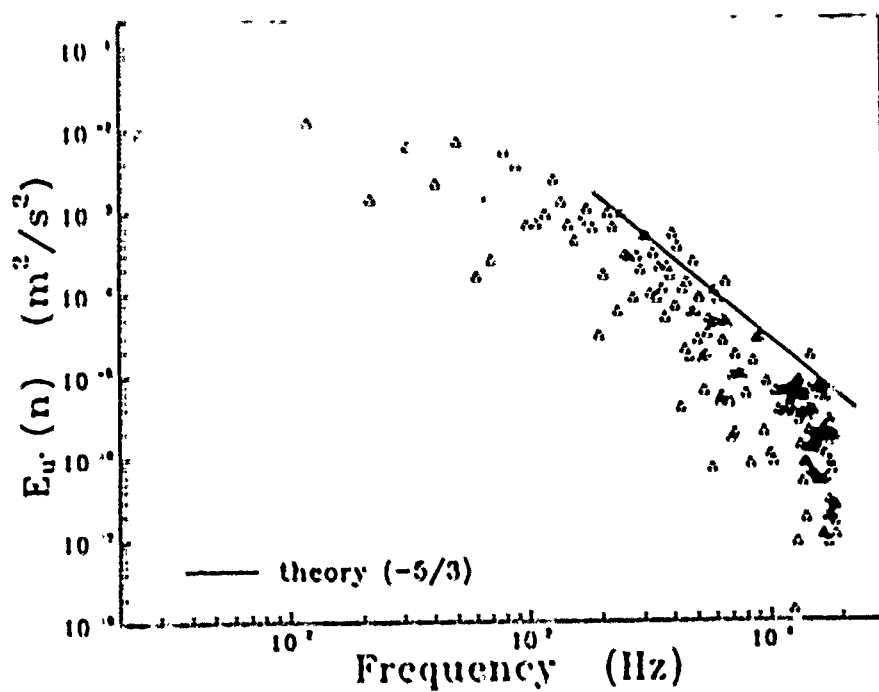
Figure B.109. Turbulence energy spectrum for u'^2: Test E33
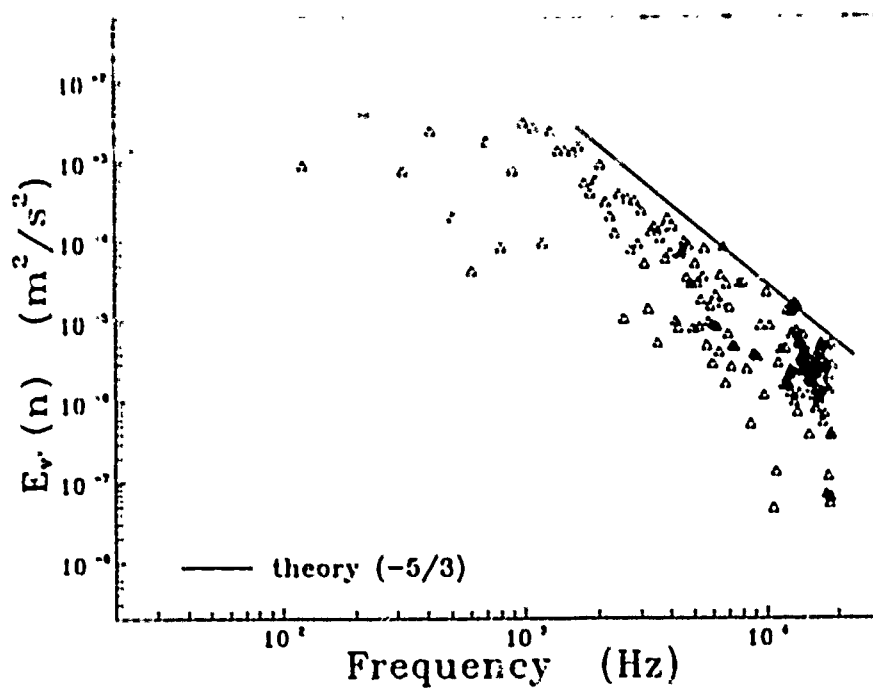
Figure B.110. Turbulence energy spectrum for v'^2: Test E33
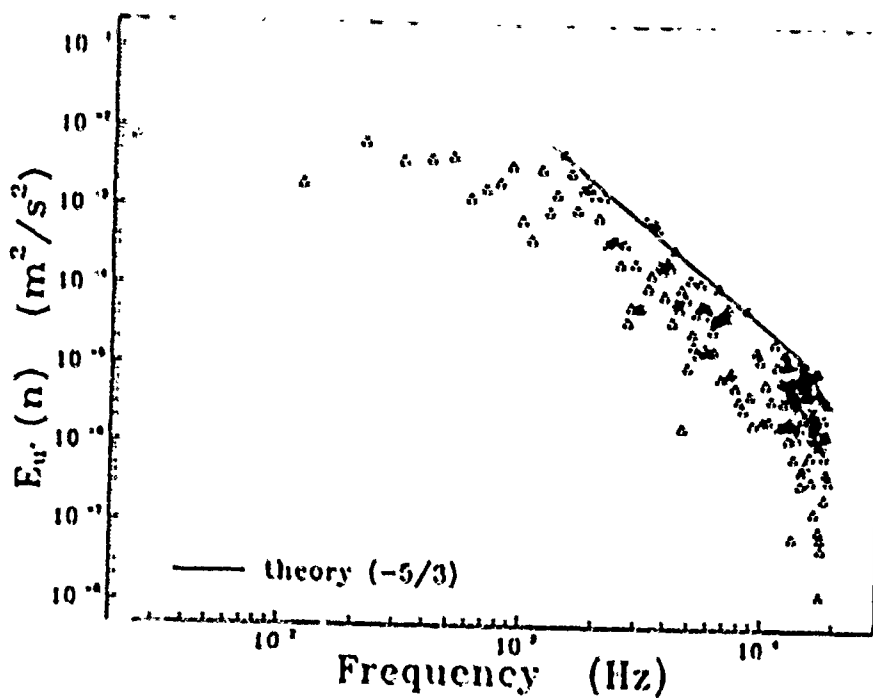
Figure B.111. Turbulence energy spectrum for u'^2: Test F11
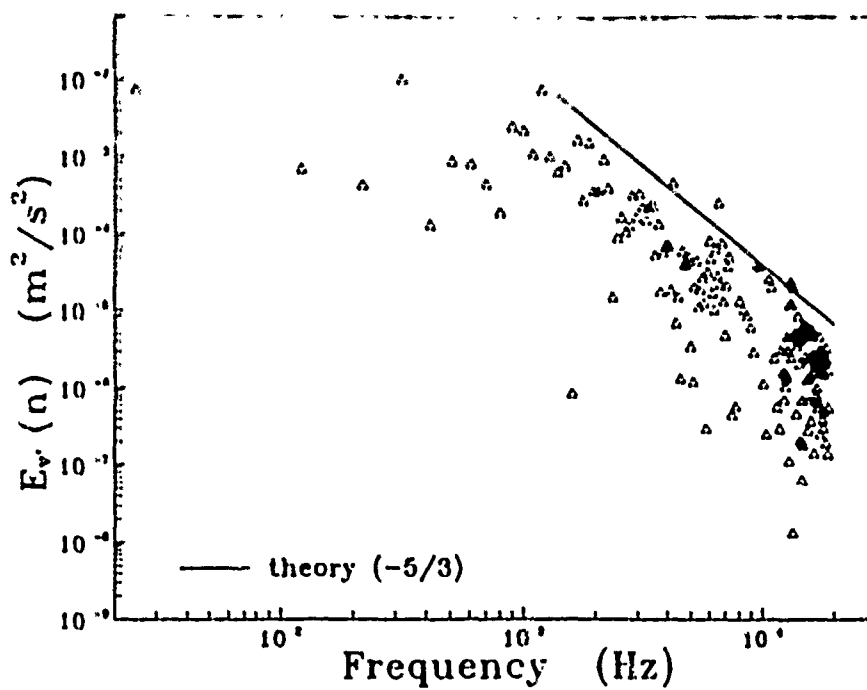
Figure B.112. Turbulence energy spectrum for v'^2: Test F11
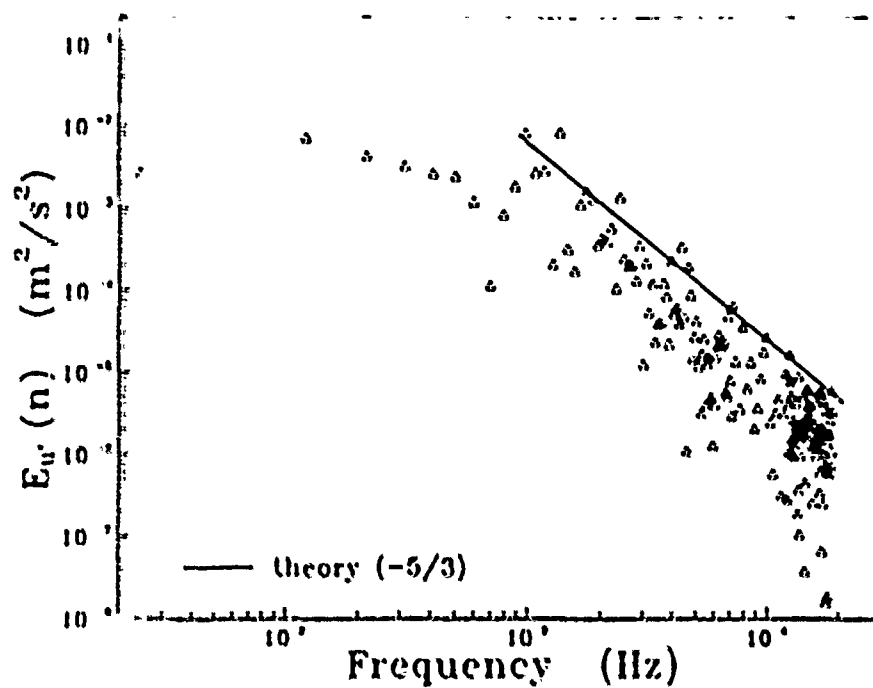
Figure B.113. Turbulence energy spectrum for u'^2: Test F12
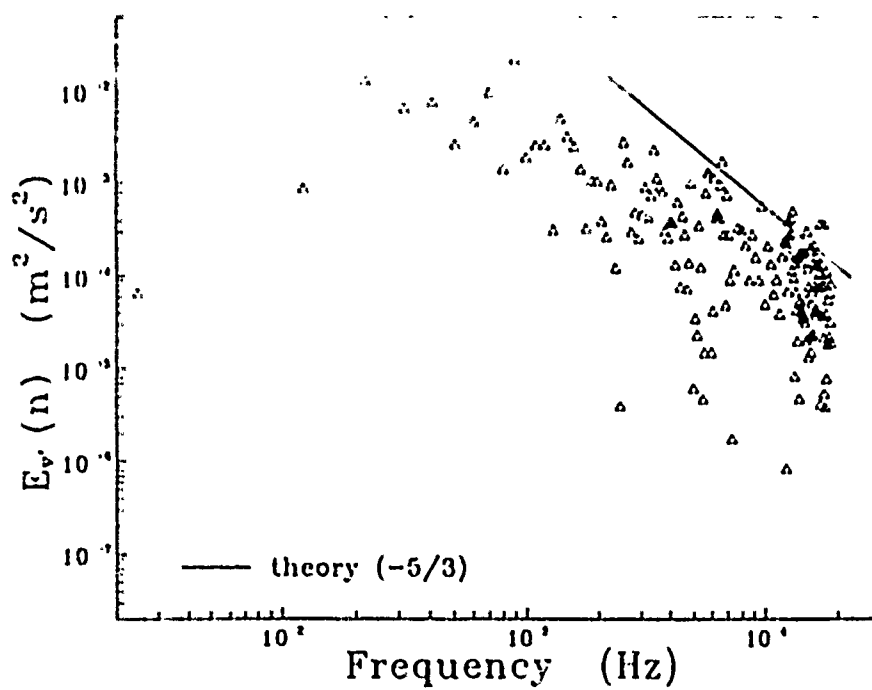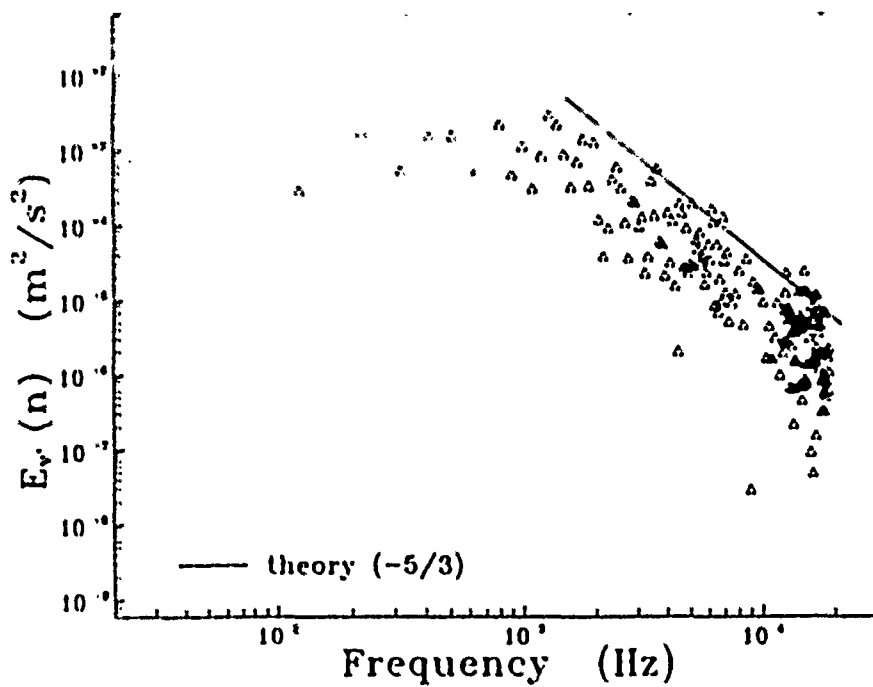

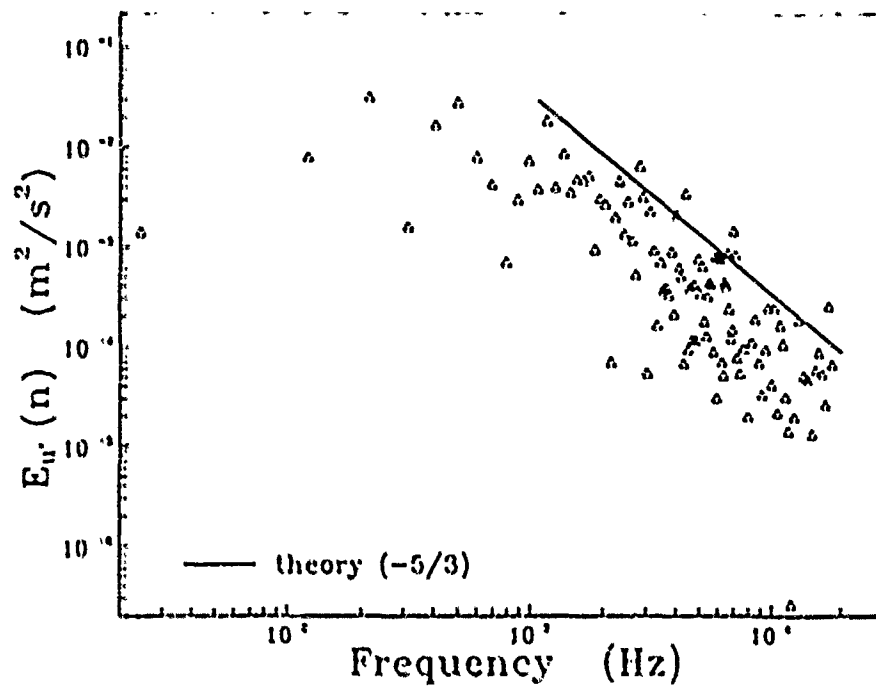Figure B.114. Turbulence energy spectrum for v'^2: Test F12
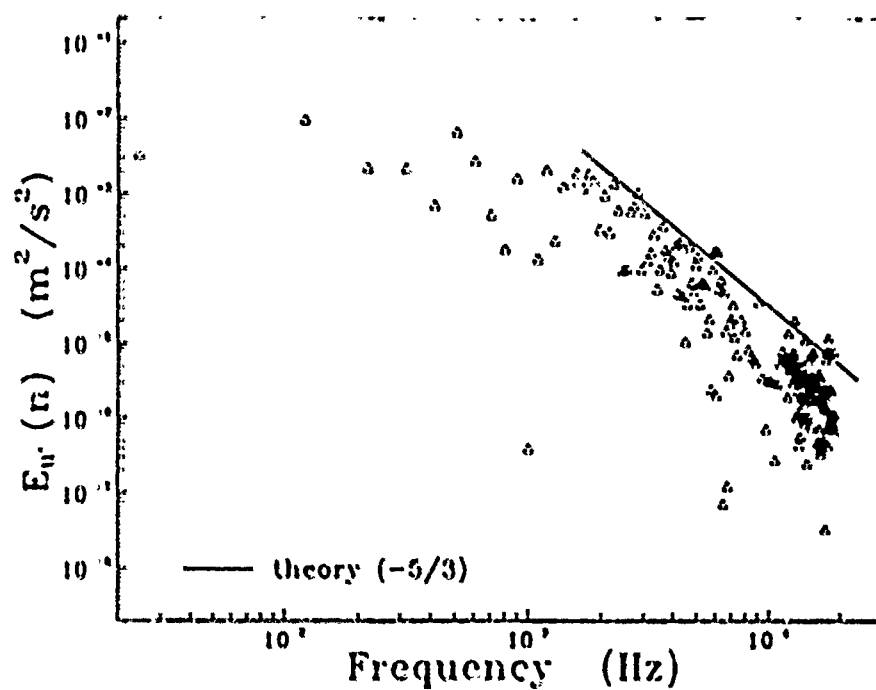
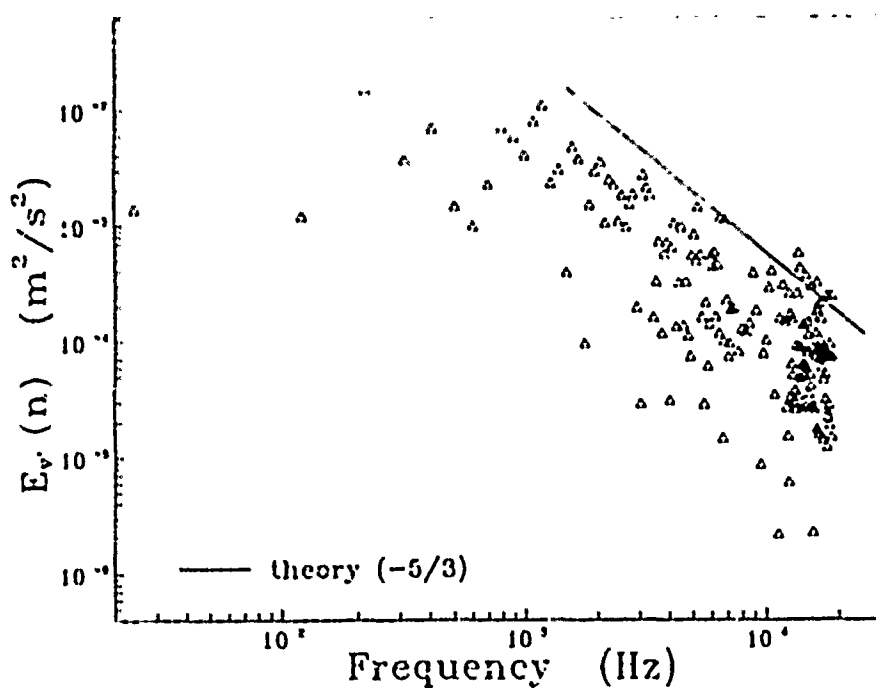Figure B.115. Turbulence energy spectrum for u'^2: Test F13
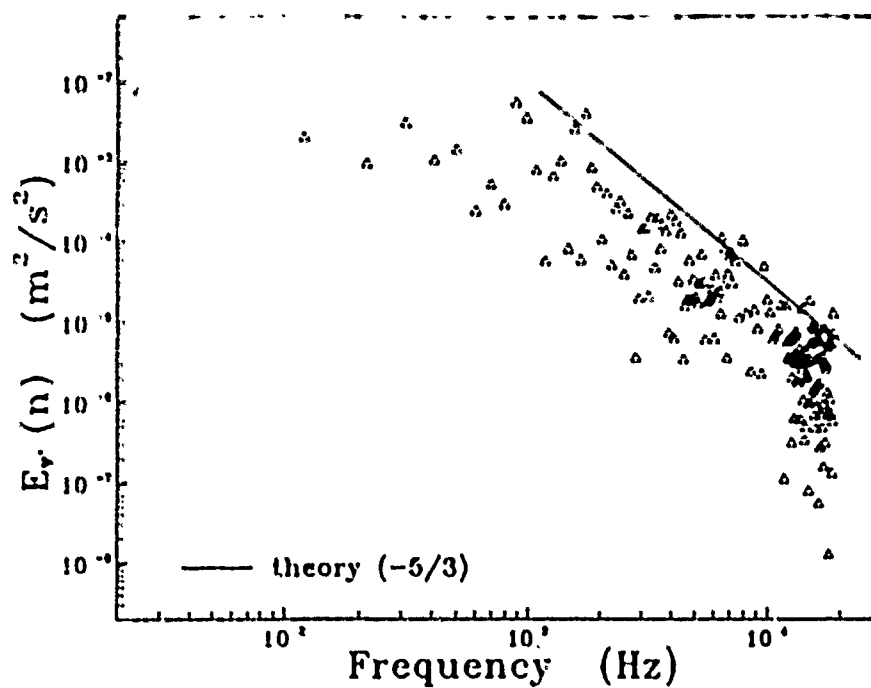
Figure B.116. Turbulence energy spectrum for v'^2: Test F13
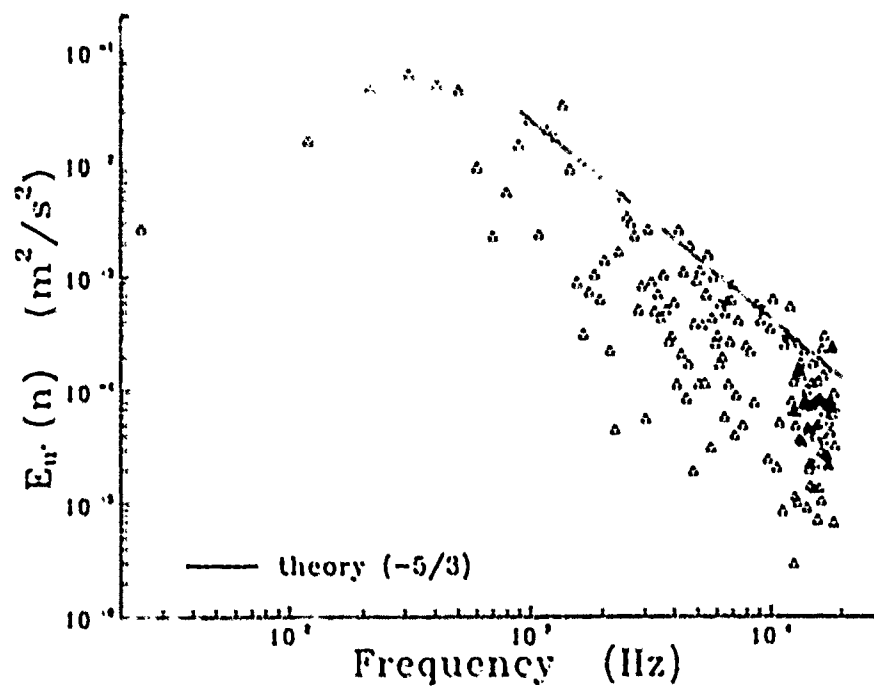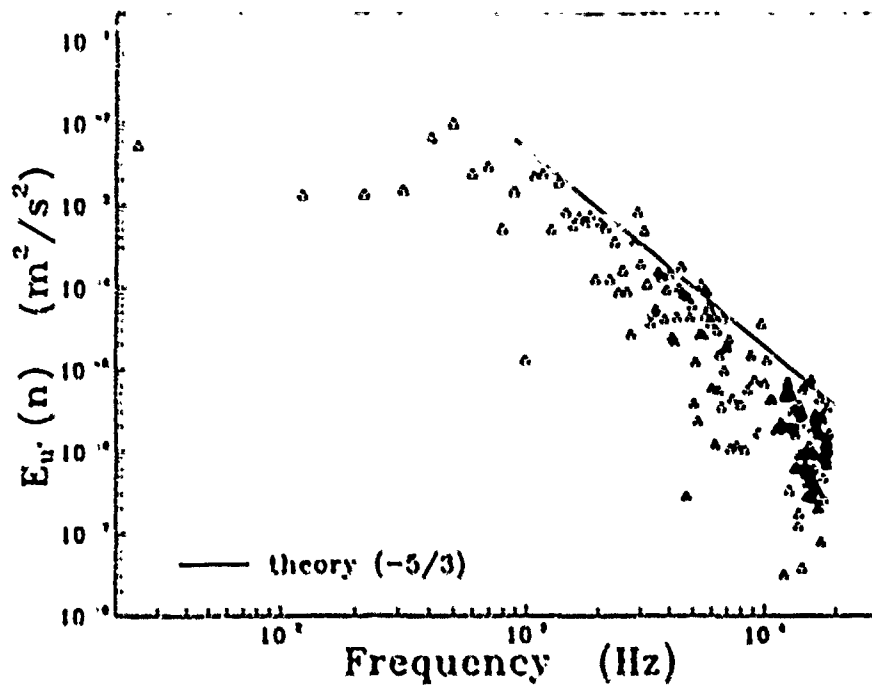
Figure B.117. Turbulence energy spectrum for u'^2: Test F21
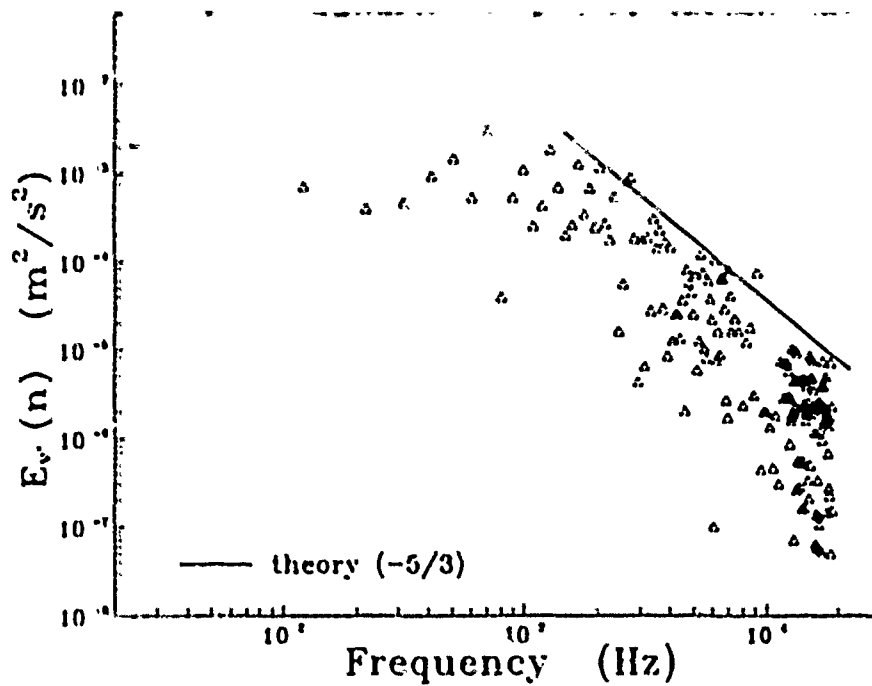
Figure B.118. Turbulence energy spectrum for v'^2: Test F21
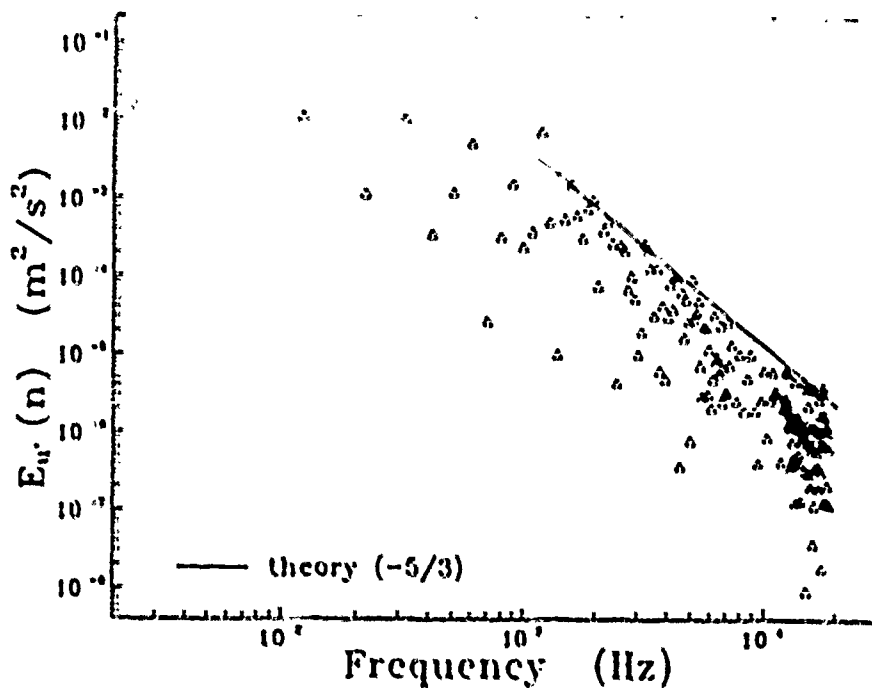
Figure B.119. Turbulence energy spectrum for u'^2: Test F22
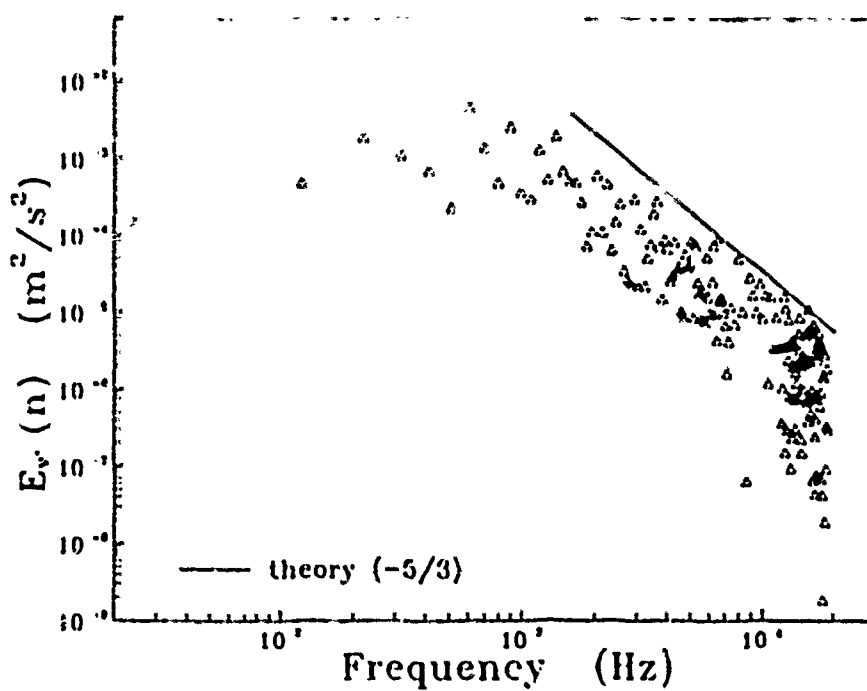
Figure B.120. Turbulence energy spectrum for v'^2: Test F22
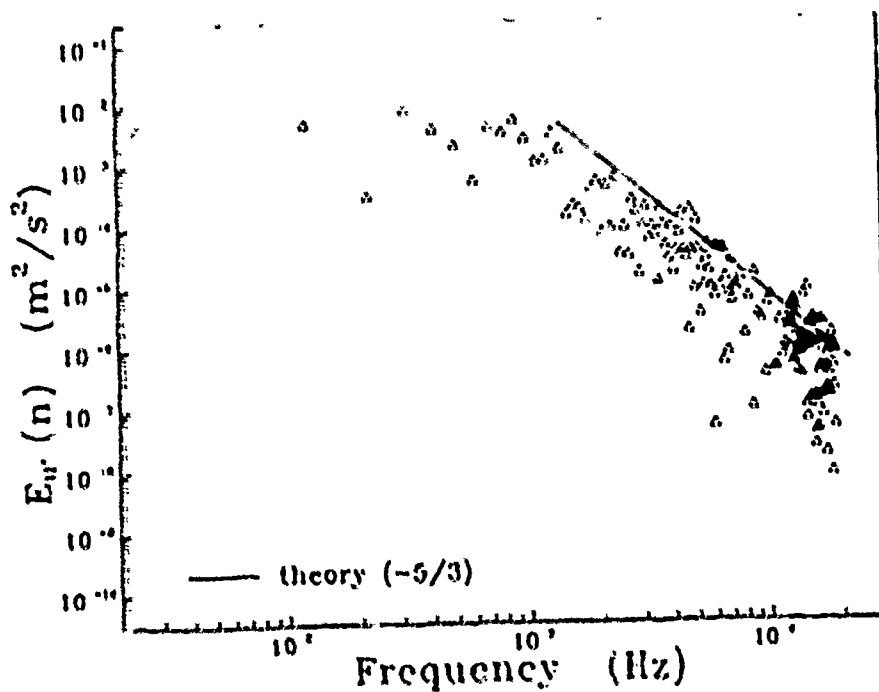
Figure B.121. Turbulence energy spectrum for u'^2: Test F23
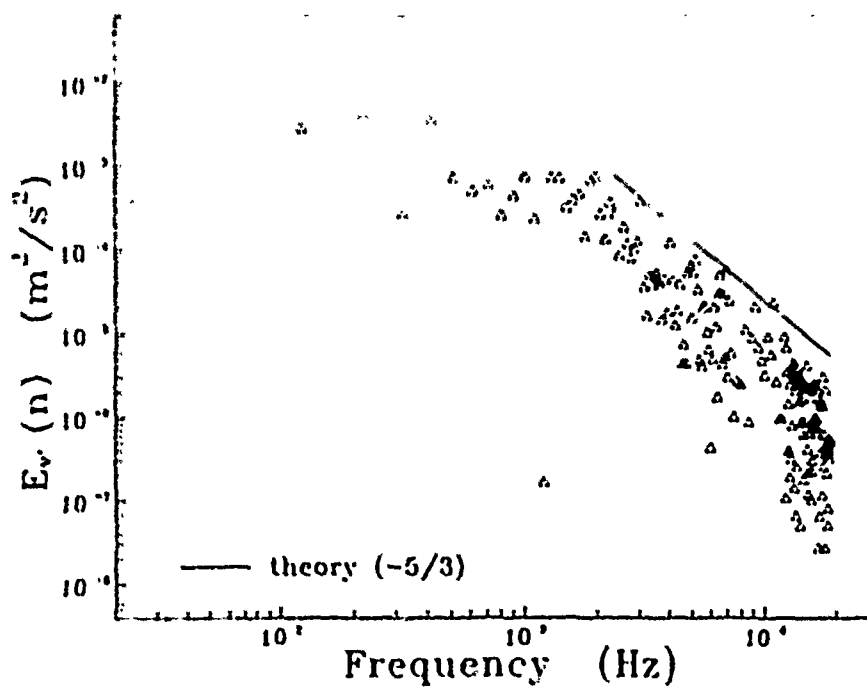
Figure B.122. Turbulence energy spectrum for v'^2: Test F23
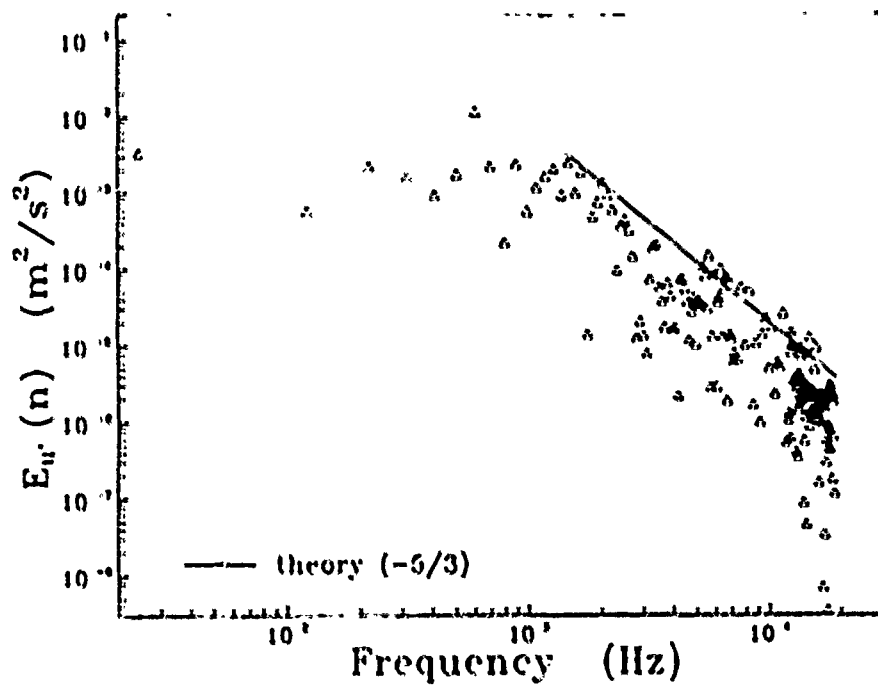
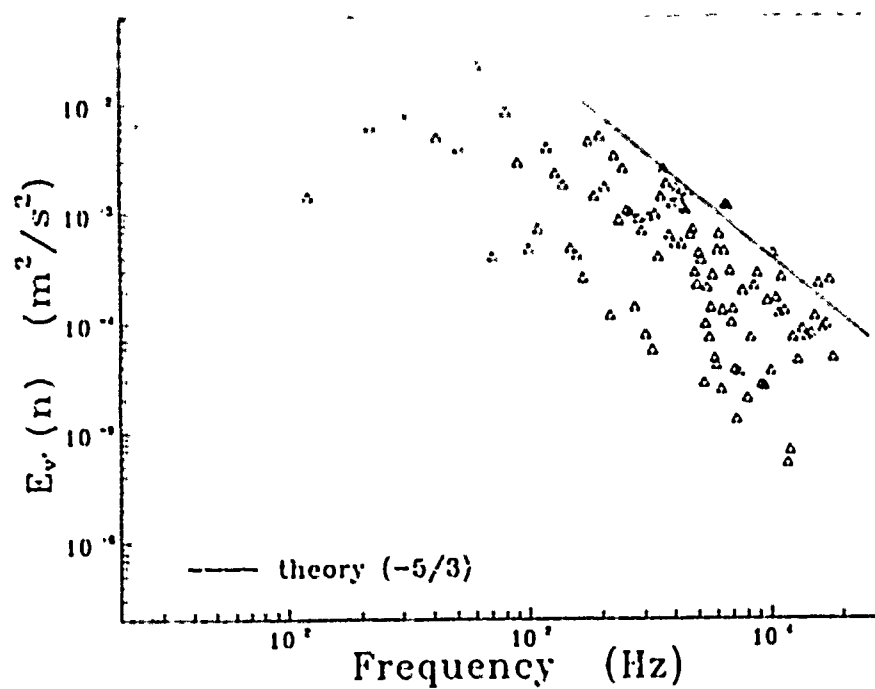Figure B.123. Turbulence energy spectrum for u'^2: Test F31
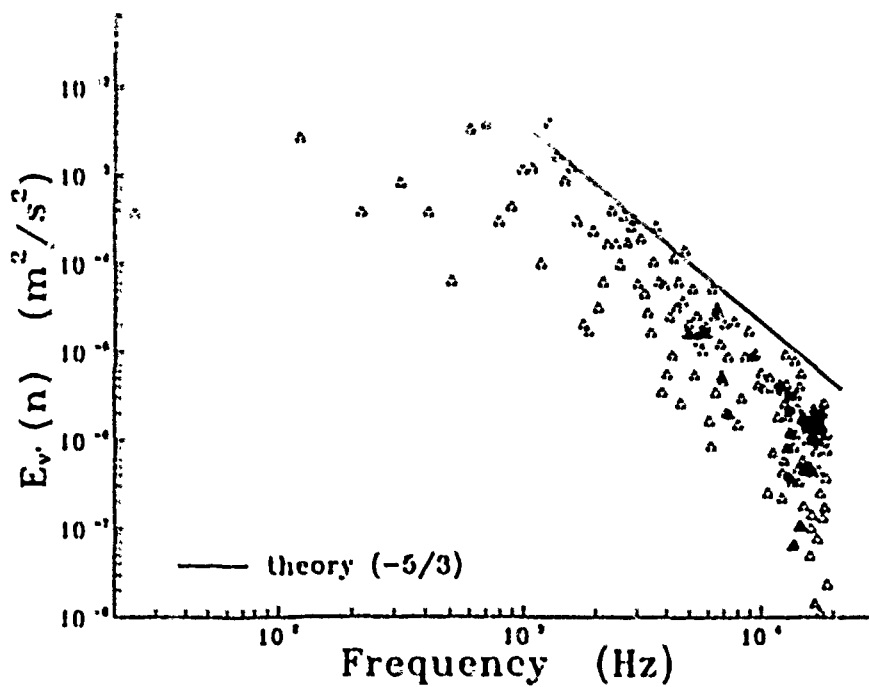
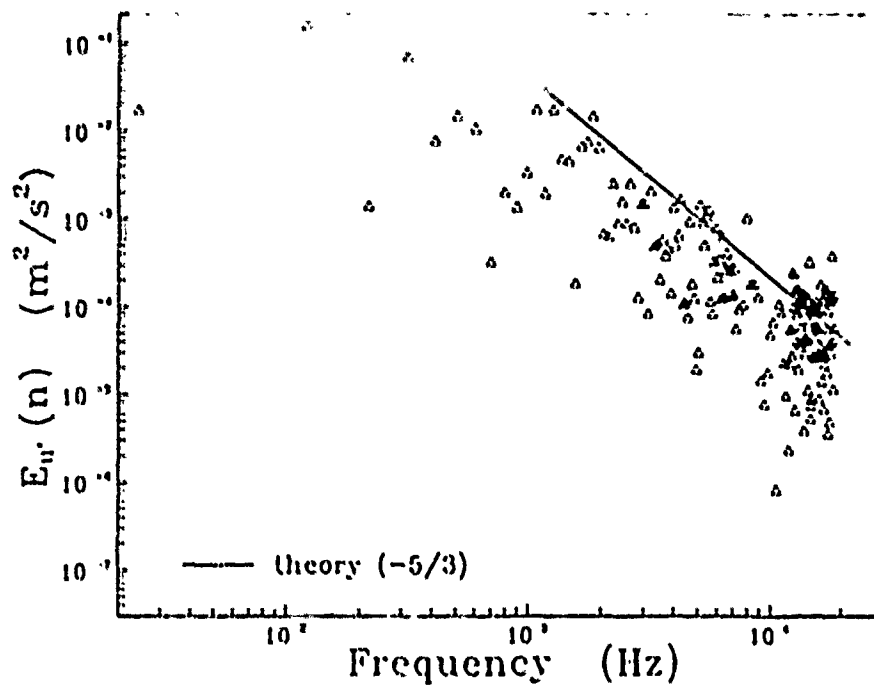Figure B.124. Turbulence energy spectrum for v'^2: Test F31
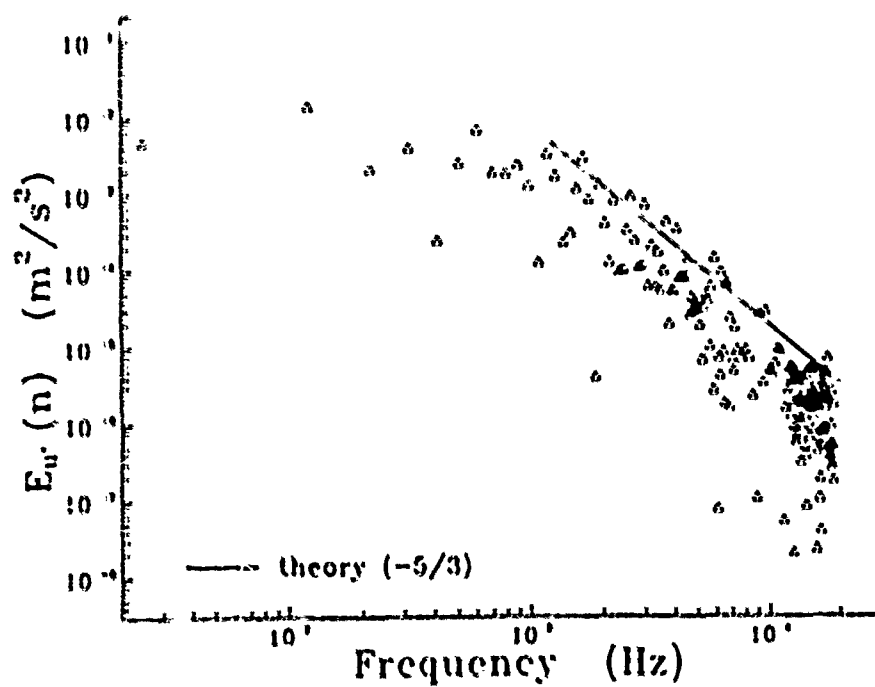
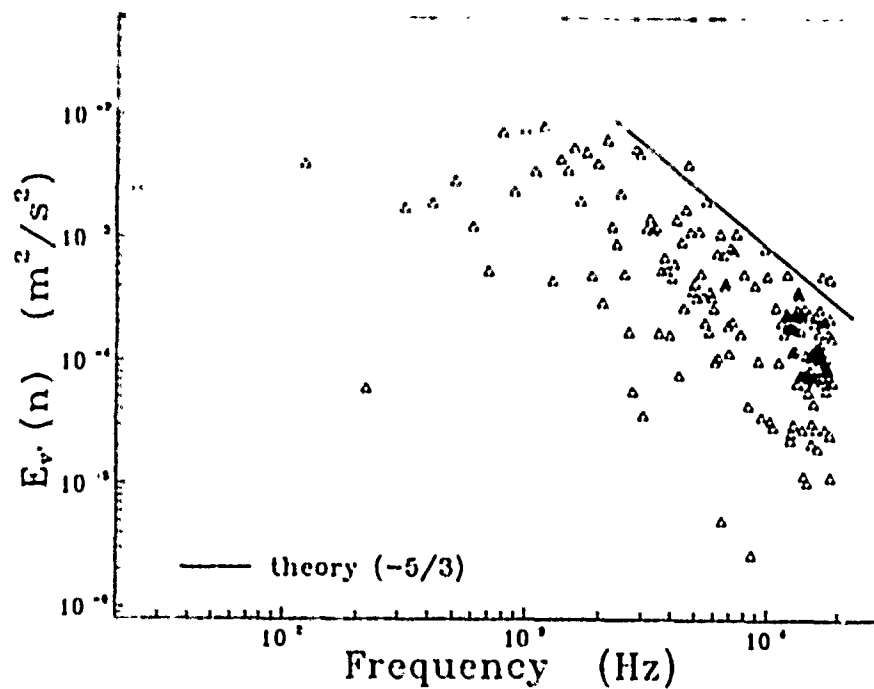Figure B.125. Turbulence energy spectrum for u'^2: Test F32
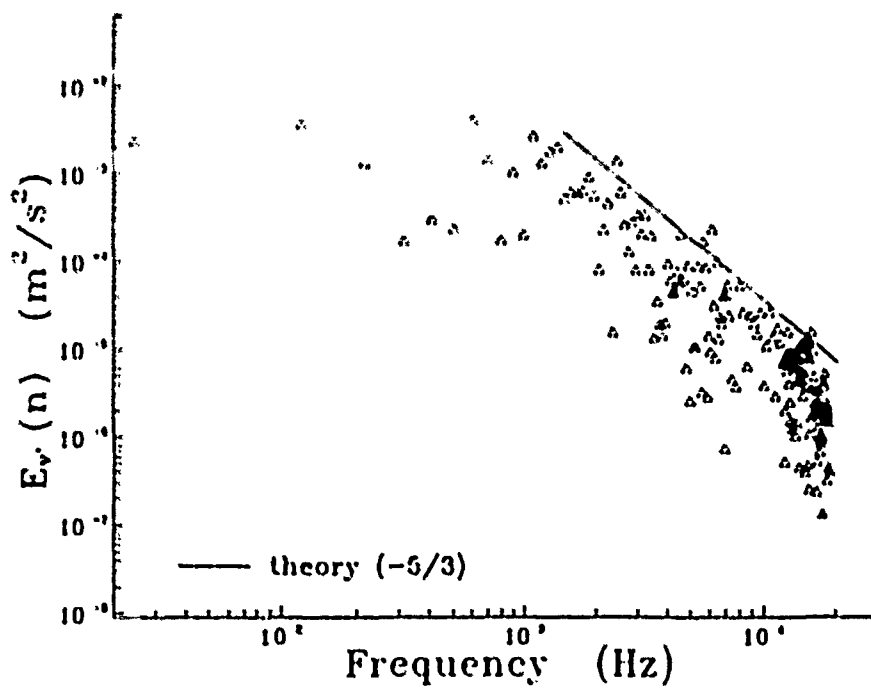
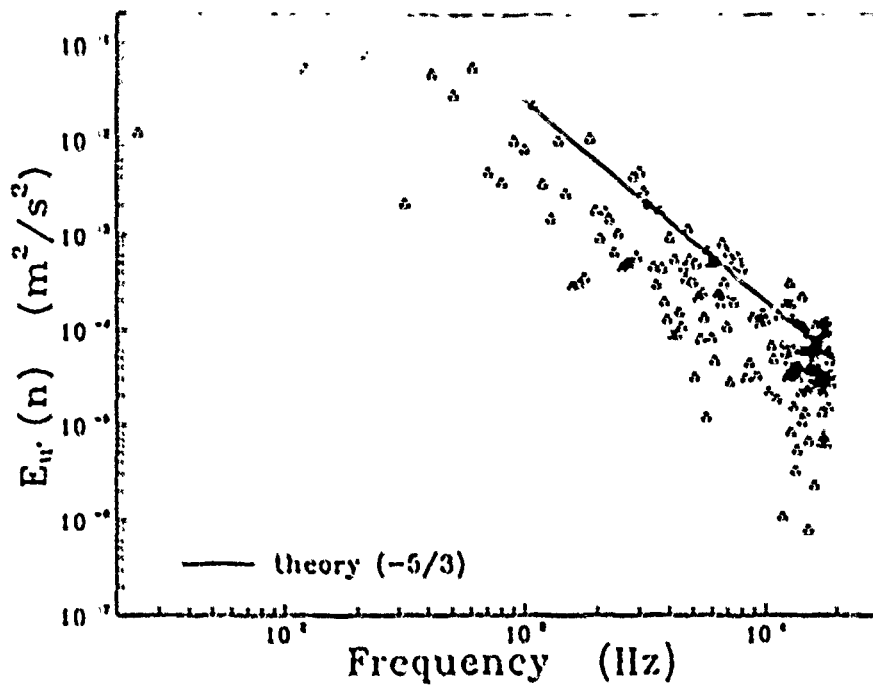Figure B.126. Turbulence energy spectrum for v'^2: Test F32
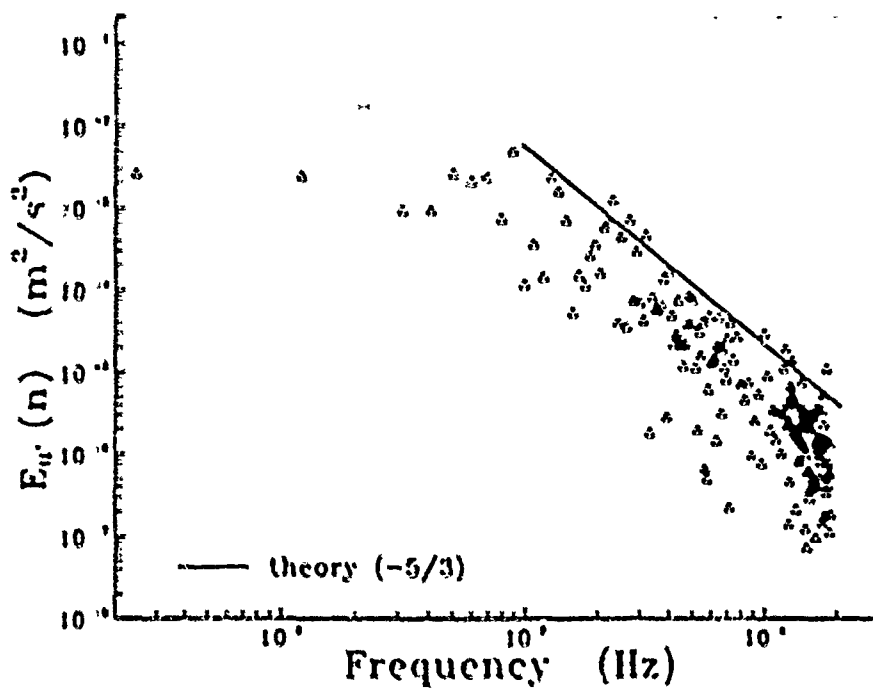
Figure B.127. Turbulence energy spectrum for u'^2: Test F33
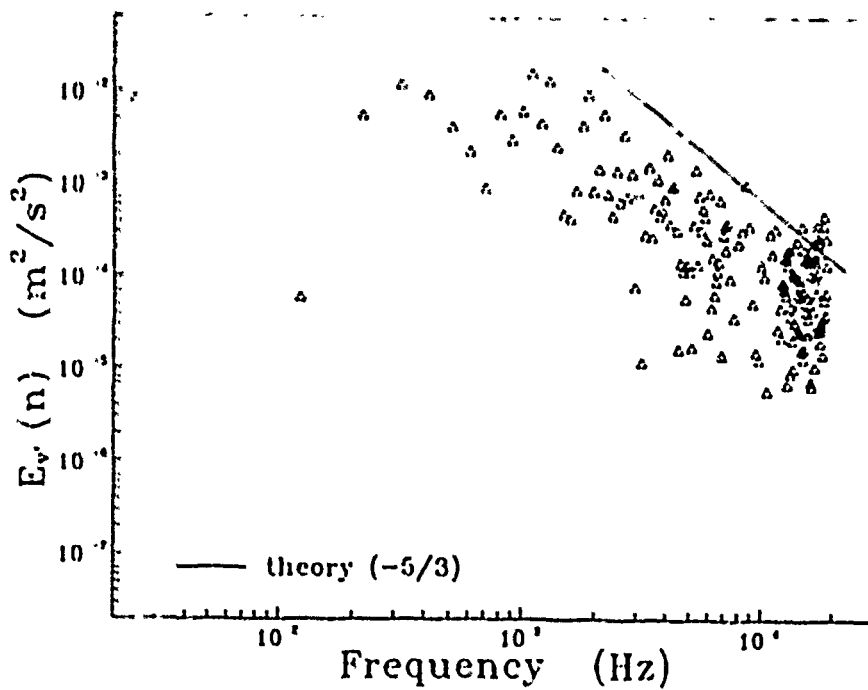

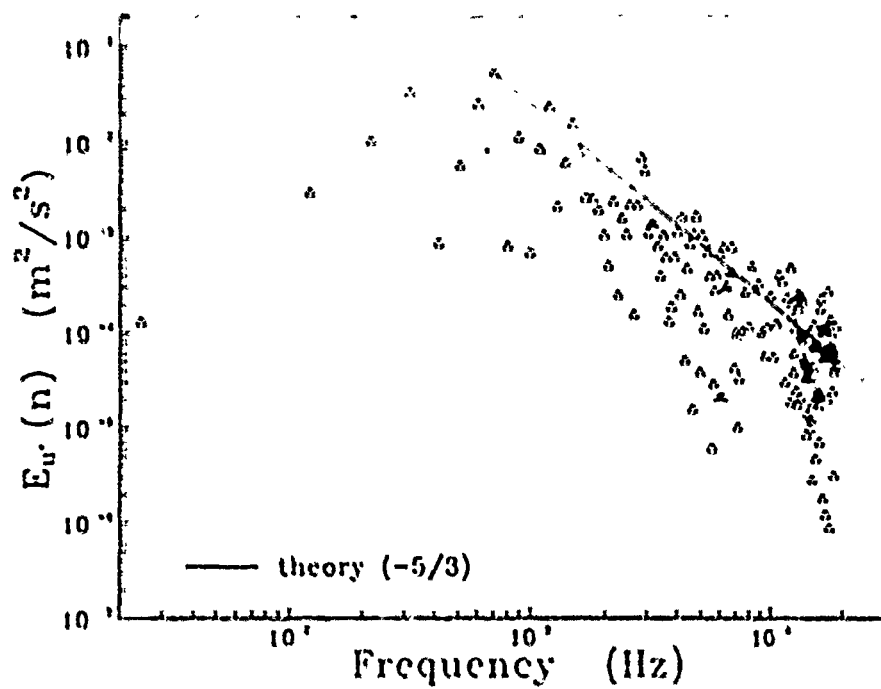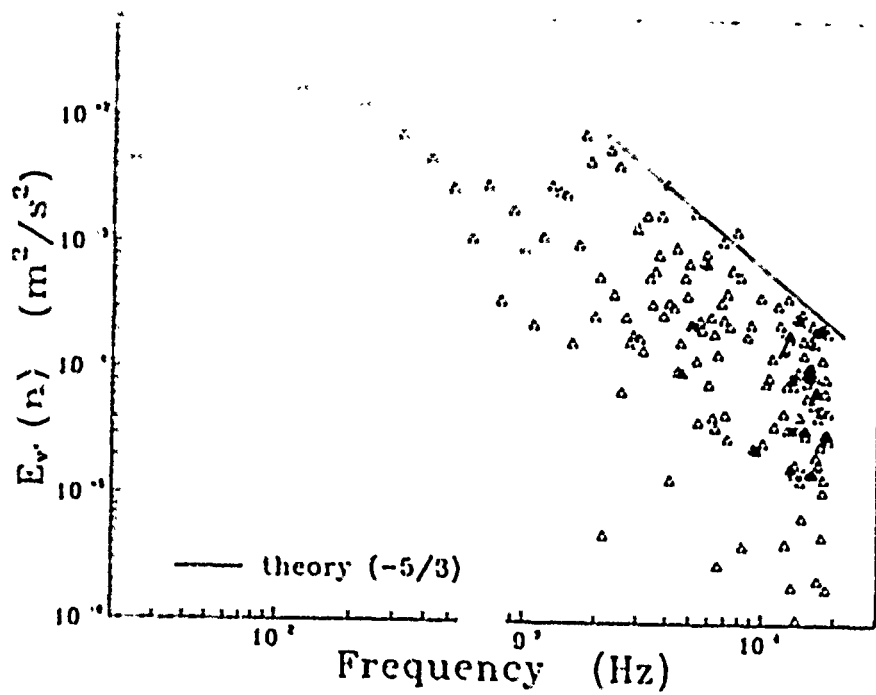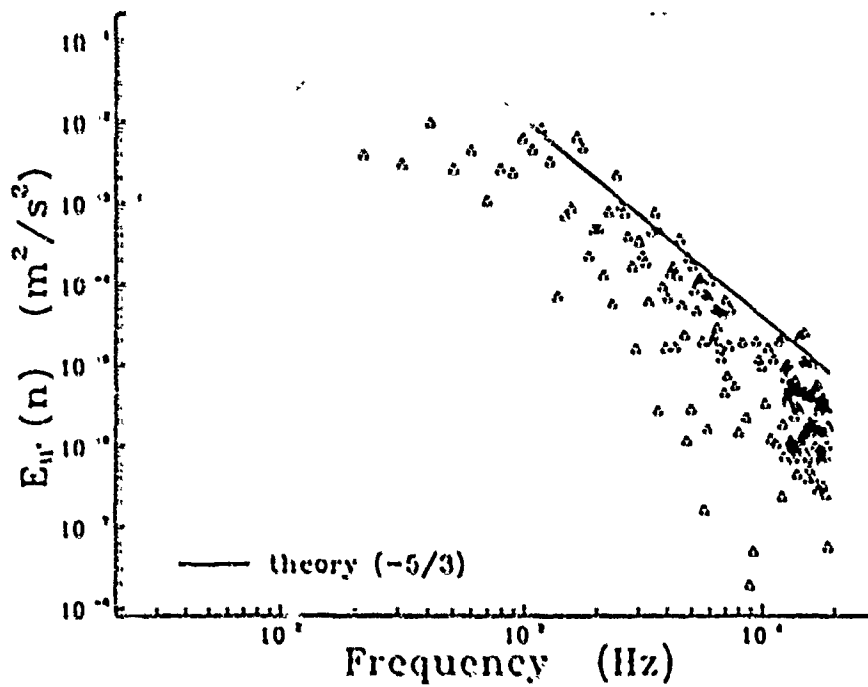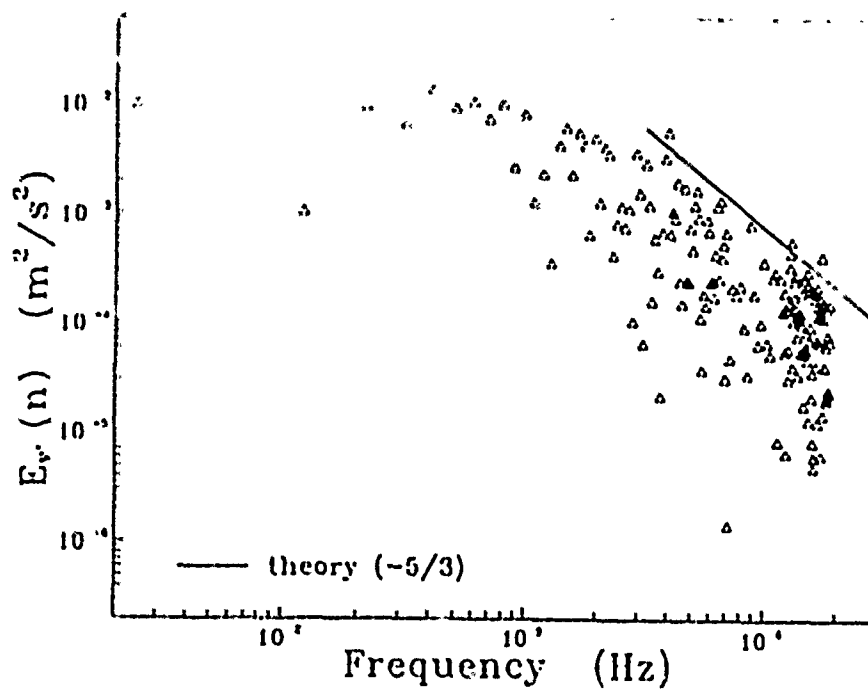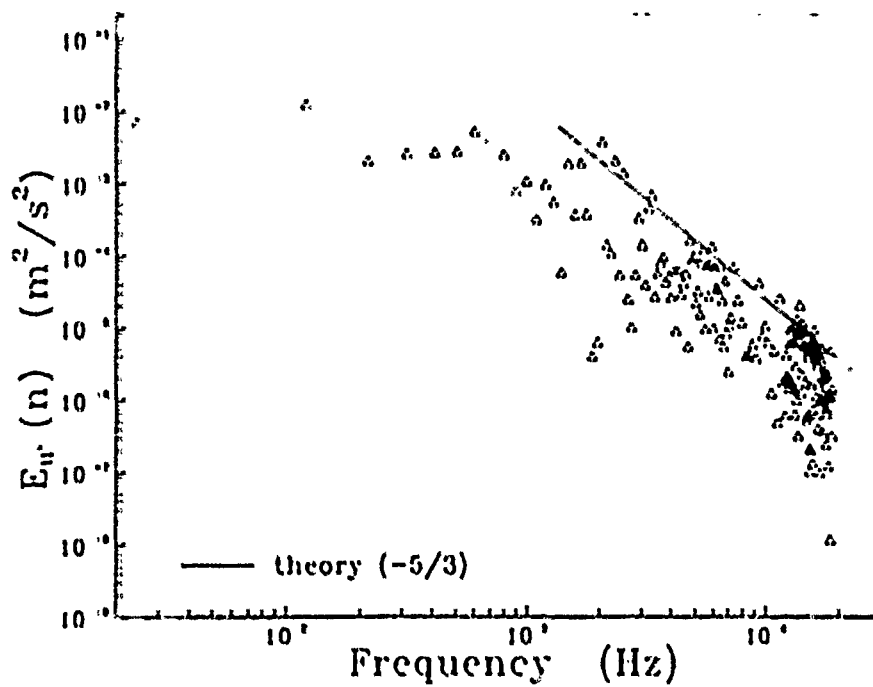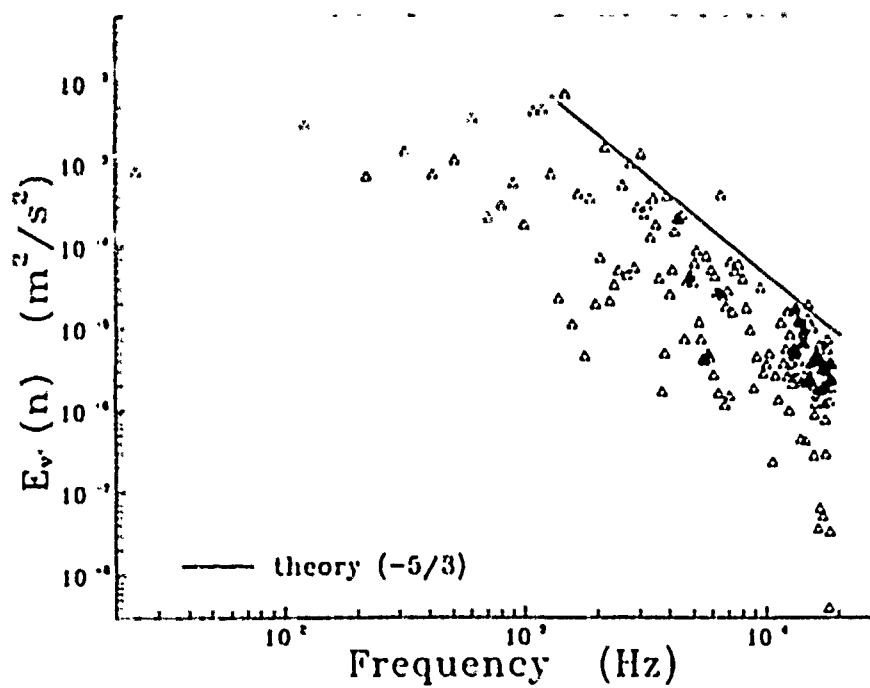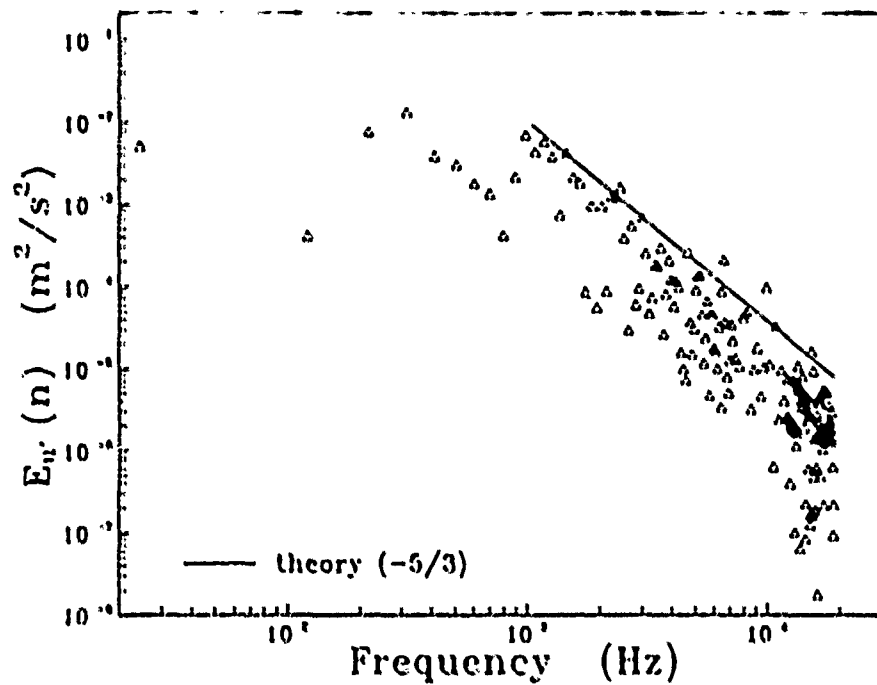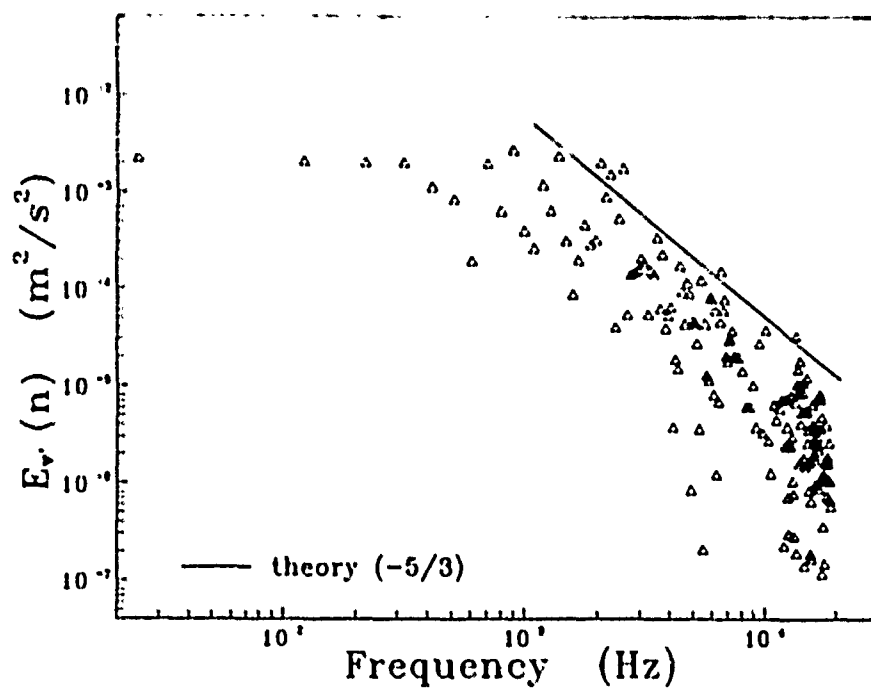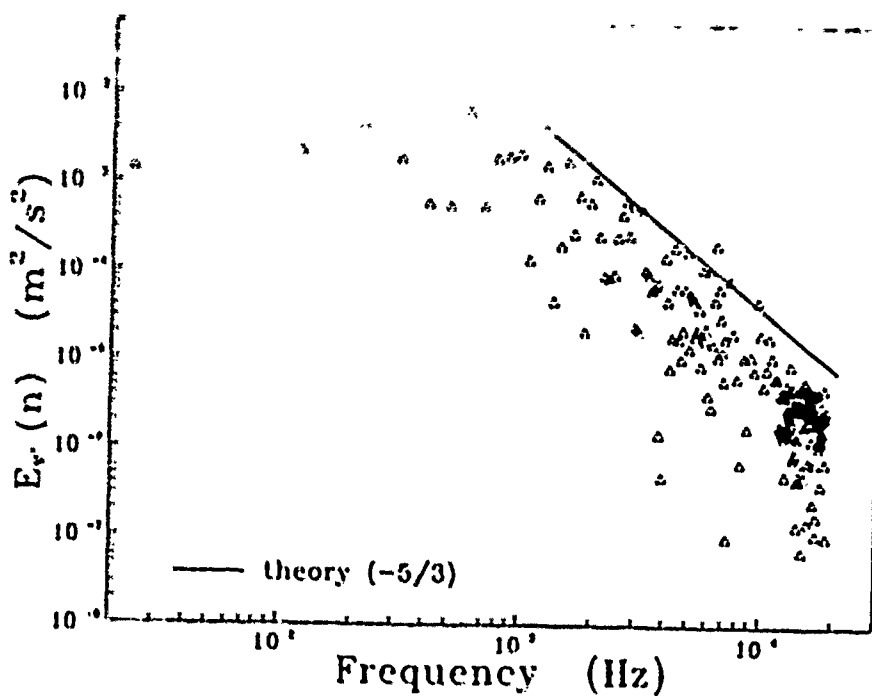Figure B.128. Turbulence energy spectrum for v'^2: Test F33

Appendix C. HOT-WIRE CALIBRATION

The X-type hot-wire, also called the X-wire, is calibrated for flow speed and angle in the turbine cascade wind tunnel.

The geometry of a cross-flow X-wire is given in figure C.1. This geometry is defined arbitrarily as a *normal* configuration for this type of X-wire, that is, wire 2 is towards the right of the oncoming flow vector U_∞ as viewed in the direction of U_∞. An *inverse* configuration of the wire geometry is defined as wire 2 to the left of U_∞.

C.1 Velocity Calibration Measurements

The following procedure details the velocity calibration method for the hot-wire probe.

Initial Probe and Probe Holder Set-up:

The hot-wire probe is inserted into the probe holder and the angle of the bisector with respect to the probe holder is recorded or set to 0 degrees. A simple protractor with a pointer attached to the probe holder is used for this measurement. The pitch angle (δ) is measured to within $\pm$ 0.5 degrees. The angle of the probe longitudinal axis with respect to the probe holder longitudinal axis is the yaw angle, denoted as ψ. The effect of varying ψ on the X-wire signal is determined to be negligible for this type of geometry; for ψ angles between 0–4 degrees.

The probe and probe holder are inserted through the wind tunnel end wall into an area where the free-stream flow angle has been determined. The bisector is set to 0 degrees with respect to the oncoming flow angle ($\beta = 0$ degrees). Refer to Figure C.1.

The Thermo Systems IFA-100 is adjusted for the proper cable, probe holder, and probe resistance for each wire of the X-type hot-wire. Similarly, the operating resistance for each wire is set. Refer to the Thermo Systems IFA-100 operator's manual (TSI Manual, 1983) for detailed instructions on the proper setup of this system.

Speed Measurement
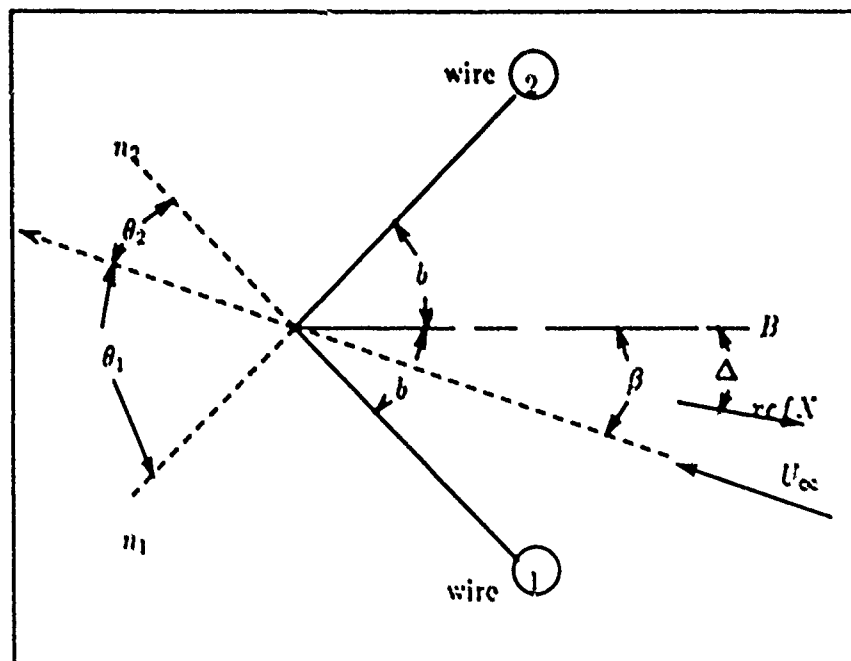
U_∞	= local flow velocity vector
W_1, W_2	= Wire 1 and Wire 2, respectively
B	= X-wire bisector
b	= angle subtended by B and either X-wire
β	= angle subtented by U_∞ and B
n_1	= normal to W_1
n_2	= normal to W_2
θ_1	= angle subtended by U_∞ and n_1
θ_2	= angle subtended by U_∞ and n_2
Δ	= angle subtended by B and the reference X-axis

Figure C.1. End-flow X-type hot-wire geometry

The wind tunnel is started and the free-stream flow is allowed to come to steady state conditions at the lowest speed setting. The output voltage from each hot-wire is measured 400 times using the Hewlett-Packard Integrating Voltmeter, Model No. 44701 and averaged to a single voltage reading. The corresponding differential height in the pitot tube manometer is measured and recorded. The wind tunnel speed is increased incrementally, and hot-wire output signals measured, until a minimum of eleven readings per hot-wire are completed. This process is automated using the Hewlett-Packard HP3852A High-Speed Data Acquisition mainframe, and the X-wire calibration program *XWIRECAL.BAS* listed at the end of this appendix.

C.2 Angle Calibration Measurements

Similar to the speed calibration procedure, the hot-wire is calibrated in the wind tunnel at the same location used for X-wire speed calibration. The wind tunnel speed is set to a single value. A tunnel speed is chosen which is representative of the expected test conditions to be used for subsequent pressure and heat transfer measurements. The probe is rotated from -10 degrees to +10 degrees in 1 degree increments. Hot-wire output voltages for each wire are measured using the Hewlett-Packard Integrating Voltmeter, Model No. 44701A. Each hot-wire output signal is measured 400 times and averaged to a single value of output voltage. The offset angle is recorded at each increment. A total of 21 angle increments and their corresponding hot-wire output voltages are measured and recorded.

A *QuickBASIC* program *XWIRECAL.BAS* automates the angle calibration data collection process for X-wire. A listing of *XWIRECAL.BAS* is included at the end of this appendix for reference. The Hewlett-Packard 3852A High-Speed Data Acquisition System measures and stores all hot-wire signal values in its internal memory buffer. Permanent data storage is on floppy disk.

C.3 Hot-Wire Probe Calibration Equations

The governing equations for the X-wire are given as follows:

$$U_{1_{eff}}{}^2 = U_\infty{}^2(\cos^2\theta_1 + k_1\sin^2\theta_1) \qquad (C.1)$$

$$U_{2_{eff}}{}^2 = U_\infty{}^2(\cos^2\theta_2 + k_2\sin^2\theta_2) \qquad (C.2)$$

where

$U_{1_{eff}}{}^2$ = component of U_∞ perpendicular to W_1

$U_{2_{eff}}{}^2$ = component of U_∞ perpendicular to W_2

k_1, k_2 = coefficients for wire 1 and wire 2, respectively

The signal output from each hot-wire, in terms of voltage, is

$$E_1{}^2 = c_1 + b_1 U_{1_{eff}}{}^{\frac{1}{2}} + a_1 U_{1_{eff}} \qquad (C.3)$$

$$E_2{}^2 = c_2 + b_2 U_{2_{eff}}{}^{\frac{1}{2}} + a_2 U_{2_{eff}} \qquad (C.4)$$

where

E_1 = predicted wire 1 output signal (volts)

E_2 = predicted wire 2 output signal (volts)

a_1, b_1 and c_1 = wire 1 velocity calibration coefficients

a_2, b_2 and c_2 = wire 2 velocity calibration coefficients

The free-stream flow velocity (U_∞) is computed from the differential height of the pitot tube manometer as

$$U_\infty = \left(\frac{2}{\rho_\infty}\Delta_h \cdot 249\right)^{\frac{1}{2}} \qquad (C.5)$$

where

ρ_∞ = free-stream static air density

Δ_h = differential height of manometer in inches of water

249 = conversion factor for inches of water to kPa conversion

Using Equation C.5 in conjunction with Equation C.1 and Equation C.2 for wires 1 and 2, respectively, $U_{1_{eff}}$ and $U_{2_{eff}}$ is computed for each wind tunnel speed measured with the

hot-wire probe. Values for k_1 and k_2 are arbitrarily specified at this point of the calibration procedure.

A quadratic fit is computed for Equations C.1 and C.2 for the independent variables $U_{1_{eff}}^{\frac{1}{2}}$ and $U_{2_{eff}}^{\frac{1}{2}}$ using matrix multiplication (*MATHCAD* Manual, 1987).

Matrices $\underline{W_1}$ and $\underline{W_2}$ are formed

$$\underline{W_1}^{<1>} = 1$$

$$\underline{W_1}^{<2>} = U_{1_{eff}}^{\frac{1}{2}}$$

$$\underline{W_1}^{<3>} = U_{1_{eff}} \qquad (C.6)$$

$$\underline{W_2}^{<1>} = 1$$

$$\underline{W_2}^{<2>} = U_{2_{eff}}^{\frac{1}{2}}$$

$$\underline{W_2}^{<3>} = U_{2_{eff}} \qquad (C.7)$$

where

$\underline{W_1}^{<1,2,3>}$ = columns 1, 2, and 3 of $\underline{W_1}$, respectively

$\underline{W_2}^{<1,2,3>}$ = columns 1, 2, and 3 of $\underline{W_2}$, respectively

Then the coefficients a_1, b_1, and c_1 of Equation C.3 are found from the matrix product

$$\left\{ \begin{array}{c} a_1 \\ b_1 \\ c_1 \end{array} \right\} = (\underline{W_1}^T \cdot \underline{W_1})^{-1} \cdot (\underline{W_1}^T \cdot E_1'^{2}) \qquad (C.8)$$

where

$\underline{W_1}^T$ = transpose of $\underline{W_1}$

E_1' = measured hot-wire output voltages for wire 1

Coefficients a_2, b_2, and c_2 of Equation C.4 are determined as

$$\left\{ \begin{array}{c} a_2 \\ b_2 \\ c_2 \end{array} \right\} = (\underline{W_2}^T \cdot \underline{W_2})^{-1} \cdot (\underline{W_2}^T \cdot E_2'^2) \tag{C.9}$$

where

$\underline{W_2}^T$ = transpose of $\underline{W_2}$

E_2' = measured hot-wire output voltages for wire 2

Hence, Equation C.8 and Equation C.9 give a quadratic fit of the speed calibration data for wire 1 and wire 2, respectively. Substitution of the coefficients determined from Equation C.8 into Equation C.3 give a predicted value E_1^2. Similarly, coefficients found in Equation C.9 are substituted into Equation C.4 to give E_2^2.

The sum of the squared error between predicted and measured output signal for all time steps, N, is computed as

$$ERR_{1_{SSE}} = \sum_i^N E_{1_i}^2 - E_{1_i}'^2 \tag{C.10}$$

$$ERR_{2_{SSE}} = \sum_i^N E_2^2 - E_2'^2 \tag{C.11}$$

where

N = total number of speed calibration data measurements for wires 1 and 2

E_1' = measured wire 1 output voltage

E_2' = measured wire 2 output voltage

Coefficients k_1 and k_2 are determined from the angle calibration data as follows.

U_∞ is computed from Equation C.5 using the tunnel speed setting from the angle calibration measurement. From Equation C.1 and Equation C.2, $U_{1_{eff}}^2$ and $U_{2_{eff}}^2$ are computed. Equation C.1 and Equation C.2 are presented below for reference.

$$U_{1_{eff}}^2 = U_\infty^2(\cos^2\theta_1 + k_1\sin^2\theta_1)$$

$$U_{2_{eff}}^2 = U_\infty^2(\cos^2\theta_2 + k_2\sin^2\theta_2)$$

Substitution of $U_{1_{eff}}$ and $U_{2_{eff}}$ into Equation C.3 and Equation C.4, respectively, yield predictions for E_1^2 and E_2^2.

The sum of the squared error between the predicted output voltage and the output voltage measured at each offset angle increment for all N values is given by

$$ERR_{1_{SSE}}^A = \sum_i^N E_1^2 - E_1''^2 \qquad \text{(C.12)}$$

$$ERR_{2_{SSE}}^A = \sum_i^N E_2^2 - E_2''^2 \qquad \text{(C.13)}$$

where

N = total number of angle calibration data measurements for wires 1 and 2

E_1'' = measured wire 1 output voltage

E_2'' = measured wire 2 output voltage

Coefficients k_1 and k_2 are chosen so as to minimize the sum of the squared error as calculated in Equations C.12 and C.13.

Actual implementation of the above X-wire calibration is coded using *MATHCAD*, version 2.1. *MATHCAD* allows the user to see plots of quadratic fits for both wire equations while simultaneously choosing coefficients k_1 and k_2 which minimize the error. A sample printout of a hot-wire calibration using *MATHCAD* is included in this appendix.

C.4 X-Type Hot-Wire Calibration Example

Sample calibration of a hot-wire probe using *MATHCAD*, version 2.1.

Serial No. 7717
Wires 8 28 G9   Voltmeter = HP 44701A   Integrating voltmeter

Environmental Conditions: The turbine cascade pilot tunnel was
                                          used to calibrate all hot wire
    $T_0 := 20.77$ deg C   measurements. The incompressible
                                          Bernoulli Equation is used to convert
    $P_0 := 1.0704$ Pa   all pressure readings to velocity.

    RH := 90 %

    $A := 1.1614$ kg m   Dewitt,"Intro. to Heat Transfer".
                                          Table A.4, page 681.

Data files are stored on "..." disk
titled)WIRE CALIBRATION.
....

Read in the data for the x-wire calibration:

    $angcal := READPRN(AS_7717)$
    $dh := READPRN(x\_2\_7717)$ $vel := dh$

                                               $E1 := dh^{1}$

                                               $E2 := dh^{2}$

Transform the manometer readings into velocity readings:

    $n := length(vel)$

    $i := 0 .. n - 1$

    $vel := \left[\left[\frac{c}{c}\right] \cdot v1 \cdot 249\right] \cdot 0$

    $velerr := \left[\frac{c}{c}\right] \cdot .005 \cdot 249$

Signal output vs sqr root of velocity

    $E1_i , E2_i$ volts

    $\sqrt{vel_i}$

Sample calibration of a hot-wire probe using *MATHCAD* version 2.1

Determine the constants of the calibration equation:

channel 1

$$deg := \frac{\pi}{180}$$

$$U1_{eff} := \left[\left[vel \left[(\cos(45 \, deg))^2 + 11 \, (\sin(45 \, deg))^2 \right] \right] \right]$$

channel 2

$$U2_{eff} := \left[\left[vel \left[(\cos(45 \, deg))^2 + 12 \, (\sin(45 \, deg))^2 \right] \right] \right]$$

$$E12_{eff} := \sqrt{\left[U1_{eff} \right]^2}$$

$$U2_{eff} := \sqrt{\left[E2_{eff} \right]^2}$$

$$W1_{i,1} := 1 \qquad W2_{i,1} := 1$$

$$W1_{i}^{1} := U1_{eff} \qquad W1_{i}^{2} := E12_{eff}$$

$$W2_{i}^{1} := U2_{eff} \qquad W2_{i}^{2} := E2_{eff}$$

$$ES01 := \sqrt{\left[E1 \right]^2} \qquad\qquad ES02 := \sqrt{\left[2 \right]^2}$$

$$b := \left[W1^T W1 \right]^{-1} W1^T ES01 \qquad b1 := \left[W2^T W2 \right]^{-1} W2^T E1.2$$

$$b = \begin{bmatrix} -22.002 \\ 10.573 \\ -0.107 \end{bmatrix} \qquad\qquad b1 = \begin{bmatrix} -12.46 \\ 4.068 \\ -0.02 \end{bmatrix}$$

$$quad1 \left[U1_{eff} \right] := b_0 + b_1 \left[U1_{eff} \right] + b_2 U1_{eff}^2$$

$$quad2 \left[U2_{eff} \right] := b1_0 + b1_1 \left[U2_{eff} \right] + b1_2 U2_{eff}^2$$

$$SSE1_0 := \sum \left[\left[ES01 - quad1 \left[U1_{eff} \right] \right] \right]^2 \qquad SSE2_0 := \sum \left[\left[ES02 - quad2 \left[U2_{eff} \right] \right] \right]^2$$

$$MSE1_0 := \frac{SSE1_0}{n-2} \qquad\qquad MSE2_0 := \frac{SSE2_0}{n-2}$$

Sample calibration of a hot-wire probe using *MATHCAD*, version 2.1.

Channel 1 Calibration Curve

Channel 2 Calibration Curve
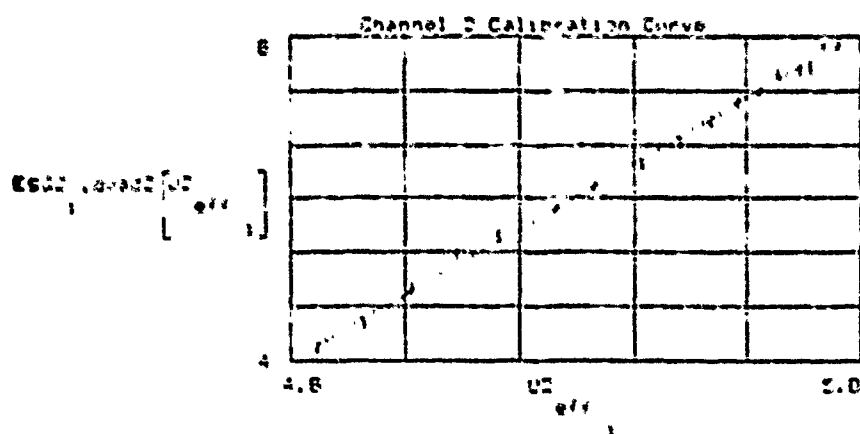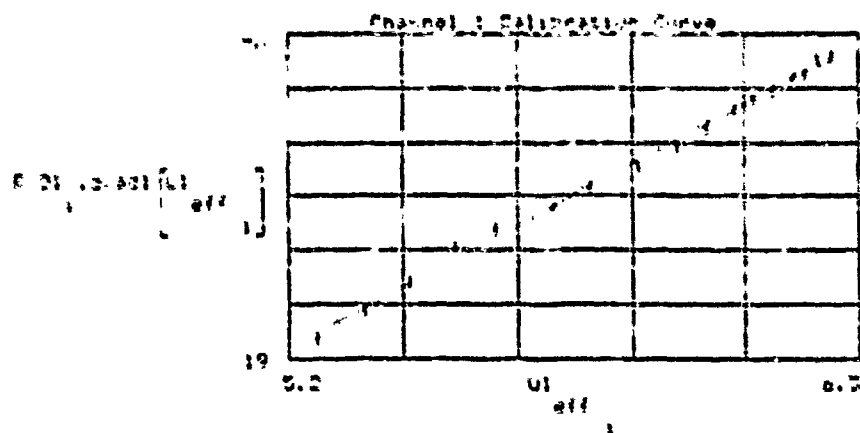
Read in the angle calibration data:

dr1 := 5.6°

$e1 := angcal^{1}$

$U_{\alpha} := \left[\sqrt{\left[\frac{E}{U}\right]} \cdot dr1 \cdot 249 \right]$

$e2 := argcal^{2}$

Sample calibration of a hot-wire probe using *MATHCAD*, version 2.1.

$$U1_{eff_i} := U_i \cdot \left[\left[(\cos(45 - \phi) \deg)^2 + k1 \cdot (\sin(45 - \phi) \deg)^2 \right] \right]$$

$$U2_{eff_i} := U_i \cdot \left[\left[(\cos(45 + \phi) \deg)^2 + k2 \cdot (\sin(45 + \phi) \deg)^2 \right] \right]$$

$$E1theory := \left[\left[a_1 + b_1 \cdot U1_{eff} + c_2 \cdot U1_{eff}^2 \right] \right]$$

$$E2theory := \left[\left[b1 + b1 \cdot U2_{eff} + b1 \cdot U2_{eff}^2 \right] \right]$$

$$err1 := \left[(E1theory - e1)^2 \right] \qquad err2 := \left[(E2theory - e2)^2 \right]$$

$$m := last(e) \qquad n = 2 \qquad i := 0 .. m$$

Minimum squared error:

Sample calibration of a hot-wire probe using *MATHCAD*, version 2.1.

errem1 := Σerr1   errsum1 = ...

errem2 := Σerr2   errsum2 = ...

Sample calibration of a hot-wire probe using *MATHCAD*, version 2.1.
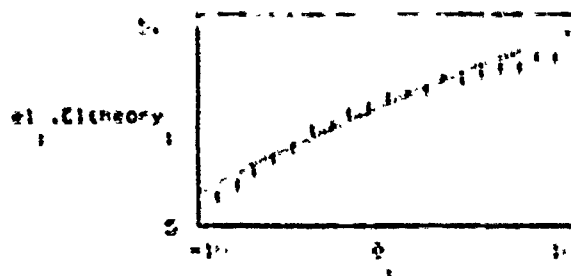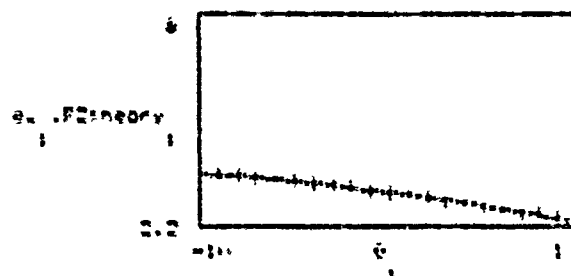
```
' Hot wire  (X type calibration program)
' High speed voltmeter is used for signal measurement.
' Written by Lello Galassi 7/1/89.
'
' This calibration program reads the voltage output by each wire
' during calibration testing. Each channel is read 500 times then
' averaged for a mean voltage.
'
' The program loops and triggers on pressing any key.
'******************************************************************

CLS

PRINT "***********************************************"

PRINT "X-wire calibration program for the HP 3852A"

PRINT "    HP44701 Integrating Voltmeter in slot 0600"

PRINT "    Disconnect the dedicated high-speed FET cable from tne HP44702B"

PRINT "": SLEEP 4

5 CLS :  INPUT "Is this a (V)elocity or (A)ngle type calibration?  ", var$

INPUT "Enter wire serial no. (data stored on A:\SR#\*.dat)? ", dir$

INPUT "Filename to store data on disk A?  ", filename$

OPEN "A:\" + dir$ + "\" + filename$ + ".dat" FOR OUTPUT AS #1

IF (var$ = "V") THEN

    INPUT "Current air density? ", rho!

END IF

PRINT "**********************************************************"

PRINT ""

VIEW PRINT 8 TO 22
```

```
CALL ibfind("hp3852", dvm%)

CALL ibwrt(dvm%, "rst")

10  PRINT "Press any key to begin scan "

DO: LOOP WHILE INKEY$ = ""

CALL ibwrt(dvm%, "disp off")

CALL ibwrt(dvm%, "real A(399),B(399),L,H,AV,S")

' This call configures the HP44701 Integrating Voltmeter as the measuring
' instrument.

CALL ibwrt(dvm%, "use 600;nplc 1")

CALL ibwrt(dvm%, "conf dcv;nrdgs 400;azero once")

' Procede with channel 1 and channel 2 voltage scan.

CALL ibwrt(dvm%, "meas dcv,321,use 600,into A;conf dcv;nrdgs 400")

CALL ibwrt(dvm%, "meas dcv,322,use 600,into B")

'Perform statistcal averaging on the measurements stored in arrays
' A and B.

CALL ibwrt(dvm%, "stat L,H,AV,S,A")

CALL ibwrt(dvm%, "vread AV")

CALL ibwrt(dvm%, "disp on; disp AV")

rd$ = SPACE$(16)

CALL ibrd(dvm%, rd$)

chan1! = VAL(rd$)

' Output to the screen and to the data storage file

COLOR 0, 5
```

```
PRINT "channel 1 voltage is:", chan1!

CALL ibwrt(dvm%, "stat L,H,AV,S,B")

CALL ibwrt(dvm%, "vread AV")

CALL ibrd(dvm%, rd$)

chan2! = VAL(rd$)

PRINT "channel 2 voltage is:", chan2!

IF (var$ = "V") THEN

    INPUT "Input the current velocity setting ", vel!

ELSE

    INPUT "Input the current angle setting ", vel!

END IF

IF (var$ = "V") THEN

   vel! = SQR(vel! * 249! * 2! / rho)

   PRINT "current air speed is: ", vel!, " m/sec"

ELSE

   PRINT "current angle setting is:", vel!, "degrees from bisector"

END IF

' Output to data storage file on disk A:

PRINT #1, vel!, chan1!, chan2!

INPUT "quit?  (y or n) ", q$

IF q$ <> "y" THEN

   GOTO 10

ELSE
```

```
      CLOSE #1

      PRINT "This stage of calibration completed - data stored in", filename$

      PRINT ""

END IF

INPUT "Do an angle calibration for the current hot wire? (y) or (n)", rst$

IF (rst$ = "y") THEN

      CLS 2

      GOTO 5

END IF

END
```

Appendix D. *ADDITIONAL HEAT TRANSFER TESTS—STANTON NUMBER RATIOS AND NUSSELT NUMBER RATIOS*
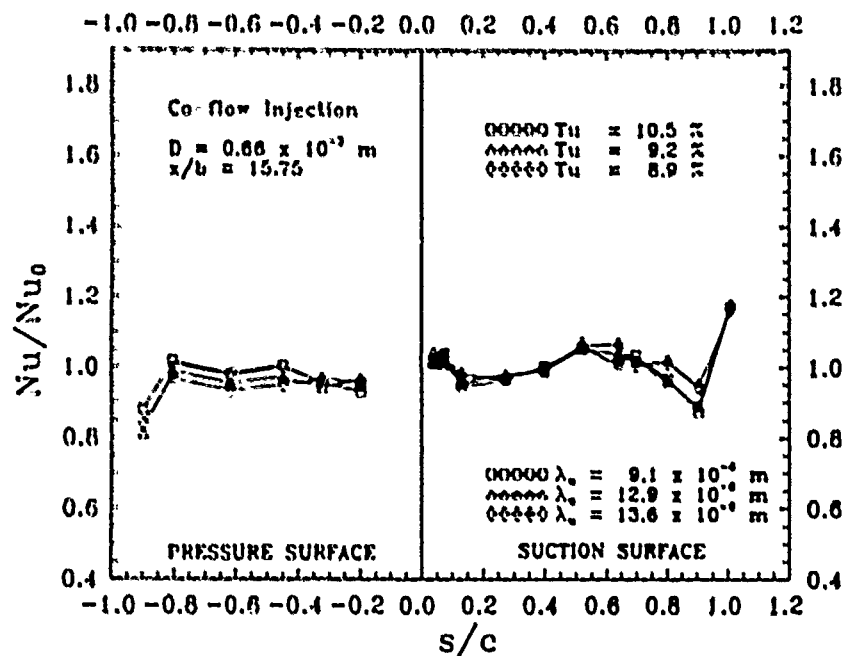
Figure D.1.   Nusselt number on the turbine blade for co-flow injection. $D = 0.66$ mm.
Test A11, A12 and A13. Jet-grid at station 0
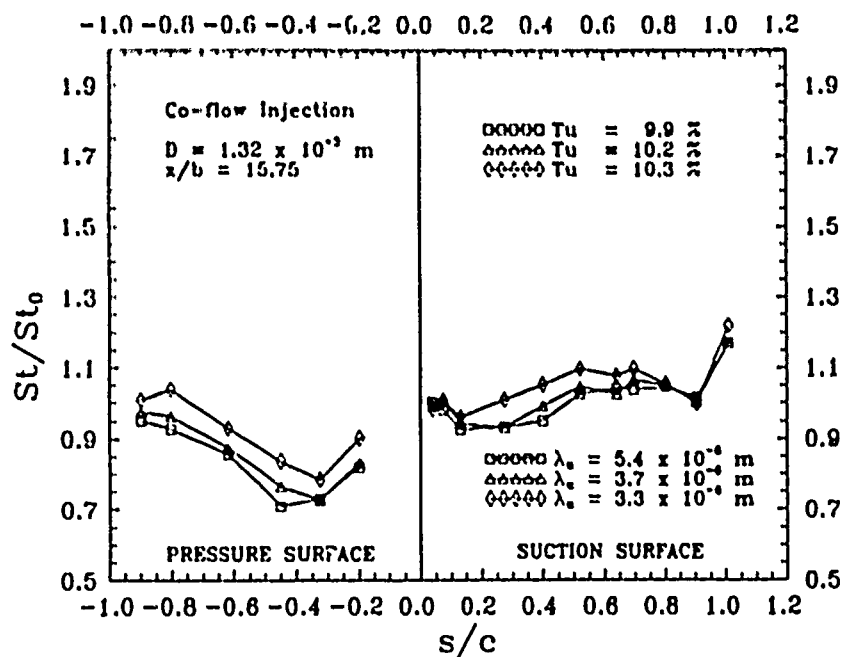
Figure D.2.   Stanton number on the turbine blade for co-flow injection. $D = 1.32$ mm.
Test A21, A22 and A23. Jet-grid at station 0
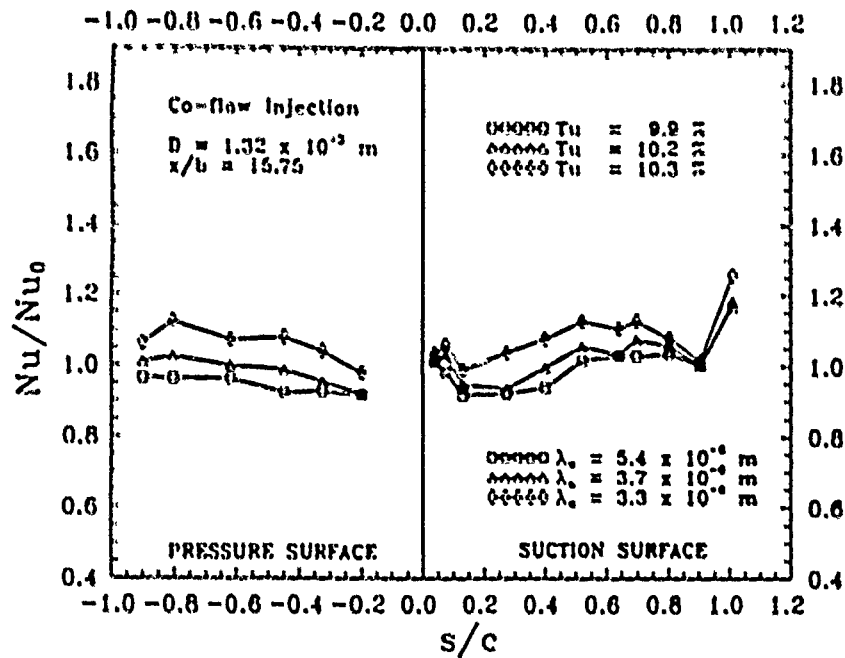
Figure D.3. Nusselt number on the turbine blade for co-flow injection. $D = 1.32$ mm. Test A21, A22 and A23. Jet-grid at station 0
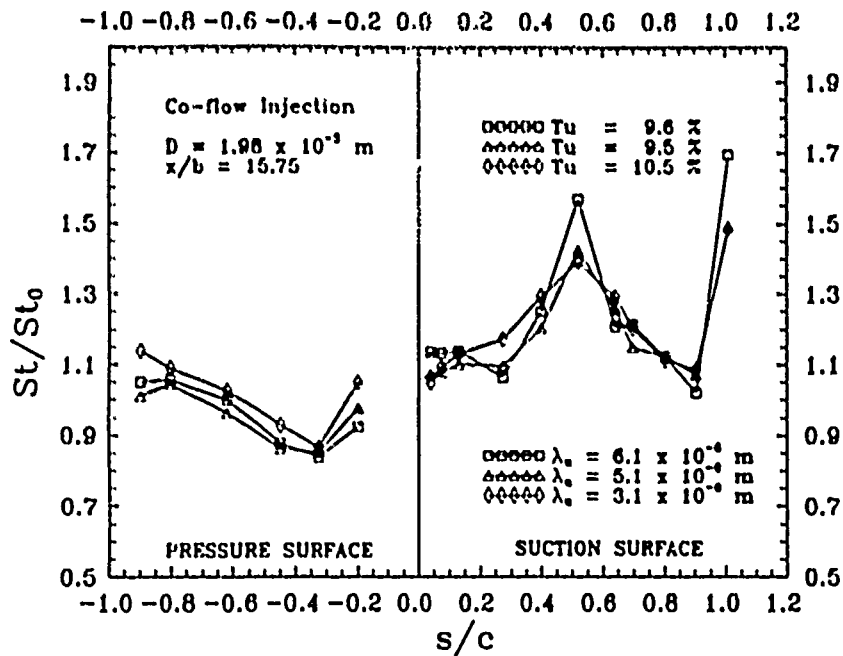
Figure D.4. Stanton number on the turbine blade for co-flow injection. $D = 1.98$ mm. Test A31, A32 and A33. Jet-grid at station 0
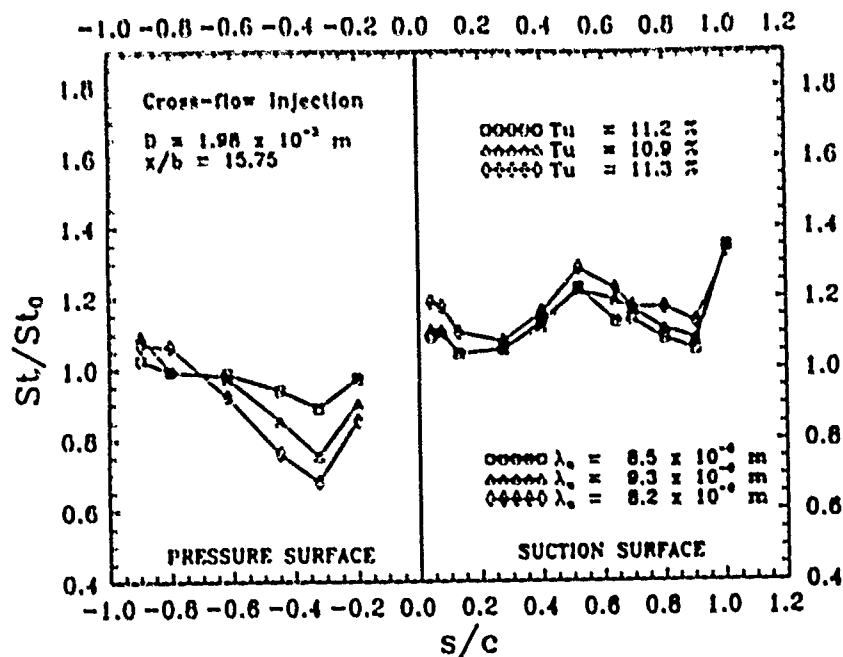
Figure D.5. Stanton number on the turbine blade for cross-flow injection. $D = 1.98$ mm. Test B31, B32 and B33. Jet-grid at station 0
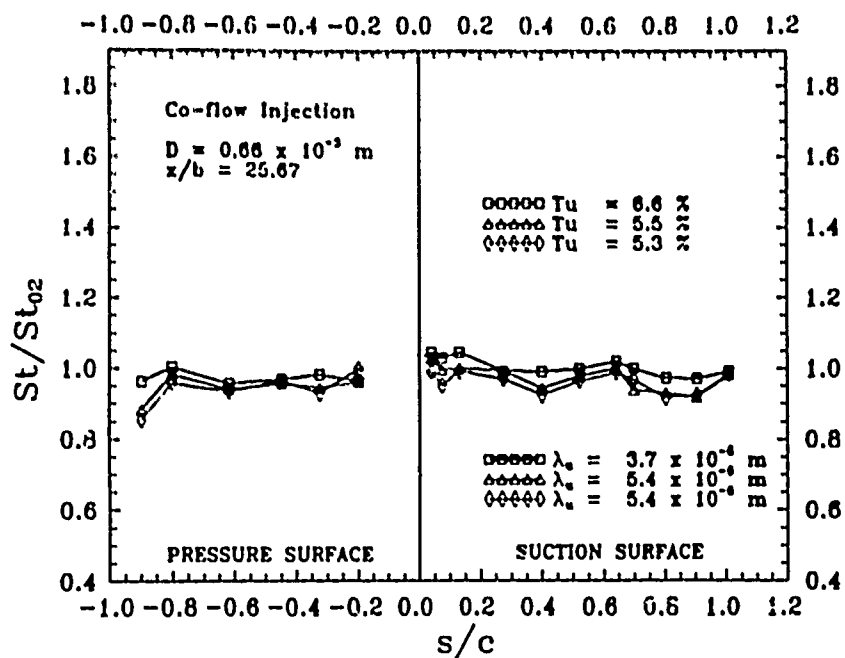
Figure D.6. Stanton number on the turbine blade for co-flow injection. $D = 0.66$ mm. Test D11, D12 and D13. Jet-grid at station 02
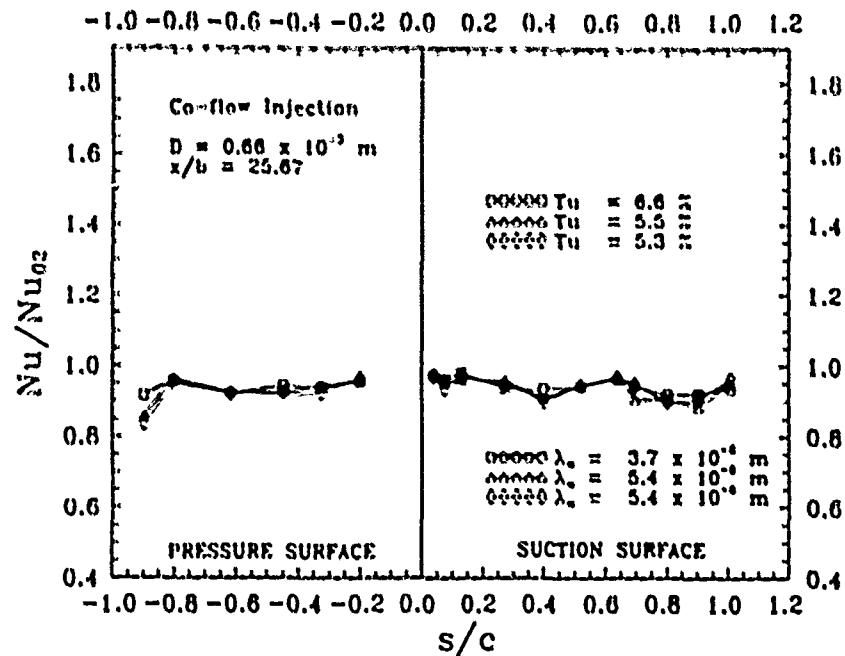
Figure D.7. Nusselt number on the turbine blade for co-flow injection. $D = 0.66$ mm. Test D11, D12 and D13. Jet-grid at station 02
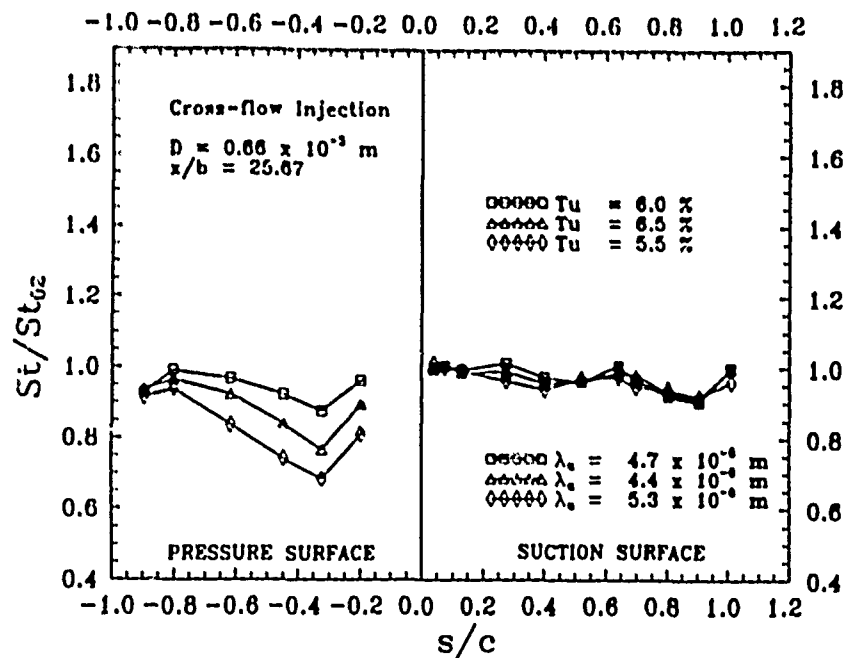
Figure D.8. Stanton number on the turbine blade for cross-flow injection. $D = 0.66$ mm. Test E11, E12 and E13. Jet-grid at station 02
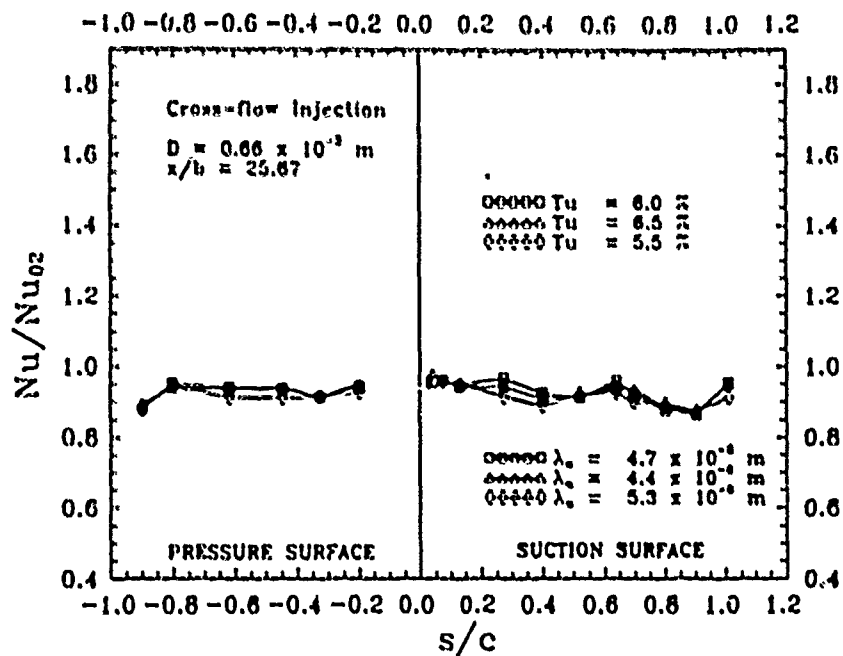
Figure D.9. Nusselt number on the turbine blade for cross-flow injection. $D = 0.66$ mm. Test E11, E12 and E13. Jet-grid at station 02
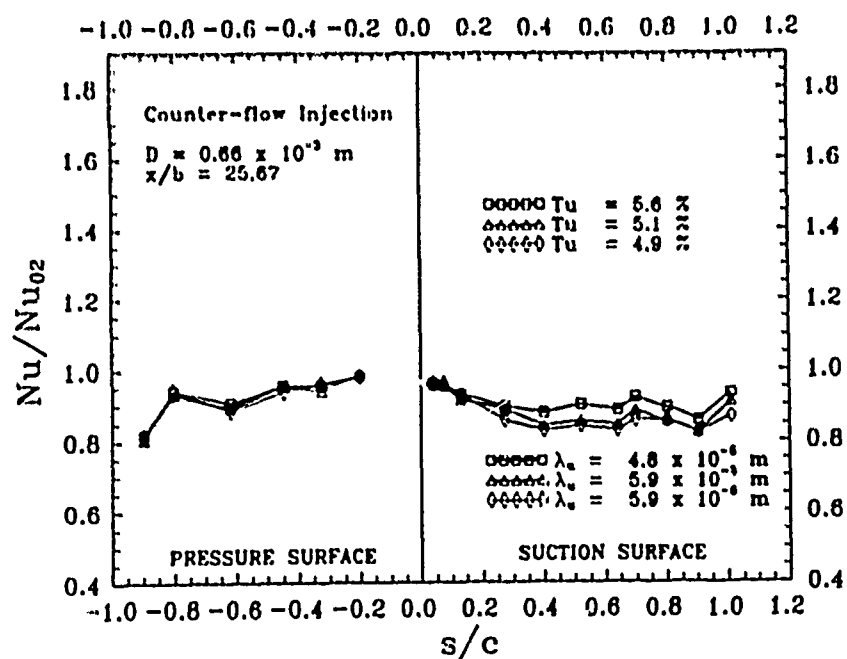
Figure D.10. Nusselt number on the turbine blade for counter-flow injection. $D = 0.66$ mm. Test F11, F12 and F13. Jet-grid at station 02
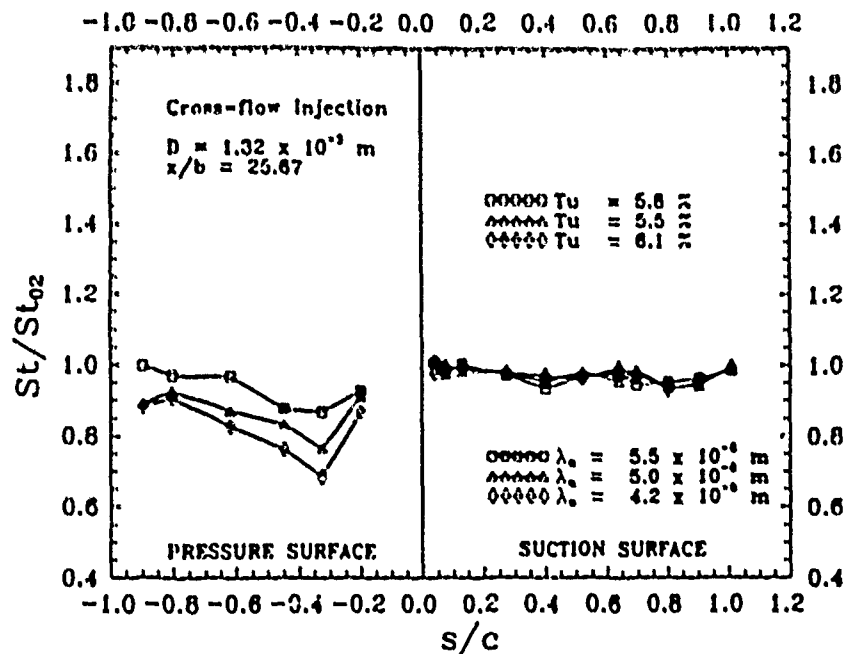
Figure D.11. Stanton number on the turbine blade for cross-flow injection. $D = 1.32$ mm. Test E21, E22 and E23. Jet-grid at station 02
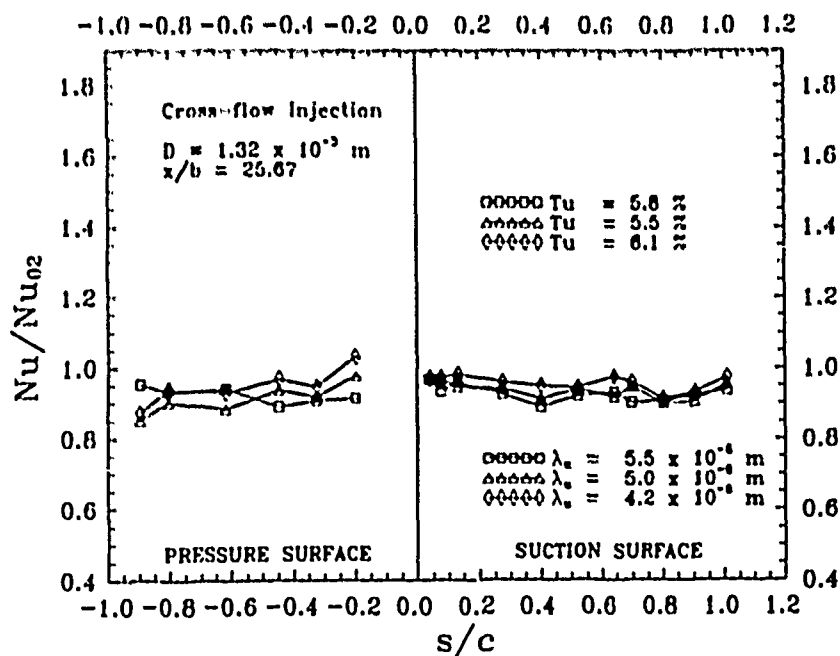
Figure D.12. Nusselt number on the turbine blade for cross-flow injection. $D = 1.32$ mm. Test E21, E22 and E23. Jet-grid at station 02
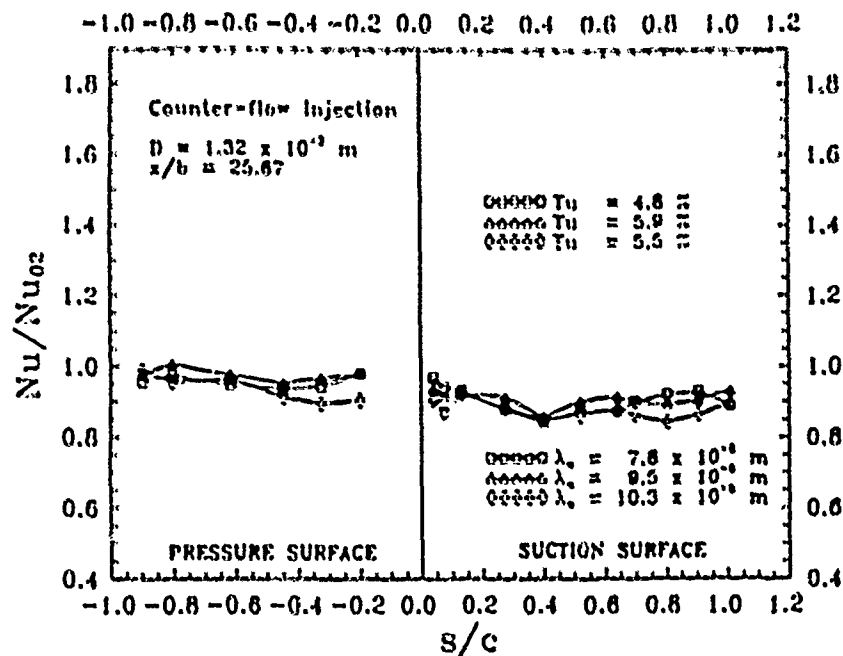
Figure D.13. Nusselt number on the turbine blade for counter-flow injection. $D = 1.32$ mm. Test F21, F22 and F23. Jet-grid at station 02
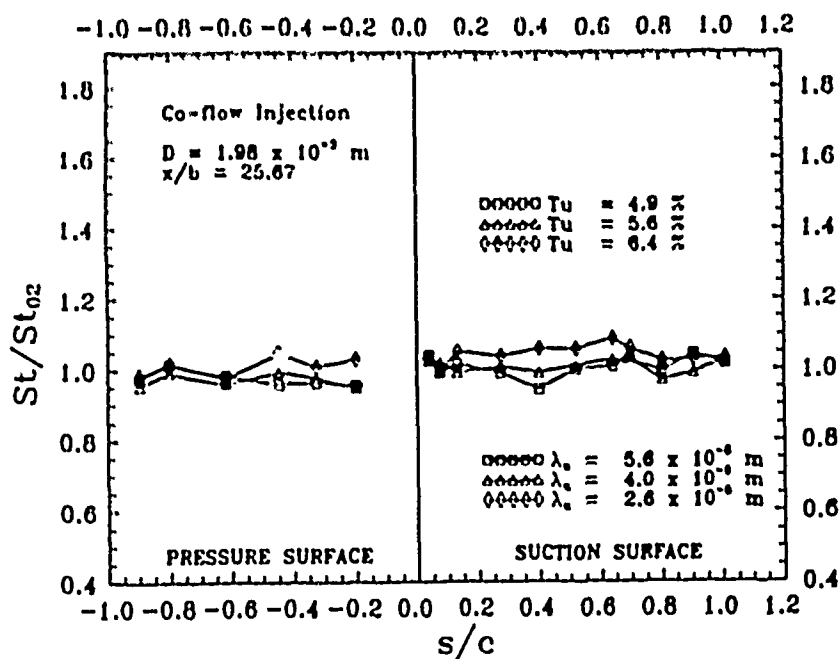
Figure D.14. Stanton number on the turbine blade for co-flow injection. $D = 1.98$ mm. Test D31, D32 and D33. Jet-grid at station 02
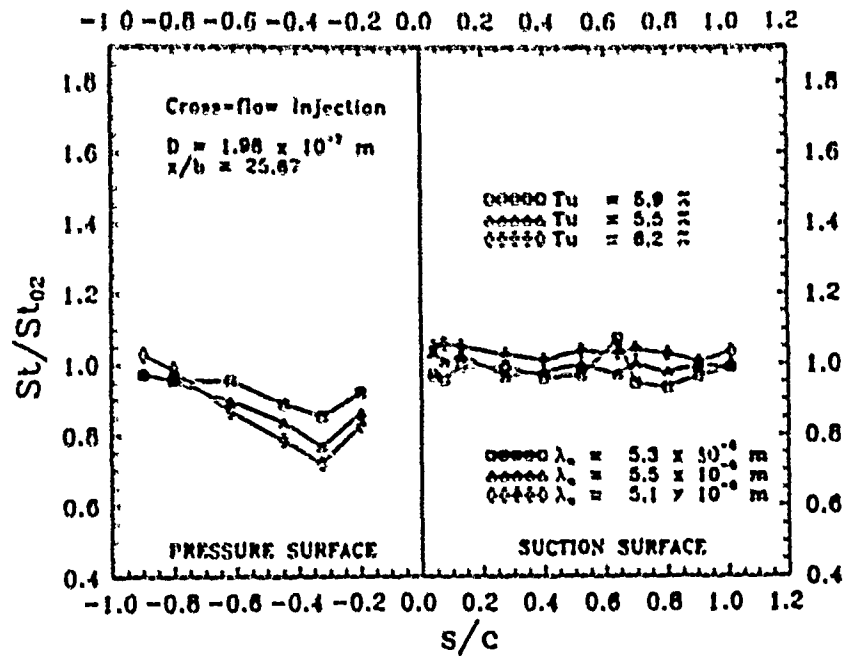
Figure D.15. Stanton number on the turbine blade for cross-flow injection. $D = 1.98$ mm. Test E31, E32 and E33. Jet-grid at station 02
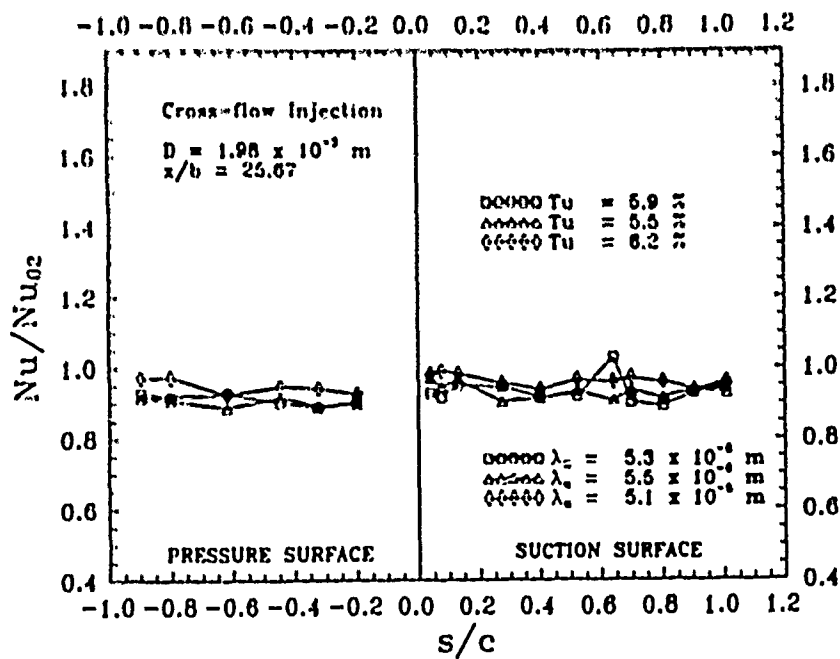
Figure D.16. Nusselt number on the turbine blade for cross-flow injection. $D = 1.98$ mm. Test E31, E32 and E33. Jet-grid at station 02

D-9

Appendix E. *DATA ACQUISITION SOURCE CODE LISTING*

HP3852A Data Acquisition System Source Code

Written by 1Lt Lello Galassi, 1989

Source code language: Microsoft *QuickBASIC*, version 4.5

```
'••••••••••••••••••••••••••••••••••••••••••••••••••••••••••••••••••••••
' HP3852A Data Acquisition Program for High Turbulence Heat Transfer
' (for use on the Linear Turbine Cascade Wind Tunnel, BLDG 19)
'
' Written by Lt Lello Galassi, 6/23/89
'••••••••••••••••••••••••••••••••••••••••••••••••••••••••••••••••••••••

' QuickBASIC Declarations Rev. C.4


' Common GPIB status variables

  COMMON SHARED ibsta%, iberr%, ibcnt%

' GPIB Subroutine Declarations

  DECLARE SUB IBBNA (BD%, BDNAME$)
  DECLARE SUB IBCAC (BD%, V%)
  DECLARE SUB IBCLR (BD%)
  DECLARE SUB IBCMD (BD%, CMD$)
  DECLARE SUB IBCMDA (BD%, CMD$)
  DECLARE SUB IBDMA (BD%, V%)
  DECLARE SUB IBEOS (BD%, V%)
  DECLARE SUB IBEOT (BD%, V%)
  DECLARE SUB IBFIND (BDNAME$, BD%)
  DECLARE SUB IBGTS (BD%, V%)
  DECLARE SUB IBIST (BD%, V%)
  DECLARE SUB IBLOC (BD%)
  DECLARE SUB IBONL (BD%, V%)
  DECLARE SUB IBPAD (BD%, V%)
  DECLARE SUB IBPCT (BD%)
  DECLARE SUB IBPPC (BD%, V%)
  DECLARE SUB ibrd (BD%, rd$)
  DECLARE SUB IBRDA (BD%, rd$)
```

```
DECLARE SUB IBRDF (BD%, FLNAME$)
DECLARE SUB IBRDI (BD%, IARR%(), CNT%)
DECLARE SUB IBRDIA (BD%, IARR%(), CNT%)
DECLARE SUB IBRPP (BD%, PPR%)
DECLARE SUB IBRSC (BD%, V%)
DECLARE SUB IBRSP (BD%, SPR%)
DECLARE SUB IBRSV (BD%, V%)
DECLARE SUB IBSAD (BD%, V%)
DECLARE SUB IBSIC (BD%)
DECLARE SUB IBSRE (BD%, V%)
DECLARE SUB IBSTOP (BD%)
DECLARE SUB IBTMO (BD%, V%)
DECLARE SUB IBTRAP (MASK%, MODE%)
DECLARE SUB IBTRG (BD%)
DECLARE SUB IBWAIT (BD%, MASK%)
DECLARE SUB IBWRT (BD%, WRT$)
DECLARE SUB IBWRTA (BD%, WRT$)
DECLARE SUB IBWRTF (BD%, FLNAME$)
DECLARE SUB IBWRTI (BD%, IARR%(), CNT%)
DECLARE SUB IBWRTIA (BD%, IARR%(), CNT%)
```

' GPIB Function Declarations

```
DECLARE FUNCTION ILBNA% (BD%, BDNAME$)
DECLARE FUNCTION ILCAC% (BD%, V%)
DECLARE FUNCTION ILCLR% (BD%)
DECLARE FUNCTION ILCMD% (BD%, CMD$, CNT%)
DECLARE FUNCTION ILCMDA% (BD%, CMD$, CNT%)
DECLARE FUNCTION ILDMA% (BD%, V%)
DECLARE FUNCTION ILEOS% (BD%, V%)
DECLARE FUNCTION ILEOT% (BD%, V%)
DECLARE FUNCTION ILFIND% (BDNAME$)
DECLARE FUNCTION ILGTS% (BD%, V%)
DECLARE FUNCTION ILIST% (BD%, V%)
DECLARE FUNCTION ILLOC% (BD%)
DECLARE FUNCTION ILONL% (BD%, V%)
DECLARE FUNCTION ILPAD% (BD%, V%)
DECLARE FUNCTION ILPCT% (BD%)
DECLARE FUNCTION ILPPC% (BD%, V%)
DECLARE FUNCTION ILRD% (BD%, rd$, CNT%)
DECLARE FUNCTION ILRDA% (BD%, rd$, CNT%)
DECLARE FUNCTION ILRDF% (BD%, FLNAME$)
DECLARE FUNCTION ILRDI% (BD%, IARR%(), CNT%)
DECLARE FUNCTION ILRDIA% (BD%, IARR%(), CNT%)
DECLARE FUNCTION ILRPP% (BD%, PPR%)
```

```
DECLARE FUNCTION ILRSC% (BD%, V%)
DECLARE FUNCTION ILRSP% (BD%, SPR%)
DECLARE FUNCTION ILRSV% (BD%, V%)
DECLARE FUNCTION ILSAD% (BD%, V%)
DECLARE FUNCTION ILSIC% (BD%)
DECLARE FUNCTION ILSRE% (BD%, V%)
DECLARE FUNCTION ILSTOP% (BD%)
DECLARE FUNCTION ILTMO% (BD%, V%)
DECLARE FUNCTION ILTRAP% (MASK%, MODE%)
DECLARE FUNCTION ILTRG% (BD%)
DECLARE FUNCTION ILWAIT% (BD%, MASK%)
DECLARE FUNCTION ILWRT% (BD%, WRT$, CNT%)
DECLARE FUNCTION ILWRTA% (BD%, WRT$, CNT%)
DECLARE FUNCTION ILWRTF% (BD%, FLNAME$)
DECLARE FUNCTION ILWRTI% (BD%, IARR%(), CNT%)
DECLARE FUNCTION ILWRTIA% (BD%, IARR%(), CNT%)

DECLARE SUB TMON (dvm%)
DECLARE SUB GPIBERR ()
DECLARE SUB PRUN (dvm%, rho!, dt$, FileName$, iflag%, Temp!)
DECLARE SUB FRUN (dvm%, FileName$)
DECLARE SUB TRUN (dvm%, Temp!, FileName$, rho!)
DECLARE SUB CONVERT (VALS!(), NN%)
DECLARE SUB FFT ()
DECLARE SUB PLOTT (xdat1!(), ydat1!(), xmin!, xmax!, ymin!, ymax!,
                   xlab$, ylab$, pltlab$, ntot%)
DECLARE SUB SECPRES (dvm%, sfa!)




DIM chord(24) AS SINGLE


'                      Initialize the screen

CLS : COLOR 3, 0: LOCATE 7, 12

PRINT "HP3852 Controller Program": PRINT

LOCATE 8, 12

LOCATE 10, 12

PRINT "This program controls the HP3852 Data Acquisition System"
```

```
LOCATE 11, 12

PRINT "for high-turbulence heat transfer measurements."

PRINT ""

SLEEP 5

CLS : LOCATE 7, 7
INPUT "Bypass turn-on sequence? ", ans$
IF ans$ = "y" THEN
GOTO 55
END IF

PRINT : PRINT "Initialization of Program:": PRINT

10 INPUT "HP3852 on? (y or n)", ans$
IF ans$ <> "y" THEN
BEEP
PRINT "TURN ON HP3852"
GOTO 10
END IF

20 INPUT "Blade and Scanivalve power supplies on? (y or n)", ans$
IF ans$ <> "y" THEN
BEEP
PRINT "TURN ON BOTH POWER SUPPLIES"
GOTO 20
END IF

30 INPUT "Scanivalve on? (y or n)", ans$
IF ans$ <> "y" THEN
BEEP
PRINT "TURN ON SCANIVALVE"
GOTO 30
END IF

40 INPUT "IFA 100 on and channels set? (y or n)", ans$
IF ans$ <> "y" THEN
BEEP
PRINT "SET-UP THE IFA 100"
GOTO 40
END IF
```

```
'****************************************************************
'Read the blade chord locations for pressure ports and thermocouples

55 OPEN "C:\LELLO\chord.dat" FOR INPUT AS #2   'blade chord locations are

FOR J = 1 TO 23                                'stored into the data file

INPUT #2, chord(J)                             'chord.dat on the C: drive.

'PRINT "chord(", J, ")=", CHORD(J)

NEXT J

CLOSE #2

'****************************************************************

' Initial Test parameters:

CLS : LOCATE 7, 7

PRINT : PRINT "Data initialization:": PRINT

INPUT "Run Designation for all data files ? ", FileName$

iflag% = 0

dt$ = DATE$

time& = TIMER

CLS : LOCATE 7, 7

INPUT "Current temperature (deg. F)? ", Deg!

Temp! = (Deg! - 32!) * 5! / 9!

rholow! = 1.3947

drho! = .4666

Tlow! = 23.15

dTemp! = 100!
```

```
CLS : LOCATE 7, 7

rho! = rholow! - drho! * (Temp! + Tlow!) / dTemp!

PRINT "Current air density is "; rho!; SPC(1); "kg/m^3"

LOCATE 12, 7

PRINT " Press any key to continue..."

DO: LOOP WHILE INKEY$ = ""

CLS : LOCATE 7, 7

PRINT : PRINT "Data Initialization Complete."

'*****************************************************************
'Assign a unique identifier to the HP3852 for use with the GPIB

CALL IBFIND("HP3852", dvm%)

IF dvm% < 0 THEN CALL GPIBERR

CALL IBWRT(dvm%, "RST")


'Routine Branching for the MAIN MENU

DO
CLS : PRINT : PRINT "          MAIN MENU": PRINT

PRINT STRING$(80, "_"): PRINT

PRINT "01) Temperature Run"

PRINT "02) Pressure Run"

PRINT "03) Turbulence Frequency Run"

PRINT "04) Temperature and Frequency Run"

PRINT "05) Temp., Freq., and Press. Run"

PRINT "06) Frequency and Pressure Run"
```

```
PRINT "07) Fast Fourier Transform of Data"

PRINT "08) Current Temperature of the blade"

PRINT "09) Secondary Pressure in Manifold"

PRINT "10) EXIT"

PRINT : PRINT "Type your selection (01-10):"

chs$ = INPUT$(2)


' Use SELECT CASE to process response.

SELECT CASE chs$

CASE "01": CALL TRUN(dvm%, Temp!, FileName$, rho!)

                CASE "02": CALL PRUN(dvm%, rho!, dt$, FileName$, iflag%,
                           Temp!)

CASE "03": CALL FRUN(dvm%, FileName$)

CASE "04": CALL TRUN(dvm%, Temp!, FileName$, rho!)
   CALL FRUN(dvm%, FileName$)

CASE "05": CALL TRUN(dvm%, Temp!, FileName$, rho!)
                CALL PRUN(dvm%, rho!, dt$, FileName$, iflag%,
                          Temp!)
   CALL FRUN(dvm%, FileName$)

                CASE "06": CALL PRUN(dvm%, rho!, dt$, FileName$, iflag%,
                           Temp!)
   CALL FRUN(dvm%, FileName$)

CASE "07": CALL FFT

CASE "08": CALL TMON(dvm%)

CASE "09": CALL SECPRES(dvm%, sfa!)

CASE "10": EXIT DO
```

```
      CASE ELSE

      BEEP
      END SELECT

      LOOP

      END

      SUB CONVERT (VALS!(), NN%)
           DEFINT I-M
           DIM VALS!(2049)
           N = 2 * NN
           J = 1
           FOR i = 1 TO N STEP 2
      IF J <= i THEN GOTO 2200
      TEMPR = VALS(J)
      TEMPI = VALS(J + 1)
      VALS(J) = VALS(i)
      VALS(J + 1) = VALS(i + 1)
      VALS(i) = TEMPR
      VALS(i + 1) = TEMPI
      2200    M = N / 2
      2210    IF M >= 2 AND J > M THEN GOTO 2240
      J = J + M
      GOTO 2310
      2240    J = J - M
      M = M / 2
      GOTO 2210
      2310 NEXT i
           MMAX = 2
      2330 IF N <= MMAX THEN GOTO 2700
           ISTEP = 2 * MMAX
           THETA# = 6.28318530717959# / ISIGN / MMAX
           WPR# = -2 * (SIN(THETA# / 2) ^ 2)
           WPI# = SIN(THETA#)
           WR# = 1#
           WI# = 0.000000000000000
           FOR M = 1 TO MMAX STEP 2
      FOR i = M TO N STEP ISTEP
      J = i + MMAX
      TEMPR = CSNG(WR#) * VALS(J) - CSNG(WI#) * VALS(J + 1)
      TEMPI = CSNG(WR#) * VALS(J + 1) + CSNG(WI#) * VALS(J)
      VALS(J) = VALS(i) - TEMPR
      VALS(J + 1) = VALS(i + 1) - TEMPI
```

```
      VALS(i) = VALS(i) + TEMPR
      VALS(i + 1) = VALS(i + 1) + TEMPI
      NEXT i
      WTEMP# = WR#
      WR# = WR# * WPR# - WI# * WPI# + WR#
      WI# = WI# * WPR# + WTEMP# * WPI# + WI#
         NEXT M
         MMAX = ISTEP
         GOTO 2330
2700 'ALL DATA IS NOW CONVERTED AND IS READY TO BE STORED
      IF ISIGN = -1 THEN RETURN
      FOR i = 1 TO NN * 2
      VALS(i) = VALS(i) / NN
      NEXT i

      END SUB


DEFSNG I-M
SUB DVMERROR STATIC
PRINT "DVM GPIB ERROR"
END SUB


SUB FFT
      'THIS ROUTINE TRANSFORMS DATA FROM THE TIME TO FREQUENCY DOMAIN
      'OR BACK USING THE DANIELSON-LANCZOS FFT METHOD
      'THE DATA FORMAT REQUIRED FOR READING IS AS FOLLOWS:
      '  TOP LINE:
      '   NN      C      R       ISIGN
      'WHERE NN = # OF SAMPLED DATA POINTS < 1025
      '      C = # OF CHANNELS READ
      '      R = (1) IF REAL DATA, (2) IF COMPLEX DATA, (3) IF MAGNITUDE DATA
      '    ISIGN= (+1) IF DATA IS IN TIME DOMAIN, (-1) IF DATA IS IN FREQ DOMAIN
      '
      '  REMAINING DATA:
      '   TIME OR FREQ    CH1      CH2      .....'
      '
      '******************** FFT ROUTINE ********************
      '******************** MAIN PROGRAM ********************
      DIM VALS!(2049)
      DIM VALU!(2049, 6)
      DIM VALM!(1025, 6)
      'GET DATA
      PRINT "AVAIL DATA FILES:"
      FILES "\LELLO\*.FFT"
      INPUT "INPUT DATA FILE NAME W/O EXTENSION (.FFT): "; ND$
```

```
        OPEN "\LELLO\" + ND$ + ".FFT" FOR INPUT AS #1
        INPUT #1, NN, C, R, ISIGN
        S1$ = "CONVERTING FROM TIME TO FREQ DOMAIN"
        S2$ = "CONVERTING FROM FREQUENCY TO TIME DOMAIN"
        IF R = 3 THEN
PRINT "NO CAN DO"
GOTO 3000
END IF
        IF ISIGN = 1 THEN PRINT S1$ ELSE PRINT S2$
        FOR i = 1 TO NN * R
FOR J = 1 TO C + 1
INPUT #1, VALU(i, J)
NEXT J
        NEXT i
        CLOSE #1
        IF R = 1 THEN DELTA = 1 / NN / (VALU(2, 1) - VALU(1, 1))
        IF R = 2 THEN DELTA = 1 / NN / (VALU(3, 1) - VALU(1, 1))
        'STRIP DATA
        FOR JJ = 2 TO C + 1
CC = 1
FOR i = 1 TU NN * 2 STEP 2
        VALS(i) = VALU(CC, JJ)
IF R = 1 THEN VALS(i + 1) = 0 ELSE VALS(i + 1) = VALU(i + 1, JJ)
CC = CC + R
NEXT i
CC = 1

        'GO TO FFT SUBROUTINE
CALL CONVERT(VALS!(), NN%)

        'REPLACE DATA (UNSTRIP)
FOR i = 1 TO NN * 2
VALU(i, JJ) = VALS(i)
NEXT i
        'GET MAGNITUDE DATA
FOR i = 1 TO NN ^ 2 STEP 2
VALM(CC, JJ) = SQR(VALS(i) * VALS(i) + VALS(i + 1) * VALS(i + 1))
CC = CC + 1
NEXT i
        NEXT JJ
        '
        'DATA STORAGE ROUTINE
        'DATA STORED IN TWO SEPARATE FILES BASED ON THE ORIGINAL FILE NAME
        'THE TWO FILES WILL BE AS FOLLOWS:
        '   (1) NAME.TSD (TIME-SPLIT DATA) OR NAME.FSD (FREQUENCY SPLIT DATA)
```

```
        '& (2) NAME.TMD (TIME MAGNITUDE DATA) OF NAME.FMD (FREQ MAG DATA)
        '
        'STEP 1: CONVERT FIRST COLUMN (TIME <--> FREQUENCY)
        VALM(1, 1) = 0
        VALU(1, 1) = 0
        VALU(2, 1) = 0
        QTY = DELTA
        CC = 2
        FOR i = 3 TO 2 + NN STEP 2
VALU(i, 1) = QTY
VALU(i + 1, 1) = QTY
VALM(CC, 1) = QTY
QTY = QTY + DELTA
CC = CC + 1
        NEXT i
        '
        'STEP 2: STORE DATA
        IF ISIGN = 1 THEN EXT1$ = "-FM.DAT" ELSE EXT1$ = "-TM.DAT"
        IF ISIGN = 1 THEN EXT2$ = "-FS.DAT" ELSE EXT2$ = "-TS.DAT"
        OPEN "\LELLO\FFT\" + ND$ + EXT2$ FOR OUTPUT AS #2
        OPEN "\LELLO\FFT\" + ND$ + EXT1$ FOR OUTPUT AS #3
        PRINT #2, NN; C; 2; ISIGN * (-1)
        PRINT #3, NN; C; 3; ISIGN * (-1)
        FOR i = 1 TO NN * 2
FOR J = 1 TO C + 1
PRINT #2, VALU(i, J);
NEXT J
PRINT #2,
        NEXT i
        CLOSE #2
        FOR i = 1 TO NN
FOR J = 1 TO C + 1
PRINT #3, VALM(i, J);
NEXT J
PRINT #3,
        NEXT i
        CLOSE #3
3000 END SUB

SUB FINDERR STATIC
PRINT "IBFIND ERROR"
END SUB

SUB FRUN (dvm%, FileName$)
```

```
' This subroutine performs the voltage scan on the hot wire for
' conversion to velocities. Two channels are scanned consecutively
' with the HP44702B and the FET Multiplexer. The FET is connected
' internally to the HP44702B via a ribbon cable.

CLS
DIM chan1(2047) AS SINGLE, chan2(2047) AS SINGLE
DEFINT I-M

'***************************************************************

LOCATE 7, 7

INPUT "Use the same root filename as in MAIN ? ", ans$

IF ans$ <> "y" THEN
CLS : LOCATE 7, 7: INPUT " Input the new file name ", FileName$
END IF

OPEN "A:\" + "TU" + FileName$ + ".dat" FOR OUTPUT AS #1

COLOR 0, 3

CALL SECPRES(dvm%, sfa!)

CLS : LOCATE 10, 7

PRINT " RIBBON CABLE CONNECTED INTERNALLY TO FET MULTIPLEXER?"
PRINT :

PRINT "  WARNING!  TURN OFF HP3852A PRIOR TO CONNECTING RIBBON CABLE"
PRINT ""

PRINT "            Press any key to initiate scan"

DO: LOOP WHILE INKEY$ = ""

CLS : LOCATE 7, 7: PRINT "Turbuence scan in process"


CALL IBWRT(dvm%, "RST 400")
CALL IBWRT(dvm%, "USE 400")
CALL IBWRT(dvm%, "REAL WAVE(4095),OUT1(2047),OUT2(2047)")
```

```
CALL IBWRT(dvm%, "DISP OFF")

'************************************************************

'Configure the HP44702B for high-speed scanning.

CALL IBWRT(dvm%, "SCANMODE ON;CONF DCV;ARMODE BEFORE")

CALL IBWRT(dvm%, "TERM RIBBON;range 9;RDGSMODE COMPLETE")

CALL IBWRT(dvm%, "SCDELAY 0")

CALL IBWRT(dvm%, "SPER 10E-6")

CALL IBWRT(dvm%, "PRESCAN 2048;POSTSCAN 0")

CALL IBWRT(dvm%, "CLWRITE SENSE,321-322;ASCAN ON;SCTRIG SGL")

CALL IBWRT(dvm%, "XRDGS 400, 4096 INTO WAVE")    'Trigger the scan

'************************************************************

CALL IBWRT(dvm%, "SUB SEPARAT")    'Separate the readings into 2 arrays

CALL IBWRT(dvm%, "INTEGER I,J")

CALL IBWRT(dvm%, "J = 0")

CALL IBWRT(dvm%, "FOR I = 0 TO 4095 STEP 2")

CALL IBWRT(dvm%, "OUT1(J) = WAVE(I)")

CALL IBWRT(dvm%, "OUT2(J) = WAVE(I+1)")

CALL IBWRT(dvm%, "J = J+1")

CALL IBWRT(dvm%, "NEXT I")

CALL IBWRT(dvm%, "SUBEND")

'************************************************************

CLS : LOCATE 7, 7: PRINT "Processing Data"
```

```
'************************************************************

CALL IBWRT(dvm%, "CALL SEPARAT")      .

CALL IBWRT(dvm%, "SCTRIG HOLD")


'************************************************************

CLS : LOCATE 7, 7: PRINT "Writing data to temporary disk storage"

'************************************************************

'output  to the controller



'Transfer all readings to the computer controller.

CALL IBWRT(dvm%, "VREAD OUT1")
CALL IBRDF(dvm%, "C:\LELLO\FREQ1.DAT")
CALL IBWRT(dvm%, "VREAD OUT2")
CALL IBRDF(dvm%, "C:\LELLO\FREQ2.DAT")

'Read from temporary files into memory.

OPEN "C:\LELLO\FREQ1.DAT" FOR INPUT AS #3
OPEN "C:\LELLO\FREQ2.DAT" FOR INPUT AS #4
FOR i = 0 TO 2047
INPUT #3, chan1(i)
INPUT #4, chan2(i)
NEXT i
CLOSE #3
CLOSE #4


'************************************************************

CLS : LOCATE 7, 7
PRINT "Writing data file to disk A:"

time! = 0!
FOR i = 0 TO 2047
PRINT #1, time!, chan1(i), chan2(i)
```

```
   time! = time! + .00002
NEXT i
CLOSE #1


'•••••••••••••••••••••••••••••••••••••••••••••••••••••••••••••••••••••


CALL IBWRT(dvm%, "DISP ON;RST 400")


CLS : LOCATE 7, 7
PRINT "Turbulence data acquisition completed"

LOCATE 9, 8

PRINT "DISCONNECT THE RIBBON CABLE IF FINISHED"

PRINT : SLEEP 2: CLS : LOCATE 7, 7

PRINT "press any key to return to main menu"

DO: LOOP WHILE INKEY$ = ""

CLS

END SUB

DEFSNG I-M
SUB GPIBERR STATIC
PRINT "GPIB ERROR"
END SUB

SUB PLOTT (xdat() AS SINGLE, ydat() AS SINGLE, xmin!, xmax!, ymin!,
           ymax!, xlab$, ylab$, pltlab$, ntot%)
'•••••••••••••••••••••••••••••••••••••••••••••••••••••••••••••••••••••
'Subroutine PLOTT
'This subroutine creates a plot of ydat vs xdat

CLS

SCREEN 9   'Hi-res graphics mode

VIEW (120, 10)-(570, 290), , 1
```

```
WINDOW (xmin!, ymin!)-(xmax!, ymax!)

style% = &HFF00

LOCATE 23, 42: PRINT pltlab$

LOCATE 1, 9: PRINT ymax!: LOCATE 10, 7: PRINT ylab$: LOCATE 21, 9

PRINT ymin!

LOCATE 22, 14: PRINT xmin!: LOCATE 22, 43: PRINT xlab$: LOCATE 22, 71

PRINT xmax!

VIEW PRINT 24 TO 25:

PRINT SPC(14); , "hit any key to return to Main Menu"

CLS

LINE (1, 0)-(0, 0), , , style%
FOR i = 1 TO ntot%
x = xdat(i)
y = ydat(i)
LINE -(x, y)
NEXT i

DO: LOOP WHILE INKEY$ = ""

CLS

SCREEN 0: COLOR 3, 0

END SUB

SUB PRUN (dvm%, rho!, dt$, FileName$, iflag%, Temp!)

'**********************************************************************
' A scanivalve driver program for the HP 3852A data acquisition system.
' Programmed by  Lt Galassi 6/21/89

'  This subroutine performs a pressure scan on the turbine blade
'  using the HP3852A data acquisition system to drive a scanivalve
'  step motor over 30 pressure ports.
'
```

```
' The ports are assigned as follows:
'
'      port 0          atmospheric
'           1-10       blade static
'           11         atmospherric
'           12-21      blade static
'           22         atmospheric
'           23,24,25   blade static
'           26         atmospheric
'           27         pitot head
'           28         pitot static
'           29-36      atmospheric
'-------------------------------------------------------------------


SHARED chord()  AS SINGLE

DEFINT I-M

DIM xdat(23) AS SINGLE, ydat(23)  AS SINGLE

DIM pscan(30) AS SINGLE

CLS 2

IF iflag% = 1 THEN
   INPUT "File name to store Cp data ? ", FileName$
END IF

   iflag% = 1

OPEN "A:\CP\" + "CP" + FileName$ + ".cp" FOR OUTPUT AS #1
      .
OPEN "A:\CP\" + "GR" + FileName$ + ".DAT" FOR OUTPUT AS #3

CLS

'CALL TMON(dvm%)

SLEEP 4

COLOR 0, 3

LOCATE 7, 7
```

```
INPUT "Secondary flow on (y) or (n)?", ans$

IF ans$ = "y" THEN
CLS : LOCATE 7, 7
CALL SECPRES(dvm%, sfa!)
PRINT "Secondary flow pressure (kPa) = ", sfa!
END IF

LOCATE 8, 7: PRINT "BLADE PRESSURE SURVEY (approx 115 sec. duration)"

'*******************************************************************
'set up the HP44701 for voltage measurements

CALL IBWRT(dvm%, "RST 600")

WRT$ = "REAL A(1),B(1), PSCAN(30),OUTPUT(30),C(49),L,H,M,S"

CALL IBWRT(dvm%, WRT$)

'   Arrays are designated as follows:
'
'               A - voltages from the pressure transducer calibration
'               B - corresponding pressures to the voltages listed in
'                   array A.
'               PSCAN - actual pressures in kPa units
'               OUTPUT - a temporary holding array for HP3852 buffer.

CALL IBWRT(dvm%, "VWRITE A,-10.000,10.000")

CALL IBWRT(dvm%, "VWRITE B,-6.8242,9.8271")

'   Perform the actual pressure scan

CALL IBWRT(dvm%, "USE 600;AZERO ONCE; NPLC 16")

CALL IBWRT(dvm%, "CLOSE 101")                'this call homes the scanivalve

CALL IBWRT(dvm%, "OPEN 101;CONF DCV")

CALL IBWRT(dvm%, "NRDGS 50")

WRT$ = "MEAS DCV, 221,INTO C"               'read atmospheric press.

CALL IBWRT(dvm%, WRT$)
```

```
CALL IBWRT(dvm%, "STAT L,H,M,S,C")

CALL IBWRT(dvm%, "PSCAN(0) = M")

CALL IBWRT(dvm%, "DISP PSCAN(0)")

CALL IBWRT(dvm%, "SUB LOOP")                    'HP 3852A subroutine

CALL IBWRT(dvm%, "INTEGER I")

CALL IBWRT(dvm%, "FOR I = 1 TO 30")

CALL IBWRT(dvm%, "CLOSE 100")

CALL IBWRT(dvm%, "OPEN 100;CONF DCV;NRDGS 50")

CALL IBWRT(dvm%, "MEAS DCV, 221, USE 600, INTO C")

CALL IBWRT(dvm%, "STAT L,H,M,S,C")

CALL IBWRT(dvm%, "PSCAN(I) = M")

CALL IBWRT(dvm%, "DISP PSCAN(I)")

CALL IBWRT(dvm%, "NEXT I")

CALL IBWRT(dvm%, "SUBEND")

CALL IBWRT(dvm%, "CALL LOOP")

SLEEP 119                                       'allow 120 seconds for scan

WRT$ = "CONV A,B,PSCAN, INTO OUTPUT"

CALL IBWRT(dvm%, WRT$)

CALL IBWRT(dvm%, "VREAD OUTPUT")

'*******************************************************************

'Read output into a temporary file on the hard disk

CALL IBRDF(dvm%, "C:\LELLO\PRESS.DAT")

OPEN "C:\LELLO\PRESS.DAT" FOR INPUT AS #2
```

```
FOR i = 0 TO 30
INPUT #2, pscan(i)
NEXT i

CLOSE #2

'*************************************************************************
'
'  Output the data into FileName$
'  Array locations are assigned as follows:
'  0,11,22,29-36 - Atmospheric pressure
'  1-10,12-21,23-25  - Blade static pressures
'  27 -Pitot head press.
'  28- Pitot static press.

CLS

COLOR 0

PRINT "Pressure Measurements on Turbine Blade #3"

PRINT #1, "Presure Measurements on Turbine Blade # 3"

PRINT : PRINT "Date of run:", dt$

PRINT : PRINT #1, "Date of run:", dt$

PRINT : PRINT "Time of run:", TIMER

PRINT : PRINT #1, "Time of run:", TIMER

PRINT : PRINT #1, "Secondary flow pressure:", sfa!

PRINT : PRINT #1, "Head and static pitot press. (Kpa):", pscan(27), pscan(28)

' Note: q is in kPa

q! = pscan(27) - pscan(28)

deltah! = q! * 1000! / 249!

PRINT : PRINT "The difference in height of the manometer columns"

PRINT "is computed by scanivalve measurements to be: "; deltah!
```

```basic
INPUT " Is this correct? (y or n) ", ans$

IF ans$ <> "y" THEN
BEEP
PRINT : PRINT "SCANIVALVE readings are faulty"
PRINT "Returning to Main Menu": SLEEP 10
CLOSE #1: CLOSE #3: COLOR 4, 11: RETURN
END IF


Vel! = SQR(2000! * q! / rho!)

PRINT : PRINT "Freestream velocity (m/sec): "; Vel!

nu! = 1.144E-05 + (Temp! + 23.15) * 9.48E-06 / 100!

Re! = Vel! * .114 / nu!     '0.144 = chord length

PRINT "Reynold's no. = ", Re!

PRINT : PRINT #1, "Freestream velocity (m/sec):", Vel!

PRINT #1, "Reynold's number :", Re!

SLEEP 5

' Perform shift on PSCAN()

FOR i = 11 TO 20
   pscan(i) = pscan(i + 1)
NEXT i

FOR i = 21 TO 23
   pscan(i) = pscan(i + 2)
NEXT i

PRINT STRING$(70, "_")

PRINT #1, STRING$(70, "_")

PRINT #1, " Port No.      CHORD LOCATION              Cp"

LOCATE 8, 1
```

```basic
PRINT " CHORD LOCATION", SPACE$(12), "Cp"

LOCATE 9, 1

PRINT STRING$(80, "_")

LOCATE 22, 1

PRINT STRING$(80, "_")

VIEW PRINT 8 TO 20

CLS 2

FOR i = 1 TO 10
  PRINT i, chord(i), (pscan(i) - pscan(28)) / q!
  PRINT #1, i, chord(i), (pscan(i) - pscan(28)) / q!
  PRINT #3, i, chord(i), (pscan(i) - pscan(28)) / q!
NEXT i

PRINT "        Hit any key to continue"

DO: LOOP WHILE INKEY$ = ""

FCR i = 11 TO 20
  PRINT i, chord(i), (pscan(i) - pscan(28)) / q!
  PRINT #1, i, chord(i), (pscan(i) - pscan(28)) / q!
  PRINT #3, i, chord(i), (pscan(i) - pscan(28)) / q!
NEXT i

PRINT "        Hit any key to continue"

DO: LOOP WHILE INKEY$ = ""

FOR i = 21 TO 23
  PRINT i, chord(i), (pscan(i) - pscan(28)) / q!
  PRINT #1, i, chord(i), (pscan(i) - pscan(28)) / q!
  PRINT #3, i, chord(i), (pscan(i) - pscan(28)) / q!
NEXT i

PRINT "Hit any key to continue"

DO: LOOP WHILE INKEY$ = ""

'This section drives the plotter.
```

```basic
ntot% = 23     'This no. corresponds to the total no. of suction side ports

ylab$ = "Cp"

xlab$ = "x/c"

pltlab$ = "Cp on the turbine blade"

xmin! = 0!

xmax! = 1!

ymin! = -4.5

ymax! = 4.5

FOR i = 1 TO ntot%
ydat!(i) = (pscan(i) - pscan(28)) / q
xdat!(i) = chord(i)
NEXT i

CALL PLOTT(xdat!(), ydat!(), xmin!, xmax!, ymin!, ymax!, xlab$,
         ylab$, pltlab$, ntot%)

CLOSE #1: CLOSE #3

CALL IBWRT(dvm%, "RST")

END SUB

DEFSNG I-M
SUB SECPRES (dvm%, sfa!)

'Measure the secondary flow manifold pressure

CALL IBWRT(dvm%, "REAL P1(1),V1(1),V2(1),OUTPUT(1)")

CALL IBWRT(dvm%, "vwrite V1,.000,.319")

CALL IBWRT(dvm%, "vwrite P1, 0.000,633.6505")

CALL IBWRT(dvm%, "RST 600;USE 600; AZERO ONCE;NPLC 16")

CALL IBWRT(dvm%, "CONFMEAS DCV,222,INTO V2")
```

```basic
CALL IBWRT(dvm%, "DISP V2(O)")

CALL IBWRT(dvm%, "CONV V1,P1,V2,INTO OUTPUT")

CALL IBWRT(dvm%, "VREAD OUTPUT(O)")

rd$ = SPACE$(16)

CALL ibrd(dvm%, rd$)

sfa! = VAL(rd$)

CLS : LOCATE 7, 7

PRINT "Secondary pressure (kPa) =", sfa!

PRINT : LOCATE 9, 7

PRINT "Press any key to continue"

DO: LOOP WHILE INKEY$ = ""

CLS

END SUB

SUB TMON (dvm%)

'*******************************************************************

'Configure the HP3852 to sense blade temperature

CALL IBWRT(dvm%, "USE 600;RST 600;REAL T;AZERO ONCE")

CALL IBWRT(dvm%, "CLOSE 104")

CALL IBWRT(dvm%, "CONFMEAS TEMPJ,206, INTO T")

CALL IBWRT(dvm%, "OPEN 104")

'*******************************************************************
'Read datum from HP3852

CALL IBWRT(dvm%, "DISP T")
```

```basic
CALL IBWRT(dvm%, "VREAD T")

rd$ = SPACE$(16)

CALL ibrd(dvm%, rd$)

'**************************************************************

T! = VAL(rd$)              'convert the string value into a
 'number
CLS

LOCATE 7, 7

PRINT "Blade Temperature (F) is currently: ", (T! * 9! / 5!) + 32!

PRINT : PRINT

IF T! > 65.56 THEN
CALL IBWRT(dvm%, "CLOSE 104")                'this call turns power
BEEP: SLEEP 1: BEEP: SLEEP 1: BEEP
PRINT "Blade temperature too high!": PRINT
PRINT "Check Power Supply": PRINT
PRINT " Press any key to continue"
DO: LOOP WHILE INKEY$ = ""
CALL IBWRT(dvm%, "open 104")
CLS 2
END IF

LOCATE 8, 7

PRINT "Press any key to continue"

DO: LOOP WHILE INKEY$ = ""

CLS

END SUB

SUB TRUN (dvm%, Temp!, FileName$, rho!)
'***************************************************************

'This subroutine performs the temperature scan on the turbine blade
'and stores the data in A:/heat/FileName$.dat. The HP3852 is used to
```

```
'acquire data along with the HP 44713 FET Multiplexer.

DIM nu(28) AS SINGLE

DIM rhol(28) AS SINGLE

DIM t2scan(28) AS SINGLE

DIM area(23) AS SINGLE

DIM Vel(23) AS SINGLE

DIM S(23) AS SINGLE

DIM Nslt(23) AS SINGLE

DIM St(23) AS SINGLE

DIM xdat!(23), ydat!(23)

SHARED chord() AS SINGLE

DEFINT I-M

CALL TMON(dvm%)

'*****************************************************************
'Read the blade temperatures

CALL IBWRT(dvm%, "RST 600; AZERO ONCE;NPLC 1")

CALL IBWRT(dvm%, "SUB TBLADE")

CALL IBWRT(dvm%, "REAL A(21)")

CALL IBWRT(dvm%, "CLOSE 104")

CALL IBWRT(dvm%, "CONFMEAS TEMPJ,200-220,223,INTO A")

CALL IBWRT(dvm%, "OPEN 104")

CALL IBWRT(dvm%, "VREAD A")

CALL IBWRT(dvm%, "SUBEND")
```

```
'••••••••••••••••••••••••••••••••••••••••••••••••••••••••••••••••••••
' Interactive input for the power parameters on the turbine blade.

DO
CLS : LOCATE 7, 7

INPUT "Input the delta H of the tunnel: ", deltah!

Vinf! = SQR(2! / rho! • deltah! • 249!)

LOCATE 9, 7

PRINT " The freestrem velocity is "; Vinf!; " m/s"

SLEEP 3

CLS : LOCATE 7, 7

INPUT "Power supply current (def. = 38.5 amps) ? ", Curr!

IF Curr! = 0! THEN Curr! = 38.5

LOCATE 8, 7

Resist! = .13        'Ohms; Blade area = 0.26192 m x 0.11000 m

7        INPUT "New filename y or n ? ", ans$

IF ans$ = "y" THEN

INPUT "Enter New file name :", FileName$

END IF

CLS : LOCATE 7, 7

INPUT "Is the secondary injection on (y or n) ? ", answer$

IF answer$ = "y" THEN

CALL SECPRES(dvm%, sfa!)

ELSE

sfa! = 0!
```

```
END IF

'•••••••••••••••••••••••••••••••••••••••••••••••••••••••••••••••••••

' Compute the total energy flux input into the blade

Qheat! = (Curr! ^ 2) * Resist!

'•••••••••••••••••••••••••••••••••••••••••••••••••••••••••••••••••••••

CLS : LOCATE 3, 7: PRINT "Temperature Scan Menu"

PRINT STRING$(80, "_"); PRINT

PRINT "1) Temperature Scan"

PRINT

PRINT "2) EXIT"

PRINT : PRINT "type your selection (1-2)"

chs$ = INPUT$(1)

SELECT CASE chs$

CASE "1"
CLS : LOCATE 7, 7
'Turbulence ON temperature scan on the blade

PRINT "Press any key to initiate scan"

DO: LOOP WHILE INKEY$ = ""

CALL IBWRT(dvm%, "DISP OFF")

CALL IBWRT(dvm%, "CALL TBLADE")

CALL IBRDF(dvm%, "C:\LELLO\T2SCAN.DAT")

CALL IBWRT(dvm%, "DISP ON")

'*******************************************************************
```

```
'Read data from storage

OPEN "C:\LELLO\T2SCAN.DAT" FOR INPUT AS #1

INPUT #1, t2scan(28)

INPUT #1, tinf!

FOR i = 23 TO 13 STEP -1
INPUT #1, t2scan(i)
NEXT i

FOR i = 12 TO 9 STEP -1    'These nodes are dead
t2scan(i) = tinf!
NEXT i

t2scan(0) = tinf!
t2scan(1) = tinf!
t2scan(2) = tinf!
t2scan(24) = tinf!


FOR i = 8 TO 3 STEP -1
INPUT #1, t2scan(i)
NEXT i

INPUT #1, t2scan(25)

INPUT #1, t2scan(26)

INPUT #1, t2scan(27)

CLOSE #1

'***********************************************************************

'Read in the Pressure Coefficients on the blade to be used in computation of
'Nusselt and Stanton numbers.

OPEN "a:\cp\gr" + FileName$ + ".dat" FOR INPUT AS #1

Vel(0) = 0!

FOR i = 1 TO 23
INPUT #1, dummy, dummy, Vel(i)
```

```
NEXT i

CLOSE #1

'read in thermocouple distances along the blade S()

OPEN "C:\lello\data\S.dat" FOR INPUT AS #1

FOR i = 1 TO 23
INPUT #1, S(i)
NEXT i

CLOSE #1

'*********************************,>**************************************
'perform energy balance calculations

'conduction constants

uk! = .026      'urethane foam thermal conductivity

ak! = .0263     'air thermal conductivity

'convection constants

Cp! = 1000.7

Pr! = .707

'compute nu(i) and rhol(i) on the blade

FOR i = 0 TO 28
nu(i) = 1.144E-05 + ((t2scan(i) + tinf!) / 2! + 23.15)
              * 9.48E-06 / 100!

              rhol(i) = 1.3947 - .3797 * ((t2scan(i) + tinf!) / 2! +
              23.15) / 100!
NEXT i

'radiation constants

eps! = .17         'emmisivity for polished stainless steel at 300 K

sigma! = 5.67E-08
```

```
'compute local velocities on the blade

FOR i = 1 TO 23
Vel(i) = SQR((Vinf! ^ 2) * ABS(1! - Vel(i)))
NEXT i

'compute local Reynold's numbers on the blade

FOR i = 1 TO 23
Vel(i) = Vel(i) * S(i) / nu(i)
NEXT i

'compute the Nusselt and Stanton numbers for the blade only in region
'of active thermocouples.

ATot! = .0288112

FOR i = 0 TO 23                     'clean the arrays
Nslt(i) = 0!
St!(i) = 0!
NEXT i

dl! = .009

FOR i = 3 TO 4
F1! = uk! * (t2scan(i) - t2scan(25)) / dl!
F2! = eps! * sigma! * (t2scan(i) ^ 4 - tinf!   4)
F3! = (t2scan(i) - tinf!)
h! = (Qheat! / ATot! + F1! - F2!) / F3!
Nslt(i) = ABS(h!) * S(i) / ak!
St(i) = Nslt(i) / (Pr! * Vel(i))
NEXT i


i = 5

F1! = uk! * (t2scan(i) - t2scan(26)) / dl!
F2! = eps! * sigma! * (t2scan(i) ^ 4 - tinf! ^ 4)
F3! = (t2scan(i) - tinf!)
h! = (Qheat! / ATot! + F1! - F2!) / F3!
Nslt(i) = ABS(h!) * S(i) / ak!
St(i) = Nslt(i) / (Pr! * Vel(i))


FOR i = 20 TO 23
F1! = uk! * (t2scan(i) - t2scan(25)) / dl!
```

```
F2! = eps! * sigma! * (t2scan(i) ^ 4 - tinf! ^ 4)
F3! = (t2scan(i) - tinf!)
h! = (Qheat! / ATot! + F1! - F2!) / F3!
Nslt(i) = ABS(h!) * S(i) / ak!
St(i) = Nslt(i) / (Pr! * Vel(i))
NEXT i

dl! = .012

FOR i = 17 TO 19
F1! = uk! * (t2scan(i) - t2scan(26)) / dl!
F2! = eps! * sigma! * (t2scan(i) ^ 4 - tinf! ^ 4)
F3! = (t2scan(i) - tinf!)
h! = (Qheat! / ATot! + F1! - F2!) / F3!
Nslt(i) = ABS(h!) * S(i) / ak!
St(i) = Nslt(i) / (Pr! * Vel(i))
NEXT i

dl! = .005

i = 6
F1! = uk! * (t2scan(i) - t2scan(27)) / dl!
F2! = eps! * sigma! * (t2scan(i) ^ 4 - tinf! ^ 4)
F3! = (t2scan(i) - tinf!)
h! = (Qheat! / ATot! + F1! - F2!) / F3!
Nslt(i) = ABS(h!) * S(i) / ak!
St(i) = Nslt(i) / (Pr! * Vel(i))

dl! = .01

FOR i = 15 TO 16
F1! = uk! * (t2scan(i) - t2scan(27)) / dl!
F2! = eps! * sigma! * (t2scan(i) ^ 4 - tinf! ^ 4)
F3! = (t2scan(i) - tinf!)
h! = (Qheat! / ATot! + F1! - F2!) / F3!
Nslt(i) = ABS(h!) * S(i) / ak!
St(i) = Nslt(i) / (Pr! * Vel(i))
NEXT i

dl! = .0045

FOR i = 7 TO 8
F1! = uk! * (t2scan(i) - t2scan(28)) / dl!
F2! = eps! * sigma! * (t2scan(i) ^ 4 - tinf! ^ 4)
F3! = (t2scan(i) - tinf!)
```

```
h! = (Qheat! / ATot! + F1! - F2!) / F3!
Nslt(i) = ABS(h!) * S(i) / ak!
St(i) = Nslt(i) / (Pr! * Vel(i))
NEXT i


dl! = .005

FOR i = 13 TO 14
F1! = uk! * (t2scan(i) - t2scan(28)) / dl!
F2! = eps! * sigma! * (t2scan(i) ^ 4 - tinf! ^ 4)
F3! = (t2scan(i) - tinf!)
h! = (Qheat! / ATot! + F1! - F2!) / F3!
Nslt(i) = ABS(h!) * S(i) / ak!
St(i) = Nslt(i) / (Pr! * Vel(i))
NEXT i


'*****************************************************************************
'save data on disk

CLS : LOCATE 1, 10: PRINT "Temperature output"

PRINT

OPEN "A:\HEAT\" + "HT" + FileName$ + ".DAT" FOR OUTPUT AS #2

PRINT #2, "File:"; SPC(1); FileName$

PRINT "Secondary flow pressure = "; SPC(1); sfa!; SPC(2); "kPa"

PRINT #2, "Secondary flow pressure = "; SPC(1); sfa!; SPC(2); "kPa"

PRINT #2, "Electrical energy input = "; SPC(1); Qheat!; SPC(1); "Watts"

PRINT , "x/c", "Re no.", "Nusselt", "Stanton"

PRINT #2, "x/c", "Re no.", "Nusselt", "Stanton"

FOR i = 1 TO 23
PRINT #2, chord(i), Vel(i), Nslt(i), St(i)
PRINT chord(i), Vel(i), Nslt(i), St(i)
NEXT i

CLOSE #2

PRINT "Press any key to continue"
```

```
DO: LOOP WHILE INKEY$ = ""

'********************************************************************
'Plot out the heat transfer solution for the blade using the
'PLOTT subroutine.
'This section drives the plotter for turbulence ON conditions.

ntot1% = 8      'This no. corresponds to the total no. of pressure side
        'thermocouples

ntot2% = 12     'This no. corresponds to the total no. of suction side
        'thermocouples

ylab$ = "Temp. (C)"

xlab$ = "x/c"

pltlab$ = "Temp. on turbine blade "

xmin! = 0!

xmax! = 1!

ymin! = 20

ymax! = 65

FOR i = 1 TO ntot1%
ydat(i) = t2scan(i)
xdat(i) = chord(i)
NEXT i

FOR i = ntot1% + 1 TO ntot2%
xdat(i) = chord(i)
ydat(i) = 0
NEXT i

FOR i = ntot2% + 1 TO ntot1% + ntot2% + 3
ydat(i) = t2scan(i - 4)
xdat(i) = chord(i)
NEXT i

ntot% = ntot1% + ntot2% + 3
```

```
CALL PLOTT(xdat!(), ydat!(), xmin!, xmax!, ymin!, ymax!, xlab$,
          ylab$, pltlab$, ntot%)

CASE "2": EXIT DO

CASE ELSE: BEEP

END SELECT

LOOP

CALL IBWRT(dvm%, "RST")

END SUB
```

Vita

Captain Lello Galassi was born on 8 June 1955 in San Jose, California. He graduated from Whitefish High School in Whitefish, Montana in 1973, and enlisted in the USAF in 1977. He attended the University of Washington from which he recieved a degree of Bachelor of Aeronautics and Astronautics in June 1985. He recieved his AF commission, through OTS, in November 1985, and was assigned as an Astronautical Engineer for the Space Defense and Surveillance Project Office, Space Division, Los Angeles AFB, California. He served as a test and development engineer on the Air-Launched Anti-Satellite Weapon System and Space Defense Initiative (SDI) systems until entering the School of Engineering, Air Force Institute of Technology, in May 1988.

Permanent address: 5935 Hwy. 93 S.
              Whitefish, Montana 59937

REPORT DOCUMENTATION PAGE			Form Approved OMB No. 0704-0188
1a. REPORT SECURITY CLASSIFICATION UNCLASSIFIED		**1b RESTRICTIVE MARKINGS**	
2a. SECURITY CLASSIFICATION AUTHORITY		**3 DISTRIBUTION/AVAILABILITY OF REPORT** Approved for public release; distribution unlimited	
2b. DECLASSIFICATION/DOWNGRADING SCHEDULE			
4. PERFORMING ORGANIZATION REPORT NUMBER(S) AFIT/GAE/ENY/89D-11		**5. MONITORING ORGANIZATION REPORT NUMBER(S)**	
6a. NAME OF PERFORMING ORGANIZATION School of Engineering	**6b. OFFICE SYMBOL (If applicable)** AFIT/ENY	**7a. NAME OF MONITORING ORGANIZATION**	
6c. ADDRESS (City, State, and ZIP Code) Air Force Institute of Technology (AU) Wright-Patterson AFB, Ohio 45433-6583		**7b. ADDRESS (City, State, and ZIP Code)**	
8a. NAME OF FUNDING/SPONSORING ORGANIZATION Wright Research and Development Center	**8b. OFFICE SYMBOL (if applicable)** WRDC/POTC	**9 PROCUREMENT INSTRUMENT IDENTIFICATION NUMBER**	

8c. ADDRESS (City, State, and ZIP Code) Wright Research and Development Center Wright-Patterson AFB, Ohio 45433	**10 SOURCE OF FUNDING NUMBERS**			
	PROGRAM ELEMENT NO.	**PROJECT NO.**	**TASK NO**	**WORK UNIT ACCESSION NO**

11. TITLE (Include Security Classification)

Turbulence Scale Effects on Heat Transfer in a Linear Turbine Cascade

12. PERSONAL AUTHOR(S)

Lello Galassi, B.S., Capt, USAF

13a. TYPE OF REPORT MS Thesis	**13b. TIME COVERED** FROM _____ TO _____	**14. DATE OF REPORT (Year, Month, Day)** 1989 December	**15 PAGE COUNT** 281

16. SUPPLEMENTARY NOTATION

17.	COSATI CODES		**18. SUBJECT TERMS (Continue on reverse if necessary and identify by block number)**	
FIELD	**GROUP**	**SUB-GROUP**	Turbomachinery	Turbulent Boundary Layer
13	07		Turbulence	Heat Transfer

19. ABSTRACT (Continue on reverse if necessary and identify by block number)

Thesis Advisor: Paul I. King, LtCol, USAF
Assistant Professor
Department of Aeronautical Engineering

20. DISTRIBUTION/AVAILABILITY OF ABSTRACT ☒ UNCLASSIFIED/UNLIMITED ☐ SAME AS RPT ☐ DTIC USERS	**21 ABSTRACT SECURITY CLASSIFICATION** UNCLASSIFIED	
22a NAME OF RESPONSIBLE INDIVIDUAL Paul I. King, Assistant Professor	**22b TELEPHONE (Include Area Code)** (513) 255-2362	**22c OFFICE SYMBOL** ENY

DD Form 1473, JUN 86   *Previous editions are obsolete*   SECURITY CLASSIFICATION OF THIS PAGE

Heat transfer for a turbine cascade is examined for turbulence scale effects. The turbulence integral scale and microscale lengths of the free-stream flow are controlled by air-jet injection through a grid placed in the free-stream flow. Air is injected into the flow in three primary directions: co-flow, cross-flow, and counter-flow, at several injection pressures. Results are obtained for heat transfer on the blade without the jet-grid in the free-stream flow. Surface pressures on the turbine blade are examined for three injection directions. Surface heat transfer on the blade and turbulence intensity and turbulence scale results are obtained for two grid locations, three air injection orientations, and three injection orifice diameters over a range of injection pressures. Turbulence integral scale and microscale lengths are measured in two free-stream flow coordinates. The turbulence intensity decay is determined. Heat transfer on the turbine blade is compared with the turbulence integral scale and microscale lengths.

Results show the integral scale length is primarily dependent on the diameter of the jet-grid tube, but may be controlled to a lesser degree by changing the orientation of the jet-grid injection to a co-flow or counter-flow direction; or by changing the secondary air-jet injection pressure. The turbulence microscale is primarily dependent on the location of the jet-grid within the flow, but, to a lesser degree, controlled by the orientation of the jet-grid injection, jet orifice diameter, and injection pressure.

In general, jet-grid injection produces a lower turbulence intensity of the free-stream flow, larger turbulence microscale, and lower surface heat transfer coefficient. The turbulence integral scale is nearly constant with turbulence intensity and its length is on the order of the outside diameter if the jet-grid tube. The Stanton number and the Nusselt number increase with increasing turbulence intensity and decreasing turbulence microscale length. Turbulent boundary layer heat transfer predictions compare favorably on the pressure surface of the turbine blade, except at the leading edge of the turbine blade for moderate free-stream turbulence levels (4-6 percent). Laminar boundary layer heat transfer predictions compare favorably on the turbine blade suction surface for low free-stream turbulence levels (0-1.3 percent).